First principle modeling and simulation of hydrogen interaction with carbon nanotubes

Ren, Yunxia

2006

Ren, Y. X. (2006). First principle modeling and simulation of hydrogen interaction with carbon nanotubes. Doctoral thesis, Nanyang Technological University, Singapore.

https://hdl.handle.net/10356/6327

https://doi.org/10.32657/10356/6327

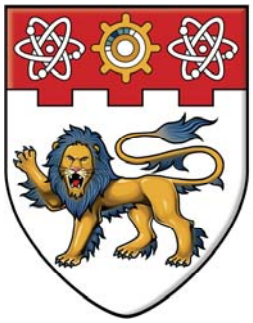

NANYANG TECHNOLOGICAL UNIVERSITY

FIRST PRINCIPLE MODELING AND SIMULATION OF HYDROGEN INTERACTION WITH CARBON NANOTUBES

REN YUNXIA

SCHOOL OF MECHANICAL & AEROSPACE ENGINEERING

2006

First Principle Modeling and Simulation of Hydrogen Interaction with Carbon Nanotubes

REN YUNXIA

SCHOOL OF MECHANICAL & AEROSPACE ENGINEERING
NANYANG TECHNOLOGICAL UNIVERSITY

A thesis submitted to the Nanyang Technological University
in fulfilment of the requirement for the degree of
Doctor of Philosophy

2006

ABSTRACT

The work presented in this thesis addresses the issues concerning the use of carbon nanotube as a storage media for hydrogen. The work is theoretical modeling and simulation based, and it attempts to make sense of vast and scattered experimental data reported in the literature with regard to the storage capacity, some so severe such that reported results are unrepeatable by other groups. In the thesis, we provide the *ab initio* theoretical framework for describing the underlying basic mechanism governing the physisorption and chemisorption processes of hydrogen on and into carbon nanotubes. We introduce the multiscale ONIOM scheme for this study, which overcomes the difficulties when using standalone methodologies which many researchers are currently applying. These are either too coarse and therefore unable to capture the reaction processes with low level methods, or too compute intensive when higher level methods are used.

In the present multiscale methodology, high level quantum mechanical DFT (density functional theory) is applied at the reaction sites while the rest of the problem domain is modeled using lower level molecular mechanics models. The results reported here therefore take into account the effects of atomospheric interaction. The natural bond orbitals and density of states are used to study bond formation, bond breaking and bond recovery. In addition, determining the transition states provides a complete picture of the entire reaction pathway for the physisorption and chemisorption processes.

The following are studied in detail:

i. state of hydrogen molecules confined in carbon nanostructures such as C_{60} fullerene and carbon nanocapsules;

ii. physisorption and chemisorption of hydrogen molecules and atoms onto the outer surface wall of (5,5) armchair SWNTs, and the flip-in mechanism for the insertion of hydrogen atoms into the SWNT; and

iii. local reactivates and the thermodynamic properties of the chemical reactions.

The major conclusions of this work are:

a. the chemisorption of hydrogen atoms onto the exterior of the CNT wall is energetically favorable;

b. the flip-in process for the first hydrogen atom is endothermic requiring an energy absorption of $0.8eV$; and

c. the flip-in process for the second hydrogen atom is energetically very unfavorable with an energy reaction barrier of $9.664eV$.

ACKNOWLEDGEMENTS

There are many people who have supported and assisted me through my last three years as a doctoral student. I would like to thank them with my most sincere words and blesses.

First and foremost, I would like to thank my supervisors Associate Professor Ng Teng Yong and Professor Liew Kim Meow for their excellent ideas, brilliant guidance, and encouraging suggestions and comments. I am extremely grateful to them for their passion to bring me into this area and their vast knowledge of the subject coupled with their dedication to research has been an inspiration to me.

I would like to thank all the research staff and graduate students at the Centre for Advanced Numerical Engineering Simulations (CANES) and Nanyang Center for Supercomputing and Visualization (NCSV), for their friendship and support. During the course of my research, I have benefited greatly from discussions with other researchers, and I would like to thank Dr. Goh Sor Koon and Dr. He Xiaoqiao for their advice on this project. In addition, I would like thank NTU for providing me with the necessary scholarship to carry out this research.

Lastly, I must take this opportunity to thank my family for their encouragement, care and support through these years. Without them, I would not have been able pursue this endeavor. To Liu Ying, my greatest love, if not for you, I would not have been able to sail through the pressures and accomplish this journey. For whatever I needed from you, you have provided and I dedicate this thesis to you. With my heartfelt thanks and love to all of you.

PUBLICATIONS

The following papers are related to the present research:

1. "State of Hydrogen Molecules Confined in C_{60} Fullerene and Carbon Nanocapsule Structures" *Carbon* 44: 379-406, 2006

2. Book Chapter on "Multiscale Modeling of Carbon Nanostructures", in contribution to Fundamentals & Applications of Multiscale Materials Modeling, Edited by Z.X. Guo (Queen Mary, University of London), Woodhead Publishing, Cambridge, U.K.

3. "Multiscale ONIOM for Fully Coupled Local Reactivity of Hydrogen Molecules On and Into Carbon Nanotubes" (in preparation)

4. "Thermodynamic Properties of the Chemical Reactions of Hydrogen Atoms Chemisorbed on (5,5) Armchair Single-Wall Carbon Nanotubes" (in preparation)

CONTENTS

LIST OF FIGURES

LIST OF TABLES

CHAPTER 1

INTRODUCTION

Today there is a growing need for alternative and clean fuels which can replace our growing dependence on fossil fuels for vehicular propulsion. One such candidate is hydrogen, the most abundant element in the universe and creating no pollutants when combusted. However, hydrogen storage and transportation is the bottleneck in the breakthrough of utilizing hydrogen as energy carrier in automotive applications. The overall criteria for choosing a storage method should be safety and ease of use. In the last few years, different storage technologies have been investigated to develop a secure and cheap way to save hydrogen, and it has been found that hydrogen could be stored in a several ways such as gas compression, hydrogen liquefaction, and compressed hydrogen or in the form of metal hydrides. However, these technologies for hydrogen storage are either unsafe or expensive as in the case of compressed gas storage or liquefaction respectively and hence other advanced materials are now being investigated for their hydrogen storage capacities. New storage concepts such as physical adsorption on nanomaterials, especially novel carbon materials, such as carbon nanotubes, activated carbon and carbon nanofibers, due to the pores of molecular dimensions can adsorb large quantities of gases inside the pores[1], and have attracted a lot of interest. The motivation for using hydrogen as an energy source, and the available techniques for storage are introduced here.

1.1 Motivation of Hydrogen as a Clean Energy Source

Global economic development in recent years has led to higher standards of living. At the same time, two urgent global issues have arisen, namely the problem of a sustainable energy resource and the preservation of the environment. Since the1990's, with urgent need of reducing atmospheric pollution and avoiding the greenhouse effect, the problem of finding alternative pollution-free fuels to replace fossil fuels has become increasingly important. The ideal candidate is hydrogen, which is the most abundant element in the universe, and usable without generating any pollutants. If it is possible to deploy hydrogen as a fuel, it would fundamentally change our existing exploitative relationship with the natural environment[2,3].

Besides being a clean source, hydrogen could also potentially provide more energy compared to gasoline or natural gas. Nevertheless, it is when we consider the weight, volume, and round-trip energy costs of the entire fuel storage system and the charging/discharging cycles, as well as the safety issues, that hydrogen's drawbacks become apparent. Furthermore, due to its explosive properties, a safe storage method is required before hydrogen can become a replacement for gasoline. Therefore, new approaches enabling more compact, light weight, and energy-efficient hydrogen storage/delivery systems are required before the widespread use of hydrogen-powered vehicles becomes a reality.

1.2 Hydrogen Storage Technologies

Currently, there are four major approaches to hydrogen storage, including (1) physical storage via compression or liquefaction, (2) chemical storage in hydrogen carriers (e.g. methanol, ammonia), (3) metal hydrides and (4) gas-on-solid adsorption (physical and chemical)[4-19], and among them, metal hydrides, nanotubes, nanofibers and activated carbons have seen continuous development. Although each storage method may possess cer-

tain desirable attributes, no one approach satisfies all of the efficiency, size, weight, cost and safety requirements required for transportation or utility usage. The US Department of Energy (DOE) Hydrogen Plan has set a standard for this discussion by providing a commercially significant benchmark for the amount of reversible hydrogen adsorption. The benchmark requires a system-weight efficiency (the ratio of stored hydrogen weight to system weight) of 6.5*wt.%* hydrogen and a volumetric density of 62*kg* H_2/m^3, since a vehicle powered by a fuel cell would require more than 3.1*kg* of hydrogen for a 500*km* range[10]. Table 1.1 compiles the advantages and disadvantages associated with the various current hydrogen storage techniques.

Table 1.1 Advantages and Disadvantages of Various Storage Techniques

Storage Technique	Advantages	Disadvantages
1. Liquefied H_2	Excellent volumetric and gravimetric energy density for large containers	Liquefaction cost, boil-off losses, poor performance in small systems
2. Chemical Storage	High gravimetric storage density	Toxicity, impure stream, rehydrogenation reaction
3. Metal Hydrides	High volumetric energy density, safe	Poor gravimetric performance, trade-off between high *wt.%* and high dissociation temperature
4. Gas-on-Solid Adsorption	Fair volumetric and gravimetric densities, potentially inexpensive	Requires compression and cooling, complexity
5. Glass Microspheres	Resist contamination; at a low pressure	Poor thermal conductivity, glass breakage

- **Liquefied H_2**

Hydrogen does exist in a liquid state, but only at extremely cold temperatures, and the first liquefaction of hydrogen was performed by James Dewar[20] over 100 years ago. Liquid hydrogen typically has to be stored at 20*K* or -253°C. The temperature requirements for liquid hydrogen storage necessitate expending energy to compress and chill the hydro-

gen into its liquid state. The cooling and compressing process requires energy, resulting in a net loss of about 30% of the energy that the liquid hydrogen eventually stores. The storage tanks are insulated, to preserve temperature, and reinforced to store the liquid hydrogen under pressure.

Hydrogen storage devices have been developed after 1990, such as pressurized hydrogen tanks and cryogenic vessels. It would seem that a small pressure vessel would be excellent for hydrogen storage in terms of energy density. However, the margin of safety concerning liquid hydrogen storage is a function of maintaining tank integrity and preserving temperatures of 20K that liquid hydrogen requires. Combine the energy required for the process to get hydrogen into its liquid state and the tanks required to sustain the storage pressure and temperature and liquid hydrogen storage becomes very expensive compared to other methods. Other disadvantages include losing up to 1% a day through boiling, and up to 30% during filling and the requirement of the pressure regulator to decrease the pressure for practical levels. Research in the field of liquid hydrogen storage is focused on the development of composite tank materials, resulting in lighter, stronger tanks, and improved methods for liquefying hydrogen.

- **Chemically Stored Hydrogen**

The hydrogen is combined in a chemical reaction that creates a stable compound containing the hydrogen. A second reaction occurs that releases the hydrogen, which is collected and utilized by a fuel cell, this process is known as irreversible. The exact reaction employed varies from storage compound to storage compound. Some examples of the various techniques include ammonia cracking, partial oxidation, methanol cracking, etc. These methods eliminate the need for a storage unit for the hydrogen produced, and the hydrogen is produced on demand.

- **Metal Hydrides**

In 1866, the property that hydrogen can be stored in a solid was first observed for the element palladium (Pd). Even though the storage gravimetric density is low, the Pd-H system is the best-studied system. Other elements, such as titanium (4*wt.%*) and magnesium (6*wt.%*), show higher storage capacity. Hydrogen is dissolved as a proton in the crystal lattice of the metal, and therefore the volumetric density in many cases exceeds that of molecular hydrogen in a liquid state. Nevertheless, elements showing a high gravimetric storage capacity usually possess a high temperature of dissolution, which is often above 500*K*, and this is a major drawback for its technical applications. Alloys based on intermetallic compounds, which can be divided into different families, such as AB_5 hydrides (e.g. $LaNi_5$), AB_2 compounds related to laves phase crystal structures, and AB hydrides (e.g. FeTi), have been developed which operate near room temperature and at pressures between 0.1*MPa* and 1*MPa*. Here A denotes the hydride-forming element and B represents the non-hydride-forming element. However, the gravimetric storage capacity is below 2*wt.%* for all compounds operating at ambient temperature. Therefore, the storage of hydrogen in these hydrides would be a factor of 15 to 20 times heavier than that for gasoline, and development was stopped in the 1980s.

It has been recently suggested that in the preparation nanostructured composite materials with additives acting as catalysts[21-24], for example, with titanium (Ti) doping the temperature can be reduced to 420*K* and a reversible storage of 5.6*wt.%* can be achieved for $NaAlH_4$[25].

There are some commercial metal hydrides available, which reduce the risk factors of gaseous or liquid hydrogen. However, the large desorption energy required, as well as the weight and cost of any resulting system, make it less than ideal for storage applications. These are yet still very specific products with a low market niche, which are unfortunately

far more expensive than would be, if properly commercialized.

- **Gas-on-Solid Adsorption**

The above technologies for hydrogen storage are either unsafe or expensive and hence new advanced materials are continually being investigated for their hydrogen storage capacities. An inherently safe and potentially high energy density hydrogen storage method is gas-on-solid adsorption, which should be more energy efficient than either chemical or metal hydrides. Consequently, the hydrogen storage properties of high surface area "activated" carbon, and zeolites (see Figure 1.1) have been extensively studied[5,14,26-30]. The activated carbon material was found to be ineffective for storing hydrogen, because only a small percentage of the surface strongly interacted with the hydrogen molecules at ambient temperature and pressures[5,14,26-28]. The zeolites (see Figure 1.1) are also effectively ruled out because of their low storage capacity[29,30]. Moreover, the spheres require far too high temperatures to release the adsorbed hydrogen. Such a chemical storage system would require a reformer and hydrogen purification system, resulting in too large a system for practical hydrogen storage.

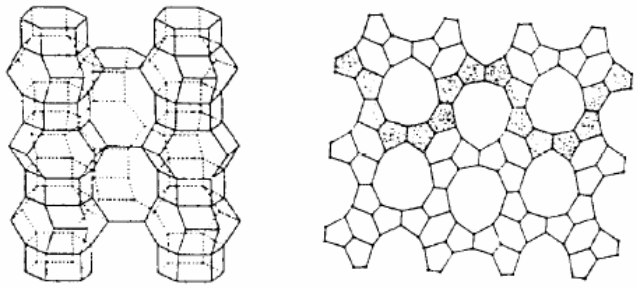

Figure 1.1 Pore structure of zeolites, a) side view, b) top view

Gas absorption is an inherently safe method that may attain the benchmark standards. Hence in recent years, carbon-based materials have attracted much attention due to the discovery of novel carbon nano-materials such as fullerenes, nanofibres, and nano-

tubes[7,10,18,19,26,31-40]. In particular, single-walled carbon nanotubes (SWNTs), which have diameters of typically a few nanometres, have been suggested as suitable materials for gas storage[7,10,26]. One reason for this is that nanotubes do not necessarily require a pressure regulator, which notably increases both the volumetric and gravimetric energy density of the system. Since pores of molecular dimensions can adsorb large quantities of gas, hydrogen can condense to high density inside narrow SWNTs, even at room temperature[10,26]. The high hydrogen uptake of these materials suggests that they could be used as hydrogen-storage materials for fuel-cell-powered electric vehicles[10]. Within all this hype, a close examination of the different types of nanostructured carbon unfortunately reveals that the experimental data reported in literature do not necessarily agree with each other.

Pederson and Broughton[41] suggested that carbon nanotubes having diameters of typically a few nanometres, should be able to draw up liquids by the capillarity effect, and store hydrogen in microscopic pores on the tubes and within the tube structures. Krishnan *et al.*[42] reported that this effect has been observed for low-surface-tension liquids in large-diameter, multi-walled nanotubes, as a consequence of the attractive potential of the pore walls. In 1997, Dillon *et al.*[10] first reported the excellent hydrogen storage properties of SWNTs, which caused a flurry of research activities world-wide on hydrogen storage in carbon nanotubes. However, till today, no other author has been able to reproduce the initial reported results. Carbon nanotubes and their hydrogen storage capacity are still very much in the research and development stage. Currently, research on this promising technology has focused on the areas of improving manufacturing techniques and reducing costs as carbon nanotubes move towards commercialization.

Figure 1.2 provides a summary of the relative volumetric and gravimetric densities of current and possible future hydrogen storage systems.

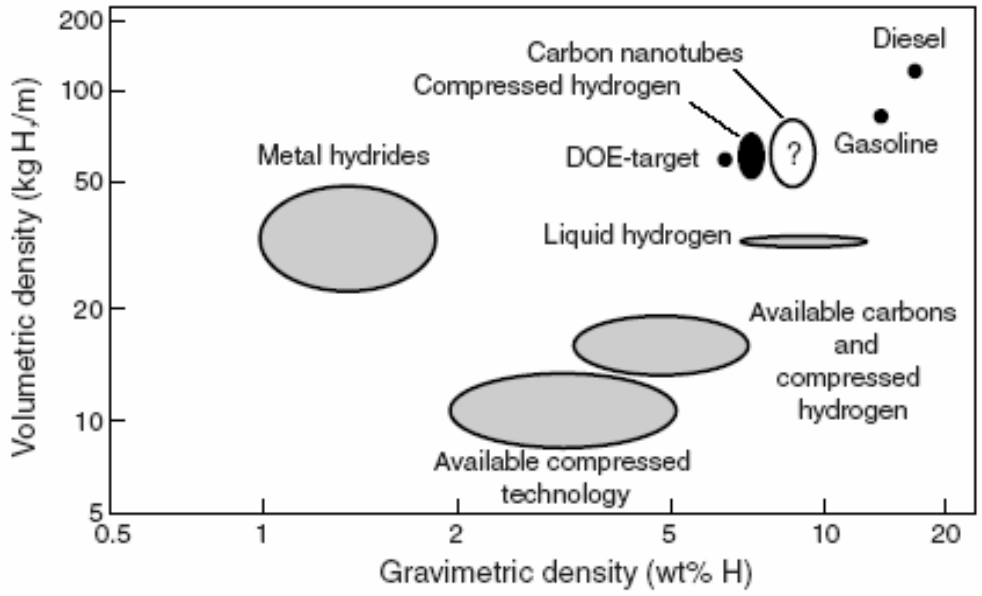

Figure 1.2 Relative gravimetric and volumetric densities of current and future hydrogen storage systems[43].

- **Hollow Glass Microspheres (HGMs)**

Besides the four methods mentioned above, it has been reported that the tiny hollow glass spheres can be used to safely store hydrogen[44,45]. The glass spheres are warmed, increasing the permeability of their walls, and filled by being immersed in high-pressure hydrogen gas, the hydrogen then diffuses through the thin wall of the hollow glass microspheres (HGMs). The spheres are subsequently cooled, locking the hydrogen on the inside of the glass balls. A subsequent increase in temperature will release the hydrogen trapped in the spheres. Microspheres have the potential to resist contamination, and contain hydrogen at a low pressure thus increasing the margin of safety. However, a traditional limitation of hollow glass microsphere has been the poor thermal conductivity of a packed bed of glass microspheres and poor conduction of heat translates to unsuitably low release rates of the hydrogen gas. Moreover, possible glass breakage also makes it unfavorable.

1.2.1 Structure of Carbon Nanotubes

Carbon nanotubes (CNT) were discovered by Iijima[46] as elongated fullerenes in 1991. Since then, research on the growth, characterization and application development has exploded, and this can be attributed to the unique electronic and extraordinary mechanical properties of CNTs. The CNTs can be metallic or semiconducting (see Figure 1.3) and thus offer possibilities of creating semiconductor-semiconductor or semiconductor-metal junctions. The high tensile strength, Young's modulus and other mechanical properties hold much promise for the realization of high strength composites for structural applications. Researchers have been exploring the potential of CNTs in a wide range of applications including: nanoelectronic devices, nanoscale sensors, field emission, displays, hydrogen storage, polymer matrix composites, body armor, reinforcement materials, nanoscale reactors, and electrodes, to name a few.

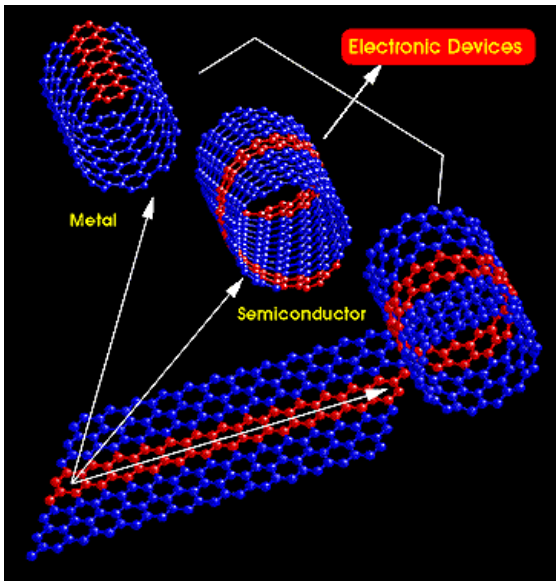

Figure 1.3 CNTs can be metallic or semiconducting

A single-wall carbon nanotube (SWCNT) is best described as a rolled-up tubular shell of graphene sheet (Figure 1.5), constituting benzene-type hexagonal rings of carbon atoms[47]. The short side of the rectangle becomes the tube diameter and therefore is "quantized" by the requirement that the rolled-up tube must have a continuous lattice structure.

Similarly, the rectangle must be properly oriented with respect to the flat hexagonal lattice, which allows only a finite number of roll-up choices. Two of these correspond to high symmetry SWNT's; in "zigzag" tubes, some of the C-C bonds lie parallel to the tube axis, while in "armchair" tubes, some bonds are perpendicular to the axis. Chiral tubes have a left- or right-handed screw axis (see Figure 1.4).

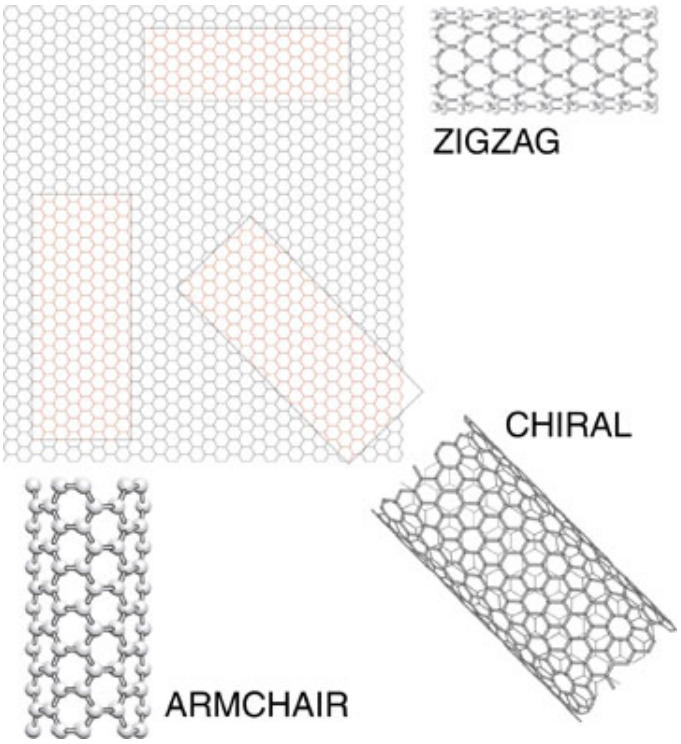

Figure 1.4 Three different nanotube structural types [48]

The body of the tubular shell is mainly hexagonal rings (in a sheet) of carbon atoms, while the ends are capped by half-dome shaped half-fullerene molecules. The natural curvature in the side-walls is due to the rolling of the sheet into the tubular structure, whereas the curvature in the end caps is due to the presence of topological (pentagonal rings) defects in the otherwise hexagonal structure of the underlying lattice. The role of a pentagonal ring defect is to provide a positive (convex) curvature to the surface, which helps in closing of the tube at the two ends. A multi-wall nanotube (MWCNT) is a rolled-up stack of graphene sheets into concentric SWNTs, with the ends again either capped by half-fullerenes or kept open. A nomenclature (n,m), (see Figure 1.6), used to identify each

single-wall nanotube, refers to integer indices of two graphene unit lattice vectors corresponding to the chiral vector of a nanotube[47]. Chiral vectors determine the directions along which the graphene sheets are rolled to form tubular shell structures, and are perpendicular to the tube axis vectors[47].

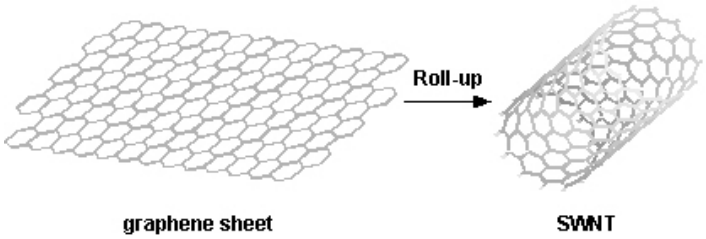

Figure 1.5 A single-wall carbon nanotube (SWNT) is best described as a rolled-up tubular shell of graphene sheet.

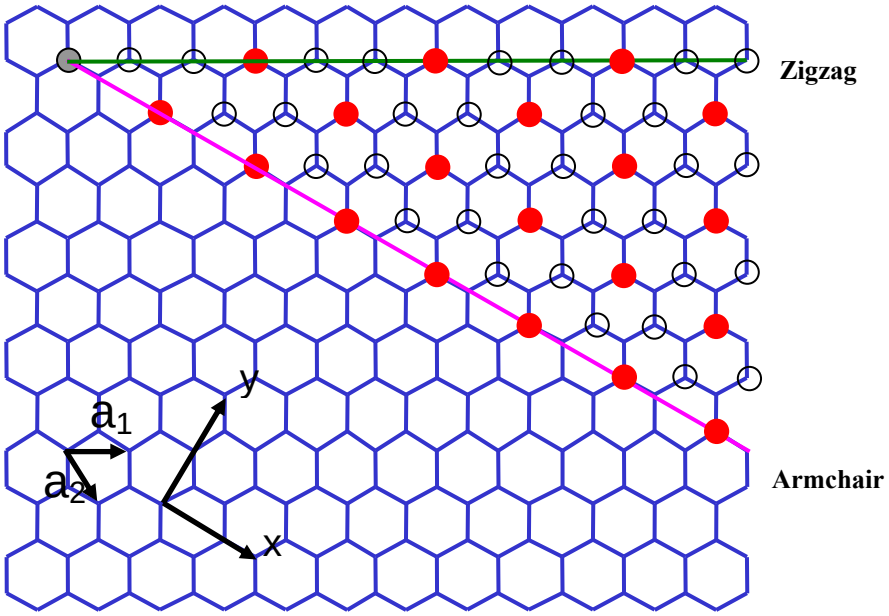

Figure 1.6 Possible vectors specified by the pairs of integers (n,m) for general carbon nanotubes, including zigzag, armchair, and chiral nanotubes. Below each pair of integers (n,m) is listed the number of distinct caps that can be joined continuously to the carbon nanotube denoted by (n,m)[49]. The red dots denote metallic nanotubes, while the hollow dots semiconducting nanotubes[47].

Nanotubes of the type (n,n), as shown in Figure 1.6, are commonly called armchair nanotubes because of the "_/‾_/" shape perpendicular to the tube axis, and have a symmetry along the axis with a short unit cell ($0.25nm$) that can be repeated to make the entire

section of a long nanotube. Another type of nanotube (n,0) is known as the zigzag nanotube because of the "/\/\/" shape perpendicular to the axis and these also have a short unit cell ($0.43nm$) along the axis[50]. All the remaining nanotubes are known as chiral or helical nanotubes, and these have longer unit cell sizes along the tube axis.

The circumference of any carbon nanotube is expressed in terms of the chiral vector $\vec{C}_h = n\vec{a}_1 + m\vec{a}_2$, which connects two crystallographically equivalent sites on a 2D graphene sheet, see Figure 1.7 [47]. The construction depends uniquely on the pair of integers (n,m) which specify the chiral vector. Figure 1.7 shows the chiral angle between the chiral vector $\vec{C}_h$ and the "zigzag" direction (θ = 0°). $\vec{a}_1$ and $\vec{a}_2$ represent the unit vectors of the hexagonal honeycomb lattice of the graphene sheet. As mentioned earlier, three distinct types of nanotube structures can be generated by rolling up the graphene sheet into a cylinder. The zigzag and armchair nanotubes, respectively correspond to chiral angles of θ = 0° and 30°. Chiral nanotubes correspond to 0°< θ <30°. The intersection of the vector $\overrightarrow{OB}$ (which is normal to $\vec{C}_h$) with the first lattice point determines the fundamental one-dimensional (1D) translation vector $\vec{T}$. The unit cell of the 1D lattice is the rectangle defined by the vectors $\vec{C}_h$ and $\vec{T}$, see Figure 1.7.

The cylinder connecting the two hemispherical caps of the carbon nanotube is formed by superimposing the two ends of the vector $\vec{C}_h$ and the cylinder joint is made along the two lines $\overrightarrow{OB}$ and $\overrightarrow{AB'}$. The lines $\overrightarrow{OB}$ and $\overrightarrow{AB'}$ are both perpendicular to the vector $\vec{C}_h$ at each end of $\vec{C}_h$ [49]. In the (n, m) notation for $\vec{C}_h = \mathrm{n}\vec{a}_1 + \mathrm{m}\vec{a}_2$, the vectors (n,0) or (0,m) denote zigzag nanotubes and the vector (n,n) denotes armchair nanotubes. All other vectors (n,m) correspond to chiral nanotubes[14]. The nanotube diameter can be calculate by

$$d = \sqrt{3}a_{C-C}\left(m^2 + mn + n^2\right)^{\frac{1}{2}} \Big/ \pi = C_h / \pi$$

where C_h is the length of $\vec{C}_h$, a_{C-C} is the C-C bond length.

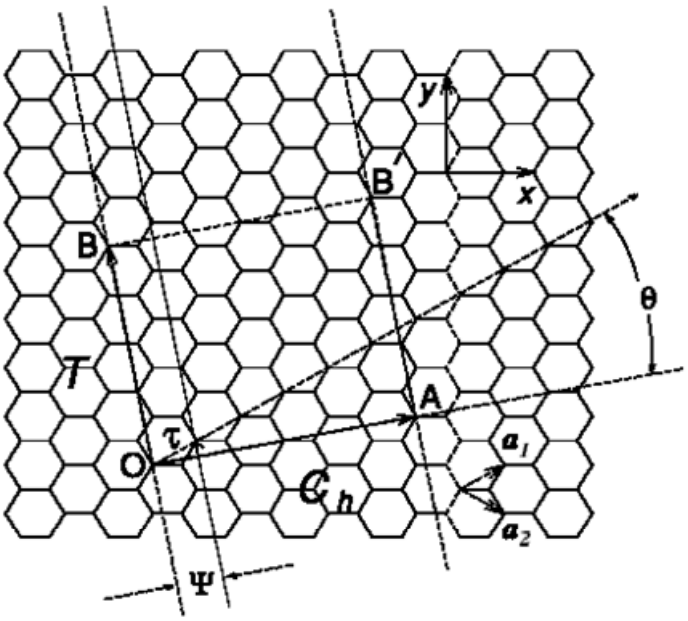

Figure 1.7 The unrolled honeycomb lattice of a nanotube. When the sites of O and A, and sites B and B' are connected, a nanotube can be constructed. $\overrightarrow{OA}$ and $\overrightarrow{OB}$ defined the chiral vector $C_h = n\vec{a}_1 + m\vec{a}_2$ and the translational vector T of the nanotube, respectively. The rectangle $OAB'B$ defines the unit cell for the nanotube. Vectors $\vec{a}_1$ and $\vec{a}_2$ are unit cell vectors, and θ is the chiral angle with respect to the zig-zag axis. Along the zig-zag axis, $\theta = 0^o$.

1.2.2 Multiwall Carbon Nanotubes and Carbon Nanotube Ropes

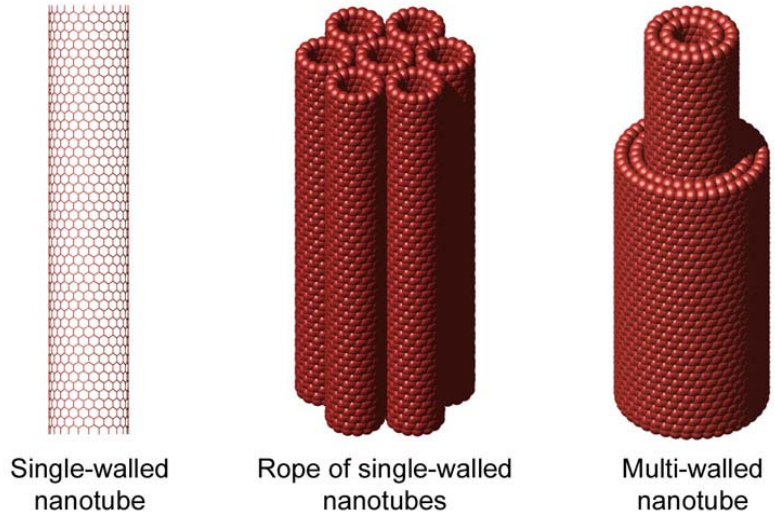

Figure 1.8 Structures of SWNT, a bundle of SWNTs, and a MWNT.

Single-wall nanotubes can be thought of as the fundamental cylindrical structure, and these form the building blocks of both multi-wall nanotubes and the ordered arrays of single-wall nanotubes called ropes (see Figure 1.8). Many theoretical studies have predicted the properties of single-wall nanotubes.

The nanotube ropes can be observed in a scanning electron microscope (SEM), where the ropes consists of aligned SWNTs on a two-dimensional lattice held together by van der Waal's forces, with intertubular spacing of 0.32*nm*. When examined in a transmission electron microscope (TEM), each rope is found to consist of a bundle of single-wall carbon nanotubes aligned along a single direction. X-ray diffraction also shows that the diameters of the single-wall nanotubes have a narrow distribution with a strong peak.

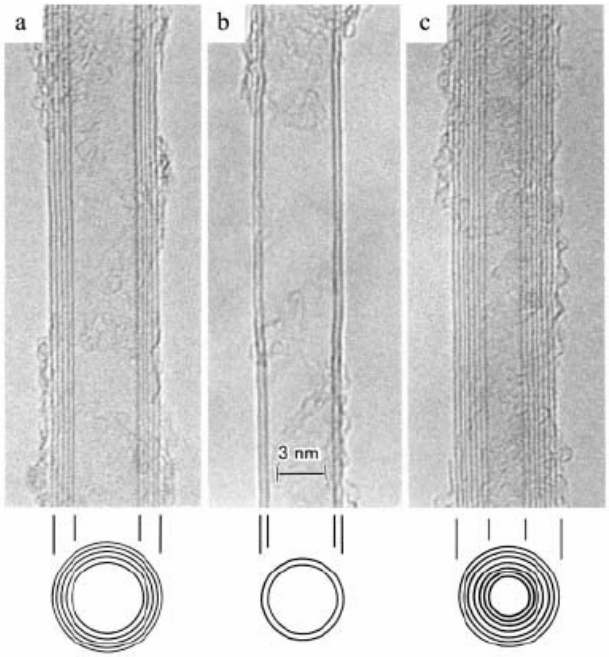

Figure 1.9 TEM (transmission electron microscopy) observation of multi-wall coaxial nanotubes with various inner and outer diameters, d_i and d_o, and number of concentric cylindrical shells N reported by Iijima[46] in 1991: (a) $N = 5$, d_o=67Å; (b) $N = 2$, d_o=55Å; and (c) $N = 7$, d_i=23Å, d_o=65Å.

Initial experimental observations on multiwall nanotubes (MWNTs) by Iijima[46] occurred about two years before single-wall carbon nanotubes were discovered experimentally at the NEC Laboratory, and the same has also been observed by Bethune and co-

workers at the IBM Almaden Laboratory[51].

MWNTs are different from SWNT as they contain several coaxial cylinders, each cylinder being a single-wall carbon nanotube (Figure 1.9). However, the discovery of MWNTs is not as important as that of the SWNT, as the latter is more fundamental, and has been the basis for a large body of theoretical studies and predictions that resulted from the experimental observations of the single-wall carbon nanotube.

As for the storage of hydrogen in MWNTs, some recent studies revealed that it is possible to use them for storing hydrogen through physisorption[38]. However, a recent study revealed that the gravimetric storage capacity in MWNT is much lower than in SWNT, as hydrogen is unable to penetrate in the inter-tube space of a MWNT.

1.2.3 Carbon Nanocapsules, Fullerenes and Carbon Toroidal/Coil Structures

The study of hydrogen encapsulated in fullerenes and carbon nanocapsules is of immense interest, not only due to the possibility of quantum improvements in the present storage technology, but also the array of new technologies that may emerge. These carbon based nano structures constitute an important subject of interest because of their very unusual structural and electronic properties.

The discovery of fullerenes and the features of their formation, structure and physical and chemical properties are also of great scientific interest. Fullerenes have made investigators pay attention to their unusual hydrogen-adsorbing properties. It is reported that the endohedral fullerene $H_2@C_{60}$ is nearly as stable as C_{60} itself. For example, the encapsulated H_2 does not escape even when heated at 500^{o}C for 10 minutes. Researchers thus suggested that $H_2@C_{60}$ can be viewed as stable hydrogen carbon molecule[52].

A more recently developed structure is the carbon circular torus/tori, where the

carbon rings form a seamless hexagonal network of carbon atoms on their shells, as shown in Figure 1.10. It is believed that a circular torus is formed by bending a single nanotube and joining its two open ends via the formation of strong C-C covalent bonds[53]. Introduction of pentagonal-heptagonal (5-7) defects into the shell of a SWCNT also changes the curvature of a tube and may lead to the formation of polygonal tori[54-57]. A coil structure is a tight solenoid-like spiral stabilised by strong shell-shell van der Waal's attractions. This type of ring was identified in the ultrasound-driven self-folding of SWCNT ropes[58]. The initial structures of the nanotubes were obtained by cutting a parallelogram from a graphene sheet and then rolling it up to form a tube. Topologically, a circular torus can be obtained either by rolling the open ends of a short, large-diameter, finite tube inside the tube and forming bonds between the atoms of the two edges, or bending a long, narrow, open-ended nanotube and joining its ends[53]. Schematics of these two ways of forming a circular torus from a finite, open-ended SWCNT are shown in Figure 1.10(a) and (b), respectively.

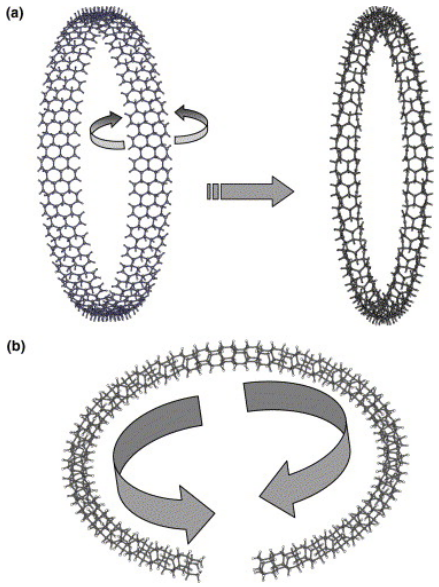

Figure 1.10 Formation of a (4,0) 60 torus from a finite nanotube: (a) by rolling the open ends of the short, large-diameter (30,30) 4 nanotube inside the tube and then forming bonds between the two edges, (b) by bending the long narrow, open-ended (4,0) 60 nanotube around and connecting its ends[59].

The application of this newly discovered carbon structure is still under investigation, where the chemisorption of hydrogen on carbon nanotubes/tori has been modeled by Ponomarenko *et al*.[59] to create a layer of hydrogen atoms bounded on their outer surface, which could be further constructed into stable CH tubes as illustrated in Figure 1.11.

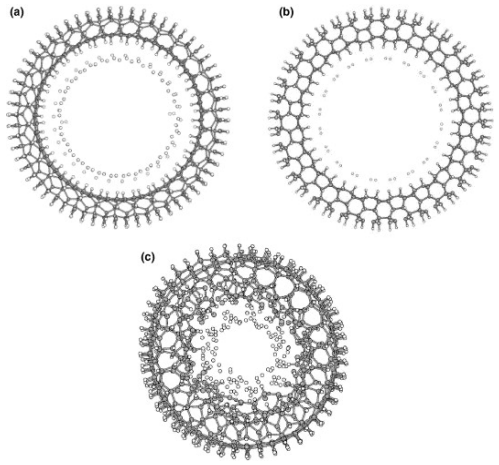

Figure 1.11 Imperfect CH circular tori formed by rolling up (a) (30,0)8, (b) (20,20)6, and (c) (24,0)12 nanotubes[59].

1.2.4 Carbon Nanotube Applications

The single and multi-wall nanotubes are interesting nanoscale materials for the following reasons:

- A single-wall nanotube can be either metallic or semiconducting, depending on its chiral vector (n,m), where n and m are two integers. A metallic nanotube is obtained when the difference between n and m is a multiple of three. If the difference is not a multiple of three, a semiconducting nanotube is obtained. In addition, it is also possible to connect nanotubes with different chiralities creating nanotube heterojunctions, which can result in a variety of nanoscale molecular electronic device components.
- Single and multi-wall nanotubes have very good elasto-mechanical properties be-

cause the 2D arrangement of carbon atoms in a graphene sheet allows large out-of-plane distortions, while the strength of carbon-carbon in-plane bonds keeps the graphene sheet exceptionally strong against any in-plane distortion or fracture. These structural and materials characteristics of nanotubes point toward their possible exploitation for development of the next generation high-strength and ultra-light composite materials.

- Nanotubes are high aspect-ratio structures with good electrical and mechanical properties. As a consequence, the commercial applications of nanotubes in field-emission displays and scanning probe microscopic tips for metrology have begun to materialize.
- Since nanotubes are hollow, tubular, and consisting of caged molecules, they have been proposed as lightweight large surface area packing material for gas-storage and hydrocarbon fuel storage devices. Other promising applications include gas or liquid filtration devices, nanoscale containers for molecular drug-delivery and casting structures for fabricating nanowires and nanocapsulates.

Carbon based materials are ideally suitable as molecular level building blocks for nanoscale systems design, fabrication and applications. From a structural and/or functional materials perspective, carbon is the only element that exists in a variety of shapes and forms with varying physical and chemical properties. For example, diamond and layered graphite forms of carbon are well known, but the same carbon also exists also in planar sheet, rolled-up tubular, helical spring, rectangular hollow box, and nano-conical forms. All basic shapes and forms required for building any complex molecular scale architectures are thus readily available with carbon. Additionally, by coating carbon based nanoscale devices with biological lipid layers and/or protein molecules, it may be possible to extend its application to the rapidly expanding area of bio-nanotechnology.

1.3 Objectives and Scope

The objective of this thesis is to advance the understanding of the interaction of hydrogen molecules with carbon nanotubes, especially the physisorption and chemisorption process. These investigations include:

(1) the physical adsorption capacity of hydrogen within the small vacuum of closed carbon nanotubes,

(2) the chemical reaction processes of the hydrogen atoms and molecules chemisorbed on and into the carbon nanotubes forming exdohydrogenated, exohydrogenated and endoexdohydrogenated CNT structures, and

(3) the effects of the physisorption and chemisorption prodess on important thermodynamic properties, such as enthalpy (ΔH), entropy (ΔS) and free energy (ΔG) of the reaction.

As the process of storing hydrogen in and/or on carbon nanotubes is complex and may involve many transition steps, the scope of this thesis is restricted to these three objectives.

1.4 Organization of Thesis

The layout of this thesis begins with this introductory chapter 1, where the use of hydrogen as an energy source and the current available hydrogen storage techniques are discussed. The structures and their unique features of the nanotube are introduced.

In chapter 2, following a review of experiments on hydrogen stored in nanotube materials and other related carbon materials, we focus on the theories developed for storage simulation. The advantages and disadvantages for the implementation of these methodologies are presented as well.

To better model and simulate the chemical adsorption processes of H or H_2 onto

CNTs, first principle *ab initio* methods should be applied, and these theoretical methods are introduced in chapter 3, where the theoretical background and mathematical formulations used for quantum molecular modeling are discussed. The Hartree-Fock (HF) method and density functional theory (DFT) as well as the semiempirical and popular hybrid methods are also briefly presented in this chapter

Since the computational cost is often unaffordable if the whole system is applied using high level calculation, the multiscale ONIOM scheme is introduced in chapter 4. Employing this scheme, we are able to perform a high-level calculation for the few carbon atoms involved in the reaction process while considering the effects caused by the remainder using lower level theories. The results have similar accuracy to a high-level calculation of the full system, but are obtained at significantly reduced computational cost.

In chapter 5, we introduce the small vacuum models of the C_{110} nanocapsule and the C_{60} fullerene structures. The interaction between the hydrogen and endofullerene is characterized by two kinds of forces, namely the repulsive forces of H_2-H_2 and the repulsive forces of H_2-C_{60}. The stable states are analyzed with the increment of the number of inserted hydrogen.

In chapter 6, the chemical reaction of the hydrogen atom being attached the exterior of the narrow armchair (5,5) nanotube is studied using the ONIOM2 scheme. This study revealed that H atoms will form C-H bonds with the nanotube and weaken the C-C bond, eventually unzipping the nanotube along the tube axis.

In chapter 7, we examine the formation of three isomers, namely the exohydrogenation process where the carbon atom is bonded to a hydrogen atom from outside of the nanotube, the endoexohydrogenation process where the hydrogen forms a the zigzag-type configuration, and the endohydrogenation process where the carbon atom is bonded to hydrogen from inside of the tube. The reaction process is studied in detail, and the stable intermediates that have all positive frequencies along the reaction pathway and the transition

states are studied. The polarization and diffusion functions are considered in this chapter.

In chapter 8, the thermodynamic properties of the chemisorption process is investigated by the entropy, enthalpy and the Gibbs free energy, which can be used to reveal the preferred reactions at various thermodynamic conditions.

In chapter 9, this thesis concludes with a summary of achievements of the present work. The recommendation for future work is discussed as well.

CHAPTER 2

LITERATURE REVIEW

This chapter provides a critical review of available literature on hydrogen storage in carbon nanostructures. Literature concerning both experimental and computational adsorption data is presented, including the classical calculations of physisorbed hydrogen molecules and the first principle calculations of chemisorbed hydrogen molecules/atoms on and in nanotube material frameworks. Of major emphasis is the theoretical simulation aspect for understanding the adsorption processes, so as to facilitate the improvement of the storage capacity. According to existing theoretical models, there are two categories of approaches used for this purpose, namely classical modeling and *ab initio* simulations, where the latter is often used to probe the chemical adsorption process, and the former for understanding the physisorption mechanism. For both methodologies, the advantages and disadvantages will be briefly discussed.

2.1 Quantifying Hydrogen Storage

Before reviewing the literature, we will first briefly introduce the measurement of hydrogen storage, so as to help us better understand and appreciate the published experimental data. Four different techniques namely, volumetric method, gravimetric method, thermal desorption spectroscopy (TDS), and electrochemical method are applied to quantify hydrogen storage in solids.

- **Volumetric Technique**

The volumetric method measures the pressure drop, due to hydrogen absorption, after applying a hydrogen pressure to the specimen contained in a constant volume[14,19]. Similarly the pressure increase due to desorption can be measured. For better accuracy, this method requires typical specimen masses of 500mg or higher. Furthermore, any leakage or temperature instability in the apparatus may give rise to large experimental errors. The advantage of this technique is that both absorption and desorption can be measured, and experimental conditions are similar to that in deployment storage tanks.

- **Thermogravimetric Analysis (TGA)**

The thermogravimetric analysis (TGA) measures the weight changes of specimens due to the absorption or desorption of hydrogen. In specially designed devices, high accuracies can be achieved even for sample masses as low as 10mg[14,60]. However, this technique is sensitive to all absorbed or desorbed gases, thus the apparatus has to be extremely clean, and high-purity hydrogen must be used, since it is based on overall weight.

- **Thermal Desorption Spectroscopy (TDS)**

Thermal desorption spectroscopy (TDS) measures only hydrogen desorption in high vacuum, utilizing mass spectrometry. Moreover, the method is selective and highly sensitive, allowing samples with masses even below 1mg[10,60]. The sensitivity and selectivity can be even further improved using deuterium loaded specimens[60]. In this case, background disturbance from water or other hydrogen containing adsorbents does not occur.

- **Electrochemical Method.**

Hydrogen can be incorporated into a sample by electrochemical reactions. To prepare the carbon-containing working electrode, the carbon material has to be mixed with conductive powder, such as nickel or gold, and compacted[61-63]. The counter electrode is,

for example, metallic nickel. Both electrodes are placed in a KOH solution, which provides the hydrogen atoms, and are separated by a polymer separator. During the charging process, water dissociates at the negative working electrode, and atomic hydrogen may intercalate into the carbon material. The following discharge process results in the recombination of water. With a constant current, the voltage is measured across the two electrodes during the charging and discharging. The amount of desorbed hydrogen is determined by measuring the electric charge in a galvanostatic setup.

2.2 Experimental Overview

2.2.1 Purification of Carbon Nanotubes (CNTs)

Large quantities of single-walled carbon nanotubes (SWNTs) can be prepared by both laser ablation and arc discharge methods[64,65], or by the pyrolysis of hydrocarbons (HiPco) on nanometer sized metal catalysts[66,67]. The SWNTs prepared by these procedures contain impurities like fullerenes, and metal catalyst particles that are most often coated with layers of carbon, generally in the amorphous form. The fraction of these carbon impurities is typically the highest for arc discharge and lowest for the HiPco method. In addition, metal clusters from the catalyst (usually Ni, Fe, and Co) can stick to the tips of the ropes. The removal of impurities in carbon nanotubes may increase the hydrogen storage capacity.

Raw SWNT samples have been purified by various methods[68-82]. Hydrothermal treatment has been used by Tohji *et al.*[68,69] to remove the amorphous carbon from the nanotube surface. Smalley *et al.*[70,71] developed an oxidation purification method that involves burning away amorphous carbon by heating the tubes with an oxidizing agent, such as nitric acid in air. The method has been shown to be destructive by decapping and inter-

acting with any defect along the body of the tube, thus destroying the integrity of the nanotube. Duesberg *et al.*[78,79] used size selection chromatography to purify as well as separate tubes by length. Although, the process does not interfere with the integrity of the tube, size selection by diameter has not been achieved. Margrave *et al.*[75,76] employed gas-phase purification to obtain pure SWNTs. High temperature annealing of the purified samples has been adopted by some procedures[72,74], which removes the chemical functional groups created on the nanotube surface due to acid treatment[67]. There are also a few procedures to purify SWNTs prepared by the arc discharge method[68,69,77]. Another purification method proposed by Dalton *et al.*[80] involves using organic polymers such as poly (*p*-phenylene-vinylene-co-2,5-dioctyloxy-*m*-phenylene-vinylene) or PmPV. The polymer, when mixed with arc-discharge nanotubes in toluene, interacts with specific tube diameters (1.2-1.4*nm*) only, separating the tubes from the amorphous carbon[80,81]. The method is non-destructive, increases the processibility of the nanotubes and selects certain tube diameters[80]. In recent experiments, nanotubes prepared by laser ablation have been purified by a method reported by Hirscher *et al.*[82] with the use of oxidation in air at 620*K* for 10 minutes followed by a treatment in 36% HCl at 390*K* for another 10 minutes.

2.2.2 Hydrogen Storage Experiments

- **Opening of Nanotube Ends and Reducing the Lengths of the SWNTs**

Nanotubes are typically closed at the ends and the bundles have a length up to several microns, which may hamper the access of the hydrogen to the tube interior, thus the fullerene-like caps or the metal clusters at the ends of the tubes are best removed but without destroying the nanotubes. Furthermore, to reduce the diffusion length of hydrogen inside the tube or to the interstitial sites of the bundles, cutting them into shorter pieces may be advantageous for hydrogen storage.

In 1998, Liu *et al.*[51] first cut purified SWNTs by sonication in a mixture of concentrated sulfuric and nitric acids. The resultant suspension was then washed and filtered in a 100*nm* filter. Sonication in dimethyl formamide for 10 hours was performed by Ye *et al.*[18] to cut the SWNTs and disrupt the rope. Sonication of SWNTs in HNO_3 was also performed by Dillon *et al.*[83,84]. However, it should be noted that sonication at high power leads to cavitations, and therefore metal particles of the ultrasonic horn material may be incorporated into the carbon samples. In 2000, Stepanek *et al.*[85] proposed using diamond particles as an abrasive material to cut and open the SWNTs. The carbon nanotubes had been ultrasonically dispersed in ethanol, and this suspension was poured onto two diamond lapping film disks. High-resolution electron microscopy observation revealed shortened and cut nanotubes. The third method is the ball milling process, which has been used by Orimo *et al.*[86] and Hirscher *et al.*[87] to change the microstructure of the carbon material. Furthermore, it was shown by Haluska *et al.*[82] that this high-energy ball milling destroys the nanotubes within a few minutes. The fourth method of heating the carbon nanotubes under high vacuum before exposure to hydrogen to ensure clean surfaces has been reported in many publications.

- **Typical Experiments of Hydrogen in SWNTs**

The first publication of hydrogen storage in SWNT appeared in 1997, by Dillon *et al.*[10]. The SWNT samples were exposed to hydrogen gas (P = 40*kPa*) at 273*K* for 10 minutes, and subsequently cooled to 133*K*. In the experiments, using a temperature programmed desorption spectroscopy, the SWNT samples showed two hydrogen peaks. The major peak occurred at 150*K*, while the second peak occurred at 300*K*. Actived and non-actived carbon SWNTs exhibited only the lower temperature peak. The hydrogen storage capacity was estimated to range between 5-10*wt.%*. Inelastic neutron scattering performed on this material showed that hydrogen is physisorbed[40], but the authors did not comment

on the total amount. In 2000, the same group of authors[36,83] claimed that they had succeeded in purifying and opening the nanotubes with a special method and were able to measure directly by thermal desorption of up to 7*wt.%* uptake where the opening and cutting procedure was an ultrasonic treatment in HNO_3. The power applied was 50W/cm^2, which is above the cavitation threshold, and therefore titanium alloy particles of the ultrasonic horn material are introduced into the sample. Hirscheer[82] claimed that the titanium was responsible for all of the adsorption, but Heben[36,83] disputed this claiming he was well aware of the titanium, which is vital to the high storage density, but not in the way that Hirscher[82] suggests. According to Heben[36,83], these metallic particles somehow stimulate the hydrogen adsorption. After heating to 1000*K* in high vacuum the SWNTs can be loaded within several minutes at room temperature and nearly ambient pressure. The hydrogen desorption is measured at moderate temperatures. However, the high storage capacity of about 7*wt.%* could not be confirmed by volumetric measurements performed by the same group, which give a value of 2.3-2.8*wt.%*[88]. A 2001 DOE report by Heben[84] declared that, unfortunately, they could not reproduce the high hydrogen storage capacities with SWNTs generated with a new laser. The hydrogen storage capacities of these new SWNTs range from 2 to 4*wt.%*. In 2002, Heben[89] reported no data points with high storage capacities; and furthermore that the values scatter and were hard to reproduce. Additionally, a new cutting process avoiding metal impurities, which is not described in their reports, results in storage capacities below 1*wt.%*.

In 1999, Liu *et al*.[37] reported that storage could take place at room temperature. In their work, SWNTs of 1.85*nm* diameter, synthesized by a semi-continuous hydrogen arc discharge method, were used. After the samples were equilibrated for approximately 300 minutes, a maximum adsorption of 4.2*wt.%* at room temperature was achieved, under modestly high pressure (12*MPa*). Up to 78.3% of the adsorbed hydrogen could be released under ambient temperature and pressure.

In 1999, Ye *et al.*[18] reported a hydrogen adsorption capacity of 8*wt.%* for purified SWNT samples at 80*K*, and over a pressure range of 0.5 to 160bar. Very little adsorption was observed at lower pressures. The authors deduced that the surface area increases because of separation of the individual SWNTs. The hydrogen could then be physisorbed on their exposed surfaces.

With an oscillating mass analyzer, Smith *et al.*[90] measured SWNTs at room temperature and pressures up to about 5*MPa*. The highest storage capacity of 1.2*wt.%* at 5*MPa* was obtained for purified SWNTs after oxidation under a stream of CO_2 at about 900*K*. Adu *et al.*[91] measured hydrogen uptake in the low pressure range up to ambient pressure with a thermo-gravimetric analyzer, and reported that the hydrogen storage capacity at ambient temperature is nearly constant and is about 0.5*wt.%*. However, at cryogenic temperatures, 6*wt.%* uptake at low pressure (0.2*MPa*) was reported by Pradhan *et al.*[92], which was obtained with the same measuring method.

To summarize, the current experimental data publish on hydrogen storage measurements of SWNTs shows a large scatter as can be observed in Figure 2.1. It can be seen that a clear controversy arose at ambient pressure, and recently Zandonella[93] delved into this carbon controversy in a publication in Nature.

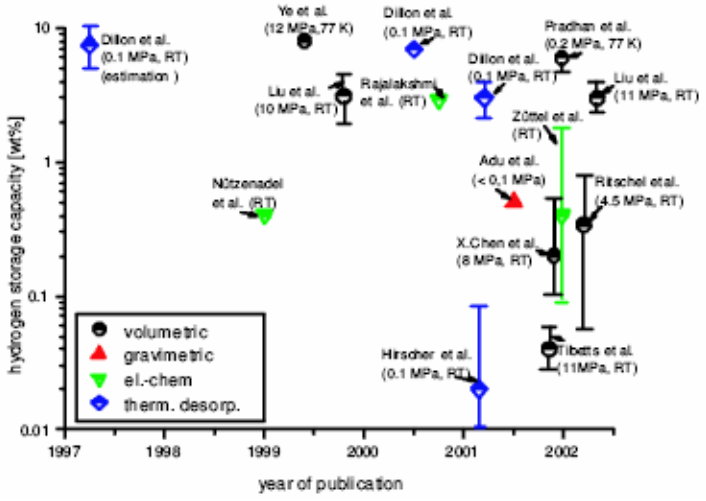

Figure 2.1 Experimental data of hydrogen storage capacities for SWNTs measured with different methods, presented in a logarithmic scale versus the publication date[94].

- **Alkali-Doped Carbon Nanotubes by Lithium and Sodium**

In 1999, Chen *et al.*[95] reported that alkali-doped carbon nanotubes showed high hydrogen uptake. They examined lithium- and potassium-doped carbon nanotubes and found hydrogen absorption of 14-20*wt.%* between 400°C and room temperature, and at a pressure of 0.12*MPa*. These values are higher than those for metal hydride and cryoadsorption systems. The stored hydrogen could be released at higher temperatures and adsorption-desorption cycles could be repeated with minor losses of the storage capacity. Subsequently substantial experimental works have been carried out to investigate the hydrogen adsorption in SWNTs with the aim of improving the storage capacity of the tubes by doping them[96-98].

However, the results of Chen *et al.*[95] were challenged by Yang[96], who attributed most of the weight uptake to moisture. Yang[96] repeated the experiments for the doped nanotubes following the same procedure described by Chen *et al.*[95], and measured the adsorption-desorption cycles using a comparable thermo gravimetric analyzer. His results showed that special care was required to remove any moisture contamination of the hydrogen in measuring the adsorption. Moisture can drastically increase the weight gain leading to errors in the results. Yang[96] subsequently suggested that heating the mixture of carbon or graphite nanofibres, with LiNO and LiCO, under hydrogen flow, results in the formation of LiO. By repeating the experiments of Chen *et al.*[95], the following chemical reactions were confirmed by X-ray diffraction and gas analysis

$$2\,LiNO_3 + C + H_2 \rightarrow Li_2NO_3 + 2NO + H_2O \qquad (2.1)$$

and

$$2\,Li_2CO_3 + H_2 \rightarrow Li_2O + CO + H_2O \qquad (2.2)$$

As LiO_2 is highly hygroscopic, the mixture used by Chen *et al.*[95] may have indeed

been very sensitive to moisture in the thermo-gravimetric experimental set-up. Yang's[96] results showed that in a dry environment, hydrogen adsorption of 2.5*wt.%* for lithium-doped nanotubes and of 1.8% for potassium-doped nanotubes, can be achieved. These results are supported by the fact that we do not find any hydrogen desorption in graphite doped with Li or K. Pinkerton *et al*.[99] confirmed Yang's observations with their own experiments on doped carbon nanotubes.

2.2.3 Electrochemical Single-Walled Carbon Nanotubes

Several groups reported on the electrochemical storage of hydrogen in armchair (*n*,*n*) carbon nanotubes[100] and zig-zag (*n*,0) CNTs[101]. Such CNTs may serve as electrodes in an electrochemical cell. Protons can be discharged in an aqueous solution on the surface of such cathodic CNT electrodes under the formation of an arch H-CNT through the reaction of $H + e^- + CNT \rightarrow$ H-CNT, which is an exothermic process, with the C-H bond energy in H-CNT being 2*eV*, according to the report. The hydrogenation of CNTs may be easily understood in analogy to the electrophilic addition of hydrogen to alkenes.

Nützenadel *et al*.[62,100] obtained results for electrochemical adsorption of hydrogen in SWNTs at room temperature (298*K*), with the sample from MER Corporation. The experiment was performed in an electrolytic cell with SWNTs used as an electrode, where hydrogen was formed in-situ by reduction of protons. Though the mechanism of adsorption in not clear, the results of the experiment are remarkable. The performance of their system (3.5*wt.%* for normal conditions) is higher than that for metal hydrides and other known adsorbents, and the authors claim high reversibility of the process.

2.2.4 Other Carbon Nanostructures

In 1998, a striking piece of experimental work on hydrogen storage in various carbon nanostructures was reported by Chambers *et al.*[7] Hydrogen gas, applied at 11.35*MPa* was absorbed at room temperature (298*K*). The hydrogen storage capacity was found to be 11.26*wt.%* for tubular CNTs, 67.55*wt.%* for herringbone carbon nanofibers (see Figure 2.2), 53.68*wt.%* for platelet carbon nanofibers (see Figure 2.2), and 4.52*wt.%* for graphite. More recently, Chambers *et al.*[7] described newer results on the interaction of hydrogen with graphite nanofibers (GNFs), and proposed that GNFs possess special structural conformation, which produces a material composed entirely of nanopores that accommodate small-sized adsorbate molecules such as hydrogen, and the nonrigid pore walls can expand to accommodate hydrogen molecules in a multilayer conformation. It was also noted that pretreatment before hydrogen storage is very important with ambient humidity being extremely detrimental to the hydrogen uptake performance.

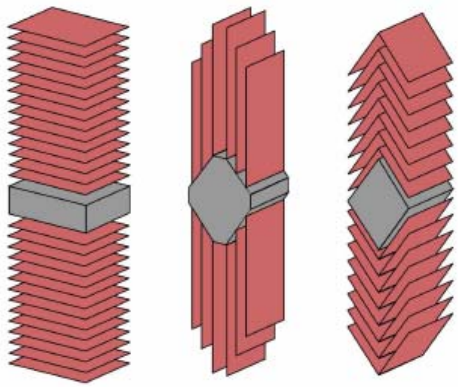

Figure 2.2 Schematic representations of the three forms of graphitic nanofibers: (a) platelet, (b) ribbon and (c) herringbone structures[102].

In 1999, Fan *et al.*[19] observed vapor-grown carbon fibers exhibiting 10-13*wt.%* hydrogen storage, almost twice as high as the 5.7*wt.%* capacity reported by Cheng *et al.*[34] for the same material. They also reported that various post-treatment methods could modify the pore structure and surface microstructure so as to significantly enhance the hydro-

gen adsorption capacity. It is therefore believed by many experts in the field that pore structure and surface microstructure exert a large influence on the hydrogen storage performance of CNFs, MWNTs and SWNTs. At about the same time, Bessel *et al*.[102] reported extremely high hydrogen uptake in GNFs. In this work, a pressure of 12*MPa* was applied, at 300*K*, and the pressure drop was monitored utilizing the volumetric method

Orimo *et al*.[86,103] also investigated hydrogen absorption and desorption in nanostructured graphite. In their experiment, the graphite was ball milled for a maximum of 80 hours in a 1*MPa* hydrogen atmosphere. The amount of hydrogen absorbed in the sample was determined by means of oxygen-combustion hydrogen analysis and it turned out to be as high as 7.4*wt.%*. These results show that high hydrogen absorption can also be realized without the hollow structure of nanotubes, and much of this hydrogen appears to be covalently bonded to the defective carbon. However, there is evidence that a large fraction of the hydrogen may be intercalated between the graphite interlayers. The issue of releasing the hydrogen was not addressed.

It should be noted that not all the groups reported high uptake rates. For example, Ahn *et al*.[9] found that in applying the volumetric method to GNFs at pressures of 8*MPa* and 18*MPa* and respective temperatures of 77*K* and 300*K*, less than 0.01*wt.%* hydrogen storage was achieved. Ströbel *et al*.[14] measured the hydrogen adsorption on different carbon materials using a microbalance at 12.5*MPa* and 296*K* and observed a maximum weight increase corresponding to a hydrogen uptake of 1.6*wt.%*. Fan *et al*.[19] initially reported a hydrogen uptake of 10-13*wt.%* at 11*MPa* and room temperature after boiling GNFs in HCl. However, in a following publication[104] the same group reduced the figures of hydrogen uptake in GNFs by a factor of two. Presently, none of these experiments have been repeated or confirmed by other groups.

The experimental storage capacities of hydrogen in carbon nanofibers and aligned carbon nanotubes has been reviewed by Hirscher et al.[94], see Figure 2.3.

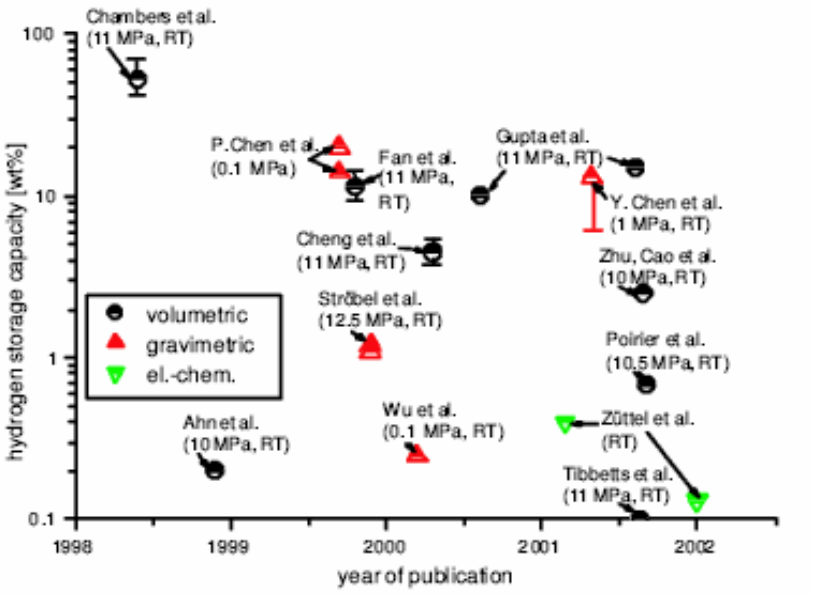

Figure 2.3 Experimental data of hydrogen storage capacities of carbon nanofibers and aligned carbon nanotubes measured with different methods, presented on a logarithmic scale versus the publication date[94].

In Table 2.1, we provide a summary of the relative volumetric and gravimetric densities of related carbon-based storage media. It should be noted that in the works tabulated in Table 2.1 reporting the gravimetric storage of H_2 in various carbon materials, many of them have not been independently verified. Furthermore, there is a lack of understanding of the basic underlying storage mechanisms of hydrogen in these materials.

Table 2.1 Reported gravimetric storage of H_2 in various carbon materials

Group	Year	Material	Temperature	Pressure (*MPa*)	Max. (*wt.%*)
Dillon *et al.*[10]	1997	SWNT 100%	133*K* (-140°C)	0.04	5-10
Dillon *et al.*[35]	1999	SWNT (High purity)	Ambient	0.067	~3.5-4.5
Liu *et al.*[37]	1999	SWNT ~50%	300*K* (27°C)	10.1	~4.2
Ye *et al.*[18]	1999	SWNT High purity	80*K* (-193°C)	~7	8.25
Chen *et al.*[105]	2000	MWNT	~300-700*K* (27-427°C)	Atmospheric	0.25
Dillon *et al.*[83]	2000	SWNT-TiAl0.1V0.4	Ambient	0.067	~7
Chen *et al.*[95]	1999	K-CNT	473-673*K*	0.1	14
Yang *et al.*[96]	2000	Li-CNT (wet H_2)	473-673*K* (200-400°C)	0.1	12
Yang *et al.*[96]	2000	Li-CNT (dry H_2)	473-673*K* (200-400°C)	0.1	2.5
Yang *et al.*[96]	2000	K-CNT (wet H_2)	<313*K* (40°C)	0.1	21
Yang *et al.*[96]	2000	K-CNT (dry H_2)	<313*K* (40°C)	0.1	1.8
Pinkerton *et al.*[99]	2000	Li-CNT	473-663*K*	0.1	0.72-4.2
Tibbetts *et al.*[106]	2001	nine different carbon materials	300*K* (27°C)	3.5	< 0.1
Hirscher *et al.*[82]	2001	purified SWNTs/graphite / diamond powder	300*K* (27°C)	Atmospheric	1.5
Ritschel *et al.*[107]	2002	MWNT/SWNT/GNF	Ambient	4.5	< 0.65
Pradhan *et al.*[92]	2002	ropes of SWNT	77*K*	0.1	<6

2.3 Theoretical Modeling

2.3.1 The Need for Theoretical Modeling

Until recently (1998), there have been little or no sound theoretical explanations of the hydrogen adsorption in SWNTs, but mere speculation about the processes. This has adversely affected both the understanding of the nature of these materials and the im-

provement of their storage capacity. Theoretical modeling is becoming more and more crucial. This is because even though experiments demonstrate the physical phenomenon, only a sound theoretical basis will explain the underlying basic mechanisms governing the experimental observations. Froudakis[108] provided a review on the theoretical analyses of hydrogen storage in carbon-based materials. For hydrogen adsorption in carbon nanotubes, theoretical calculations can be extremely useful for better understanding the elementary steps of the adsorption procedure. The theoretical simulations in this field can be generally classified into two categories according to the theoretical approximations they are based on. The first category involves Monte Carlo[109] and molecular mechanics (MM) classical algorithms to investigate the physisorption of hydrogen in SWNTs, while the second uses *ab initio* or semiempirical quantum techniques to study predominantly the chemisorption of hydrogen in SWNTs.

2.3.2 Simplistic Geometric Estimate and Qualitative Discussion

Since hydrogen molecules at elevated pressures on a solid surface are expected to form a close-packed configuration, Dresselhaus *et al*.[38] obtained a simple geometric estimate for the close-packing capacity of hydrogen molecules above a plane of graphite using purely geometric arguments, which yielded either 2.8*wt.%* or 4.1*wt.%* of hydrogen uptake for one layer of H_2 adsorbed on a single graphite layer, see Figure 2.4.

As for nanotubes, Dresselhaus *et al*.[38] presented two geometrical estimates for the filling of a rope (crystalline lattice) of SWNTs. One assumption made is that hydrogen is a completely deformable fluid filling the space not occupied by the carbon nanotubes, with the packing of hydrogen molecules of kinetic diameter 0.29*nm* on the inner walls and in the interstitial volume of the nanotubes, as shown in Figure 2.5. Using the geometrical model with close-packing of hydrogen molecules within the core of a (10,10) tube leads to

a 3.3*wt.%* hydrogen adsorption within the tube and 0.7*wt.%* adsorption within the interstitial space, or a total of 4.0*wt.%* hydrogen adsorption.

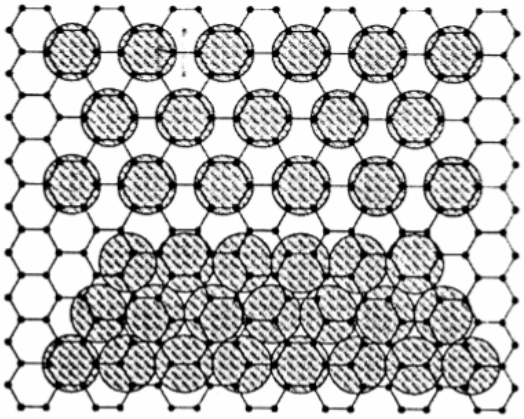

Figure 2.4 Relative density of a $\sqrt{3}\times\sqrt{3}$ commensurate (top) and an incommensurate (bottom) monolayer of hydrogen on a graphite surface[39].

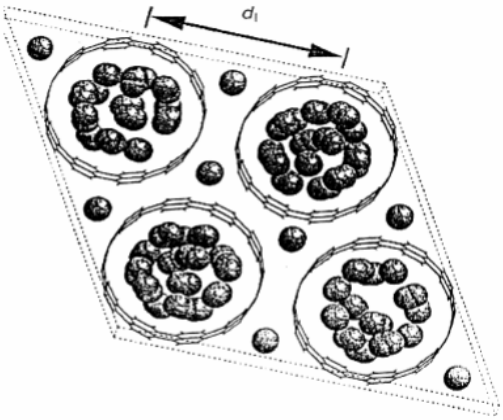

Figure 2.5 A typical configuration of H_2 molecules adsorbed on a triangular array of carbon nanotubes. This configuration resulted from a classical Monte Carlo calculation in which the simulated storage pressure was 10*MPa* and the simulated temperature was 50*K*[32].

Moreover, Dresselhaus[38] concluded that a hydrogen molecule adsorbed in the interstitial space undergoes much stronger surface attraction than on a single planar graphene surface, since it is in close proximity to three graphene surfaces. Therefore, the hydrogen adsorbed in the space would be expected to be denser than on the single graphite surface. In short, through a simple physical discussion, it was concluded that for SWNTs, hydrogen

can be stored both in the pores formed by the inner tube cavities and the inter-tube space, and the storage density is possibly higher than that on a planar graphite surface.

2.3.3 Classical Simulation of Hydrogen Physisorption - A Brief Overview

- **Monte Carlo and Molecular Dynamics Simulation**

Several groups have investigated the hydrogen uptake of carbon materials by calculations based on empirical classical potentials describing the interaction between hydrogen and carbon. Monte Carlo simulations[110,111] and molecular dynamics[112] have been extensively carried out to verify and predict the adsorption capacity of hydrogen in carbon nanotubes based on the assumption of physical adsorption. For all these approaches, the most important parameter in the simulation is the choice of the intermolecular potential functions employed to describe the molecular interaction between hydrogen and carbon atoms.

In late 1998, Darkrim *et al.*[31,113] first used the Lennard-Jones potential to perform a grand canonical Monte Carlo simulation of hydrogen storage in a cell of SWNTs, and investigated the influence of the tube diameter on the storage capacity. The simulation results showed that the adsorption decreases as the SWNT diameter increases. This is due to the fact that a large proportion of the volume inside or outside the tube is out of the attractive field of the solid-gas interaction. However, it was noted that their results were highly dependent on the intermolecular potentials used for the hydrogen-carbon interactions. This is the major drawback of classical simulations, and it showed the need for *ab initio* calculations in this field. In the same year, Rzepka *et al.*[114] used a grand canonical ensemble Monte Carlo program to calculate the amount of absorbed hydrogen for a slit pore and a tubular geometry. The amount of absorbed hydrogen depends on the surface area of the sample, and the maximum was found to be $0.6wt.\%$ ($P = 6MPa$, $T = 300K$). The calcula-

tion was experimentally verified with excellent agreement. At a temperature of 77*K*, the amount of absorbed hydrogen is about one order of magnitude higher compared to 300*K*. Rzepka *et al*.[114] also studied the influence of geometry, size, storage pressure, and temperature on the hydrogen uptake of carbon nanotubes. They found a maximum volumetric storage capacity at 300*K* and 10*MPa* for a pore size of about d = 7Å[27]. The peak value for the volumetric storage capacity is 12.5kg/m^3 corresponding to a gravimetric storage capacity of 0.5*wt.%*. In this case, one hydrogen molecule fits exactly in the tube core leading to strong capillary adsorption forces[27]. For larger pore sizes, the volumetric storage capacity decreases asymptotically with the density of the pure compressed gas (7.6kg/m^3) while the gravimetric storage capacity, i.e., the total amount of stored hydrogen compared to the pore mass, increases linearly with d [27]. At d = 7Å and 10*MPa* at low temperatures, the total amount of gas inside the tube saturates at a value corresponding to a particle density inside the accessible tube volume exceeding the density of liquid hydrogen. A comparison of the volumetric storage capacity with the density of pure compressed hydrogen gas shows that storage by adsorption is most effective in the medium-temperature range with a maximum at about 150-200*K*. At 77*K* and d = 7Å, increasing storage pressure was found to increase the hydrogen uptake in carbon nanotubes.

In 1999, Johnson and co-workers[115,116], using the Silvera-Goldman potential for the H_2-H_2 interactions and the Crowell-Brown potential for the H_2-tube interactions, studied the hydrogen adsorption in neutral as well as positively and negatively charged SWNTs. Their results showed that idealized graphitic nanofibres (slit pores) gave significantly better performance for hydrogen storage as compared to SWNT arrays. They also underlined the importance of the packing geometry of the SWNTs in the storage capacity.

In 2000, Williams *et al*.[117] performed grand canonical Monte Carlo simulations of H_2 physisorption in finite-diameter carbon SWNT ropes and found an increasing amount of

adsorbed hydrogen with decreasing temperature from 1.4*wt.%* (P = 10*MPa*, T= 300*K*) to 9.6*wt.%* (P = 10*MPa*, T = 77*K*). For lower hydrogen pressure this range is shifted to considerably lower amounts of adsorbed hydrogen, i.e. 0.2*wt.%* (P = 1*MPa*, T = 300*K*) to 5.9*wt.%* (P = 1*MPa*, T = 77*K*). Their simulation clearly showed that small-diameter ropes are preferable for hydrogen storage. They also pointed out an essential difference between models and experiments, which is the "atomically clean" surfaces of the tubes in the simulation. In addition, they suggested that physisorption of hydrogen occurs in carbon nanotubes by trapping hydrogen molecules inside the cylindrical structure of the nanotube, or by trapping hydrogen at the exterior of the nanotubes under high pressure conditions. Figure 2.6 shows the interstitial channels between the SWNTs in a bundle, the central pore of the SWNTs, and the external surfaces of the bundle, namely the tube wall and the grooves formed at the contact between adjacent tubes. Williams *et al.*[117], using Monte Carlo simulations, determined the binding energies of these sites and found the following order: E_B (channel) > E_B (grooves) > E_B(pores) > E_B(surface). They suggested that access to the internal tube pores is through either open SWNT ends or defects in the tube walls.

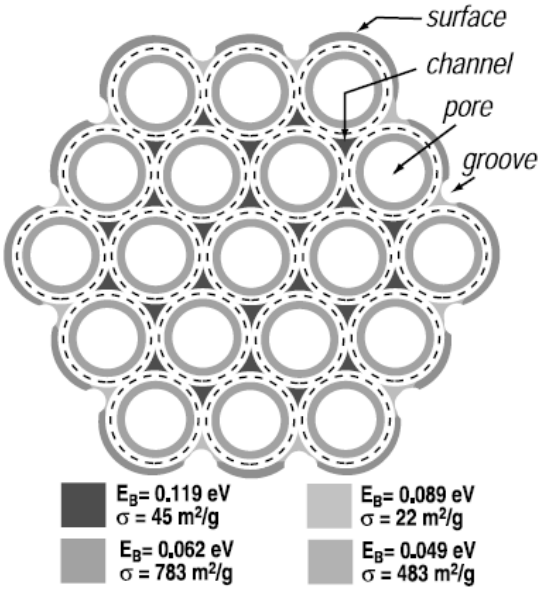

Figure 2.6 Available sites for hydrogen adsorption in a bundle of SWNTs: pore, groove, channel, and surface sites. The binding energy (E_B) and specific surface area contributions for hydrogen adsorption on these sites are indicated[91].

For more studies of physical adsorption of H_2 on carbon nanotubes using Monte Carlo simulations, please refer to[32,113-116,118-123].

- **Advantages and Disadvantages of Classical Approaches**

The main advantage of classical approaches is the feasibility of accounting for relatively much larger systems, as compared to first principle quantum *ab initio* methods. In addition, there is account for temperature in classical simulations. On the other hand, the accuracies of classical approaches are very parameter dependent, and furthermore cannot provide insights into the chemical bond effects, which *ab initio* methods can.

2.3.4 Quantum Approaches

Monte Carlo and Molecular Dynamics calculations based on classical potentials are not well suited to study chemical processes. Indeed, it is likely that hydrogen and carbon react chemically in storage applications. In fact the infrared experiments of Chen *et al.*[95] indicate the formation of C-H bonds. In order to study this kind of process, a more sophisticated method capable of quantum-mechanically treating the bond breaking and the bond formation is required. First principle *ab initio* formulations are capable of describing these chemical effects.

By using quantum approaches, it is now possible to compute the energy of a material with no more input parameters other than the nuclear charge and number of electrons on all the atoms and the values of a few physical constants. Although quantum mechanics allows one, in principle, to determine physical properties with higher accuracy, its application in condensed matter is usually accompanied by several approximations. These approximations have led to various methodology variations, termed by different acronyms. Before we discuss these approximations, it would be useful to evaluate the conditions un-

der which we may wish to use quantum mechanical analysis.

Since 2001, the quantum aspect was introduced into the molecular dynamics study of hydrogen in SWNTs, either by quantum molecular dynamics algorithms[33] or minimal *ab initio* calculations in parts of classically optimized tube geometries[124]. In the first case, Cheng *et al.*[33], using an *ab initio* simulation package, performed a quantum mechanical molecular dynamics simulation of H_2 absorption in a trigonal two-dimensional lattice of armchair (9,9) SWNTs. The potential energy surface near the equilibrium point was found to be relatively flat, and significant changes of the lattice constants (>0.5Å) resulted in only small changes in the lattice energy (<1*kcal/mol*). Cheng *et al.*[33] also investigated the site selectivity during the adsorption, since arrays of SWNTs with open ends may accommodate hydrogen inside the tube (endohedral adsorption) or inside the channel formed by different tubes (exohedral adsorption). According to their studies, exohedral adsorption is more favorable from an energy basis.

Ma *et al.*[124] first used a many-body Tersoff-Brenner potential to simulate low-energy collision of atomic H on the side-wall of an armchair (5,5) SWNT. In addition to this, they performed minimal HF/STO-3G *ab initio* calculations on selected snapshots of the molecular dynamics simulations. The interesting part of their work was the sorting of the collision results with respect to the hydrogen energy, and results indicated that if the hydrogen energy is in the range 1-3*eV*, the H atoms will be adsorbed onto the tube side-wall, while for energy levels between 4*eV* and 14*eV*, the H atoms have a high probability of rebounding off the wall. With energy levels within the interval 16-25*eV*, the hydrogen have a high probability of penetrating into the tube and being trapped inside, forming hydrogen molecules and gradually condensing to produce liquid hydrogen inside the tube. Finally, for the energy range from 20*eV* to 30*eV*, the H atom can enter the tube from one side and escape through the opposite side, or break a C-C bond.

Chan *et al.*[125], using first principle calculations, studied the interaction between a

hydrogen molecule with a single carbon nanotube, as in gas phase conditions, and with a solid array of carbon nanotubes under high pressure, and found chemical adsorption to be unfeasible under gas phase conditions, but possible in the latter solid case. They also suggested that the dissociative chemisorption of hydrogen molecules in the interstitial region on the exterior of carbon nanotubes is made possible by the high-pressure environment in the storage experiment.

Since only quantum chemistry calculations can provide credible insights into the interaction of hydrogen with SWNTs, Pierre *et al.*[126] used semi-empirical AM1 simulations to obtain the binding sites, energetics, and orbital pictures of lithium and molecular hydrogen adsorption in SWNTs. They found that Li can adsorb both inside and outside a zigzag tube, and the most stable site is that above the centre of a tube hexagon. After the Li adsorption, molecular hydrogen can be bound to the Li atom with a binding energy of $0.5eV$. Their AM1 calculation showed also that molecular hydrogen is repelled from the tube wall if the tube is not doped.

The combination of *ab initio* and semiempirical methods together was also used by Barajas-Barraza *et al.*[127] in 2002. They used MNDO as well as *ab initio* density-functional theory to analyze the hydrogen storage behavior in spheroidal C_{60}, C_{82}, and (5,5) armchair C and BN fullerenes. They found that, in their closed shell system, the molecular hydrogen clusters would form into well-defined configurations, and transition from 1D to 3D formations. However, based on their result of the single point energy results, the authors could not explain why such configuration transitions occurred.

In 1999, Jeloaica and Sidis[128] used density functional theory to investigate hydrogen adsorption on a graphitic cluster model, but it was only in 2000 that first principle calculations of hydrogen adsorption in SWNTs appeared in the literature[129-132]. The main reason *ab initio* calculations for SWNTs have appeared only recently is the system size. In order to take into account for a sufficiently large SWNT model, approximately 200 atoms

are required. The problem that arises in such an attempt is how to treat a large enough system, using a sufficiently accurate *ab initio* method, without ending up with a prohibitively large calculation. Presently, there are two different ways to deal with this problem. The first is to use the periodicity of the SWNTs in combination with an *ab initio* method with periodic boundary conditions[129,130]. The second is to use a two-level quantum mechanics/molecular mechanics (QM/MM) approach[131-134]. In the latter, the tube is divided into different sub-domains and these sub-domains are treated with different methods. The advantage of the former is that the total system is treated with *ab initio* techniques, while the obvious disadvantage is that an external periodicity is forced on the system. For the QM/MM model, there is no periodic constraint but the disadvantage is that only a relatively small part of the system is treated quantum mechanically. In addition, both approaches have the disadvantage of excluding temperature from the calculations.

- **Periodic DFT Models**

Lee *et al.*[61,135,136] performed density-functional and density-functional-based tight binding calculations to search for hydrogen chemisorption sites and predict the maximum storage capability in single-walled carbon nanotubes (SWCNTs). Their calculations are performed at $0K$ and show two energetically favored configurations in which hydrogen atoms are chemisorbed on the nanotubes. The lower energy one (zigzag type) is that in which the hydrogen atoms are bonded alternately outside and inside the tube. Stable but $0.56eV$ higher in energy per C-H bond is the arch-type arrangement. These configurations are stable in spite of the deformations induced on the C-C bonds by the chemisorption process. They also investigated the possibility of absorbing all the hydrogen atoms on the inside. It was, however, energetically favorable for the hydrogen atoms to recombine and form molecules, which were then physisorbed inside the nanotube, leading to physisorption. The maximum possible adsorption was reported to be an encouraging $14wt.\%$.

Lee and Lee[129] first employed the periodic DFT approach for studying chemisorption sites of atomic hydrogen outside and inside (5,5) and (10,10) SWNTs. The supercells they used consist of eight layers along the tube axis. Their calculations showed two hydrogen chemisorption sites in SWNTs. They also predicted that hydrogen molecules could exist in the empty space inside the nanotube. The maximum storage capacity is mainly determined by the steric interaction between different H_2 molecules, and also between the H_2 molecules and the tube wall. It was reported that the capacity increases linearly with the tube diameter, and excessive hydrogen storage would result in large repulsion energies that eventually break down the tube wall.

- **QM/MM Mixed Models**

The QM/MM mixed or multiscale model has been employed for the study of hydrogen interaction with SWNTs by Bauschlicher[131,133,137] and Froudakis[132]. In this approach, the total system can be simplified by treating the active part with an accurate quantum chemistry method and the far-field region with a MM force field. This two-level approach combines the high accuracy of the *ab initio* treatment of the part of the tube (see Figure 2.7) where the interactions with hydrogen will take place, with a relaxation in accuracy using MM methodology for the other portions of the SWNT.

Bauschlicher[131,133,137] used a (10,0) carbon nanotube for studying hydrogen and fluorine binding onto the nanotube wall, and examined the maximum coverage on the tube wall. The entire model consisted of 200 carbon atoms, with the *ab initio* section consisting of 24 carbon atoms. The ONIOM (our Own N-layered Integrated molecular Orbital and molecular Mechanics) two-level method of Morokuma *et al.*[134] was used. The B3LYP/4-31G was employed for the QM part, while the UFF (universal force field)[138] was used for the MM part. The preferred sites for the chemisorption of one, two, and four hydrogen atoms on the tube walls were reported together with the binding energies.

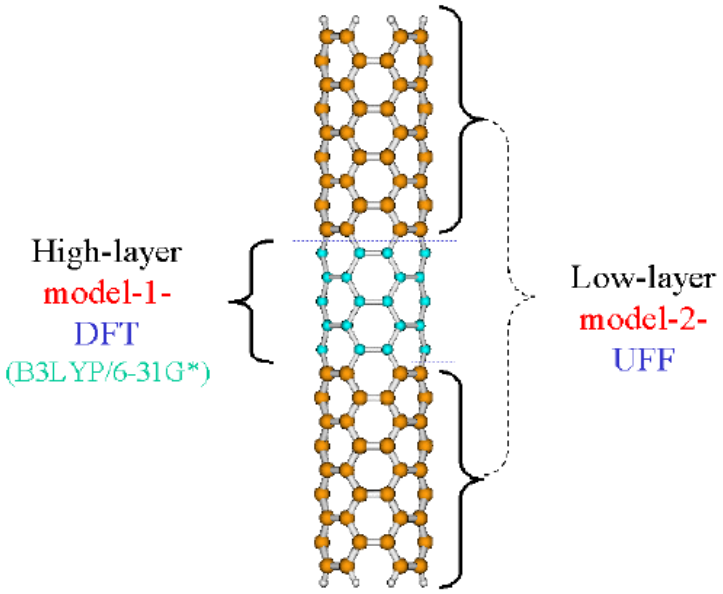

Figure 2.7 QM/MM models simulating a (4,4) SWNT[132]. The total 200 atoms tube was separated into three cylindrical parts. The inner one was treated with DFT (40 open color carbon atoms) and the two outer parts with molecular mechanics (darker color carbon atoms). The dangling bonds at the ends of the tube were saturated with hydrogen atoms.

Froudakis[132] also used the QM/MM method to investigate the nature of hydrogen adsorption in SWNTs. For the QM part, the B3LYP functional was used; while for the MM part, the universal force field (UFF) method was used. Their model included up to 64 carbon and 32 hydrogen atoms in the QM region and up to 200 carbon atoms of a (4,4) SWNT in the MM region. Their results showed that hydrogen atoms would bind to the tube walls and not enter in the tube interior. This binding will take place in zigzag rings around the tube walls and not along lines parallel to the tube axis.

2.4 Conclusion

In general, it is often very difficult to reach a consensus for the maximum adsorption capacity of hydrogen storage in carbon nanostructures, and theoretically explain the experimental observations through various methods of calculations and predictions. All things considered, the present state of theoretical analysis is still very immature, and the

process is most likely to be more complicated than anticipated. However, much information can still be obtained from these analyses, which can be very helpful for substantiating experimental claims. Furthermore, a better understanding of the pore structure and adsorption processes in carbon nanotubes will facilitate the selection of optimum intermolecular potential functions for faster and more refined calculations and ultimately direct the development of carbon nanotube based hydrogen storage systems.

CHAPTER 3

THE FIRST PRINCIPLE SCHEME FOR MOLECULAR MODELING

In this chapter, we will review some of the fundamental aspects of quantum chemistry and lay the foundation for subsequent theoretical discussion on hydrogen interaction with carbon nanotubes. It begins with a comparison of various methods for electronic structure calculation. The Schrödinger equation is then introduced for the description of the physical and chemical properties of ensembles of particles. The assumptions and methods for obtaining the solutions of the Schrödinger equation are then presented and discussed. These include the Hartee-Fock (HF) method, density functional theory (DFT), semi-empirical methodology, and some post HF methods. In addition, some of the analysis techniques used to investigate the chemical reactions between hydrogen and the CNT in chapters 6 and 7, are also discussed. These include the frequency calculations of the Hessian matrix used to detect transition and stable intermediate states, as well as the Mulliken population analysis, natural bond orbital analysis and the density of state, which are used for analyzing the electronic properties.

3.1 Overview of Computational Methods

Many computational methods are used for electronic structure calculations. These methods span form very accurate quantum chemistry techniques applied to a small number

of molecules up to tight-binding semi-empirical schemes which make it possible to simulate systems composed of about one thousand molecules. Figure 3.1 depicts the relative level of the sophistication of these methods, and the corresponding typical number of atoms in the system.

The various quantum mechanical methods can be divided into the following groups:

- Quantum Monte Carlo (QMC): scaling with the number of atoms N
- Hartree-Fock (HF) : scaling: $\sim N^4$ or higher
- Density-Functional : scaling: $\sim N^3$; $\sim N$ for some specific problems
- Tight-Binding (TB) :scaling : $\sim N^3$; $\sim N$ for some specific problems

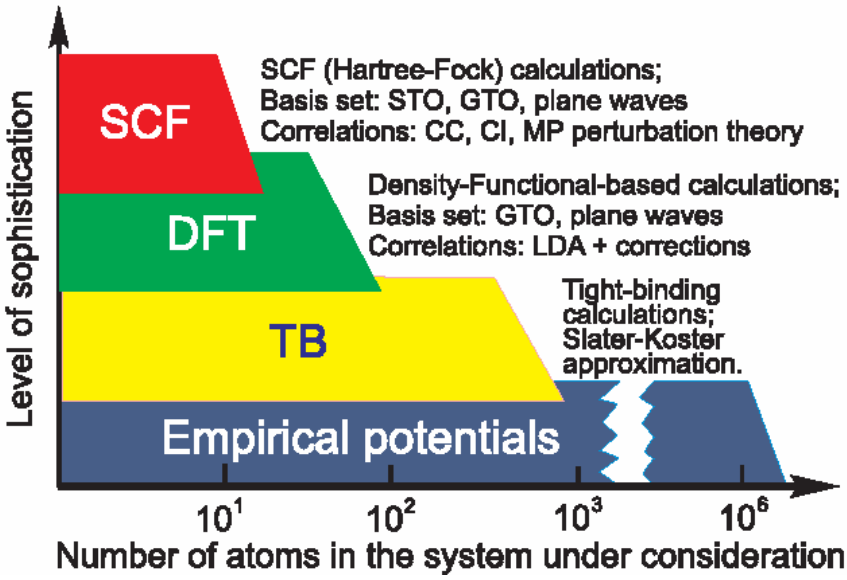

Figure 3.1 Methods for electronic structure calculation.

The scaling of the computation time depends not only on the number of atoms N but the number of the basis functions as well. All these techniques, except for the TB schemes, are *ab initio* methods. In the following discussion, we will be looking into various *ab inito* methods.

3.2 The Schrödinger Equation

The ensembles of particles are often used for the microscopic description of the physical and chemical properties of matter, which can be very complex. However, it does not matter if these particles are in the gas or condensed phase, solid or liquid states, or whether their distribution profile in the system is homogenous, amorphous or heterogeneous, they can be unambiguously treated as a collection of interacting atoms. All their properties can be described by a number of nuclei and electrons interacting through coulombic (electrostatic) forces. The governing Schrödinger equation is written as

$$\begin{aligned}\hat{H} &= \hat{T}_N + \hat{T}_e + \hat{V}_{N-N} + \hat{V}_{e-e} + \hat{V}_{e-N} \\ &= -\sum_{I=1}^{M}\frac{\hbar^2}{2M_I}\nabla_I^2 - \frac{1}{2}\sum_{i=1}^{N}\frac{\hbar^2}{2m_i}\nabla_i^2 + \frac{e^2}{2}\sum_{I=1}^{M}\sum_{J\neq I}^{M}\frac{Z_I Z_J}{|R_I - R_J|} + \frac{e^2}{2}\sum_{i=1}^{N}\sum_{j\neq i}^{N}\frac{1}{|r_i - r_j|} - e^2\sum_{I=1}^{M}\sum_{i\neq i}^{N}\frac{Z_I}{|R_I - r_j|}\end{aligned} \tag{3.1}$$

where I and J denote the I^{th} and J^{th} nuclei, while i and j correspondingly represent the electrons. $R=\{R_I\}$ $(I= 1...M)$, is a set of M-nuclear coordinates, and correspondingly we have $r = \{r_i\}$, $i = 1...N$, for the set of N-electronic coordinates. $|R_I - R_J|$ is the distance between nuclei I and J, while $|r_i - r_j|$ is the distance between the electrons i and j. Z_I and M_I are respectively the charges and masses of the nuclei, while m_i is the mass of the electrons. ∇_I^2 and ∇_i^2 are the Laplacian operators with respect to the nuclear and electronic coordinates respectively. The two constants appearing in Eq. (3.1) are e and $\hbar$, which are respectively the electron charge ($1.60217733e^{-19}$) and the reduced Planck's constant (1.05457266×10^{-34} m^2kg/s). The first two terms in Eq. (3.1) are kinetic energy of nucleus and electrons, respectively. The third and forth terms are respectively the electrostatic repulsion between the nuclei, and between electrons. The last term is the electrostatic attraction between electron j and nuclei I. In principle, if all the system parameters are known, then all properties can be derived by solving the many-body Schrödinger equation

$$\hat{H}\Psi_i\left(\vec{r},\vec{R},t\right)=E_i\Psi_i\left(\vec{r},\vec{R},t\right) \tag{3.2}$$

where $\Psi_i\left(\vec{r},\vec{R},t\right)$ is the time (t) dependent many-body wave functions of the coordinates $\vec{r}$ and $\vec{R}$ for the N electronic and M nuclei eigenstates, and E_i is the total energy of a given configuration.

However, the problem is intractable except for a small number of physically uninteresting cases, such as the interaction between two hydrogen atoms. Consequently, we need to reduce the complexity of Eq. (3.1), which is mainly is caused by the multicomponent many-body systems and the coulombic correlations.

The masses of the nuclei are much greater than those of the electrons, and the approximate ratio of the mass of a proton to that of an electron is 1:1836. Therefore the nuclear motion is much slower than the electron motion and the nuclei can be considered to be fixed. This leads to reasonable approximations that the electrons in a molecule adjust their distribution to changing nuclear positions rapidly and the electron distribution depends only on the instantaneous positions of the nuclei instead of their velocities. The separation of the general problem into two nuclei and electron parts is frequently called the *adiabatic* or *Born-Oppenheimer* approximation. With this approximation, we may separate the wavefunction into its electronic and nuclear components as

$$\Psi\left(\vec{R},\vec{r},t\right)=\Theta\left(\vec{R},t\right)\Phi\left(\vec{r},t\right) \tag{3.3}$$

where $\Theta\left(\vec{R},t\right)$ and $\Phi\left(\vec{r},t\right)$ are the nuclear and electronic wavefunctions respectively. Equation (3.3) above ignores the possibility of having non-radiative transitions between different electronic eigenstates.

The total energy is now the sum of the electronic energy and the electrostatic repulsion between the positively charged nuclei and the electrons. The electronic Hamilto-

nian can thus be written as

$$\hat{H} = -\frac{1}{2}\sum_{i=1}^{N}\nabla_i^2 + \frac{e^2}{2}\sum_{i=1}^{N}\sum_{j\neq i}^{N}\frac{1}{|r_i - r_j|} - e^2\sum_{i}^{N}\frac{Z}{r_i} \tag{3.4}$$

and the corresponding Schrödinger equation now has the form of

$$\left[-\frac{1}{2}\sum_{i}\left(\nabla_i^2 - \frac{Z}{r_i}\right) + \sum_{i}\sum_{j>i}\frac{1}{|\vec{r}_i - \vec{r}_j|}\right]\Psi(\vec{r}_1,...,\vec{r}_n,t) = E_{el}\Psi(\vec{r}_1,...,\vec{r}_n,t) \tag{3.5}$$

where E_{el} is the minimized energy of the given configuration. From the wavefunction $\Psi(\vec{r}_1,...,\vec{r}_n,t)$, we are now able to determine the probability of finding an electron in the electronic coordinates of $\vec{r}$ at time t by calculating $\|\Psi(\vec{r},t)\|^2$.

Applying the assumption that $\Psi(\vec{r},t) = \psi(\vec{r})f(t)$, we then obtain the stationary Schrödinger equation as

$$\hat{H}\psi(\vec{r}) = E_{el}\psi(\vec{r}) \tag{3.6}$$

3.3 Variational Principle

In order to solve the Schrödinger equation for an arbitrary molecule, we first need to set up the specific Hamilton operator of the target system. Once the Ψ are determined, all properties of interest can be obtained by applying the appropriate operators to the wave function. Unfortunately, this simple and innocuous-looking equation is of hardly any practical relevance, since apart from a few trivial exceptions, the Schrödinger equation admits few exact solutions for atomic and molecular systems. This is where we employ the variational principle to systematically solve for the ground state wave function.

When a system is in the state Ψ, which may or may not satisfy the Schrödinger equation, the average of many measurements of the energy, is given by the formula

$$E[\Psi] = \frac{\langle \Psi | \hat{H} | \Psi \rangle}{\langle \Psi | \Psi \rangle} \tag{3.7}$$

$E[\Psi]$ is always greater than or equal to E_0, and it reaches this minimum if and only if it is the true ground state. For simplification in Eq. (3.7), we introduced the very convenient and well-known bracket notation for integrals.

$$E[\Psi] \geq E_0 \tag{3.8}$$

The variational principle states that the energy computed form a guessed state Ψ is an upper bound on the true ground-state energy E_0 and minimization of the functional $E[\Psi]$ with respect to all allowed *N*-electron wave functions will lead to the true ground state energy $E[\Psi] = E_0$. This can be compactly expressed as

$$E_0 = \min_{\Psi \to N} E[\Psi] \tag{3.9}$$

where $\Psi \to N$ indicates that Ψ is an allowed *N*-electron wave function. Such a search over all acceptable *N*-electron wavefunctions is obviously not possible, and we need to define a suitable subset, which offers a physically reasonable approximation to the exact wave function without it being numerically unmanageable. The simplest, yet physically sound approximation is the Hartree-Fock approximation that we will discuss subsequently. In this approximation, the subset consists of antisymmetric products (Slater determinants) composed of *N* spin orbitals.

3.4 Slater Determinant

As discussed above, the behavior of the system is described by the multi-electron wavefunction, which depends on the coordinates and spins of all the *N* electrons. First, we note that the following functional form of the wavefunction is inappropriate:

$$\psi\left(\vec{r}_1,\vec{r}_2,...,\vec{r}_N\right)=\varphi_1\left(\vec{r}_1\right)\varphi_2\left(\vec{r}_2\right)...\varphi_N\left(\vec{r}_N\right) \tag{3.10}$$

This product of spin orbitals, known as the Hartree product, is unacceptable because it does not satisfy the antisymmetry principle, that is, the exchanging pairs of electrons does not give the negative of the wavefunction.

The determinant is the most convenient way to write down the permitted functional forms of a polyelectronic wavefunction that satisfies the antisymmetry principle. The acceptable form of the wavefunction can be written as

$$\psi\left(\vec{r}_1,\vec{r}_2,...,\vec{r}_N\right)=\frac{1}{\sqrt{N!}}\begin{Vmatrix}\varphi_1\left(\vec{r}_1\right) & \varphi_2\left(\vec{r}_1\right) & \cdots & \varphi_N\left(\vec{r}_1\right)\\ \varphi_1\left(\vec{r}_2\right) & \varphi_2\left(\vec{r}_2\right) & \cdots & \varphi_N\left(\vec{r}_2\right)\\ \vdots & \vdots & \ddots & \vdots\\ \varphi_1\left(\vec{r}_N\right) & \varphi_2\left(\vec{r}_N\right) & \cdots & \varphi_N\left(\vec{r}_N\right)\end{Vmatrix} \tag{3.11}$$

where $\varphi_\lambda\left(\vec{r}_j\right)$ is used to indicate a function that depends on the space and spin coordinates of the electron at $\vec{r}_1$, and λ is the spin orbital number. The factor $1/\sqrt{N!}$ ensures that the wavefunction is normalized. This functional form of the wavefunction is called a Slater determinant and is the simplest form of an orbital wavefunction that satisfies the antisymmetry principle.

The Slater determinant satisfies the Pauli principle, which states that no two electrons can have the same set of quantum number, and each spatial orbital can only accommodate two electrons of opposite spins.

3.5 Hartree-Fock Theory

The Hartree-Fock (HF) theory was developed to enable a solution to the Schrödinger equation and includes the effects of the electrostatic repulsion of electrons. This is an approximate method. The first simplification it used is the *Born-Oppenheimer* approximation, which has been stated in section 3.2. The second approximation is that we

replace the many-electron Hamiltonian with an effective one-electron Hamiltonian, which acts on one-electron wave functions called orbitals. The Coulomb repulsion between electrons is represented in an averaged manner. In other words, the HF method is a mean-field approach.

The derivation of the Hartree-Fock equations consists of a variational calculation for the Schrödinger equation with *Born-Oppenheimer* Hamiltonian. The total wave function is represented by a Slater determinant and the total energy is minimized with respect to the spin-orbitals $\varphi_\lambda(\vec{r}_i)$ in the determinant.

$$\left[-\frac{1}{2}\nabla_i^2+\sum_I\frac{Z_I}{|R_I-r_j|}\right]\varphi_\lambda(\vec{r}_i)+\left[\sum_\mu\int\varphi_\mu^*(\vec{r}_j)\frac{1}{|\vec{r}_j-\vec{r}_i|}\varphi_\mu(\vec{r}_j)d\vec{r}_j\right]\varphi_\lambda(\vec{r}_i)- \sum_\mu\left[\int\varphi_\mu^*(\vec{r}_j)\frac{1}{|\vec{r}_j-\vec{r}_i|}\varphi_\lambda(\vec{r}_j)d\vec{r}_j\right]\varphi_\mu(\vec{r}_i)d\vec{r}=\varepsilon\varphi_\lambda(\vec{r}_i) \tag{3.12}$$

$$\psi(\vec{r}_1,\vec{r}_2,...,\vec{r}_N)=\|Slater\| \tag{3.13}$$

In order to find the ground state it is necessary to minimize the energy while keeping the orbitals $\varphi_\lambda(\vec{r}_i)$ orthonormal. This is done by the variational principle, which states that the energy calculated from an approximation to the true wavefunction will always be greater than the true energy. Consequently, the better the wave function, the lower the energy. The "best" wavefunction is obtained when the energy is minimized. At the minimum, the first derivative of the energy, δE, will be zero.

To solve the HF equation, the self-consistent approach can be used. As the Hamiltonian itself contains the various φ that we are trying to determine, we can use a self-consistent approach where the initial wavefunction is guessed. Solutions yield values of the corresponding eigenvectors that are used to obtain better values of the wavefunction until convergence is achieved. In addition, to solve the HF equations, one has to introduce a ba-

sis and expand the operators in that basis. This will result in a set of non-linear equations that can be solved iteratively. The flowchart of the HF method is shown in Figure 3.2.

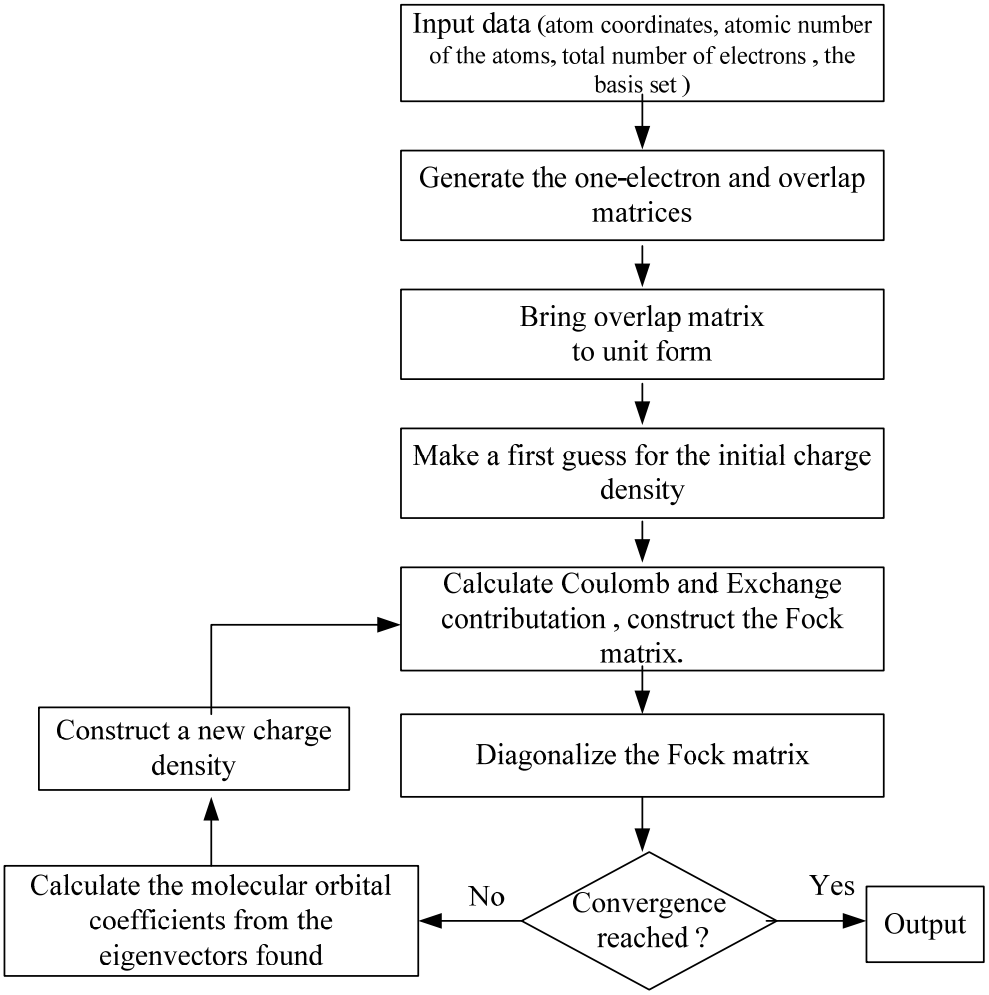

Figure 3.2 Flow chart describing the Hartree-Fock algorithm.

3.6 Basis Set Expansion

3.6.1 Linear Combinations of Atomic Orbitals (LCAO)

Although there are no exact analytical solutions to the Hartree-Fock equation for systems containing more than one electron, approximate solutions can be obtained using standard numerical techniques. The approach of all *ab initio* techniques is to build the total

wavefunction from a basis set of mathematical functions capable of reproducing critical properties of the system. An individual molecular orbital may then be expressed as linear combinations of basis set χ.

$$\varphi_i = \sum_k^M c_{ik}\chi_k \tag{3.14}$$

where φ_i is the i-th molecular orbital, χ_k the k-th atomic orbital, c_{ik} the coefficients of linear combination, and M the number of atomic orbitals. For a molecular wavefunction, the electronic orbitals of the constituent atoms form a natural set of basis functions. These atomic orbitals can in turn be represented by different types of mathematical functions.

3.6.2 STO and GTO

A highly accurate set of atomic orbitals called the Slater-type orbitals or STOs are based on hydrogenic wavefunctions having the form

$$\chi_{STO} = \frac{\zeta^3}{\pi^{0.5}} e^{-\zeta r} \tag{3.15}$$

where r is the radius and ζ the orbital exponent. Although the STO equation is an excellent approximation for the molecular orbitals, the exponential functions are not well suited for numerical manipulation. Thus, most electronic structure calculations approximate STOs with a linear combination of Gaussian-type functions, giving rise to the Gaussian type orbitals or GTOs

$$\chi_{GTO} = \frac{2\alpha}{\pi^{0.75}} e^{-\alpha r^2} \tag{3.16}$$

where α is the normalization constant.

The shape of the STO function can be summed up by a number of GTOs with dif-

ferent exponents and coefficients. By doing so, the computational speed increases but at the price of numerical accuracy. To compensate for this loss, more Gaussian functions are required for combination. This can be seen from Figure 3.3, where the Gaussian-type functions provide reasonable approximations of STOs.

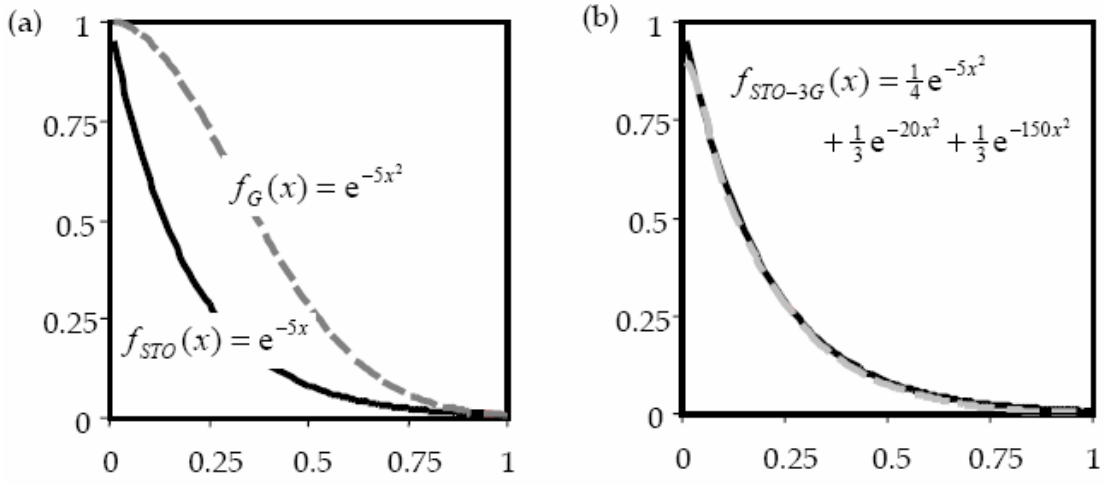

Figure 3.3 (a) Comparison of exponential and Gaussian functions. (b) Comparison of the same exponential function and a sum of three Gaussian functions.

Thus we have the STO-nG basis sets, where the "STO" here means that the STO equation will be used for the molecule, and "nG" implies that n gaussian primitives will be combined. The larger n is, the more accurate will be the result. In Figure 3.4, we show the comparison of the 1s Slater type orbital with Gaussian expansions of up to four terms. It can be seen that when the n reaches 4, the fitting Gaussian function is very close to the STO.

All basis set equations in the STO-nG form are considered to be "minimal" basis sets, and are used for every orbital in the atom. Although the minimal basis set provides a tool for visualizing qualitative aspects of chemical bonding, they are not good for accurately predicting the molecular energies. Thus improved basis sets are required for describing more complicated orbitals.

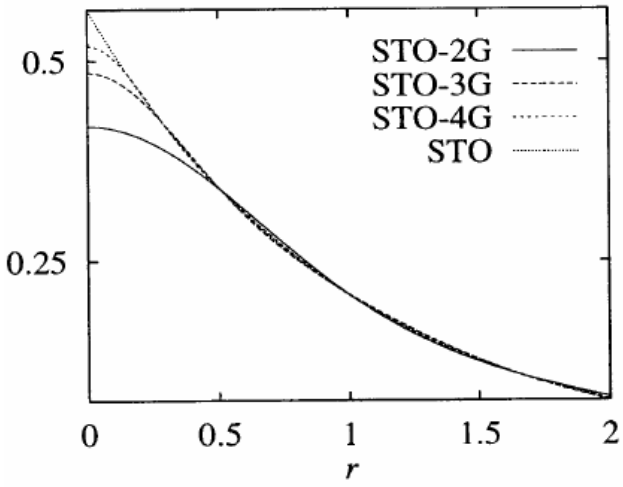

Figure 3.4 Comparison of 1s Slater type orbital and various Gaussian expansions.

3.6.3 Extended Basis Sets

- **Double-Zeta Basis Sets**

For the minimal basis sets, all the orbitals are approximated to be of the same shape, which can be inaccurate. The double-zeta basis set is thus important as it allows us to treat each orbital separately when we conduct the Hartree-Fock calculation. This gives us a more accurate representation of each orbital. In order to do this, each atomic orbital is expressed as the sum of two Slater-type orbitals (STOs). The two equations are the same except for the value of the zeta exponent. The zeta value accounts for how diffused (large) the orbital is. The two STOs are then added in some proportion.

The triple and quadruple-zeta basis sets work the same way, except that we use three and four Slater equations instead of two. There will obviously be a trade-off here, with better accuracy obtained at a higher computational cost.

- **Split Valence Basis Sets**

As the computational effort for calculating a double-zeta for every orbital may be

too high, a simplified method has been proposed. Since the inner-shell electrons are not as vital to the calculation as the valence orbitals, the double-zeta functions are only used for calculating the valence orbitals, see Figure 3.5. These functions in this method are called a split-valence basis set.

- **Polarized Basis Sets**

Polarization functions can be added to basis sets to allow for non-uniform displacement of charges away from atomic nuclei, as shown in Figure 3.5, thereby improving descriptions of chemical bonding. Polarization functions describe orbitals of higher angular momentum quantum number than those required for the isolated atom (e.g., *p*-type functions for H and He, and *d*-type functions for atoms with nucleic charge Z>2), and are added to the valence electron shells.

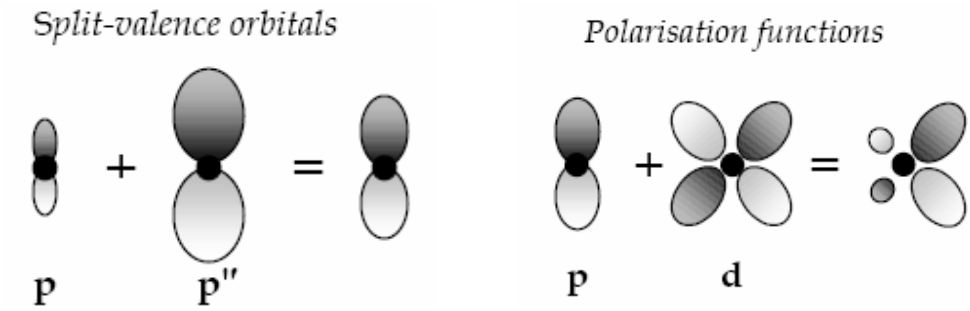

Figure 3.5 Set improvements-split-valence orbitals and polarization functions.

- **Diffuse Basis Sets**

Species with significant electron density far removed from the nuclear centers (e.g., anions, lone pairs and excited states) require diffuse functions to account for the outermost weakly bound electrons. Diffuse basis sets are recommended for calculations of electron affinities, proton affinities, inversion barriers and bond angles in anions.

3.6.4 Basis Sets and Computation Accuracy

The relationship between basis sets and accuracy is represented in Figure 3.6. The ultimate goal is to obtain a solution to the Schrödinger's Equation. However, current computational capabilities are still a long way from being able to carry out computations spanning the complete range of theoretical models with the different basis sets. Presently, feasible computations for reasonably sized systems are confined to the top left corner of the chart. In the left-most column, we are treating each electron independently of the others. As we move across to the right, we progressively account for the interactions of electrons. As we move down the rows, we are progressively using more complex and thus more accurate basis sets in the calculations. Due to high computational costs, it is important to select the most efficient basis set for accurate, yet tractable calculations.

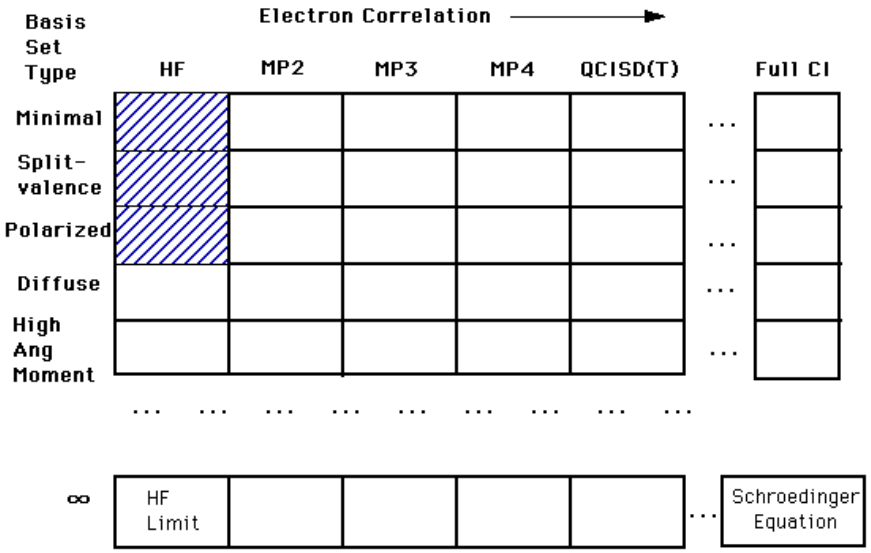

Figure 3.6 Schematic representation of theoretical models showing basis set improvement vertically and correlation improvement horizontally. The MPn (n=2,3,4) stands for the n-th order Møller-Plesset perturbation theory, and QCISD(T) denotes the Quadratic Configuration Interaction with Single and Double Excitation (T excitations) method, while full CI refers to the full Configuration Interaction method. These three are post Hartree-Fock (HF) methods, which include the effect of electron correlation by adding excitations to the HF wavefunction.

3.6.5 Limitations of HF Theory

The HF theory has been demonstrated to be a successful *ab initio* approach for molecular modeling, appropriate for many different electronic structure calculations, especially for the ground states of molecules near their equilibrium geometries. However, it does have two major shortcomings, namely, it ignores much of the electron correlation, and excited states are difficult to calculate.

The first drawback of HF theory is that electron correlation is ignored[139], except of course in an averaged sense. In the self-consistent field method, the electrons are assumed to be moving in an average potential of all the other electrons, and so the instantaneous position of an electron is not influenced by the presence of a neighboring electron. In fact, the motions of electrons are correlated and they tend to "avoid" each other more than HF theory would suggest, giving rise to a lower energy. The correlation energy is defined as the difference between the Hartree-Fock energy and the exact energy. Neglecting electron correlation can lead to some clearly anomalous results, especially as the dissociation limit is approached.

Another shortcoming of HF theory is that it is often difficult for excited states of the wavefunctions to achieve solution convergence[140]. Unless the excited state has a different overall symmetry than the ground state, it generally collapses to the ground state upon orbital optimization. This prevents HF theory from providing chemically useful information on excitation energies and charge densities of excited states.

To better understand these shortcomings, a typical example is provided in Figure 3.7, which displays the computed RHF and UHF as well as the exact potential curves for the ground state of the hydrogen molecules. At the equilibrium point, the RHF scheme provides a good approximation to the geometry optimization of the H_2 molecule. However, the values of the total energies were not satisfactory.

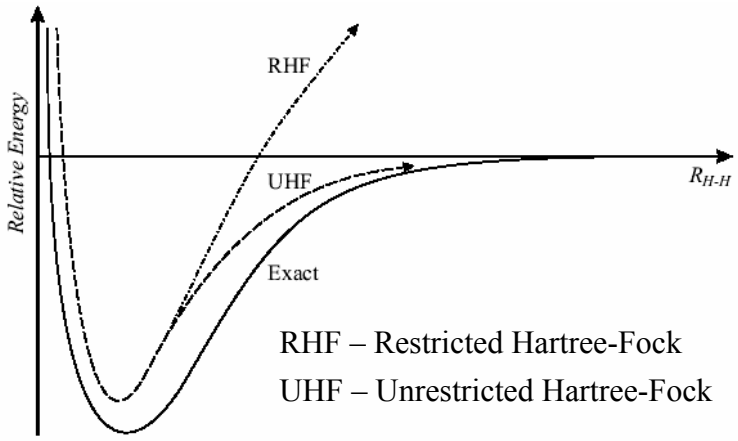

Figure 3.7 Potential curves for H_2.

Despite the shortcomings the HF theory, it must be emphasized that it is continues to be widely used. This is because the Hartree-Fock wavefunction is a well-controlled approximation to the many-body wavefunction. Its level of accuracy can often be determined, and is therefore useful for deriving qualitative information such as trends in a structural parameter with system size.

3.7 Post Hartree-Fock Methods

There are a number of ways to reduce the limitations of the Hartree-Fock method. Two categories of approaches are broadly used, namely, those based on perturbation theory (e.g. Møller-Plesset Perturbation Theory) and those based on the variational principle. Among the latter approaches is the configuration interaction (CI) method that focuses on obtaining accurate many-body wavefunctions by incorporating the excited states in the description of an electronic state. A configuration interaction calculation is variational as the energy obtained is guaranteed to be greater than the true energy.

The Møller-Plesset (MP) theory proposes an alternative manner to deal with the problem of electron correlation. It is basically the Rayleigh-Schrödinger perturbation theory[141], in which the non-perturbed electronic Hamiltonian is the Hartree-Fock Hamiltonian,

and the perturbation is the difference between the true multi-electron Hamiltonian and the HF Hamiltonian. The MP perturbation theory is however not variational and can sometimes give energies that are lower than the "true" energy. Another limitation is, as in any perturbation theory, the effectiveness of the MP perturbation theory heavily depends on how close the starting wavefunctions are to the exact wave function. When this is the case, convergence of the MP series is rapid. However, when bonds are stretched, the MP series becomes oscillatory. Moreover, higher order forms of MP perturbation theory can even diverge to infinity. This can happen even for systems where the Hartree-Fock analysis has a good starting point, see Figure 3.8. In fact, studies on small molecular systems[142] posed serious questions about the usefulness of high-order MP perturbation theory.

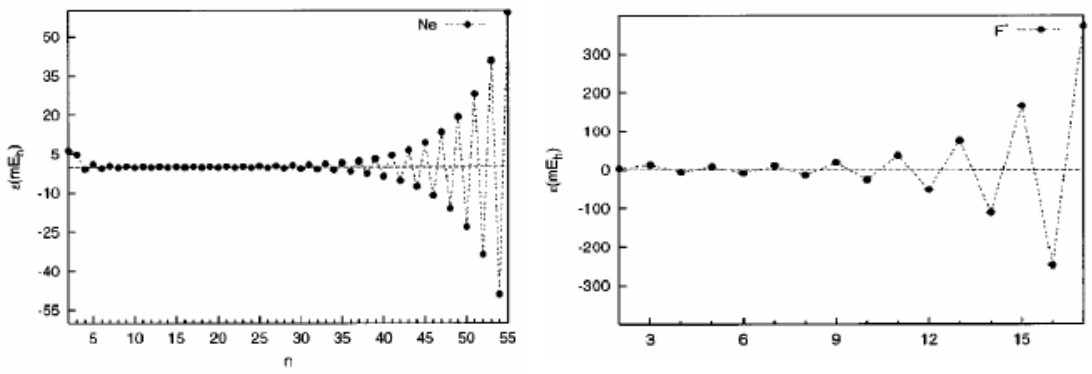

Figure 3.8 Convergence (divergence) behavior of MP series toward the exact value of energy[142].

Another popular post-Hartree-Fock technique is the coupled cluster method, which is not as transparent as the two computational schemes just described, and we will therefore simply mention it in passing here.

We must stress that almost all post Hartree-Fock methods share the combined limitations of poor scaling with system size and strong basis set dependence. For the CI method, the determinant grows exponentially with system size, which makes the method impractical for all but the smallest systems.

3.8 Semi-Empirical Methods

Ab initio calculations can be extremely expensive in terms of the computer resources required. Since we have noticed that the greatest proportion of the time required performing an *ab initio* HF SCF calculation is invariably spent calculating and manipulating integrals, the most obvious way to reduce the computational effort is to neglect or approximate some of these integrals. Semi-empirical (SE) methods achieve this approximation in part by explicitly considering only the valence electrons of the system, and the core electrons are subsumed into the nuclear core. The rationale behind this idea is that the electrons involved in chemical bonding and other phenomena of interest, are those in the valence shell. The SE calculations invariably use basis sets comprising Slater type s, p and sometimes d orbitals. The orthogonality of such orbitals enables further simplifications to be made to the equations.

A feature common to the semi-empirical methods is that the overlap matrix is set to the identity matrix I. It is important to note that setting the overlap matrix to the identity matrix does not mean that all overlap integrals are set to zero in the calculation of the Fock matrix elements. Indeed, it is important specifically to include some of the overlaps in even the simplest of the SE models.

3.8.1 Zero-Differential Overlap Approximation

Many semi-empirical theories are based upon the zero-differential overlap approximation (ZDO). In this approximation, the overlap between pairs of different orbitals is set to zero. Thus, some important approximations are used in the SE method, and these are:

- only valance electrons are taken into account;

- zero-differential overlap (ZDO): the overlap between pairs of different orbitals is set to zero for all volume elements;
- one s and three p orbitals are used for each atom;
- overlap integrals in the secular (Hartree-Fock) equation are ignored;
- neglect of three and four center integrals;
- practically all matrix elements are approximated by analytical functions of interatomic separation and atomic environment. Parameters are chosen to reproduce the characteristics of the reference systems;
- core-core Coulombic repulsion is replaced with a parameterized function.

3.8.2 Limitations of Semi-Empirical Methods

MNDO, AM1, and PM3 are presently the state-of-the-art of semi-empirical MO (Molecular Orbital) methods, which are capable of reproducing a wide variety of geometric and electronic molecular properties for a wide variety of molecules, giving good agreement with experimental data in the majority of cases.

However, since a number of approximations are introduced into the original Hamiltonian, some care must be taken in the application of such methods to chemistry problems. As such, we provide here several general remarks on the limitations of treated semi-empirical approaches:

- partially based on experimental data - the parameters are thus no better than the information used to obtain them;
- neglect or parameterization of overlap integrals can lead to errors;
- omission of core orbitals can lead to errors;
- electron correlation is included implicitly through parameterization
- there is no systematic way to improve a semi-empirical MO calculation.

3.9 Density Functional Theory

Density functional theory (DFT) methods[143] are the most wide-spread *ab initio* methods in computational material science and solid-state physics. This is due to their relatively high computational efficiency (among the first-principle methods) and very good accuracy.

In contrast to the Hartree-Fock procedure, which begins conceptually with a description of the individual electrons' interaction with the nuclei and other electrons in the system, the DFT starts with a consideration of the entire electron system. Recall that if there are N electrons in the system, the wave function of the electron system is a function of $3N$ variables (since the electron wavefunction is usually expanded over some basis functions, the actual number of the variables is governed by the number of basis functions which is typically much larger than $3N$). However, within DFT, all aspects of the electronic structure of the system of interacting electrons are "lumped" into an "external" potential $V_{ext}(\vec{r})$ (in this case, the potential generated by atomic cores), which is completely determined by the electronic charge density $n(\vec{r})$.

At the heart of DFT is the Hohenberg-Kohn (H-K) theorem[144], which shows that the energy of a quantum-mechanical system is *uniquely* determined by its electron density. It states that, for a given ground-state density $n_0(\vec{r})$, it is possible in principle, to calculate the corresponding unique ground-state wavefunctions.

The H-K theorem radically simplifies the problem of calculating electronic structure. For a system of N electrons, the Schrödinger equation and density operators can be written as

$$\hat{H}\psi = E\psi \tag{3.17}$$

$$\hat{H} = \sum_{i=1}^{N}\left(-\frac{1}{2}\nabla_i^2\right) + \sum_{i=1}^{N} V_{ext}\left(\vec{r}_i\right) + \sum_{i<j}^{N}\frac{1}{r_{ij}} \tag{3.18}$$

$$n\left(\vec{r}_i\right) = N\int\ldots\int\left|\psi\left(\vec{r}_1,\vec{r}_2,\ldots,\vec{r}_N,\right)\right|^2 d\vec{r}_2\ldots\vec{r}_N \tag{3.19}$$

where $\psi\left(\vec{r}_1,\vec{r}_2,\ldots,\vec{r}_N,\right)$ is the many-electron wavefunction, and $n\left(\vec{r}_i\right)$ is the electron density at $\vec{r}_i$. According to the Hohenberg-Kohn theorem, the ground state energy and wavefunction can be found by minimizing the energy with respect to ψ, and at the same time, for a given system, the ground state wavefunction (and hence charge density) is wholly determined by the number of electrons *N*, and the external potential (generally due to the atoms) $V_{ext}\left(\vec{r}\right)$.

The Hohenberg-Kohn theorem vastly simplifies the problem by proving that, to within an additive constant $V_{ext}\left(\vec{r}\right)$, and *N* are determined solely by $n\left(\vec{r}\right)$. This is effectively reversing the previous statement that $n\left(\vec{r}\right)$ determines $V_{ext}\left(\vec{r}\right)$ and thus the uniqueness. We can then write:

$$E\left[n\left(\vec{r}\right)\right] = T_s\left[n\left(\vec{r}\right)\right] + V_{Ne}\left[n\left(\vec{r}\right)\right] + V_{xc}\left[n\left(\vec{r}\right)\right] \tag{3.20}$$

$$V_{Ne}\left[n\left(\vec{r}\right)\right] = \int n\left(\vec{r}\right)V_{ext}\left(\vec{r}\right)d\vec{r} \tag{3.21}$$

$$T_s\left[n\left(\vec{r}\right)\right] = -\frac{1}{2}\sum_{i=1}^{N}\left\langle\psi\left(\vec{r}\right)\left|\nabla^2\right|\psi\left(\vec{r}\right)\right\rangle \tag{3.22}$$

where $T_s\left[n\left(\vec{r}\right)\right]$ is defined as the kinetic energy of a *non-interacting* electron gas with density $n\left(\vec{r}\right)$, and $V_{Ne}\left[n\left(\vec{r}\right)\right]$ is the electron-nuclear interaction. In addition $V_{xc}\left[n\left(\vec{r}\right)\right]$, the exchange-correlation energy includes all the kinetic terms due to interactions with the electron gas. Notice that $T_s\left[n\left(\vec{r}\right)\right]$ is not the kinetic energy of the real system, since there are no electron-electron interactions.

The Hohenberg-Kohn theorem makes this transformation useful, as it shows that for any trial density, $n(\vec{r})$, which satisfies the physically reasonable conditions that $n(\vec{r}) \geq 0$ and $\int n(\vec{r}) d\vec{r} = N$,

$$E(n_0) \leq E\left[n(\vec{r})\right] \tag{3.23}$$

Thus, the minimum energy is given by the ground state charge density only, and that density is formed from the ground state wavefunction. This means that the charge density can be treated as the variational parameter in a minimization.

In Eq. (3.20), the kinetic energy T_s, and the exchange correlation energy E_{xc} are more difficult to express in terms of the charge density. To determine T_s we have to invoke the Kohn-Sham theory, and to express E_{xc}, the local density approximation is usually used.

3.9.1 Kohn-Sham Theory

Obtaining an expression for the kinetic energy of the electrons in terms of the charge density is a difficult task. Thomas[145] proposed a quantum statistical model of electrons to obtain the kinetics, but it is quite crude and unsatisfactory for atoms and molecules in particular. On the other hand, the kinetic energy is easily calculated from the wavefunction that can be written in terms of *non-interacting* orbitals

$$n(\vec{r}) = \sum_{i=1}^{N} \left|\psi_i(\vec{r})\right|^2 \tag{3.24}$$

For this reason, Kohn and Sham[146] proposed an ingenious method of marrying wave function and density approach. To do this, the total energy functional is decomposed into the following parts

$$E\left[n(\vec{r})\right] = T_s\left[n(\vec{r})\right] + \frac{1}{2}\iint \frac{n(\vec{r})n(\vec{r}')}{|\vec{r}-\vec{r}'|} d\vec{r}\vec{r}' + E_{xc}\left[n(\vec{r})\right] + \int n(\vec{r}) V_{ext}(\vec{r}) d\vec{r} \tag{3.25}$$

The second term in Eq. (3.25) is the *self-interaction*, which represents interaction of $n(\vec{r})$ with itself. $V_{ext}(\vec{r})$ is the external potential, i.e., the potential due to the nuclei

$$V_{ext}(\vec{r}) = \sum_I \frac{-Z_I}{|\vec{R}_I - \vec{r}|} \tag{3.26}$$

The last functional, $E_{xc}\left[n(\vec{r})\right]$, called exchange-correlation energy, consists of all the interaction terms.

The only term in Eq. (3.25) for which no explicit form can be given is E_{xc}. Similar to the Hartree-Fock approximation; we apply the variational principal and introduce a normalization constraint on the electron density $\int n(\vec{r}) d\vec{r} = N$. The resulting equations are:

$$\left[-\frac{1}{2}\nabla^2 + \left(V_{ext}(\vec{r}) + \int \frac{n(\vec{r}')}{|\vec{r}-\vec{r}'|} d\vec{r}' + V_{xc}(\vec{r})\right)\right]\psi_\lambda = E_\lambda \psi_\lambda \tag{3.27}$$

where ψ_λ is the wavefunciton for the λ^{th} orbital, and $V_{xc}(\vec{r})$ is the potential due to the exchange-correlation energy E_{xc}, which is defined as the functional derivative of E_{xc} with respect to $n(\vec{r})$

$$\frac{\delta E_{xc}\left[n(\vec{r})\right]}{\delta n(\vec{r})} = V_{xc}(\vec{r}) \tag{3.28}$$

and the effective potential is thus

$$V_{eff}(\vec{r}) = V_{ext}(\vec{r}) + \int \frac{n(\vec{r}')}{|\vec{r}-\vec{r}'|} + V_{xc}(\vec{r}) \tag{3.29}$$

It can be seen that Eq. (3.27) is a single particle Schrödinger equation, and the self-consistent solution of these leads to the ground state charge density of the system.

Thus, by introducing the K-S approach, we are effectively considering *N* fictitious, *non-interacting* particles moving in an effective potential as shown in Figure 3.9. In addition, the Schrödinger equation has been simplified into a simple single-particle system rather than a *N*-electron one.

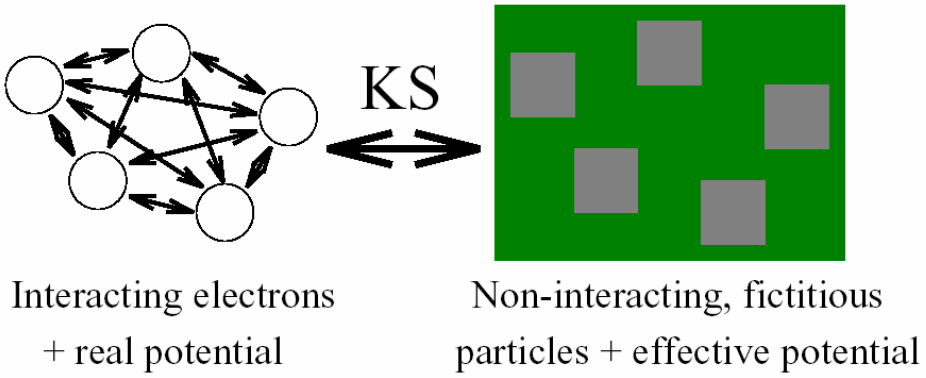

Figure 3.9 Schematic of Kohn-Sham assumption.

However, there still remains the problem with V_{xc}. The following subsections describe the local density and generalized gradient approximations to handle this problem.

Figure 3.10 presents the comparison of the H_2 potential curves computed using RHF, UHF, and Kohn-Sham (RKS and UKS) formulations. The energy calculated by HF is higher than that by KS, and this is a consequence of neglecting electron correlation in the HF.

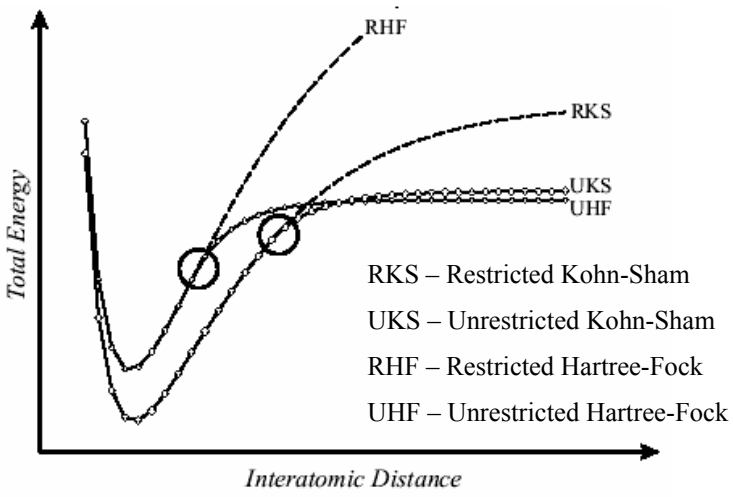

Figure 3.10 H_2 potential curves computed using HF and KS formulations formulations.

3.9.2 The Local Density Approximation

The effective potential that occurs in the one-particle equations of the non-interacting reference system is local in the sense that it is a function of only the spatial variable $\vec{r}$ and is independent on the value at other points in space. The local density approximation (LDA) states that, for regions of a material where the charge density is slowly varying, the exchange correlation energy at that point can be considered the same as that for a locally uniform electron gas of the same charge density. In this case, the exchange-correlation energy functional E_{xc} is given as

$$E_{xc}^{LDA}\left[n(\vec{r})\right] = \int \varepsilon_{xc}\left[n(\vec{r})\right] n(\vec{r}) d\vec{r} \tag{3.30}$$

where $\varepsilon_{xc}\left[n(\vec{r})\right]$ is the exchange and correlation energy per particle of a uniform electron gas of density $n(\vec{r})$. Although this approximation is extremely simple, it is surprisingly accurate, and forms the core for most modern DFT codes. However, it tends to under-predict atomic ground state energies and ionization energies, while over-predicting binding energies. It is also known to overly favor high spin state structures. Many researchers[147-151] have suggested that since the major source of error in the LDA is in the exchange energy, we should therefore consider the gradient of the density, as well as the value, at a given point. This generalized gradient approximation (GGA), they argue, will make the exchange energy more accurate.

3.9.3 Generalized Gradient Approximation (GGA)

As stated above, the LDA uses the exchange-correlation energy for the uniform electron gas at every point in the system regardless of the homogeneity of the real charge density. For non-uniform charge densities, the exchange-correlation energy can deviate

significantly from the uniform result.

In order to account for the non-homogeneity of the electron density, we use not only the density $n(\vec{r})$ at a particular point *r*, but supplement the density with information regarding the gradient of the charge density, $\nabla n(\vec{r})$. As a result of this procedure the GGA can be conveniently written in terms of an analytic function known as the enhancement factor, $F_{xc}\left[n(\vec{r}),\nabla n(\vec{r})\right]$, that directly modifies the LDA energy density. Thus, we arrive at

$$E_{xc}^{GGA}\left[n(\vec{r})\right]=\int n(\vec{r})\varepsilon_{xc}\left[n(\vec{r})\right]F_{xc}\left[n(\vec{r}),\nabla n(\vec{r})\right]d\vec{r} \tag{3.31}$$

For the exchange functional F_{xc}, two main classes of realization have been put forward. The first is based on a GGA exchange functional developed by Becke[150,152-158]. Functionals which are related to this approach include the FT97 functional[159], and the PW91 exchange functional[148]. The second class of GGA exchange functional uses a rational function of the reduced density gradient. The prominent representative is the PBE functional[147]. Generally, current GGAs seem to give reliable results for the main chemical bond types (covalent, ionic and metallic).

3.9.4 Hybrid Functionals

In spite of these advances in functional development, the quest for more accurate functionals goes on, and in both chemistry and physics areas, various post-GGA functionals have appeared in the literature. Perhaps the most popular functional in chemistry is B3LYP[151,156]. This is a combination of the LYP GGA[150,151] (for correlation) with Becke's three-parameter hybrid functional B3[155] (for exchange).

Common hybrid functionals, such as B3, mix a fraction of Hartree-Fock exchange

into the DFT exchange functional (other mixtures are also possible). This mixing involves a certain amount of empiricism (the weight factors given to the HF and DFT exchange terms are adjustable) and optimization is usually carried out for selected classes of molecules. In practice, B3 has proven to be the most successful exchange functional for chemical applications, and in particular when combined with the LYP functional. More extreme examples of this semiempirical mode of construction of functionals are Becke's[156] hybrid functional, which contains 10 adjustable parameters, each of which contains 21 parameters.

A flow chart for the DFT subroutine which calculates the energy is given in Figure 3.11.

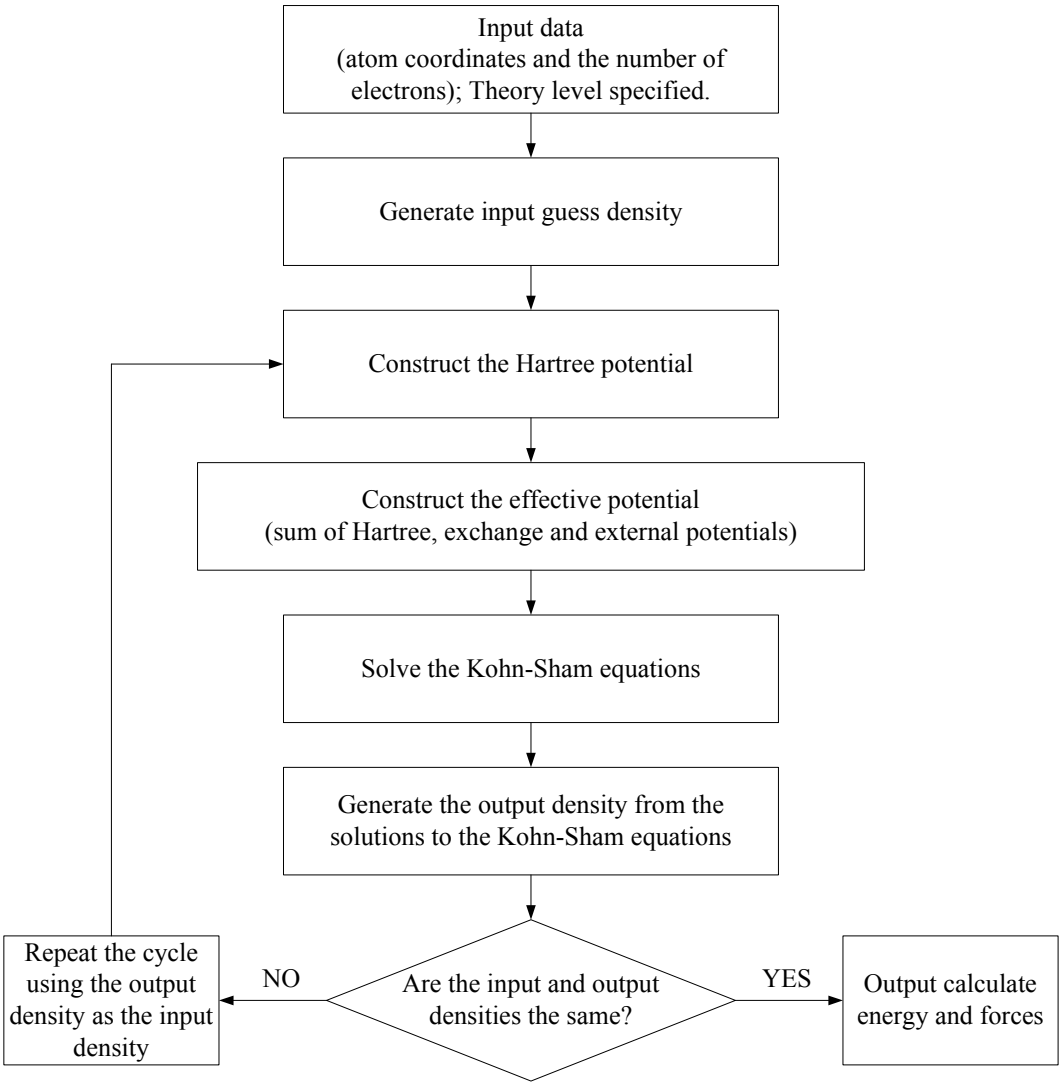

Figure 3.11 Flow chart describing the DFT method.

3.9.5 Limitations of DFT

We need to note that DFT also has a few shortcomings. As a ground state theory, any physical interpretation of calculated excited states is not theoretically justified. It consistently under-predicts semiconductor band gaps, and in some cases the band gap predictions are qualitatively wrong. Take NiO for example, DFT predicts metallic behavior whereas experimentally it is a good insulator.

3.10 Pseudopotentials

With today's level of high performance computing facilities, the DFT method described above would still prove computationally too extensive for system sizes useful for point defect modeling. It is therefore necessary to simplify the system further, and one important way of achieving this is through the use of pseudopotentials. These rely on the fact that the core electrons sit tightly bound to their nuclei, and only the valence electrons are involved in chemical bonding. The core states are incorporated into the pseudopotentials, and we only deal with the valence electrons separately.

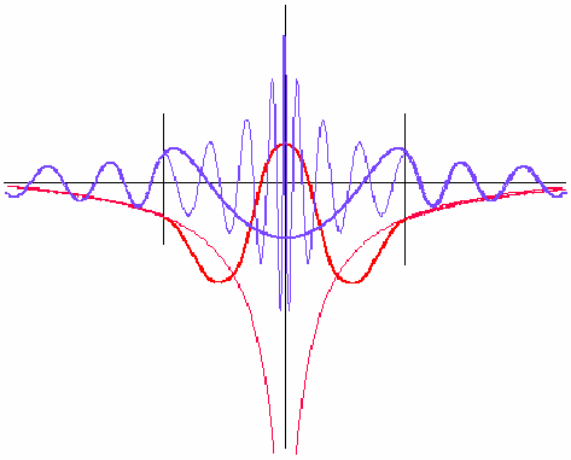

Figure 3.12 A schematic representation of the potentials (red lines) and wave functions (blue lines) for an atom. The real potential and the wavefunction are shown with thin lines, while the pseudopotential and wavefunction are shown in thick lines. Outside the cutoff region (vertical black lines), the two are identical.

It can been seen from Figure 3.12 that the core wavefunctions are rapidly varying, and will require a large number of fitting functions to model accurately. The use of pseudopotentials overcomes this as a smoothly varying pseudo-wavefunction is assumed within a certain core radius. In addition, the Coulombic interaction of core states would tend to swamp any total energy calculations when attempting to compare small differences in valence bond energies. In order to remain orthogonal to the core states the valence states are also forced to become rapidly oscillating near the atomic core, requiring large numbers of fitting functions to model accurately. Pseudopotentials overcome all of these problems. They become particularly important for the heavier elements when the number of core electrons vastly outweighs the valence electrons. For heavier atoms in which relativistic effects are important, the Dirac equation is required, and the valence electrons can be treated non-relativistically. Therefore, removal of the core electrons allows a non-relativistic approach to be maintained, but some corrections are required in the core electron pseudopotentials to account for relativistic effects.

Pseudopotentials assume that the localized core states do not take part in bonding and so can be incorporated as a change in the charge state of the nucleus. Between the nucleus and some cutoff radius r_c, all the electron valence wavefunctions can be replaced with a smoothed form but beyond this radius the pseudo-wavefunction must be identical to the real wavefunction. In addition, there will still be exchange interactions between core and valence electrons that must be included in the potentials. Finally, if self-consistency is to be easily achieved in the calculations then the potentials must have the correct atomic charge density outside the core.

3.11 Hessian Matrix in Geometry Optimization

The state of the optimized structures corresponds with the minimum or saddle

points in the potential energy surfaces (PESs). Searches for stationary points on the PESs are usually performed using an initial guess of the Hessian matrix, which consists of the second partial derivatives of the potential energy E with respect to displacement of the atoms in Cartesian coordinates.

$$H_{i,j} = \left(\frac{\partial^2 E}{\partial \xi_i \partial \xi_j} \right)_0 \tag{3.32}$$

This is a $3N \times 3N$ matrix (N is the number of atoms), where $\xi_1, \xi_2, \xi_3 \cdots \xi_{3N}$ are used to represent the displacements in Cartesian coordinates $x_1, x_2, \ldots x_N$, $y_1, y_2, \ldots, y_N, z_1, z_2, \ldots, z_N$. The $(\,)_0$ refers to the fact that the derivatives are taken at the equilibrium positions of the atoms, and that the first derivatives are zero.

In order to calculate the vibrational frequencies, the Hessian matrix is first mass-weighted:

$$H^m_{i,j} = \frac{H_{i,j}}{\sqrt{M_i M_j}} \tag{3.33}$$

Diagonalization of the resulting matrix yields a set of $3N$ eigenvalues λ_i. The square roots of the eigenvalues $\sqrt{\lambda_i}$, are the frequencies of the molecule.

At those minimum and saddle points, the unit for the eigenvalues λ_i are often converted to cm^{-1} via the relationship $\lambda_i = 4\pi^2 \tilde{\nu}_i^2 c^2$ and $\nu_i = \tilde{\nu}_i c$, where c is the speed of light in $cm.s^{-1}$. The eigenvalues can thus be written as

$$\tilde{\nu}_i = \sqrt{\frac{\lambda_i}{4\pi^2 c^2}} \tag{3.34}$$

$$\nu_i = \frac{\sqrt{\lambda_i}}{2\pi} \tag{3.35}$$

The following test can be applied at a non-degenerate critical point (x_i, y_i,. z_i). If the frequencies are all positive definite at (x_i, y_i,. z_i), then the total energy of E attains a local minimum at (x_i, y_i,. z_i), which indicates a stable intermediate state. If the Hessian has one negative eigenvalue with the rest being positive, then we have a saddle point at (x_i, y_i,. z_i) which corresponds to a transition state.

3.12 Population Analysis

Determining the charge or spin density distribution of a molecule or cluster is a very important aspect of quantum chemistry research as it can be used to interpret the results in terms of qualitative concepts. The nature of the chemical bonding in molecular systems and the changes in the electron density distribution upon the electron excitation is helpful for understanding the nature of the chemical reactions. In chapters 6 and 7, we use the population analysis methods to analyze the chemical structure, namely the bonding/antibonding nature of molecular orbitals. The Mulliken population analysis, natural bond orbital (NBO) analysis and the density of states (DOS) analysis are employed and are thus presented in this section.

3.10.1 Electron Density Distribution

The electron density at a point r, $\rho(\vec{r})$ can be expressed as:

$$\rho(\vec{r}) = \sum \left|\psi_i(\vec{r})\right|^2 \tag{3.36}$$

For a system with N electrons occupying $N/2$ levels, it becomes:

$$\rho(\vec{r}) = 2\sum_{i=1}^{N/2} \left|\psi_i(\vec{r})\right|^2 \tag{3.37}$$

which is due to the Pauli principle. As ψ can be expressed as the linear combination of ba-

sis function of Eq. (3.14), thus the electron density at a given point can be expressed as

$$\rho(\vec{r}) = 2\sum_{i=1}^{N/2}\left(\sum_{\mu=1}^{M} c_{\mu i}\phi_{\mu}(\vec{r})\right)\left(\sum_{\nu=1}^{M} c_{\nu i}\phi_{\nu}(\vec{r})\right) \tag{3.38}$$

$$\rho(\vec{r}) = 2\sum_{i=1}^{N/2}\sum_{\mu=1}^{M} c_{\mu i}c_{\nu i}\phi_{\mu}(\vec{r})\phi_{\nu}(\vec{r}) + 2\sum_{i=1}^{N/2}\sum_{\mu=1}^{M}\sum_{\nu=\mu+1}^{M} 2c_{\mu i}c_{\nu i}\phi_{\mu}(\vec{r})\phi_{\nu}(\vec{r}) \tag{3.39}$$

where M is the number of atoms, and Eq. (3.39) can be simplified if considered in terms of the elements of the density matrix:

$$P_{\mu\nu} = 2\sum_{i=1}^{N/2}\sum_{\mu=1}^{M} c_{\mu i}c_{\nu i} \tag{3.40}$$

Thus Eq. (3.39) is rewritten as follow:

$$\begin{aligned}\rho(\vec{r}) &= \sum_{\mu=1}^{M} P_{\mu\nu}\phi_{\mu}(\vec{r})\phi_{\nu}(\vec{r}) \\ &= \sum_{\mu=1}^{M} P_{\mu\nu}\phi_{\mu}(\vec{r})\phi_{\nu}(\vec{r}) + 2\sum_{\mu=1}^{M}\sum_{\nu=\mu+1}^{M} P_{\mu\nu}\phi_{\mu}(\vec{r})\phi_{\nu}(\vec{r})\end{aligned} \tag{3.41}$$

Integrating the electron density over all space should produce the number of valence electrons in the system:

$$N = \int dr\,\rho(\vec{r}) = 2\sum_{i=1}^{N/2} P_{\mu\nu}\phi_{\mu}(\vec{r})\phi_{\nu}(\vec{r}) \tag{3.42}$$

Finally, if the overlap of two basis orbital $\phi_{\mu}(\vec{r})$ and $\phi_{\nu}(\vec{r})$ can be written as $S_{\mu\nu}$, then one could write the following compact expression for N:

$$N = \sum_{\mu=1}^{N/2} P_{\mu\mu}S_{\mu\mu} + 2\sum_{\mu=1}^{n}\sum_{\nu=\mu+1}^{n} P_{\mu\nu}S_{\mu\nu} \tag{3.43}$$

3.10.2 Mulliken Population Analysis

There are several ways to partition the atomic charges, among which probably the most well-known is the Mulliken population analysis (MPA)[160], where the electron density in an orbital $P_{\mu\nu}$ of Eq. (3.40) is assigned to the atom on which ϕ_μ is located. The overlap part $\phi_\mu\phi_\nu$ is assigned in halves to the two atoms that ϕ_μ and ϕ_ν are based. In addition, the charge on atom A is given by:

$$q_A = Z_A - \sum_{\substack{\mu=1 \\ \mu on A}}^{K} P_{\mu\mu}S_{\mu\mu} + 2\sum_{\substack{\mu=1 \\ \mu on A}}^{K}\sum_{\nu=+1 \atop \nu\neq\mu}^{K} P_{\mu\nu}S_{\mu\nu} \tag{3.44}$$

Although MPA can yield very good results, it can also give rise to various contradictions. For example, the charge associated with a particular orbital will be exclusively assigned to the atom that the orbital is based on, even though the orbital may be extended far beyond the nucleus of that atom. This is a drawback of the method, as the basis functions have to be based on the atomic centers of the MPA to be valid.

Other schemes to partition the overlap population have been proposed, such as, MMPA (modified Mulliken population analysis) by Stout and Politzer[161], SCPA by Ros and Schuit[162], Löwdin Population Analysis[111,163,164], and NBO[165,166] (natural bond orbital) analysis. The NBO is the most frequently used today, and provides the information such as charge distribution, bond types, hybrid directions, resonance weights, bond orders and other familiar valence descriptors.

3.10.3 Natural Bond Orbital Analysis

The NBO[165,166] (natural bond orbital) overcomes the problem of lower or greater than two electron populations by incorporating two important physical effects that distin-

guish them from isolated-atom natural orbitals as well as from standard basis orbitals, namely:

- The spatial diffuseness of the natural atomic orbitals (NAOs) is optimized for the effective atomic charge in the molecular environment (i.e., more contracted if A is somewhat cationic; more diffused if A is somewhat anionic). NAOs therefore automatically incorporate the important "breathing" responses to local charge shifts that usually require variational contributions from multiple basis functions of variable range (double zeta, triple zeta, or higher) to describe accurately.

- The outer fringes of NAOs incorporate the important nodal features due to steric confinement in the molecular environment (i.e., increasing oscillatory features and higher kinetic energy as neighboring NAOs begin to interpenetrate, preserving the interatomic orthogonality required by the Pauli exclusion principle). The valence NAOs of an atom therefore properly incorporate both the inner nodes that preserve orthogonality to its own atomic core as well as the outer nodes that preserve orthogonality to filled orbitals on other atoms. Both features are necessary for realistic steric properties in the molecular environment (i.e., proper Fermi-Dirac anticommutators of the associated second-quantized NAO field operators), but both are commonly ignored in standard basis orbitals.

Natural Bond Orbital analysis transforms the input basis set $\{\chi_i\}$ to various localized basis sets (natural atomic orbitals NAOs, hybrid orbitals NHOs, bond orbitals NBOs, and localized molecular orbitals NLMOs). The localized sets may be subsequently transformed to delocalized natural orbitals (NOs) or canonical molecular orbitals (MOs). Each step of the above sequence involves an orthonormal set that spans the full space of the input basis set and can be used to give an exact representation of the calculated wavefunction and the expectation values of selected operators (properties) of the system.

Mathematically, the natural orbitals (NOs) $\{\Theta_k\}$ of a wavefunction Ψ can be defined as the eigenorbitals of the first-order reduced density operator $\mathbf{\Gamma}$.

$$\mathbf{\Gamma}\Theta_k = p_k\Theta_k \quad (k = 1, 2,\ldots) \tag{3.45}$$

where k indicates the k^{th} orbital, the eigenvalue p_k represents the population (occupancy) of the engenfunction Θ_k for the molecular electron density operator $\mathbf{\Gamma}$ of Ψ. The density operator is merely the 1-electron "projection" of the full N-electron probability distribution (given by the square of the wavefunction $|\Psi|^2$). Thus, Ψ is the only quantity that enters into the definition of the NOs, and these orbitals are truly Ψ's "own" (*eigen*) orbitals, intrinsic ("natural") to the description of the electron density and other single-electron properties of Ψ. As for any Hermitian eigenvalue problem, the NOs form a complete orthonormal set. $\{\Theta_k\}$ can be characterized as maximum occupancy orbitals. The electronic occupancy p_φ of any normalized "trial orbital" φ can be evaluated as the expectation value of the density operator:

$$p_\varphi = \langle\varphi|\mathbf{\Gamma}|\varphi\rangle \tag{3.46}$$

The subsystem density operator $\mathbf{\Gamma}$ for atom A are defined as eigenorbitals of $\mathbf{\Gamma}^A$.

$$\mathbf{\Gamma}^A\Theta_k^A = p_k^A\Theta_k^A \quad (k = 1, 2,\ldots) \tag{3.47}$$

The Natural Atomic Orbitals (NAOs) population p_k^A properly sum to the total number of electrons N and lead unambiguously to the corresponding net natural atomic charge Q_A

$$Q_A = Z_A - \sum_k p_k^A \tag{3.48}$$

where Z_A is the nuclear charge. The natural populations automatically satisfy physical positivity and Pauli constraints ($0 \le p_k^A \le 2$ for closed shells).

NAO orbitals allow the calculation of an improved natural population analysis cor-

recting some of the Mulliken population analysis deficiencies. Once the NAOs are evaluated, the core orbitals (with occupancies >1.999 e^-) are set. Following this, among the one-center blocks, the lone-pairs (with occupancies >1.90 e^-) are defined, and finally, the bond-vectors (occupancy >1.90 e^-) are located among the two center blocks. In this way, a "natural Lewis structure" is obtained.

The NBOs are localized 1 or 2-center orbitals that describe the Lewis-like molecular bonding pattern of electron pairs analysis. For example, the NBO summary of the 2-center σ_{AB} localized bond is formed:

$$\sigma_{AB} = c_A h_A + c_B h_B \tag{3.49}$$

where h_A and h_B are the valence hybrids, and c_A and c_B are the polarization coefficients, which satisfy $c_A^2 + c_B^2 = 1$. Depending on the values of these coefficients of c_A and c_B, a bond NBO may range between covalent ($c_A = c_B$) and ionic ($c_A >> c_B$) limits. However, no sharp distinction can be drawn between a 2-center σ_{AB} of highly polar form and a 1-center ($c_A = 1$, $c_B = 0$) case. To conform to common chemical usage, the NBO identifies a highly polar σ_{AB} as a lone pair whenever 95% or more of the electron density is on a single center ($c_A^2 \geq 0.95$).

Such natural localized functions require simultaneous orthonormality and maximum occupancy, leading to compact expressions for atomic and bond properties. *Ab initio* wave functions transformed to NBO form are found to be in good agreement with Lewis structure concepts and with the basic Pauling-Slater-Coulson picture of bond hybridization and polarization. The NBO summaries of the "natural Lewis structures" are therefore well adapted to describing covalency effects in molecules. The NBO summary also describes the non-covalency effects like the antibonds σ_{AB}^*,

$$\sigma_{AB}^* = c_A h_A - c_B h_B \tag{3.50}$$

which, arise from the same set of atomic valence-shell hybrids that unite to form the bond functions σ_{AB}. The anitbond is derived from the same unfilled valence hybrids that give rise to the bonding NBOs, and σ^*_{AB} represents unused valence shell capacity of the constituent atoms, unsaturated by covalent bond formation.

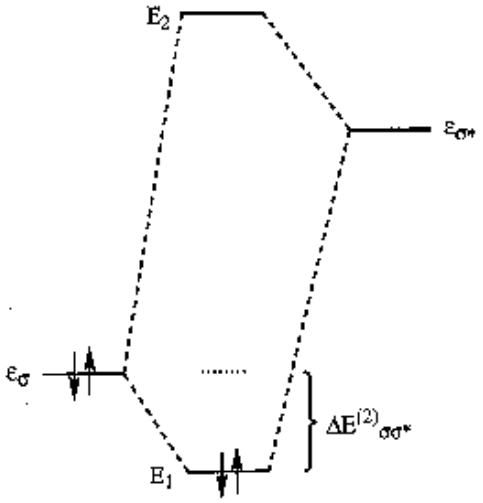

Figure 3.13 Perturbative donor-acceptor interaction, involving a filled orbital σ and an unfilled orbital σ^*.

The antibonding orbital contribution to the energy $E_{\sigma\sigma^*}$ are typically much less than 1% of the covalent contributions, reflecting the dominance of the Lewis-type component of the bonding. These corrections to the Lewis picture are usually too small to be well approximated by simple second-order perturbative expressions of the type illustrated in Figure 3.13.

This figure depicts the interaction of a filled orbital σ of the formal Lewis structure with one of the unfilled antibonding orbitals σ^* to give the second-order energy lowering, $\Delta E^{(2)}_{\sigma\sigma^*}$. Based on SCF-MO (self-consistent field molecular orbital) theory

$$\Delta E^{(2)}_{\sigma\sigma^*} = -2\frac{\left\langle \sigma \middle| \hat{F} \middle| \sigma^* \right\rangle}{\varepsilon_{\sigma^*} - \varepsilon_{\sigma}} \tag{3.51}$$

where $\hat{F}$ is the Fock operator and ε_σ and ε_{σ^*} are the NBO orbital energies. The NBO perturbative framework permits one to apply qualitative concepts of valence theory to describe the non-covalent energy lowering.

Since the non-covalent delocalization effects are associated with $\sigma \rightarrow \sigma^*$ interactions between filled (donor) and unfilled (acceptor) orbitals, it is natural to describe them as being of "donor-acceptor", "charge transfer", or generalized "Lewis base-Lewis acid" type. An excellent illustrative review of NBO analysis and its applications, is found in Reed *et al*.[165,166].

3.13 The Density of State

To calculate various optical properties such as the rate of absorption or emission and how electrons and holes distribute themselves within a solid, the number of available states per unit volume per unit energy are often used to analyze the result. We will calculate the available states in *k*-space and then use the energy-momentum relation in parabolic bands to give the density of states in terms of energy which is used in subsequent chapters 6 to 8.

By considering the electrons in a solid as a free electron gas, the free electron of mass m has a velocity $\mathbf{v}$ and a momentum $\mathbf{p} = m\mathbf{v}$. Its energy consists entirely of kinetic energy (V=0) therefore

$$E = \frac{1}{2} m\mathbf{v}^2 = \frac{|\mathbf{p}|^2}{2m} \tag{3.52}$$

The idea of particle-wave duality allows us to give the electron a wave number $\mathbf{k}$

$$\mathbf{k} = \frac{\mathbf{p}}{\hbar} \tag{3.53}$$

If we consider the equation for the energy of the electron in terms of **k**

$$E = \frac{\hbar^2}{2m}\left(k_x^2 + k_y^2 + k_z^2\right) = \frac{\hbar^2 |\mathbf{k}|^2}{2m} \tag{3.54}$$

rearranging gives

$$|\mathbf{k}| = \sqrt{\frac{2mE}{\hbar^2}} \tag{3.55}$$

The solution of the Schrödinger equation leads to wavefunctions of the form

$$\psi(\mathbf{r}) = C\exp(i\mathbf{k}\cdot\mathbf{r}) \tag{3.56}$$

Following we consider the 3D density of states (DOE).

For example, in 3D *k*-space as shown in Figure 3.14, the restriction according to the PBC (periodic boundary conditions) requires the wavefunction to be exactly the same at the opposing. Thus only certain values of *k*-space lead to acceptable electron wavefunctions solutions. If considering the cubic unit cell with dimension of $L\times L\times L$ (L is the wavelength), then we have $(x+L, t) = (x, t)$, and this yields $\exp(i\cdot kL) = 1$ or $k = n\cdot 2\pi/L$ (n = …-2, -1, 0, 1, 2, 3, …). Explicitly, the volume of 3D *k*-space would be

$$V_{3D} = \left(\frac{2\pi}{L}\right)^3 \tag{3.57}$$

In 3D, the volume between the two shells is given by

$$v_{s3D}\mathrm{d}\mathbf{k} = 4\pi|\mathbf{k}|^2\,\mathrm{d}\mathbf{k} \tag{3.58}$$

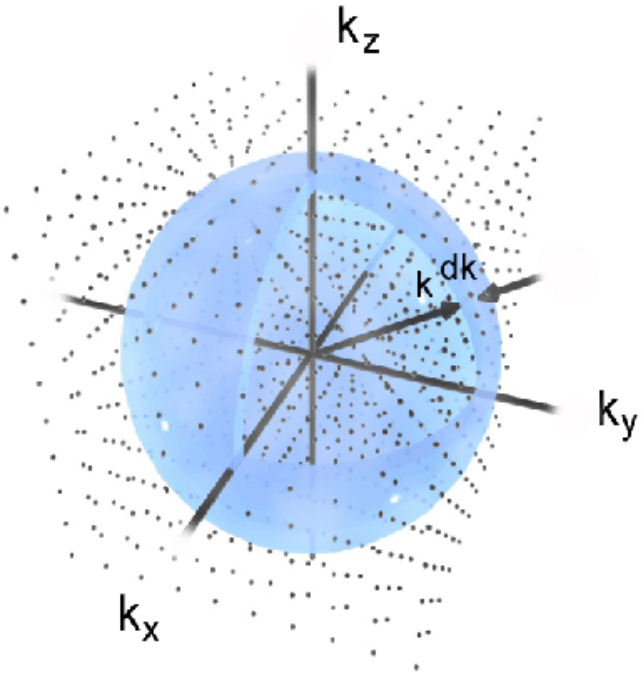

Figure 3.14 Visualization of *k*-space showing values of **k** as points. The number of allowed states is the number of these points contained in the shell of radius **k** and thickness d**k**.

Therefore, the number of states is given simply by dividing this volume by the volume of a single energy state. At this point is convenient to introduce an additional factor of two to account for the intrinsic angular momentum of the electrons or spin states. The resulting density of states is

$$g(\mathbf{k})_{3D}\,\mathrm{d}\mathbf{k} = 2\times\frac{v_{s3D}}{V_{3D}}\mathrm{d}\mathbf{k} = \frac{|\mathbf{k}|^2\,\mathrm{d}\mathbf{k}}{\pi^2}L^3 \tag{3.59}$$

To obtain the density of states per unit volume in terms of the energy we use Eq. (3.55), and we then differentiate this with respect to the energy.

$$\mathrm{d}\mathbf{k} = \left(\frac{2mE}{\hbar^2}\right)^{-\frac{1}{2}}\frac{m}{\hbar^2}\mathrm{d}E \tag{3.60}$$

Taking the bulk case as an example, the density of states in terms of energy is then

$$g(E)_{3D}\mathrm{d}E = \frac{|\mathbf{k}|^2\,\mathrm{d}\mathbf{k}}{\pi^2} = \frac{2mE}{\pi^2\hbar^2}\left(\frac{2mE}{\hbar^2}\right)^{-\frac{1}{2}}\frac{m}{\hbar^2}\mathrm{d}E = \frac{1}{2\pi^2}\left(\frac{2m}{\hbar^2}\right)^{\frac{3}{2}}E^{\frac{1}{2}}\mathrm{d}E \tag{3.61}$$

This gives the density of states per unit volume at a wave vector **k**.

In chapters 6 and 7, we will use the DOS to help us analyze the properties of the hydrogenated carbon nanotubes.

3.14 Conclusion

The main problem of Hartree-Fock and DFT methods is the underlying treatment of electron correlation. In the Hartree-Fock method, electron correlations beyond a mean field picture are entirely neglected, whereas in the DFT they are included approximately via a functional $E_{xc}\left[n(\vec{r})\right]$. Both methods provide a relatively inexpressive route to performing computational physics, chemistry and materials science.

Post Hartree-Fock methods are potentially very accurate, but their poor scaling with system size limits their usefulness, restricting their application to small molecular systems and exclusion to most topics in condensed matter.

Semi-empirical methods are much faster, but the neglect or parameterization of overlap integrals and the omission of core orbitals may lead to errors. Besides, the parameters based on experimental data are no better than the information used to obtain them.

CHAPTER 4

HYBRID CALCULATIONS WITH MULTISCALE ONIOM

The applications of computational chemistry to real world chemistry span from predicting the structure, spectra and reactivity of complicated molecules to understanding the chemical reaction property of a given site. To serve as a predictive tool, however, the methods should be applicable to a sufficiently large portion of the system, in such a way that the computed properties do reflect the features of the real system. For instance, one cannot restrict the chemical reaction of hydrogen onto the CNT by adopting too small clusters, because the limited structural and electronic properties cannot reflect the effect brought by the environment atoms which may be significant. However, the computational cost usually increases very quickly to unreasonably high levels when we attempt to increase the system size.

The multiscale ONIOM scheme, a hybrid method developed by Morokuma and co-workers[167-169], allows the partitioning of a chemical system into layers and different layers are treated by different levels of computational techniques, and combined to produce a consistent energy expression, see Figure 4.1. The objective of this scheme is to perform a high-level calculation only on a small part of the system while considering the effects caused by the remainder at lower levels of theory, with the result being of similar accuracy to a high-level calculation on the full system, but now obtained at a reasonable computa-

tional cost.

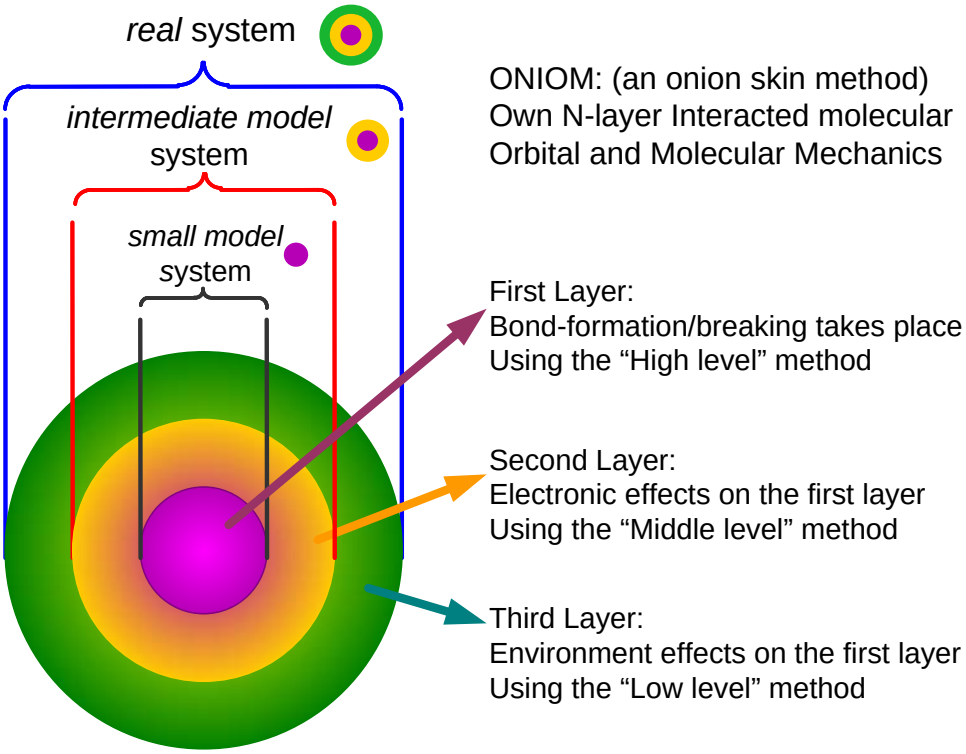

Figure 4.1 The onion skin-like layers and models. An example of a three-layer partitioning scheme[170].

However, it must be noted that the system is not randomly divided into different parts, but rather depends on the purpose each region serves and the level of interest in particular regions. Due to the division of the system, link atoms like hydrogen and fluorine are often used to replace the broken bonds. A typical case is that if one is interested in the accurate description of a particular region of a large organic molecule or a macromolecule, covalent bonds have to be cut in order to generate the inner model system, leavening dangling bonds at the border of the inner layer which have to be saturated in order to avoid a chemically unrealistic model. Hydrogen atoms are often used as the link atoms, and it is one of the critical features of treating the interface between layers in ONIOM method.

4.1 Link Atoms

When the layers are not covalently bound, the model system is identical to the high level layer. In that case, the ONIOM formulation does not need link atoms. However, when covalent bonds do exist, the resulting dangling bonds should be saturated with link atoms, which are chosen so that they best mimic the substituent. The link atoms for bonds spanning two regions are generated from the bond information, where the additional parameters on the model and real systems are derived to describe the broken bonds including scale factors for placement of the link atom and the type of link atom. Usually the default link atom is hydrogen.

In Figure 4.2, we provide more details on the treatment of the link atoms by taking the two-layer ONIOM2 model as an example. In this model, the atoms are divided into four groups of sets 1, 2, 3 and 4. The atoms present both in the model system and the real system are called set 1 atoms and their coordinates are donated by $\mathbf{R}_{model}$, and for simplicity, it is written as $\mathbf{R}_1$. The set 2 atoms are the artificially introduced link atoms, such as hydrogen atoms. They only occur in the model system and their coordinates are described by $\mathbf{R}_{\mathrm{LAH}}$, and simplified as $\mathbf{R}_2$, with LAH denoting the link atom hosts, which represent the atoms replaced by the link atoms in the model system. In the real system they are replaced by the atoms described by $\mathbf{R}_{link\text{-}real}$, and denoted by $\mathbf{R}_3$. Atoms that belong to the outer layer and are not substituted by link atoms are the set 4 atoms with the coordinates $\mathbf{R}_{real}$, and simplified as $\mathbf{R}_4$. The geometry of the real system is thus described by $\mathbf{R}_1$, $\mathbf{R}_3$ and $\mathbf{R}_4$ and they are independent coordinates for calculating the ONIOM energy.

$$E_{\mathrm{ONIOM}} = E_{\mathrm{ONIOM}}\left(\mathbf{R}_{model}, \mathbf{R}_{link-real}, \mathbf{R}_{real}\right) = E_{\mathrm{ONIOM}}\left(\mathbf{R}_1, \mathbf{R}_3, \mathbf{R}_4\right) \tag{4.1}$$

For the model system, it is described by $\mathbf{R}_{model}$ and the link atom $\mathbf{R}_{\mathrm{LAH}}$, which is defined as a function of $\mathbf{R}_{model}$ and $\mathbf{R}_{link\text{-}real}$, and the explicit functional form of $\mathbf{R}_{\mathrm{LAH}}$ de-

pendency can be written as:

$$\mathbf{R}_{\mathrm{LAH}} = f\left(\mathbf{R}_{model}, \mathbf{R}_{link-real}\right) \tag{4.2}$$

or

$$\mathbf{R}_2 = f\left(\mathbf{R}_1, \mathbf{R}_3\right) \tag{4.3}$$

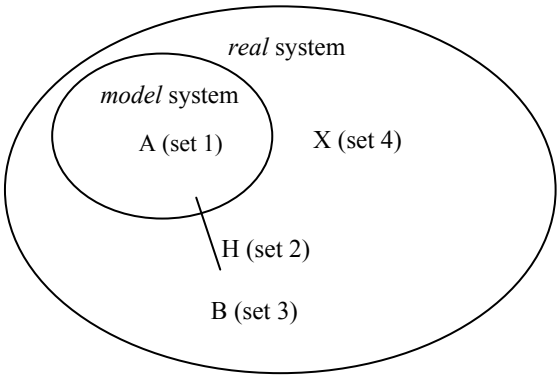

model system = inner layer + link atoms

real system = inner layer + outer layer

Figure 4.2 The scheme for link atoms

Considering the fact that the link atoms are introduced to mimic the corresponding covalent bonds of the real system, they should follow the movement of the atoms they replace. A coupling scheme is introduced here to handle this. If atom *A* belongs to set 1 (model system) and atom *B* to set 3 (atoms in real system but not substituted by the artificially introduced atoms), and the link atom in set 2 (artificially introduced link atoms in model system) is placed onto the bond axis *A*-*B*, see Figure 4.2. In terms of the internal coordinates, the same bond angles and dihedral angles is chosen for both set 2 atoms and set 3 atoms. Thus, link atoms are placed along the bond vector connecting the first to the second atom according to the equation

$$\mathbf{R}_2 = \left(1-g\right)\mathbf{R}_1 + g \times \mathbf{R}_3 \tag{4.4}$$

or

$$\mathbf{R}_{\mathrm{LAH}} = (1-g)\mathbf{R}_{model} + g \times \mathbf{R}_{link\text{-}real} \tag{4.5}$$

where g is the scale factor. If the scale factor is one, then the link atom is placed where the second atom was. More usually, the scale factor is less than one, in which case the link atom is placed between the original two atoms, and is always aligned along the bond vector of the real system. The scale factor should be chosen so that the link atom (usually hydrogen) is placed near its equilibrium bond length from the model atom. For example, when breaking a single carbon-carbon single bond (typical length 1.528Å for the sp^3 hybrid bond) using a hydrogen link atom we will want a carbon-hydrogen bond length of about 1.084Å, so the scale factor should be chosen as $1.084/1.528 \approx 0.709$ [134].

In this thesis, we will use the two-layer ONIOM scheme to study the chemical reaction processes for hydrogen atoms and molecules on the exterior and interior of the CNT. The whole system is partitioned into the model and real systems described above, where the atoms involved in the chemical reaction are treated by higher level calculation and the rest by a lower level method. Since the layers of different level calculations are covalently bound, the resulting dangling bonds due to the partition of the system into two different layers will be saturated with link atoms, which are chosen so that they best mimic the substituted atoms. As is the practice in the ONIOM method, hydrogen link atoms are used and this yielded good results. The C_{model}-H_{link} bonds are assigned the same angular and dihedral values as the C_{model}-C_{real} in the real system. The scaling factor is used for obtaining the bond length of C_{model}-H_{link}, which ensures that the number of degrees of freedom remains at $3N$-6, so that any method for conventional the investigation of potential energy surfaces can be used in this ONIOM scheme.

Theoretically, the ONIOM scheme allows a partition of the molecular system into two, three, or even more layers, and 'distribute' the computational methods (QM or MM) among these layers. The domain of greatest interest forms the innermost layer that is de-

scribed by the highest level theory. Subsequent layers are treated using progressively computationally cheaper lower-level approaches. The ONIOM scheme approximates the energy of a molecular structure subdivided into *n* layers as

$$\begin{aligned} &E_{\text{ONIOM}}\left(n\left(Level(1):Level(2):\cdots:Level(n)\right)\right) \\ &= E\left(Level(1),Layer(1)\right)+\sum_{i=2}^{n}\left[E\left(Level(i),\bigcup_{j=1}^{i}Layer(j)\right)\right]-\sum_{i=2}^{n}\left[E\left(Level(i),\bigcup_{j=1}^{i-1}Layer(j)\right)\right] \end{aligned} \quad (4.6)$$

where Level(i) is the level of theory used for layer i, starting from the highest Level(1) and ending with the lowest Level(n), while $\bigcup_{j=1}^{i}Layer(j)$ denotes the part of molecular structure consisting of layers 1 through i, where the entire sub-domain is given by $\bigcup_{j=1}^{n}Layer(j)$. The geometries of the subsequent fragments Layer(1), Layer(1) U Layer(2), Layer(1) U Layer(2) U Layer(3), etc., represent unmodified cutouts of the entire molecular structure with one exception - bonds connecting atoms belonging to subsequent layers are saturated by adding link atoms.

The idea of partitioning a molecular system into two or more parts or layers, where the interesting or difficult part of the system (the inner layer) is treated by a more refined level of theory and the rest of the system by a lower and therefore computationally less demanding method, is not new. Literature on the QM/MM hybrid method have referred to this onion-like layered scheme[168]. The simple QM/MM simulation without a smoothing scheme suffered a surge in the total energy from time to time due to the solvent exchange, and such abrupt changes in the total energy occurred during particle exchanges between the QM and MM subsystems, and is essentially due to a large difference in background potential energy calculated by different levels of theory. Accordingly, the simple QM/MM simulation may not be able to reach equilibrium, where an abrupt change in the forces on

exchanging particles causes the simulation to be terminated due to error in the integrator module.

4.2 ONIOM Energy Definition

4.2.1 Energy Calculation for ONIOM2

In the two-layered ONIOM method, see Figure 4.3, the total energy of the system is obtained from independent calculations:

$$E_{\mathrm{ONIOM2}}=E_3+E_2-E_1 \tag{4.7}$$

where E_3 denotes energy calculated at the lower level method, while the E_1 denotes the part of the system of which the energy is calculated at both the high and low levels. The energy of the real molecular system, calculated at the low level (E_3), is corrected using the energy difference ($\Delta E_{high\text{-}low}=E_2-E_1$) between the high ($E_2$) and low ($E_1$) levels of calculation on the inner layer, also called the 'model system' (see Figure 4.3). Such a definition in principle also holds for the first and second derivatives of the energy, and both geometrical optimizations and frequency computations can be performed. Equation (4.7) can also be comprehended as a system effect of (E_3-E_1) being added to a high level computation on the model system (E_2). Such a rationale of the equation recently lead Morokuma and coworkers[171] to define a test to gauge the applicability of the coupling scheme where the '*S* value test' was performed on E_3-E_1.

In the current work we deal with two-layer QM:MM combinations, for which the total energy of the system is obtained from three independent calculations:

$$E^{\mathrm{ONIOM}} = E^{\mathrm{QM}}_{model} + E^{\mathrm{MM}}_{real} - E^{\mathrm{MM}}_{model} \tag{4.8}$$

where *real* denotes the full system, which only needs to be calculated at the MM level, and *model* denotes the part of the system that needs to be calculated at both the QM and MM levels.

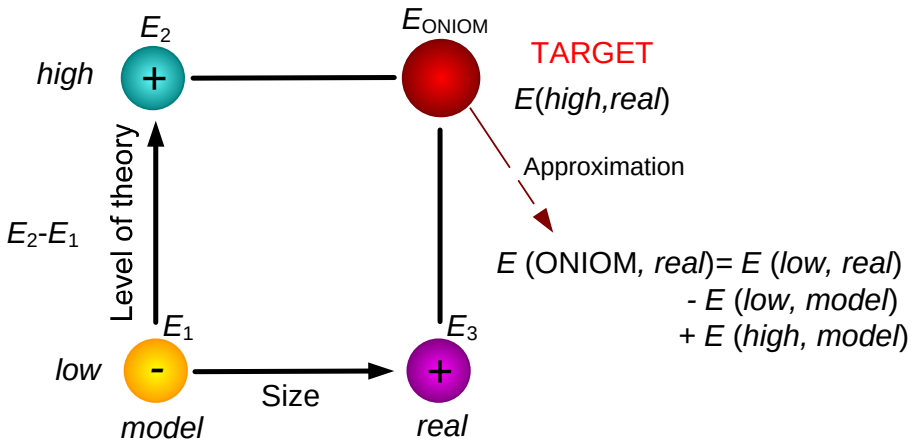

Figure 4.3 The two-layer ONIOM method[170].

4.2.2 Energy Calculation for ONIOM3

The schematic representation of a three-layer partitioning scheme is shown in Figure 4.1 and Figure 4.4. The high level method is used to probe the first and smallest layer. The intermediate technique in the ONIOM3 is applied to the union of the inner layer and the outer layer. The low level method is reserved for the real system (i.e. the union of the first, second, and third layers). The ONIOM approach provides an extrapolated energy for a system partitioned in this manner.

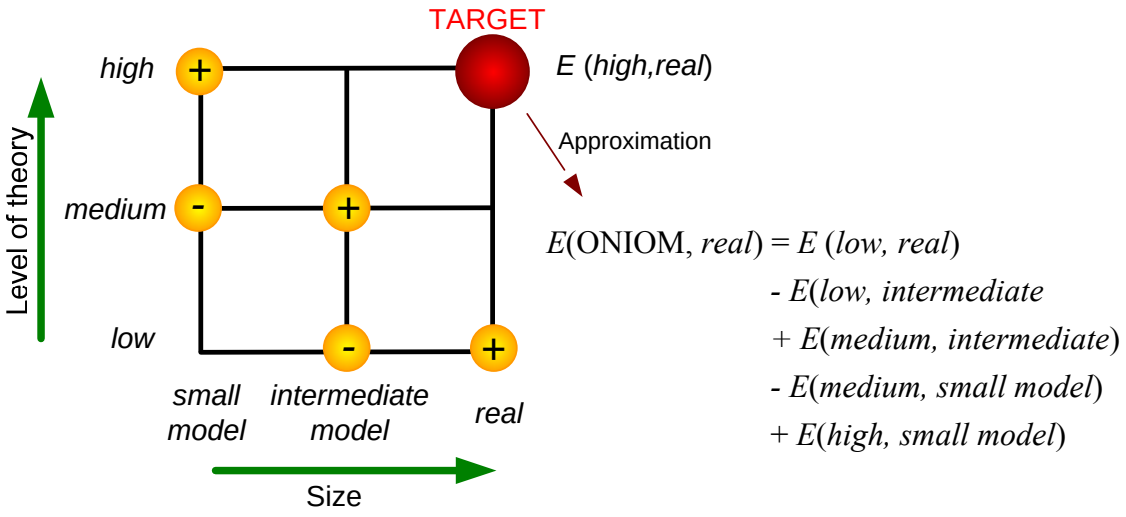

Figure 4.4 Schematic representation of a three-layer ONIOM method[170].

The energy expression for the three-layer ONIOM scheme can be written as

$$E_{\mathrm{ONIOM3}} = E^{high}_{small\ model} + E^{medium}_{intermediate\ model} - E^{medium}_{small\ model} + E^{low}_{real} - E^{low}_{intermediate\ model} \tag{4.9}$$

4.3 Geometry Optimization

In the construction of the ONIOM model system, atoms that belong to the high-level layer have the same coordinates as the corresponding atoms in the real system. Even during geometry optimizations, these coordinates remain identical to one another. When no bond exists between the two layers, the first derivative of the energy with respect to the geometry can easily be obtained according to

$$\frac{\partial E^{\mathrm{ONIOM}}}{\partial \mathbf{q}} = \frac{\partial E^{high}_{model}}{\partial \mathbf{q}} + \frac{\partial E^{low}_{real}}{\partial \mathbf{q}} - \frac{\partial E^{low}_{model}}{\partial \mathbf{q}} \tag{4.10}$$

where **q** stands for the coordinates. The assumption for the link atoms, that they are connected to the high-level layer with the same angular and dihedral values as the link atom hosts (the atoms replaced by the link atoms in the model system), is still used in the ge-

ometry optimization. However, in most cases, there exist bonds between the lower-level layer atoms and those of the high-level layer, and simply using Eq. (4.10) for geometry optimization in this case will lead the loss of one degree-of-freedom for each link between the high- and low-level layers. This causes problems with dynamic or frequency calculation etc. Thus, bond distances between the high-level layer and the link atoms have to be obtained by scaling the corresponding distances between the high-level layer and the LAH atoms using Eq. (4.4) or (4.5). The geometrical derivatives of the ONIOM energy now can be obtained in a similar fashion as the energy, where the correct number of degrees of freedom ensures that the potential energy surface is properly defined, and all gradients and higher derivatives are available[134]. In this case, the link atoms are present, thus the Jacobian **J** must be used to convert the coordinate system for the model system to that of the real system. The gradient can be written as

$$\frac{\partial E^{\mathrm{ONIOM2}}}{\partial \mathbf{q}} = \frac{\partial E^{high}_{model}}{\partial \mathbf{q}} \cdot \mathbf{J} + \frac{\partial E^{low}_{real}}{\partial \mathbf{q}} - \frac{\partial E^{low}_{model}}{\partial \mathbf{q}} \cdot \mathbf{J} \tag{4.11}$$

or

$$\nabla E^{\mathrm{ONIOM2}} = \nabla E^{high}_{model} \cdot \mathbf{J} + \nabla E^{low}_{real} - \nabla E^{low}_{model} \cdot \mathbf{J} \tag{4.12}$$

The Jacobian matrix **J**, projects the forces on all the set 2 link atoms $\mathbf{R}_{\mathrm{LAH}}$ onto the set 1 $\mathbf{R}_{model}$ and set 3 atoms $\mathbf{R}_{link\text{-}real}$. Adopting the Eq. (4.4) or (4.5), the differentiation of the vector components of one set 2 atom $\mathbf{R}_{\mathrm{LAH}}$ with respect to the components of $\mathbf{R}_{model}$ and $\mathbf{R}_{link\text{-}real}$ yields a simple Jacobian:

$$\frac{\partial R_{\mathrm{LAH},a}}{\partial R_{link-real,b}} = g\delta_{a,b} \tag{4.13}$$

$$\frac{\partial R_{\mathrm{LAH},a}}{\partial R_{real,b}} = (1-g)\delta_{a,b} \tag{4.14}$$

where the indices a and b denote the Cartesian components x, y and z, and δ is the Kronecker.

Specifically, we apply Eq. (4.11) to the hydrogen storage problem in the latter part in this thesis, with QM density functional theory (DFT) for the model system and the Universal Force Field (UFF)[138], which is a MM method, for the real system. Thus the above equation can be written as

$$\frac{\partial E^{\mathrm{ONIOM2}}}{\partial \mathbf{q}} = \frac{\partial E^{\mathrm{QM}}_{model}}{\partial \mathbf{q}} \cdot \mathbf{J} + \frac{\partial E^{\mathrm{MM}}_{real}}{\partial \mathbf{q}} - \frac{\partial E^{\mathrm{MM}}_{model}}{\partial \mathbf{q}} \cdot \mathbf{J} \tag{4.15}$$

From Eq. (4.8) it follows that the interaction between the QM and the MM layer is included at the MM level, via the E^{MM}_{real} term. This type of embedding is referred to as mechanical embedding. In fact, in the ONIOM scheme, the interaction between any two layers is always included at the lower of the two associated levels.

The higher-order derivatives can be uniquely defined in a similar fashion and will be discussed in the next section. Any method for the investigation of potential energy surfaces based on conventional techniques can therefore be applied with the ONIOM method.

4.4 Second Derivatives of ONIOM

For the frequency problem calculation, the second derivatives of the ONIOM total energy E^{ONIOM} with respect to the nuclear coordinates, the Hessian matrix $\boldsymbol{H}^{\mathrm{ONIOM}} = \nabla^2 E^{\mathrm{ONIOM}}$ can be achieved according to

$$\boldsymbol{H}^{\mathrm{ONIOM2}} = \nabla^2 E^{\mathrm{ONIOM2}} = \mathbf{J}^T \cdot \nabla^2 E^{high}_{model} \cdot \mathbf{J} + \nabla^2 E^{low}_{real} - \mathbf{J}^T \cdot \nabla^2 E^{low}_{model} \cdot \mathbf{J} \tag{4.16}$$

The force constant matrix of the model system at low level $\boldsymbol{H}^{low}$ and at high level $\boldsymbol{H}^{high}$ have to be transformed by applying the Jacobian $\mathbf{J}$ and its transpose $\mathbf{J}^T$, see Eq. (4.16).

Using the same method, the gradient and second derivative expressions can be de-

rived for three- or any n-layer ONIOM partitioning.

In most computations, it is common practice to include an empirical scale factor of 0.89 to the frequencies, which leads to a good agreement with experimental data for a wide range of the systems[172]. The reason is that the normal vibrational frequencies computed with MO methods are well known to be overestimated due to the incomplete consideration of electron correlation and the harmonic approximation. In comparison with experimental fundamental frequencies, it would result in overestimation of about 10% compared to the experimental fundamental frequencies, thus the scale factor is introduced. In the ONIOM scheme, different methods are used for different parts of a molecule and therefore, different scale factors should be used for the Hessians at different levels. As ONIOM combines the Hessian matrices at different theoretical levels, the scaling process has to be performed for the Hessian matrix at each level:

$$\boldsymbol{H}^{\mathrm{ONIOM2}} = \nabla^2 E^{\mathrm{ONIOM2}} = c_2^2 \cdot \mathbf{J}^T \cdot \nabla^2 E_{modle}^{high} \cdot \mathbf{J} + c_3^2 \cdot \nabla^2 E_{real}^{low} - c_1^2 \cdot \mathbf{J}^T \cdot \nabla^2 E_{model}^{low} \cdot \mathbf{J} \tag{4.17}$$

where c_1, c_2 and c_3 represent the scale factors for different sets, see Figure 4.2. Since the frequency corresponds to the square-root of the Hessian, the square of the frequency scale factor has to be used for Hessian scaling.

Other derivatives like density, dipole moment and polarization tensor can be defined as follow.

For the two-layered ONIOM, the density can be obtained

$$\rho_{\mathrm{ONIOM2}} = \rho_{real}^{low} - \rho_{model}^{low} + \rho_{model}^{high} \tag{4.18}$$

When doing the calculation of the Nuclear Magnetic Resonance (NMR) chemical shifts, the elements of a 3×3 shielding tensor for a nucleus can be written as[173]

$$\sigma_{ab} = \frac{\partial^2 E}{\partial B_b \partial \mu_a} \tag{4.19}$$

where μ and B are respectively the nuclear magnetic moment and external magnetic field, and indices a, b denote the Cartesian components x, y and z. When the isotropic shielding is required, the integrated nuclear shielding constant can be calculated with an expression analogous to the ONIOM energy expression

$$\sigma_{\text{iso}}^{\text{ONIOM2}} = \sigma_{\text{iso}}^{low,real} - \sigma_{\text{iso}}^{low,model} + \sigma_{\text{iso}}^{high,model} \tag{4.20}$$

and the ONIOM2 dipole moment, which is related to the electronic field $\mathbf{F}$[174] is defined as

$$\mu = \frac{\partial E_{\text{ONIOM2}}}{\partial \mathbf{F}} = \frac{\partial E_{real}^{low}}{\partial \mathbf{F}} - \frac{\partial E_{model}^{low}}{\partial \mathbf{F}} + \frac{\partial E_{model}^{high}}{\partial \mathbf{F}} \tag{4.21}$$

The polarizability tensor for ONIOM2 is

$$\alpha = \frac{\partial^2 E_{\text{ONIOM2}}}{\partial \mathbf{F}_a \partial \mathbf{F}_b} = \frac{\partial^2 E_{real}^{low}}{\partial \mathbf{F}_a \partial \mathbf{F}_b} - \frac{\partial^2 E_{model}^{low}}{\partial \mathbf{F}_a \partial \mathbf{F}_b} + \frac{\partial^2 E_{model}^{high}}{\partial \mathbf{F}_a \partial \mathbf{F}_b} \tag{4.22}$$

The third order hyperpolarizability tensor for ONIOM2 is

$$\beta = \frac{\partial^3 E_{\text{ONIOM2}}}{\partial \mathbf{F}_a \partial \mathbf{F}_b \partial \mathbf{F}_c} = \frac{\partial^3 E_{real}^{low}}{\partial \mathbf{F}_a \partial \mathbf{F}_b \partial \mathbf{F}_c} - \frac{\partial^3 E_{model}^{low}}{\partial \mathbf{F}_a \partial \mathbf{F}_b \partial \mathbf{F}_c} + \frac{\partial^3 E_{model}^{high}}{\partial \mathbf{F}_a \partial \mathbf{F}_b \partial \mathbf{F}_c} \tag{4.23}$$

The infrared intensities for ONIOM2 is

$$I_{IR} = \frac{\partial^2 E_{real}^{low}}{\partial \mathbf{R} \partial \mathbf{F}} - \frac{\partial^2 E_{model}^{low}}{\partial \mathbf{R} \partial \mathbf{F}} \cdot \mathbf{J} + \frac{\partial^2 E_{model}^{high}}{\partial \mathbf{R} \partial \mathbf{F}} \cdot \mathbf{J} \tag{4.24}$$

The ONIOM Raman intensities for ONIOM2 can be written as

$$I_{\text{Raman}} = \frac{\partial^3 E_{real}^{low}}{\partial \mathbf{R} \partial \mathbf{F}_a \partial \mathbf{F}_b} - \frac{\partial^3 E_{model}^{low}}{\partial \mathbf{R} \partial \mathbf{F}_a \partial \mathbf{F}_b} \cdot \mathbf{J} + \frac{\partial^3 E_{model}^{high}}{\partial \mathbf{R} \partial \mathbf{F}_a \partial \mathbf{F}_b} \cdot \mathbf{J} \tag{4.25}$$

4.5 Conclusion

The advantages of the ONIOM scheme provide us with a tool for the study of larger molecular systems. In the following chapters 6, 7 and 8, we will use the ONIOM2 to

study the pore structure and adsorption processes in carbon nanotubes, which can be used to direct the development of carbon nanotube based hydrogen storage systems.

CHAPTER 5

STATE OF HYDROGEN MOLECULES CONFINED IN C_{60} FULLERENE AND CARBON NANOCAPSULES

The combination of PM3 semi-empirical method for geometry optimization, and *ab initio* DFT (density functional theory) for energy calculation, is used to study the configurations of hydrogen molecules at zero-temperature within the vacuum of C_{60} fullerene and carbon nanocapsules. The present calculations show that the storage capacity and the configuration of the hydrogen are mainly determined by two kinds of repulsive energies, namely that between the H_2 molecules and the wall of the spheroidal or capsule like carbon structure, and that between interacting H_2 molecules. It is further established that the repulsive energy among the H_2 molecules is not purely a function of the number of encapsulated H_2, and there is a tradeoff between the two kinds of repulsive energies.

5.1 Introduction

After the first discovery of C_{60} fullerene by Kroto *et al.*[175] in 1985, and the carbon nanotube by Iijima[46] in 1991, various carbon-based nanocage structures, such as fullerene clusters[176-181], single-walled nanotubes[182,183], multi-walled nanotubes[46], nanocapsules[184,185], nanopolyhedra[186], cones[42,187], cubes[188], polyhedra[184], spheres[189], and carbon onions[190], have

been studied due to their the promising potential for applications in various fields. The characteristic features of their structural formation, and physical and chemical properties are of immense interest to the scientific community. The envisioned high hydrogen uptake capacity for these closed cage carbon nanostructures have stimulated investigators to dedicate much attention to their unusual hydrogen-absorbing properties, since hydrogen as a fuel is emerging as the ideal candidate for the next generation of energy resource due to its high energy value and pollution-free combustion. Scientists expect to find safe and highly efficient techniques for handling hydrogen in the near future, and in the process open new challenging opportunities for overcoming the main difficulties associated with hydrogen storage and its safe delivery. Of all these carbon-based nanocage structures, C_{60} fullerene is most amenable to large-scale synthesis[180]. It is often chosen by scientists as a model variant to conduct studies of its physical and chemical properties for better understanding the compounds from this class of carbon-based nanocage structures. The interaction of C_{60} with hydrogen has been intensively studied both experimentally[191,192] and theoretically[193-196]. The possibility of the existence of hydrofullerenes associated with C_n cage structures has been discussed[194,197], and investigators have reported that the C_{60} nanocage may accommodate a significant number of hydrogen molecules[194]. These endohedrally hydrogen doped structures are stable but highly endothermic. For endohedral nanocapsules, the closed-cage carbon nanostructure which incorporate hydrogen molecules within the nanocapsule has only been discussed in recent years[127,198-200].

In this chapter, *ab initio* calculations are used to explain the various ordered configurations according to the increasing number of H_2 molecules, which are confined inside the small vacuum of C_{60} fullerene and nanocapsule structures. Present calculations show that the storage capacity and the configuration of the hydrogen have close relation with the two kinds of repulsive energies, namely that between the H_2 molecules and the wall of

nanocapsule, and that between interacting H_2 molecules. Generally, the relative distances among the adsorbed hydrogen molecules in a denser case are shorter, resulting in stronger repulsive energies. The various states of the adsorbed hydrogen molecules within the vacuum of the capsules, namely the axis phase, shell phase, axis-shell phase and multi-shell phase, with respect to the repulsive energies are examined in detail in this chapter.

5.2 Computational Methods

For the present calculations, the model developed and methods used are outlined as follow. The (5,5) capped nanocapsule of length 12.8Å is chosen, and optimized using the PM3[201,202] semi-empirical method, with both ends capped with C_{60} hemispheres.

Usually the endohedral nanocage structures are formed during the synthesis of the fullerenes. Alternative possibilities include the application of high temperatures and high pressures for the encapsulation of gas atoms into the fullerene structure[203], atomic collision scheme[204], ion implantation[205], organic synthesis method[52], or electrochemical hydrogen storage[206,207]. The number of atoms involved in the present problem adds up to about 200, thus limiting the application of density-functional optimization-based method. We therefore combine two different theoretical approaches, namely the PM3 for geometry optimization and the DFT method for the energy computation. Barajas-Barraza and Guirado-López[127] simulated the state of hydrogen atoms and molecules in fullerenes and (5,5) tube-like arrangements using the MNDO (Modified Neglect of Diatomic Overlap)[208,209] method. However, MNDO has a tendency to overestimate the repulsion between atoms when they are separated by a distance approximately equal to the sum of their van der Waals radii, resulting in difficulties in accurately modeling the intermolecular system involving hydrogen bonds. In the present calculations, apart from PM3 for the geometry optimization, the B3LYP (Becke's three-parameter hybrid method[153-158] with the exchange functional of Lee,

Yang, and Parr[151]) was chosen for single point energy calculation, which was performed based on the 6-31G(d) basis set, where the polarization functions are included to allow for non-uniform displacement of charges away from the atomic nuclei, thereby improving the bonding description.

To ensure the accuracy of the PM3 method, the present results of the important geometrical features such as the equilibrium bond distances of C_{60} are compared with those of higher level methods as well as published experimental data. Table 5.1 summarizes the comparison of single- and double- bond lengths of carbon atoms in C_{60}. It can be seen that, for the ground state, the two unique bond lengths obtained using PM3 results differs on average by 0.64% with the experimental data, where the double bond length is about 1.21% lower, and the corresponding difference for the single bond is only 0.07%. The use the higher level method MP2[210-213] with a triple zeta basis set and polarization functions leads to an average corresponding difference of 0.59%, while for the AM1[214-216], the corresponding difference is 1.7%. From the consistency of these results, we conclude that the PM3 is suitable and effective for geometry optimization of fullerene.

Table 5.1 Equilibrium bond distances of fullerene C_{60}.

Methodology	AM1	PM3	TZP/MP2	Expt.
C-C single bond length (Å)	1.464[a]	1.457[c]	1.446[a]	1.458[b]
C=C double bond length (Å)	1.358[a]	1.384[c]	1.406[a]	1.401[b]

[a] Reference [217]
[b] References [218,219]
[c] Present

Table 5.2 Total energy of optimized fullerene C_{60} by different methodologies.

Method	PM3/B3LYP	STO-3G/SCF	DZP/MP2	TZP/MP2
Single point energy (Hartree)	-2286.17130[c]	-2244.22125[a]	-2279.73496[b]	-2280.41073[b]

[a] Reference [220]
[b] Reference [217]
[c] Present

Similarly, to justify the feasibility of the *ab initio* B3LYP method for computing

the single point energies of C_{60} and nanocapsule, we compare presently obtained results with other higher level methods. Again, taking the well-known C_{60} fullerene for comparison, the single point energy is -2279.73496 Hartree (see Table 5.2) when using the MP2 method with DZP (Double Zeta plus Polarization) basis and -2280.41073 Hartree when using TZP (Triple Zeta plus Polarization) basis. Using the present PM3/B3LYP method, we observe only 0.28% discrepancies. Present results are also significantly better than results obtained via the STO-3G/SCF method, which show up to 1.5% discrepancy from the TZP/MP2 results.

5.3 Results and Discussion

5.3.1 Repulsive Energy in H_2-C_{60} System

Before examining hydrogen in carbon nanocapsules, we first consider hydrogen encapsulated in C_{60} fullerene, so as to obtain an initial physical insight into the structural properties of hydrogen molecules confined within small carbon nanostructures. The interest of this chapter is to investigate the relationship between the encapsulated H_2 molecular distributions and the associated repulsive energies in the confined system. In Figure 5.1, the variation of the energy per H_2 molecule with the density of the confined H_2 molecules, is carefully examined. The corresponding average H_2-H_2 repulsive energies are calculated by[127,129]

$$E_{rep}\left(H_2 - H_2\right) = \left(E_{total}\left(H_n\right) - N_{H_2}E_{H_2}\right)\Big/N_{H_2} \tag{5.1}$$

where $E_{total}\left(H_n\right)$ is the total energy of the H_2 molecules in the C_{60}, E_{H_2} the average energy of a single H_2 molecule confined in the fullerene, and N_{H_2} the total number of hydrogen molecules in the system. The average H_2-C_{60} repulsive energies are calculated by[129]

$$E_{rep}\left(H_2 - C_{60}\right) = \left(E_{total}\left(H_2 + C_{60}\right) - E_{total}\left(H_n\right) - E_{C_{60}}\right) \Big/ N_{H_2} \tag{5.2}$$

where $E_{total}\left(H_2 + C_{60}\right)$ and $E_{C_{60}}$ are the total energy of the system with and without encapsulated hydrogen molecules, respectively.

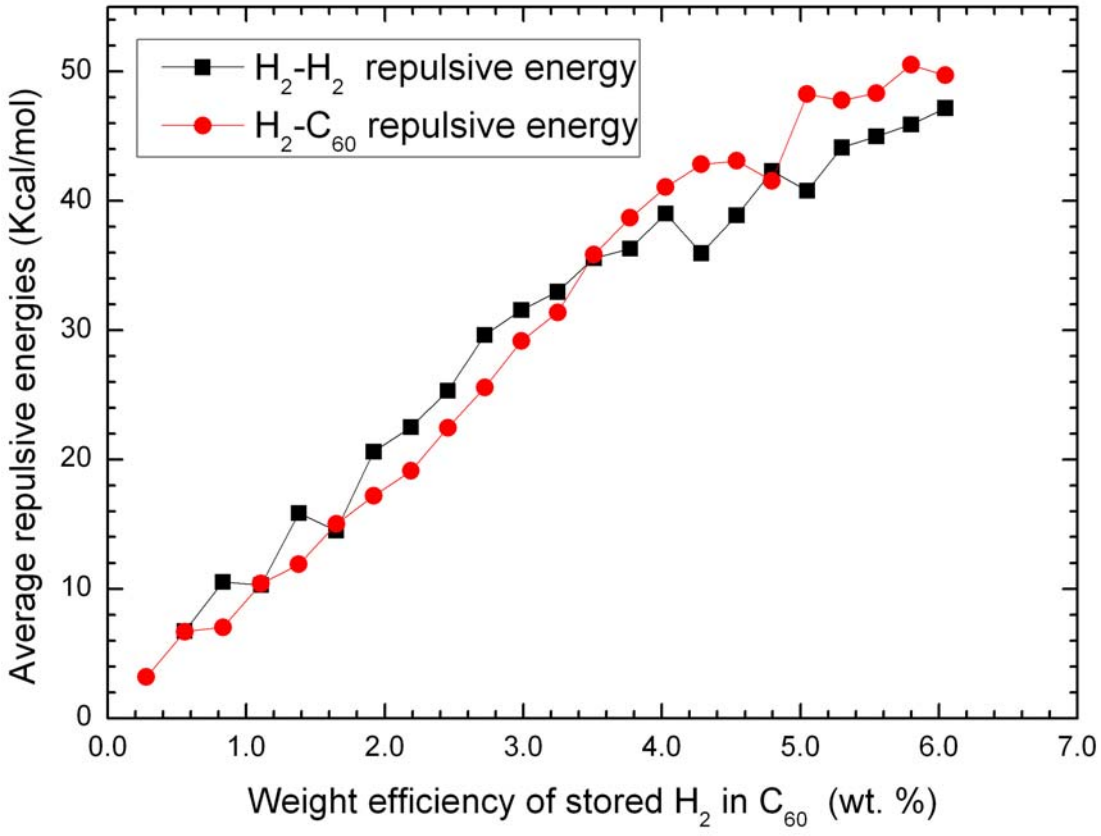

Figure 5.1 Variation of average H_2-H_2 and H_2-C_{60} repulsive energies with the uptake weight percentage of H_2 molecules confined in C_{60} fullerene.

It is noted from Figure 5.1 that both repulsive energies are positive, and that between the hydrogen molecules and the fullerene wall is generally lower that that between the hydrogen molecules when the adsorption weight efficiency is below 3.51%, where the corresponding hydrogen molecules is less than 13. As more hydrogen molecules are stored, the repulsive energy between the H_2-C_{60} overtakes the H_2-H_2 repulsive energy. Both the repulsive energies are also observed to increase with the number of stored H_2 molecules. Here, the density of the absorbed hydrogen molecules can be calculated by

$$\rho_w = \frac{N_{H_2} m_{H_2}}{N_{H_2} m_{H_2} + N_C m_C} \times 100 \ wt.\% \tag{5.3}$$

where N_{H_2} and N_C are respectively the number of stored hydrogen molecules and carbon atoms, while m_{H_2} and m_C are the corresponding molecular and atomic masses.

When only one H_2 molecule is confined within the C_{60}, present results show that it behaves as a free molecule residing at the centre. This phenomenon has also been experimentally observed[221]. The reason is that the distance between the centre of the cage and the carbon cage shell is about 3.7Å, which is too large for any bonding interaction between hydrogen and carbon. However, with more hydrogen molecules being encapsulated, the formation of the various hydrogen molecular clusters within the C_{60} display a variety of well-defined shapes, and the H_2-H_2 repulsive energy begins to increase. However, it is noticed that the energy between H_2-H_2 is not purely dependent on the number of stored hydrogen molecules, but also influenced by the geometrical distribution of the molecules as well.

Present results for the variation of the average H_2-H_2 distance with the number of encapsulated H_2 molecules are shown in Figure 5.3 It is observed that with the initial increase in the number of encapsulated H_2 molecules, the average H_2-H_2 distance first rises until N_{H_2}=5, at which the H_2-H_2 distance reached is 1.90Å. Following this, the average distance drops to the minimum of 1.69Å, where N_{H_2}=15. When N_{H_2}=16, a special configuration is observed, whereby a H_2 molecule resides at the centre of the configuration. Even though the average repulsive energy of the case of N_{H_2}=16 is smaller than that of N_{H_2}=15, the average space is larger. The existence of a central H_2 molecule occurs for the cases where N_{H_2}=16, 17 and 18. For the cases of N_{H_2}=19 to 23, two H_2 molecules reside near the centre, which result in the average H_2-H_2 distance of the N_{H_2}=19 case being larger

than that of the N_{H_2}=18 case. In addition, as one would expect, the increase of N_{H_2}=19 to N_{H_2}=23 results in a general drop of the average H_2-H_2 distance.

Referring back to Figure 5.1, there is an unexpected drop in the H_2-H_2 repulsive energy at density of 4.28*wt.%* (N_{H_2}=16), where the repulsive energy is lower than that of 4.03*wt.%* (N_{H_2}=15). Comparing the configuration of the stored hydrogen molecules for N_{H_2}=15 and N_{H_2}=16, see Figure 5.2, the main difference is that the N_{H_2}=16 configuration possesses highly symmetric structures than that of the N_{H_2}=15 configuration. Looking closely at Figure 5.2 for the case of N_{H_2}=16, one hydrogen molecule resides at the centre of the configuration, resulting in the repulsive energy of this hydrogen cluster being significantly decreased. This result is very consistent with observations from geometry optimization analyses. It is generally found that for molecular systems possessing very high symmetries, the energy of the system will converge to a much lower energy state than those with highly disordered arrangements.

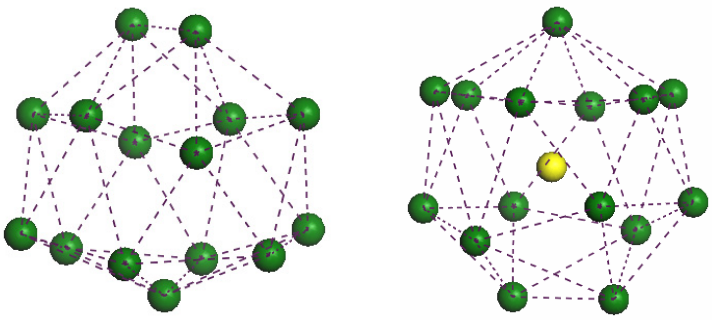

Figure 5.2 Stable configurations for N_{H_2} =15 (left) and N_{H_2} =16 (right). The dots represent the mid-point of the hydrogen molecules.

To explain the initial increase in average H_2-H_2 distance, we note that it is well established that the hydrogen molecules have a tendency to condense at the centre of the fullerene, where the energy of the whole system reaches the minimum, see Figure 5.3. However, the distance between two neighboring H_2 molecules cannot be very close as the

repulsive energies among the hydrogen molecules become so strong that it compels the molecules to diffuse from the centre. As this is a confined system, the repulsive energy between the wall and the H_2 molecules cause the cluster to organize into distributed formations inside the C_{60} structure. Thus, when the H_2 density is low, the available space vacuum inside the fullerene, and the interacting repulsive energies, allow the hydrogen molecules to display an initial upward trend in their average relative distances.

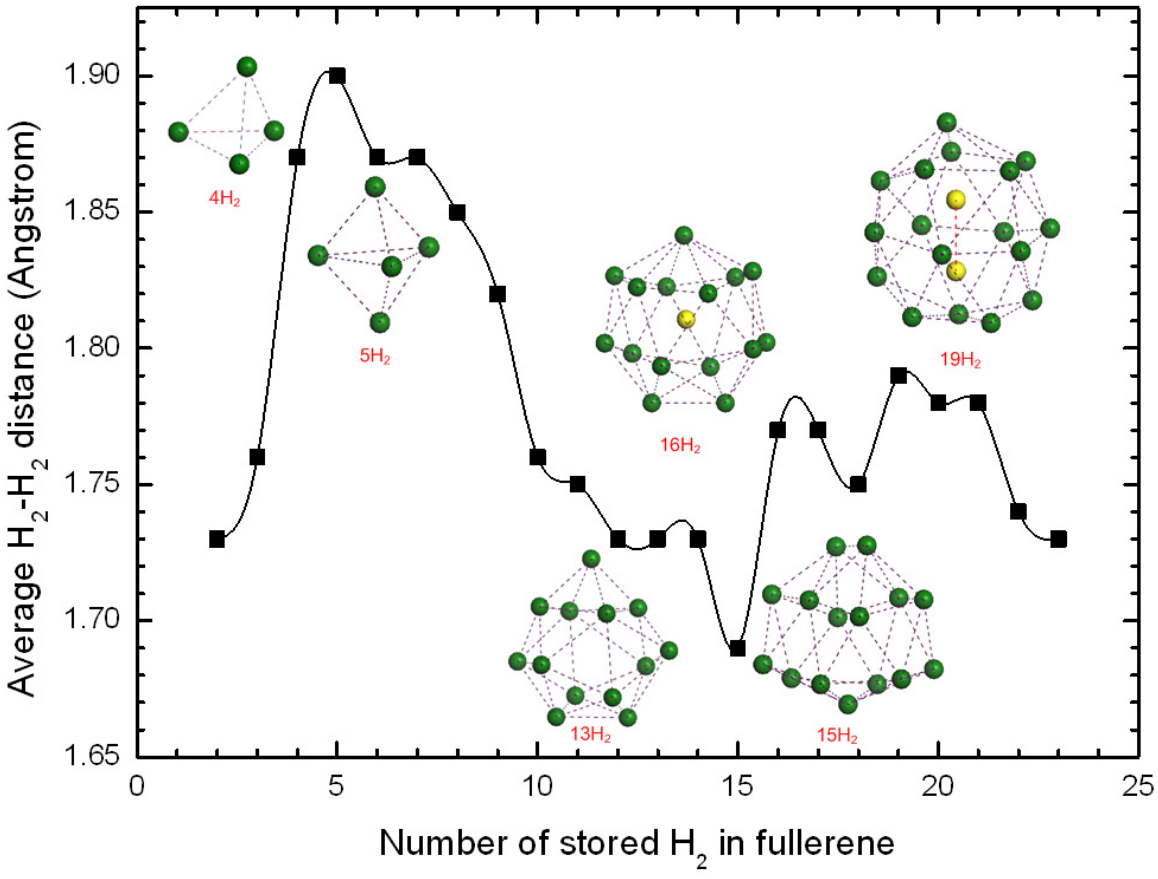

Figure 5.3 Relationship between the average distance between the H_2 molecules and the H_2 uptake in C_{60}.

From the discussions of these present results, it is evident that the repulsive interactions among the encapsulated H_2 molecules and the fullerene wall, as well as that the between the hydrogen molecules themselves, play an important role in determining the storage capacity in the hollow carbon structure. Since the repulsive energy is a function of the ground state energy, it is thus also of critical importance to the ground-state structure and

stability.

5.3.2 Repulsive Energy in H_2-Nanocapsule System

Here we perform calculations for H_2 molecules confined within carbon nanocapsules, which is a short 12.8Å segment of a (5,5) carbon nanotube, with both ends terminated by perfect fullerene caps.

The repulsive energies between the capsule wall and H_2 molecules and that between interacting H_2 molecules, are analyzed as before. Figure 5.4 shows the respective calculated repulsive energies in relation to the H_2 molecular storage weight efficiency. For the interacting hydrogen molecules, the repulsive energy can be calculated by[16]

$$E_{rep}\left(H_2 - H_2\right) = \left[E_{total}\left(H_n\right) - N_{H_2}E_{H_2}\right] / N_{H_2} \tag{5.4}$$

where $E_{total}\left(H_n\right)$ is the total energy of all H_2 molecules within the capsule, E_{H_2} the average energy of a single confined H_2 molecule, and N_{H_2} the total number of H_2 molecules. Similarly, for the repulsive energies between the tube wall and H_2 molecules is calculated by

$$E_{rep}\left(H_2 - Nanocapsule\right) = \left[E_{total}\left(H_2 + Nanocapsule\right) - E_{total}\left(H_n\right) - E_{nanocapsule}\right] \Big/ N_{H_2} \tag{5.5}$$

where $E_{total}\left(H_2 + nanocapsule\right)$ is the total energy of the tube with the encapsulated H_2 molecules, and $E_{nanocapsule}$ is solely the energy of the carbon nanocapsule.

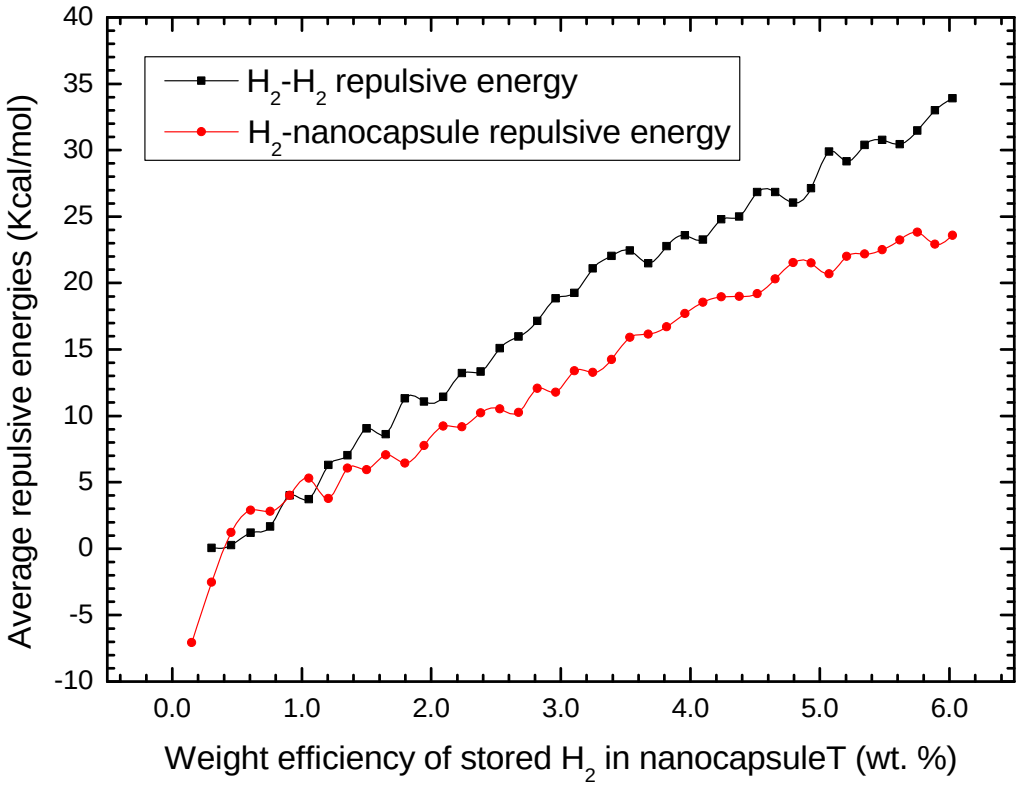

Figure 5.4 Variation of H_2-H_2 and H_2-nanocapsule repulsive energies.

Quite unlike the repulsive energies for the H_2-C_{60} system where both are generally positive, Figure 5.4 shows that when few H_2 molecules are enclosed, such as when $N_{H_2} \leq 2$ (see Figure 5.5), negative H_2-nanocapsule repulsive energies result, implying attraction between the H_2 molecules and the capsule wall. From Figure 5.5, we observe that when only one H_2 is enclosed, it resides close to the cap end instead of the center of the capsule. This is due to the greater attraction forces of the cap ends, since in microporous solids, the potential fields from the adjacent carbon atoms at the caps will overlap significantly, such that the attractive forces from the caps will be higher compared with that from the inner surface of the capsules. For this configuration, the corresponding repulsive energy is -7.07*kcal/mol*. For the case of N_{H_2}=2, the energy increases to -2.54*kcal/mol*, indicating the attraction between the H_2 molecules and the caps decreases when there is a second H_2. Even though the two H_2 molecules still reside near to the ends, the distance between the H_2

molecules and the caps increases 0.17Å caused by the weak attractive van der Waals forces between the two hydrogen molecules. These results are similar to Xia *et al.*'s[222] who used MD simulation, as well as Gordillo *et al.*'s[223] who employed the DMC method. Both reported negative interaction between the H_2 and capsule at low uptake. The present results in Figure 5.4 differ however from those of Barajas-Barraza and Guirado-López's[127], who showed that for higher H_2 uptakes, H_2-H_2 repulsive energies increase almost linearly with N_{H_2}, and no negative repulsive energy was observed.

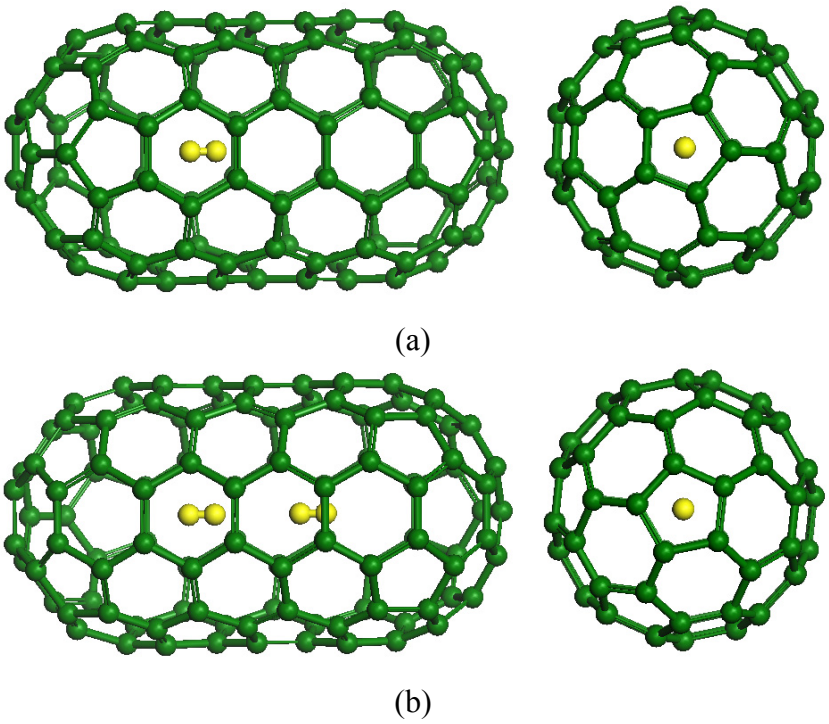

(a)

(b)

Figure 5.5 Stable structures for (a) N_{H_2}=1, and (b) N_{H_2}=2, where the H_2-nanocapsule repulsive energies are negative. The left are the side views, while the right show the views from the end.

The interactions rapidly become highly repulsive as more H_2 molecules are stored. The H_2-H_2 repulsive energy enforces distance between two adjacent molecules and causes them to distribute within the tube, while the H_2-nanocapsule repulsive energy compels the H_2 molecules stay away from the inside wall. The coupling of these two effects increases the dimensions of the carbon structure accordingly, until the capsule side wall eventually breaks. It can be clearly seen that the H_2-H_2 and H_2-wall interactions ultimately determine

the maximum storage capacity and the stability of the nanocapsule.

In Figure 5.4, we also notice that the H_2-nanocapsule repulsive energy is generally higher than the H_2-H_2 repulsive energy when the H_2 uptake is low, N_{H_2}=3 to 7, see also corresponding Figure 5.6 and Figure 5.7. However, with the rise of H_2 uptake, the H_2-H_2 repulsive energy generally exceeds that between H_2-nanocapsule. Relating these energy differences with the H_2 configurations, it is noticed that the H_2-H_2 and H_2-nanocapsule repulsive energies play an important role in determining the H_2 molecules' phase transition between the various axis and shell states.

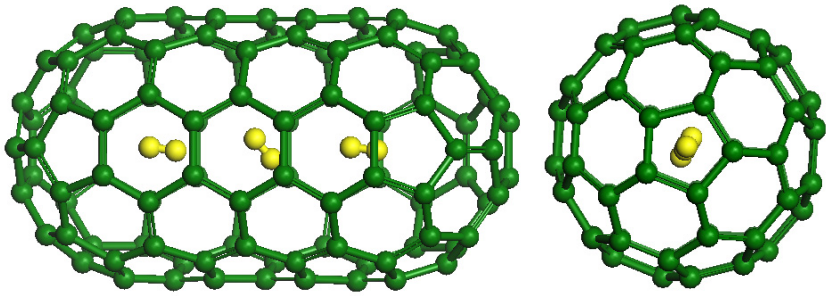

(a)

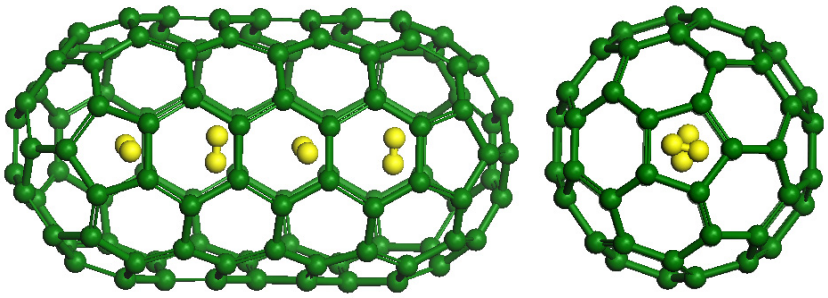

(b)

Figure 5.6 Stable structures for (a) N_{H_2}=3, and (b) N_{H_2}=4, where the H_2 molecules express a 1D axis phase. The left are the side views, while the right show the views from the end.

From Figure 5.5 to Figure 5.9, we observe the seven phases, progressively representing the 1D, 2D and 3D configurations of the enclosed H_2 cluster of molecules, namely the axis phase (1D), zigzag phase (2D), disordered phase (3D), shell phase (3D), shell-axis coexist phase (3D), shell-zigzag coexist phase (3D), and shell-disordered coexist phase (3D). Close observation of Figure 5.4 reveals that when H_2 uptake densities are low,

$N_{H_2} \leq 4$ (see Figure 5.6), the H_2-H_2 repulsive energy is initially almost zero, and reaches only 1.29*kcal/mol* when N_{H_2} =4. For the H_2-nanocapsule repulsive energy, it is initially negative but quickly increases to 2.30*kcal/mol* when N_{H_2} =4, which is higher than that between H_2-H_2. The negative repulsive energy indicates attraction between the carbon nanocapsule and H_2 molecules as discussed earlier. With the positive, though small H_2-capsule repulsive energy, the H_2 molecules are forced to align along the central axis of the tube so as to reduce the energy of the system. This distinctive 1D formation is shown in Fig 6. When progressively more H_2 molecules are enclosed, the axis phase is unable to accommodate all the H_2 molecules as the H_2-H_2 repulsive energy increases with the decrease of the H_2-H_2 distances, thus compelling the H_2 molecules to change from a 1D to a 2D configuration to allow more H_2 molecules to be encapsulated. In this new 2D phase, the H_2-H_2 repulsive energy is still generally lower than that of the H_2-capsule, and the cluster of H_2 molecules form a kind of zigzag configuration. The differences between the two repulsive energies are 1.16*kcal/mol*, 0.017*kcal/mol* and 1.58*kcal/mol*, corresponding to N_{H_2} =5, 6 and 7 respectively, and the configurations are shown in Figure 5.7.

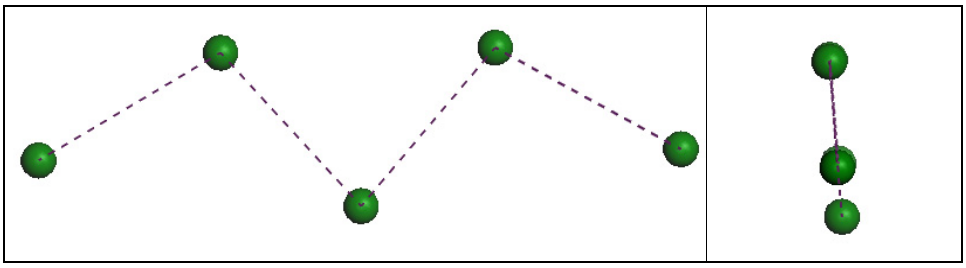

(a)

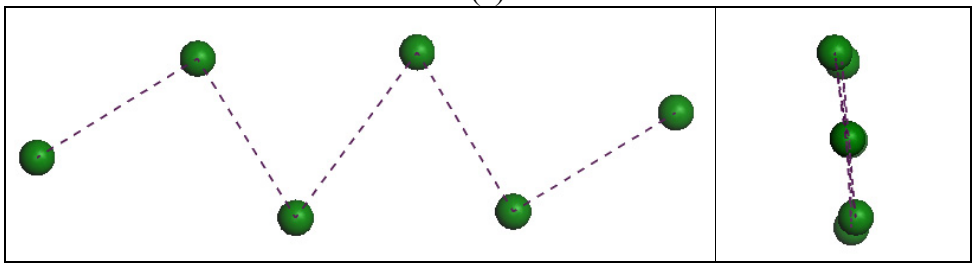

(b)

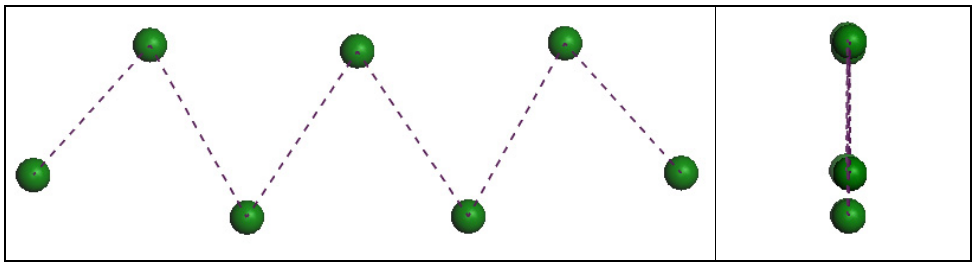

(c)

Figure 5.7 Stable structures for (a) N_{H_2}=5, (b) N_{H_2}=6, and (c) N_{H_2}=7 where the H_2 molecules express a 2D zigzag phase. The left are the side views, while the right show the views from the end.

With the subsequent further increase in N_{H_2}, the H_2-H_2 repulsive energy overtakes and increases at a faster rate than that of the H_2-nanocapsule. Also, the energy difference increases from 2.51*kcal/mol* (N_{H_2}=8) to 5.87*kcal/mol* (N_{H_2}=21). The configuration of the H_2 cluster becomes 3D, and gradually transforms from a disordered phase (see Figure 5.8) to a shell phase (see Figure 5.9). However, with further increase in N_{H_2}, the shell phase becomes unstable, and a new shell-axis coexist phase emerges when N_{H_2}=22 (see Figure 5.9). The formation of the shell-axis coexist phase begins at N_{H_2}=22 and ends at N_{H_2}=35. The configuration of the H_2 cluster then transforms to a shell-zigzag coexist phase for N_{H_2}=36 to 38 (see Figure 5.9). Before the carbon nanocapsule eventually breaks at N_{H_2}=42, the H_2 cluster forms a shell phase addition with a disordered configuration for the H_2 molecules near to the axis, and this shell-disordered coexist phase occurs for N_{H_2}=39 to 41 (see Figure 5.9). It is also observed that during the various phase transitions from N_{H_2}=8 to N_{H_2}=41, the difference between the two repulsive energies continues to increase.

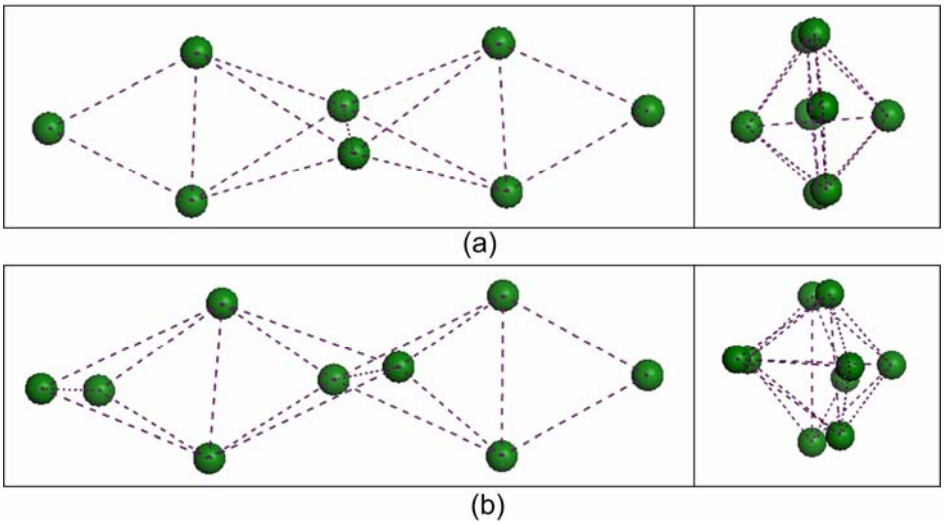

Figure 5.8 Stable structure for (a) N_{H_2} =8 and (b) N_{H_2} =9, where the H_2 molecules express a 3D disordered phase. The left are the side views, while the right show the views from the end.

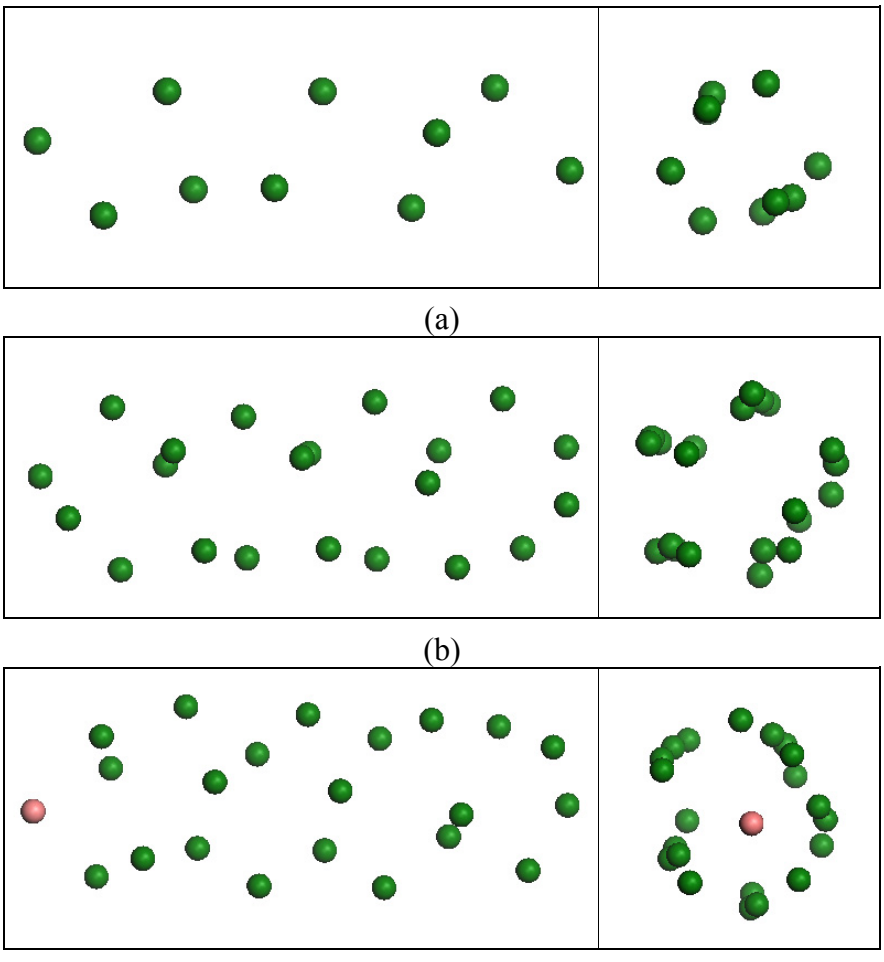

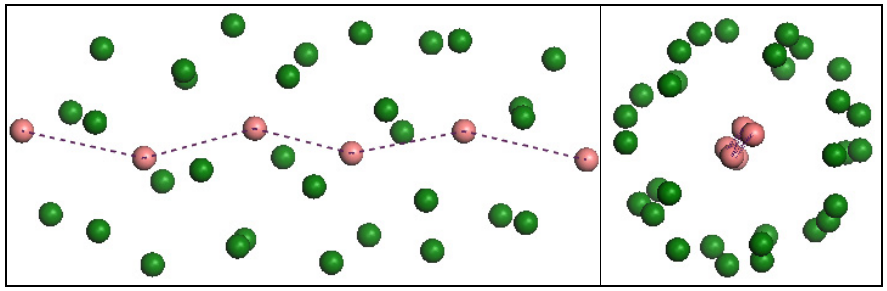

(d)

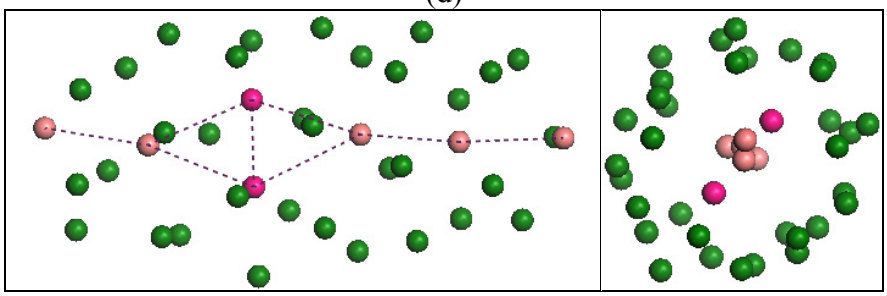

(e)

Figure 5.9 Stable structures for (a) N_{H_2}=10 (b) N_{H_2}=21, (c) N_{H_2}=22, (d) N_{H_2}=37, and (e) N_{H_2}=40. The encapsulated hydrogen molecules arrange themselves into a cylindrical shell phase for N_{H_2}=10 to 21. For N_{H_2}=22 to 35, we observe the shell-axis coexist phase. For N_{H_2}=36 to 38, the shell-zigzag coexist phase occurs. For N_{H_2}=39 to 41, we see the shell-disordered coexist phase.

Before ending this discussion, we will look at another important parameter, namely, the minimum H_2-H_2 distance. Figure 5.10 shows the minimum distance between the H_2-H_2 molecules as a function the uptake density. It can be observed that the in the small confined vacuum of the nanocapsule, the minimum distance between H_2 molecules is as high as 3.03Å when there are only two H_2 molecules, and this drops to 2.71Å for three hydrogen molecules, owing to the interaction between H_2-capsule. The corresponding uptake densities are 0.3*wt.%* and 0.5*wt.%* respectively. This is because at these low densities, there is sufficient space in the nanocapsule, and according to Diep and Johnson[224,225], two H_2 molecules cannot stay close together as the mutual repulsive energy increases very quickly if the distance goes below 2.0Å. However, with more H_2 molecules enclosed, the H_2-nanocapsule repulsive energy changes from negative to positive, implying that the interaction between the H_2 and nanocapsule changes from attractive to repulsive, and it

gradually increases to values which cannot be neglected. This energy confines the H_2 molecules within the nanocapsule and thus reduces the distance between H_2 molecules. However, the distance cannot be too small since the repulsive energy between the H_2-H_2 will increase sharply. In this case, as the smallest distance based on present calculations reaches 1.50Å, upon which the nanocapsule side wall rupture.

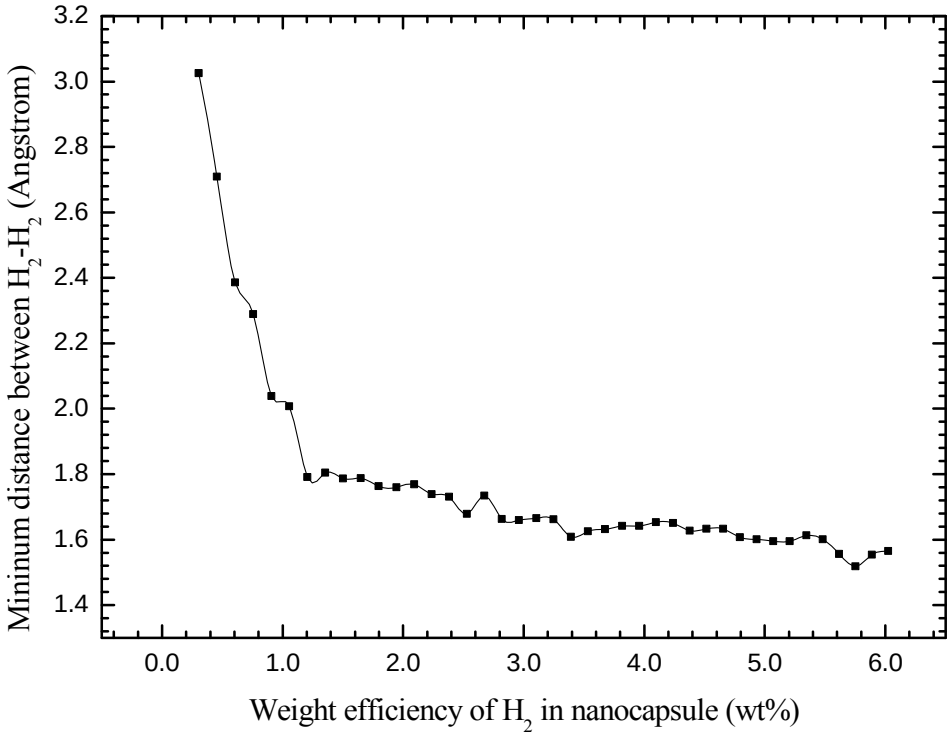

Figure 5.10 Minimum mutual distance between H_2 molecules versus weight efficiency in H_2-nanocapsule system.

5.3.3 Conclusion

In this chapter, we have investigated the relationship between the configurations of H_2 molecules in C_{60} fullerene and (5,5) nanocapsule, with the H_2-H_2 and H_2-wall repulsive energies. This was carried out using semi-empirical PM3 method for geometry optimization, and *ab initio* DFT for energy calculation. In addition, polarization functions were included in the analysis to allow for non-uniform displacement of charges away from atomic nuclei. It was found that the storage capacity and the configuration of the enclosed H_2

molecules have close relation with the two kinds of repulsive energies. Due to the coupled effects of these two repulsive energies, the H_2 molecules transition from 1D to 2D, and then to different 3D phases. Seven different phases are observed, namely the axis phase (1D), zigzag phase (2D), disordered phase (3D), shell phase (3D), shell-axis coexist phase (3D), shell-zigzag coexist phase (3D), and shell-disordered coexist phase (3D). From the present results, we realize that high-capacity hydrogen storage (>6.5*wt.%*) cannot be simply explained through physisorption, and appropriate and viable chemisorption processes are required. The present physisorption results show maximum 6.05*wt.%* uptake for the H_2-C_{60} system and maximum 6.02*wt.%* uptake for the H_2-nanocapsule system.

CHAPTER 6

CHEMISORPTION OF ATOMIC HYDROGEN WITH (5,5) ARMCHAIR SWNT

The interaction of hydrogen atoms with the sidewall of carbon nanotubes is studied in this chapter using the two-level ONIOM (our own n-layered integrated molecular orbital and molecular mechanics) method describe in chapter 4. In this technique, the higher *ab initio* level is treated with B3LYP/6-31G, while the lower level is described using Universal Force Field (UFF)[138] molecular mechanics. We predict the transition states, stable intermediates and the reaction pathway for the process of H atoms chemisorbed onto the exterior of a narrow (5,5) armchair carbon nanotube. It is found that the chemical reaction of H atoms on the outside of the tube is exothermic and stable, and is hence entirely feasible. The reaction process follows three steps, and the chemical adsorption energies are -1.31eV, -2.56eV and -0.26eV for the three respective stages. The two H atoms prefer to be adsorbed on the carbon atoms of the same layer, which are perpendicular to the axis of the tube, and the bonds between these two carbon atoms are broken when both of the H atoms are chemisorbed.

6.1 Introduction

Presently, it is well accepted that physisorption and chemisorption are the two distinct types of possible interaction between hydrogen and carbon nanotubes (CNTs). Under

most conditions, molecular physisorption is preferred, where the hydrogen molecules do not dissociate, and the interactions between the CNT and the hydrogen molecules are usually described by weak van der Waals forces. This interaction is attributed to the exchange and correlation effects arising from the weak overlap between the electron densities of the nanotube and the closed-shell H_2 molecule[226].

Experiments have indicted that chemisorption will occur during the storage process. However, under normal conditions, chemisprtion is difficult due to the defect-free SWNT which is highly resistant to chemical attack by free hydrogen atoms or molecules. Not only is the kinetic barrier to hydrogen chemisorption generally large, but an isolated hydrogen atom being sp^3 bonded to the CNT is also energetically unfavorable. However, it has been proven that by impacting and/or under high pressure, H_2 molecules can approach sufficiently close to the nanotube wall for possible dissociation, and atomic chemisorption thus becomes possible[18,37]. This process also substantially weakens the C-C bonds[227]. Liu *et al*.[37] showed in their experiments that after treating CNTs with hydrogen gas under high pressure, there was residual H_2 during the desorption cycle that could be released only upon heating to temperatures above 400*K*. They therefore suspected that these residuals may be related to chemical adsorption. A more recent experimental process by Ye *et al*.[18] using SWNTs of high purity found a first order phase transition under high H_2 pressure, similar to the hydride phase observed in metal-hydrogen systems.

For chemisorption mechanisms, several interesting schemes have been proposed recently. Nikolaev *et al*.[228] put forth an H-activated coalescence mechanism, in which the gas phase H atoms attack the side of neighboring nanotubes breaking the C-C bonds and producing defective sites on adjacent nanotubes. This idea was generated based on the discovery that under atomic hydrogen atmosphere, single-walled armchair nanotubes annealed up to 1500^{o}C coalesce with neighboring tubes, resulting in larger nanotubes with twice and occasionally three times the diameter of the original ones. Terrones *et al*.[229] sug-

gested that once these adjacent defects are formed, the strong thermodynamic force, resulting from the released strain energy, drives the two neighboring smaller tubes to join together forming larger tubes[229]. Another interesting storage mechanism is that of a H atom flipping into the CNT and this was proposed by Lee *et al*.[136]. However they assumed that the chemisorption took place via a hypothetical electrochemical process in solutions, which are rather different from typical conditions reported for storage experiments.

A frequently used theoretical technique used by many researchers to investigate chemisorption parameters is to keep the single walled carbon nanotube (SWCNT) fixed while changing the distances and/or angles of the H atoms with reference to the SWCNT. For example, Arellano *et al*.[230] kept the SWCNT geometry fixed while employing a plan-wave basis set, obtaining binding energies of about -1eV. Verónica *et al*.[231] kept the SWCNT structure fixed as well, and allowed the H atom approach from the center of the nanotube (inner wall) to several exohedral positions in the radial direction (outer wall). However, this scheme is usually unable to provide very satisfactory results. This is because when reaction occurs, the nature of the two bonding atoms determines the chemical reaction but they will be modified by the effects of the rest of molecules as well. These effects cannot be reflected by these methods.

Another method in several reported theoretical works is the use of a finite cluster cut from the actual surface, with the distances between the atoms forming the cluster kept at their bulk values[128,232]. One fundamental problem for the cluster modeling of a surface is the convergence of the adsorption energy and other properties with respect to cluster size. Generally, a very large cluster is required. However, if more than a few molecules are explicitly described by quantum calculation, computational costs rapidly become prohibitive. The multiscale ONIOM method of Morokuma and co-workers[134,167-169,173,233,234] can improve this situation, allowing the division of a large molecular system into several layers and treating them using different theoretical methods. The advantage of using the ONIOM

method is that it imposes the geometrical constraints of the tube during the geometry optimization. To date, this multiscale framework has been mostly applied to large organic molecules and organometallic complexes.

In this chapter, we calculate the energies of fully optimized hydrogenated nanotubes using two-layer ONIOM2 integrated schemes, which divide the entire system into two levels. The small section, essential for studying the properties of the chemisorption, is treated using quantum mechanical density function theory (DFT). The remaining layer constrains the general geometry and is described by a molecular mechanics method, and the Universal Force Field (UFF)[138] molecular mechanics model is chosen here. Based on this methodology, a systematic and fully coupled study of the interaction of H atoms with the sidewall of CNTs is carried out where the basic and integral features of the interaction are outlined.

6.2 Computational Method - Two-Level ONIOM2 Scheme

In this study, the initial structure used is a relatively narrow armchair (5,5) CNT consisting of 180 carbon atoms with the tube length being 22.6Å, and the dangling bonds at both ends are tied off with hydrogen atoms. The reactions of H atoms with the CNT sidewall are described by a two-level ONIOM2 approach implemented in the Gaussian03 software, and GaussView03 is the graphical medium used for visualizing the optimized structures including the optimized transition states (TS). The atoms localized around the adsorption sites, including electron correlation effects, are defined by a small model system. The remaining system is treated as the "real" part, which is described by a lower level method. The small model system is treated by density functional theory (DFT) with the hybrid functional B3LYP (Becke's three-parameter hybrid method[153-158] with the exchange functional of Lee, Yang, and Parr[151]). The universal force field (UFF) molecular mechanics is used as the low-level treatment. This B3LYP:UFF combination has been suggested by

several researchers[108,131,132,137,235]. Basiuk *et al.*[236] also tested the semi-empirical AM1 method for the low-level treatment, but they reported that this was inaccurate when calculating for the force-constant and frequency, even though the estimation itself was completed smoothly. Hence we do not employ a semi-emperical method here for the lower-level calculation, as without the accurate force-constant for each step, we cannot obtain the optimization results for the TS.

First and foremost, a convergence test was carried out to determine the appropriate size of the small model to be employed. In this convergence test, we varied the size of the small model from 6 to 16, and then to 28 carbon atoms, see Figure 6.1. Comparison of the adsorption energy results obtained from the 6-carbon and 16-carbon small model systems showed significant discrepancies. The subsequent comparison of the 16-carbon and 28-carbon small model systems revealed very small discrepancy of less than 0.1%, and we can therefore confirm that the solutions have converged when using the 16-carbon small model. Thus all subsequent calculations were carried out using the 16-carbon small model.

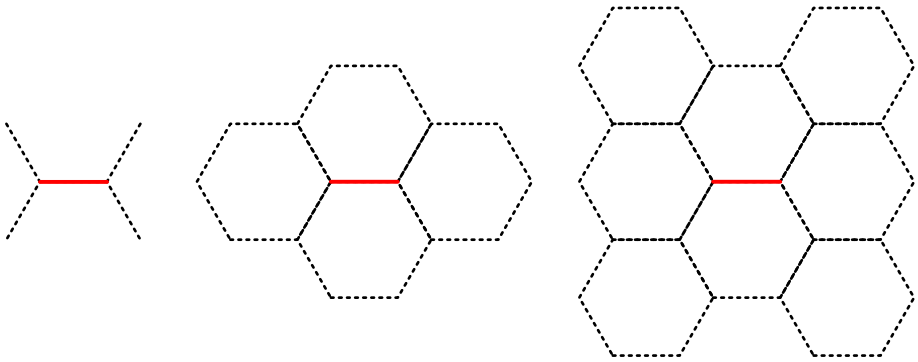

Figure 6.1 Configurations of the small model system of carbon atoms used in the convergence test. Left: 28 atoms; Middle: 16 atoms; Right: 6 atoms.

6.3 Results and Discussions

Even though CNTs are found to be stable, the literature has reported that hydrogen

as an atomic state may penetrate the CNT wall more easily than the hydrogen molecule[237]. Thus the present chapter will focus on H atoms adsorbed at the exterior of the CNT and it is interesting to note that there is no energy barrier for hydrogen atoms been chemisorbed at the outside the tube wall, regardless of initial placement. The optimized structure is calculated using the ONIOM2 scheme. To investigate the activation energy of the reaction, the transition states (TS) are calculated. Our simulation shows that three TS are required for the entire reaction. The TS search is carried out using the ONIOM2 method as well, and the transition state species is verified by frequency analysis through the Gaussview program. Initially, the bare CNT and the H atom are free of external stresses, and all the atomic coordinates are fully optimized.

6.3.1 Chemisorption of H Atom and Initial Weakening of C-C bond.

In the first part of this chapter, we will consider how the effects of hydrogen atoms on the geometry structures and the energy changes of the CNTs when the H atoms approach the sidewall of the CNT. We perform calculations of the adsorption of an H atom by a (5,5) SWNT, and the reaction path scheme of the H atom to the tube is studied in detail. Following optimization of a free (5,5) SWNT structure, giving an average C-C bond length of 1.42Å, a hydrogen atom is placed at different sites exterior to the nanotube, and the geometry optimization and energy calculation of the system was carried out using the ONIOM2 method. As shown in Figure 6.2(b), after geometry optimization, the H atom adsorbed at the outer surface of the tube, and the preferred site for the adsorption is above a carbon atom (perpendicular to the wall surface). This observation is in accordance with those reported by Arellano *et al*.[227,230], Bauschlicher *et al*. [131,133,137] and Lee *et al*.[129,238]. In the simulation, the atoms which are directly involved in bond breaking and formation are highlighted and labeled in the manner shown in Figure 6.2 (c). An inspection of the TS

structure of Figure 6.2 (a, d) reveals that the distance between the H atom and C_1 is 2.90Å, and the angle $\angle HC_1C_2$ is 108.49°. The distance between neighbouring atoms C_1 and C_2 increases from 1.42Å for the pure nanotube to 1.553Å. For the relaxed system shown in Figure 6.2 (b,e), the calculated H-C_1 bond length is 1.11Å, which is close to the value of 1.10Å for CH_4 molecules. The chemisorbed H atom results in an increase of the bond length of its neighbour atoms, where the C_1-C_2 carbon bond is further elongated to 1.555Å which is close to the typical sp^3 C-C bond length of 1.545Å, while that of the C_1-C_3 and C_1-C_{13} bonds increase to 1.52Å. The related Mulliken population changes as well. From the small model of the system, we note that the population between C_1-C_2 decreases from 0.40 to 0.24, and for the other two neighboring sets of carbon atoms C_1-C_3 and C_1-C_{13}, it has dropped from 0.41 to 0.30, indicating that the chemisorbed H atom weakens the carbon bonds in the vicinity of the chemisorbed site.

The H-C_1 Mulliken population analysis shows 0.35, which is higher than those of nearest carbon neighbors C_1-C_2 which is around 0.3. Nevertheless the mutual distances for C_2-C_6 and C_2-C_{10} remain almost the same as the pure nanotube at about 1.41Å. The corresponding distances for C_4-C_5 and C_{11}-C_{12}, on the other hand, diminish to 1.38Å, while the Mulliken population between them increased significantly to 0.53. Bond angles $\angle C_3C_1C_2$ and $\angle C_{13}C_1C_2$ reduced from 120° to 109.4°, which are in good agreement of the typical bond angles found in diamond of 109.47°. For the atoms far away from the H atom, their angles remain as 120°, which is the typical bond angle for pure CNTs.

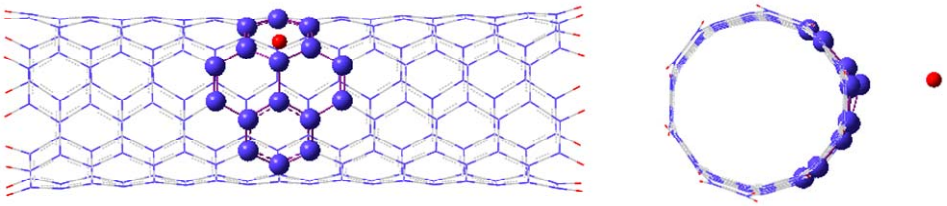

(a) Transition State I

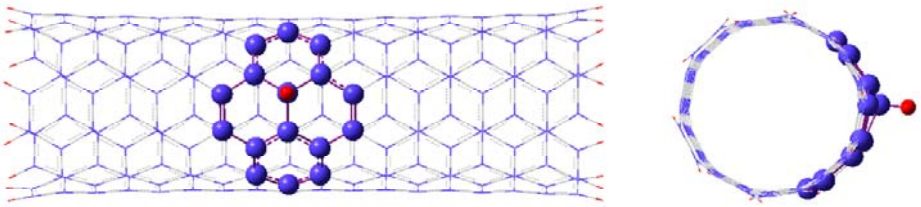

(b) Optimized structure of the stable intermediate I

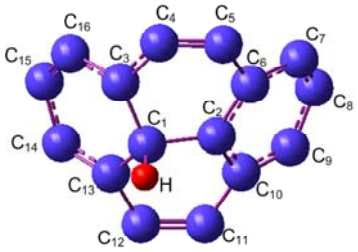

(c) Label of the atoms

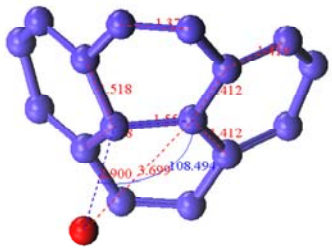

(d) Transition State Parameters

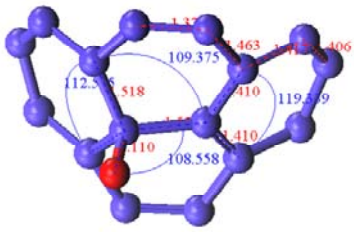

(e) Relaxed System Parameters

Figure 6.2 Sideview along the SWNT axis of the optimized structure of Transition State and the optimized structures for the stable intermediate. The fragments represent the small model system. (inter-atomic distances in Å, bond angles in degrees)

The interaction energy of the H atom with the exterior wall of the (5,5) SWNT is summarized in Table 6.1, where the reaction energy include the calculated energy for the H and CNT reactants, TS, and the products of H-CNT. For the single H atom, the chemisorption adsorption energy is calculated as the difference between the energy of the H-CNT and the isolated energies of the H atom and pure nanotube[231]

$$E_{chemisorption} = E(CNT-H) - E(CNT) - E(H) \tag{6.1}$$

where $E(CNT-H)$ denotes the energy of the nanotube and the H atom, $E(CNT)$ the energy of the bare nanotube, and $E(H)$ the energy of the single H atom. According to this definition, a stable system is supposed to have a negative binding energy. The correspond-

ing chemisorption energy for the reactants, TS structure and the stable intermediate I are plotted in Figure 6.3.

Table 6.1 Relative energy of reactants, TS, and reaction products for the reaction between H atom and SWNT, calculated with ONIOM2(B3lYP/6-31G:UFF) approach.

System	Method	SCF Energy (Hartree)
Reactant: H atom	B3lYP/6-31G:UFF	-0.5003
Reactant: CNT	B3lYP/6-31G:UFF	-615.5241
Product: CNT-H	B3lYP/6-31G:UFF	-616.0784
CNT-H Transition State (TS)	B3lYP/6-31G:UFF	-615.9874
Forward Reaction Activation Energy (*eV*)		1.01
Reverse Reaction Activation Energy (*eV*)		2.32
Energy of Reaction (*eV*)		-1.31

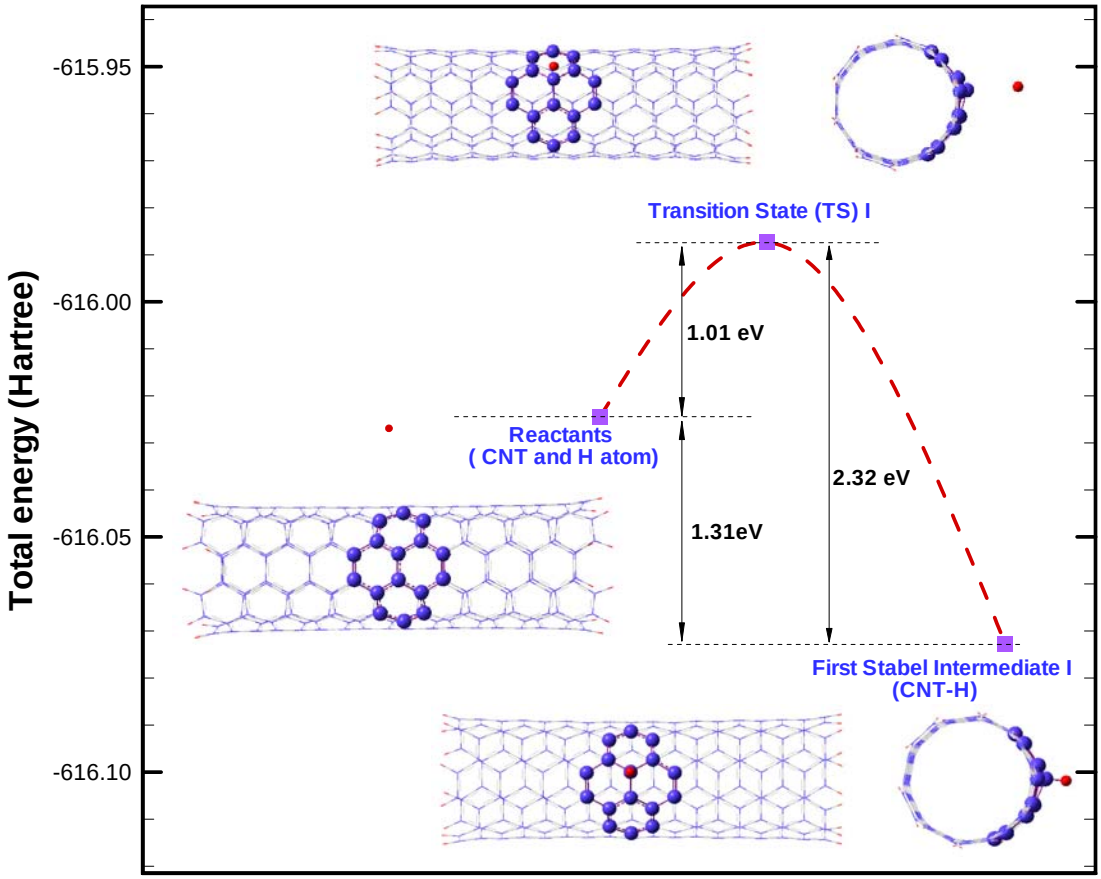

Figure 6.3 Schematic pathway for the chemisorption of one H atom on an (5,5) SWNT.

From the calculation, it is found that adsorption process on the sidewall of the tube is exothermic, with the H-C bonding energy being -1.31*eV* as indicated in Figure 6.3. Thus

it is evident that the reactants achieve an energetically favorable state during the chemical reaction process. This decrease in energy is lower than that of 2.82eV for the formation of the second H-C bond, which will be discussed shortly.

To obtain more insights into the change of electronic structure associated with the H chemisorption process, we calculate the orbital overlap population for the stable intermediate state I. The orbital overlap population curve indicates that the H-C_1 corresponding to the highest occupied molecular orbital (HOMO) are bonding, while those of H-C_2 and C_1-C_2 are antibonding. On the other hand the bonds of H-C_1, H-C_2 and C_1-C_2 at the lowest unoccupied molecular orbital (LUMO) energy level are nonbonding, while those of C_4-C_5, C_{11}-C_{12} exhibit strong antibonding, which is consistent with the results shown in the LUMO representation in Figure 6.4. The bonds of C_3-C_{18}, and C_{13}-C_{14}, which are at the neighbor level to C_1-C_2, are also antibonding, but are weaker than that between C_4-C_5, C_{11}-C_{12}. For one H atom chemisorbed, we obtained E_{HOMO} as -4.45eV, and E_{LUMO} as -1.20eV, and E_{gap} as 3.25eV.

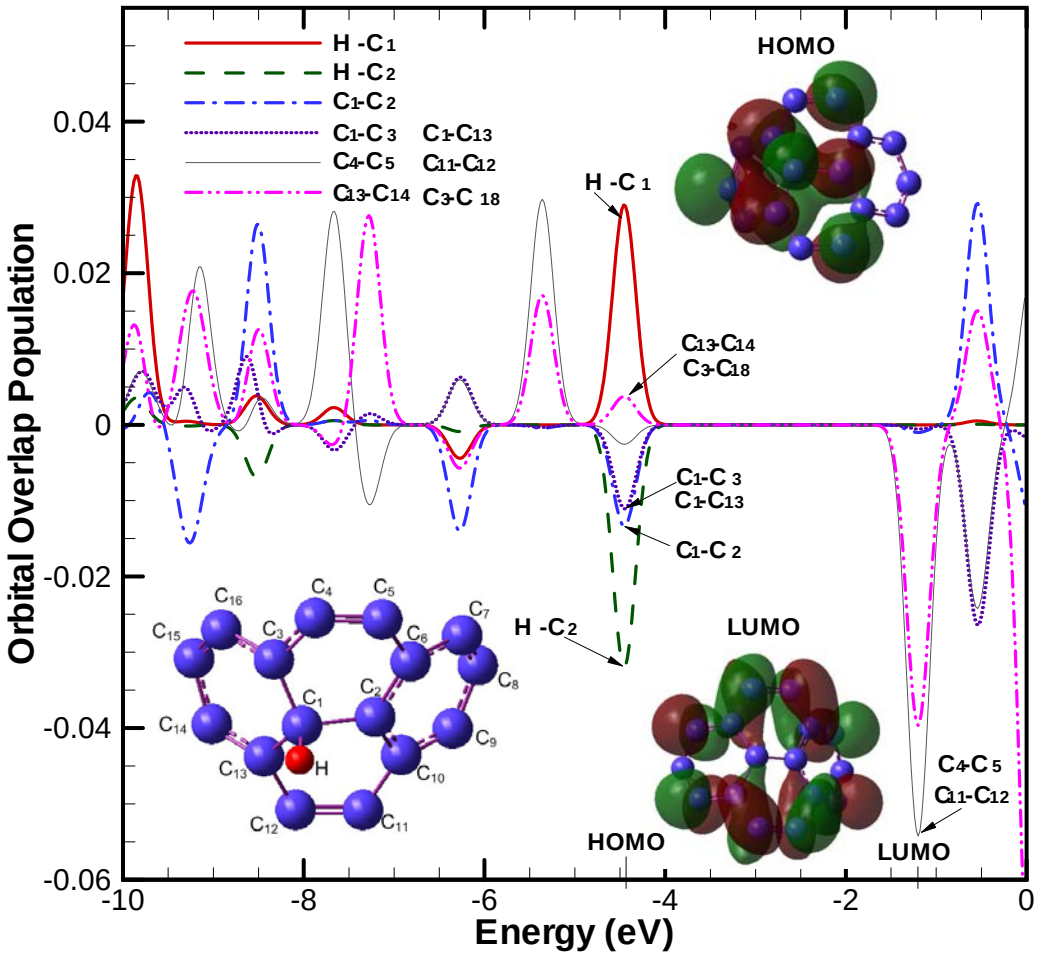

Figure 6.4 Orbital overlap population contributed from H, C_1, C_2, C_3, C_4, C_5 and C_{13} which are involved in the chemisorption process for the intermediate state I. Inset: LUMO and HOMO of the small model system.

In this first part of the present chapter, we have discussed the chemical reaction process of one hydrogen atom approaching the sidewall of the pure nanotube. The geometry and energy changes during the process have been analyzed in detail. It can been seen that when one H atom approaches the side wall of a pure CNT, it will eventually be chemisorbed on the tube, resulting in the weakening of the sp^2 bonds between its two nearest carbon atoms, C_1 and C_2. In addition, there is large charge transfer occurring from the H atom to C_1, filling up the p valence orbital of C_1. In Figure 6.4, the HOMO depicts C_1 exhibiting typical sp^3 hybrid bonds with the nearby carbon atoms, and a σ covalent bond forms between H and C_1. During the formation of the H-C bond, the Mulliken analysis of

bond populations shows that 0.339 electrons are transferred from the neighbouring atoms to C_1, with 0.17 electrons from the H atom, after the H atom has been adsorbed onto the side wall of the (5,5) SWNT, and this is consistent with earlier reported calculations for fully hydrogenated nanotubes[239].

6.3.2 ONIOM Calculations on Chemisorption of Two Hydrogen Atoms on CNT.

In the second part of this chapter, we will consider the reaction of a second hydrogen atom chemisorbed on the side wall of the (5,5) SWNT. Once again, we carry out simulations based on the ONIOM2 method but for the case of two hydrogen atoms being chemisorbed and these simulations start with the stable intermediate structure I that was obtained in the preceding computation in the first part of this chapter. The second hydrogen atom is placed close the tube wall, which can be physically achieved under high-pressure conditions, or by injecting hydrogen atoms with high kinetic energies into the reaction cell.

Similar to the results in the previous calculation for the first H atom, the results here show that the adsorption of the second H atom on the CNT wall results in a distortion of the CNT structure as well, and the corresponding configurations are shown in Figure 6.6, while the energy parameter variation is shown in Figure 6.5. The distance between C_1 and C_2 is 1.73Å for stable intermediate state II and elongates to 2.50Å in the final products. Another important parameter is the distances between the two hydrogen atoms, which generally decreases in the manner 2.78Å → 2.08Å → 1.97Å → 1.74Å from TS II to the final product of 2H-CNT.

From the simulation results, we notice that the second H atom prefers to be chemisorbed with C_2, which is located at the same layer as C_1. The chemical adsorption energy

for the second H-C bond is about 2.82eV, which is a dramatic increase compared to the corresponding value for the single H case of 1.31eV. The average binding energy for forming the C-H bonds is about 2.07eV for the whole process. This energy value has also been previously estimated by Gülseren *et al.*[240] and Han *et al.*[241]. The present results indicate that the adsorption of H atoms on the outside wall of the (5,5) SWNT are preferred with neighboring carbon atoms which are perpendicular to the tube axis, and this adsorption is exothermic and stable. These conclusions are consistent with the results of Gülseren[240], Han[241] and Yang[232].

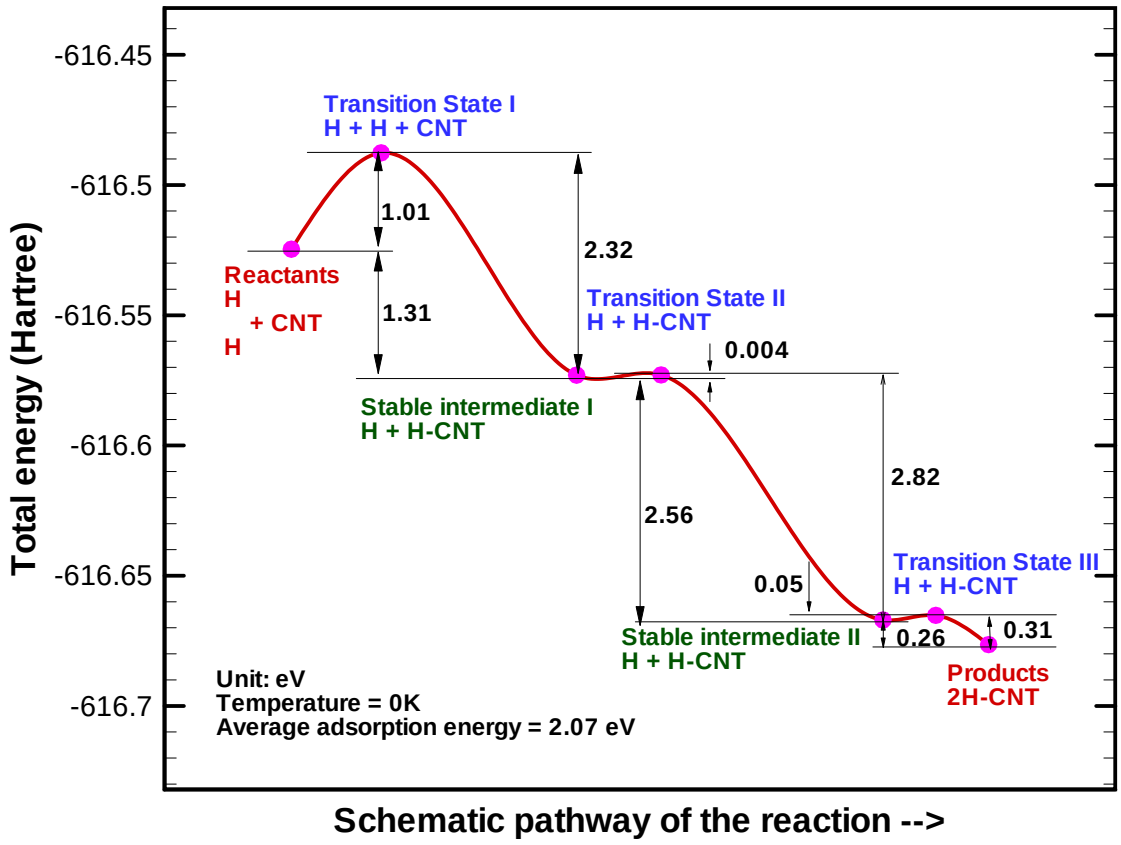

Figure 6.5 Schematic pathway for the chemisorption of two H atoms on a (5,5) SWNT. Three transition states are found during the reaction.

From Figure 6.5, we note that the reaction will follow the process of the H atoms first approaching sufficiently near the surface of the CNT, which could happen under high pressure or high kinetic energy injection, and substantially weakening the C-C π bond of the adjacent tube surface while forming the first H-C σ bond (stable intermediate I). Next

the weakening of the C-C bond results in an unpaired electron in the π orbital of the carbon atom and thus initiates another H atom to form the other second H-C σ bond with the carbon atom (stable intermediate II). This second C-H bond further weakens the C-C bond and elongates the bond length. The attraction between the hydrogen atoms reduced the mutual H-H distance and increases the C-C bond until it eventually breaks and the 2H-CNT products are formed.

It is obvious from the results that the adsorption energy for forming the C-H bonds is different in the three stages. For the first H atom, it is found that $1.31eV$ is released during the adsorption process, while for the second H atom forming the C-H bond with the adjacent C-C bond still intact, $2.56eV$ of energy is emitted. When the adjacent C-C bond is broken, a further $0.26eV$ is released. It turns out that the energy values for the two stable intermediates and the final products are lower than the energies of the reactants, indicating that during the chemisorption, the hydrogen ions will be exothermically adsorbed to the side wall of the CNT.

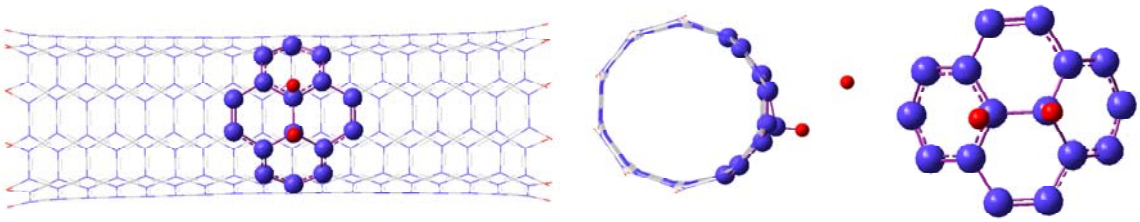

(a) Transition State II

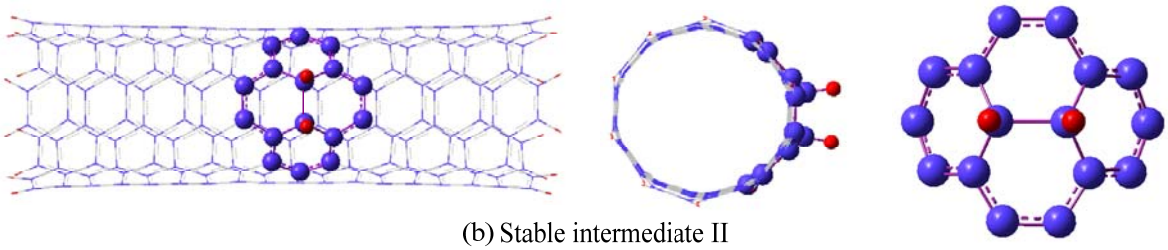

(b) Stable intermediate II

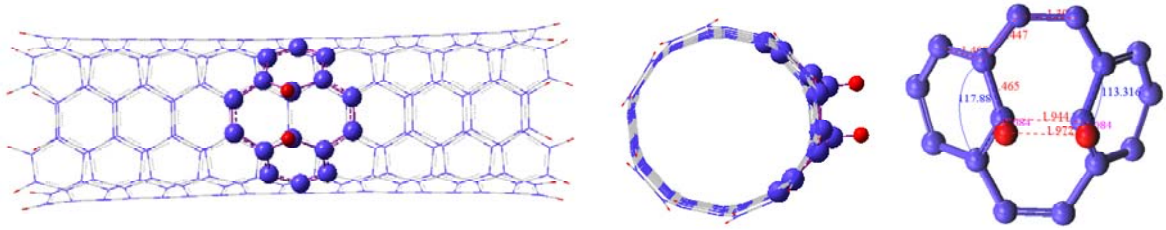

(c) Transition State III

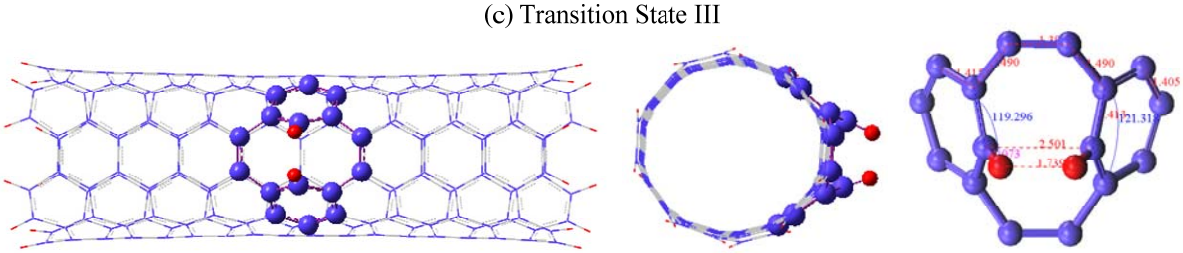

(d) Optimized structure of products

(e) Labels of the atoms

Figure 6.6 Optimized structure for the transition state and the final products.

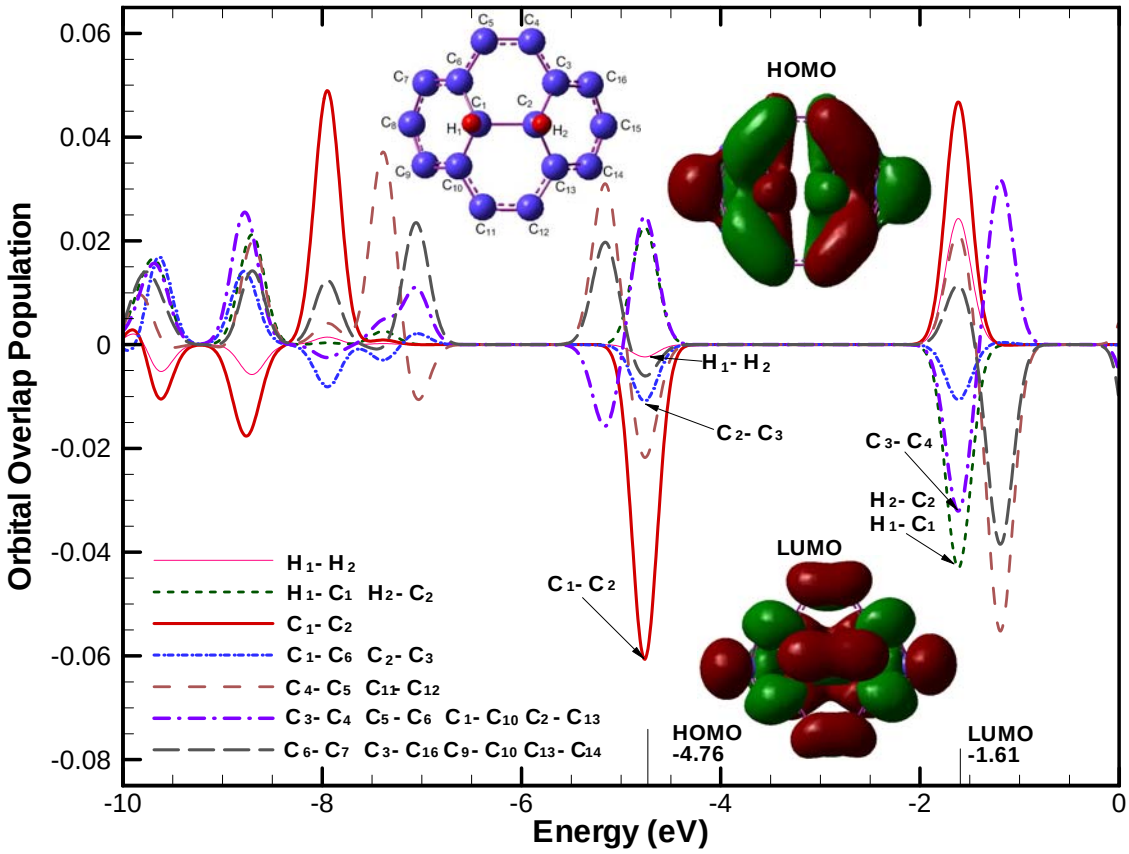

Figure 6.7 Orbital overlap population of the small model system for stable intermediate state II.

The orbital overlap population plots and the HOMO and LUMO orbitals for the small model clusters of the stable intermediate state II are studied and shown in Figure 6.7. The energies of the HOMO and LUMO are -4.76*eV* and -1.61*eV* respectively. Promotion of a bonding HOMO electron to the LUMO is called a $\pi \rightarrow \pi^*$ or $\sigma \rightarrow \sigma^*$ transition, and the HOMO-LUMO gap in the stable intermediate state II has dropped to 3.15*eV*. The orbital overlap population curve for C_1-C_2 bond shows very strong antibonding at HOMO level and strong bonding at LUMO level, which is consistent with the results of the surfaces obtained for the HOMO and LUMO orbitals. The properties of the C_2-C_3, C_1-C_6, C_1-C_{10} and C_2-C_{13} bonds at HOMO and LUMO level are qualitatively similar to that of C_1-C_2 bond, but showing relative weak antibonding at HOMO level and weak bonding at LUMO level. The situation for the H_1-C_1 and H_2-C_2 and H_1-H_2 bonds are the converse of that observed

for the above carbon-carbon bonds. Bonds between hydrogen and carbon indicate bonding at HOMO and non-constructive overlap between the two H atom gives rise to non-bonding at HOMO level, but shows antibonding at LUMO level.

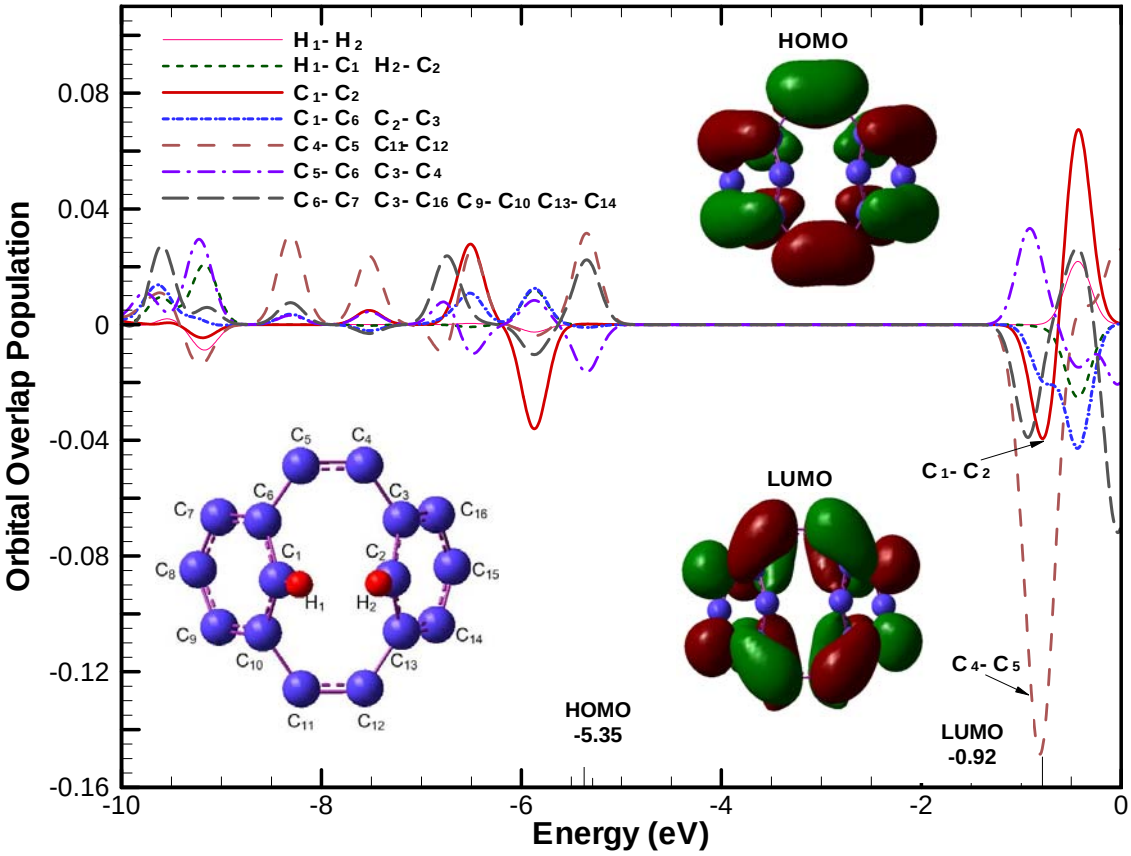

Figure 6.8 Orbital overlap population between hydrogen and carbon atoms in the small model system of the final product.

A similar analysis is also carried out for the relaxed atomic structure of the products, where two H atoms have been adsorbed onto the tube wall and the electron clouds predict that the C_1-C_2 bond is severed. The equilibrium H_1-C_1, H_2-C_2, C_1-C_2 lengths for the final products is 1.07Å, 1.07Å, 2.50Å, respectively, see Figure 6.6(d). The present result for the H-C bond length is consistent with the outcome of Yang *et al.*[232] in that the reported distance between C and H is 1.09Å, when two hydrogen atoms are bonded to two adjacent carbon atoms on a basal plane of graphite. The H_1 and H_2 atoms show positive charges of 0.151, while the neighboring C_1 and C_2 carbon atoms show negative charges of -0.216. The

Mulliken population analysis for H_1-C_1, H_2-C_2, and C_1-C_2 and H_1-H_2 are 0.364, 0.364, 0.007 and 0 respectively, indicating that H_1 and C_1 has form a covalent bond, and the same can be concluded for the H_2 and C_2 atoms. The Mulliken population between H_1 and H_2, and between C_1 and C_2 are almost zero, inferring the non-binding between C_1 and C_2, and between H_1 and H_2. This result is consistent with the fact that the C-C bonds in smaller radii nanotubes are under relatively greater strain, especially those perpendicular to the tube axis[242,243]. These C-C bonds are therefore more susceptible to be weakened or broken to form H-C bonds when H atoms are appropriately introduced. Gang *et al*.[244] predicted that two rows of H atoms chemisorbed on selective sites exterior to the smaller armchair nanotubes can break the nearest-neighbor C-C bonds of the tube. To verify the above results, the orbital overlap population are also calculated for the products and illustrated in Figure 6.8. For the optimized structure of the small model, we obtained E_{HOMO} as -5.35eV, E_{LUMO} as -0.92eV, and E_{gap} as 4.43eV, which is greater than both the stable intermediate states discussed earlier. The orbital overlap population curve indicates that the H_1-C_1, H_2-C_2 bonds corresponding to the HOMO level are bonding, while those of H_1-C_2 and C_1-C_2 are non-bonding. On the other hand, the LUMO level coincides with the C_4-C_5 and C_{11}-C_{12} bonds exhibiting strong antibonding.

The present simulation results illustrate the exothermic nature of the reaction when H atoms are adsorbed onto the outside of the CNT wall. However, as dissociating one hydrogen molecule into two hydrogen atoms requires about 4.57eV (105.269$kcal/mol$)[241,245] which is higher than the exothermic energy of 4.13eV for two H atoms been chemisorbed outside on the side wall of the tube, the entire reaction may still be required to absorb a certain amount of energy if we include the dissociation of the hydrogen molecule into hydrogen atoms. As a final note, it should be stressed that we have used a relative narrow CNTs, which are under higher strain, especially the bonds associated with the carbon atoms aligned perpendicular to the tube axis[242,243]. For those nanotubes with relatively higher

radii, the C-C bonds are expected to remain intact[244]. Furthermore, the interaction of atomic hydrogen with single-wall carbon nanotubes (SWNT) has been studied using the density functional theory (DFT) by Gülseren *et al*.[240,246] and Yildirim *et al*.[239] who found that the binding energy is sensitive to the curvature of the nanotube.

6.3.3 Conclusion

In this chapter, we have obtained an insight into the atomic adsorption process of hydrogen onto carbon nanotubes. Multiscale ONIOM results reveal that the lowest energy states of the system are achieved for hydrogen atoms chemisorbed on the wall of the nanotube. Three transition states and two stable intermediate products are observed in the chemisorption process. The first arriving hydrogen atom weakens the π bond of the C-C bond and forms a H-C covalent bond. The next approaching hydrogen atom will react with the neighboring carbon of the same layer perpendicular to the nanotube axis and form another H-C covalent bond. The original C-C bond is then further weakened and finally breaks when the two H atoms are adsorbed, and this is also due to the mutual attraction between the two hydrogen atoms. The simulation results show that the adsorption of H atoms on the outside of the tube is exothermic and stable, and is hence entirely feasible.

CHAPTER 7

LOCAL REACTIVITY OF HYDROGEN MOLECULES ON/IN CARBON NANOTUBE

The hydrogen storage process of hydrogen molecules adsorbed onto the exterior wall and into the carbon nanotube will be analyzed so as to understand the mechanisms of the hydrogen chemisorption and desorption processes. In our modeling and simulation, the results indicate that the initial geometry results from the physisorption by the weak van der Waals forces followed by the dissociation of the hydrogen molecules before reacting with the nanotube. The following intermediate states and the corresponding transition states in the reaction path are predicted using the ONIOM2 scheme, and frequency calculation used to verify these optimized configurations. A further investigation is performed by NBO (natural bond orbitals) analysis to predict the chemical bonding and separation and the corresponding change in SWNT atomic structure induced by an external chemical reaction with a chemisorbing species. In this chapter we will present the simulation method used for the analysis, followed by the results of the external and internal chemical reactivity analyses.

7.1 Introduction

In chapter 6 we have discussed the chemical reaction process of hydrogen atom with the exterior of the nanotube, and it was shown that hydrogen atoms chemisorbed onto

the exterior wall of the SWNT is thermodynamically favorable. These findings intrigue us to raise many questions with regard to the intermolecular reaction of H_2 with the tube. Do H_2 molecules have the same property as that of the H atoms? Will the H-H bond will break before the chemisorption? Furthermore the interaction between molecular physisorption and atomic chemisorption has not been studied. Recently several groups have carried out hydrogen molecule adsorption studies related with CNTs[33,129,132,136,230,247]. Nonetheless, their results do not reflect the true physical situation as these studies invariably considered physisorption and chemisorption separately. The most common model applied in the previous studies were based upon classical simulations, and the most common assumption considered the nanotube as a rigid model where all the carbon atoms are fixed during the simulation. This results in the H_2-CNT interaction energy becoming unreasonably high as the distance between H_2 and CNT decreases, see Figure 7.1. In these circumstances, no chemical reaction will occur. In this chapter, we perform multiscale ONIOM calculations to investigate the entire process of an H_2 molecule approaching a nanotube without artificially fixing the SWNT.

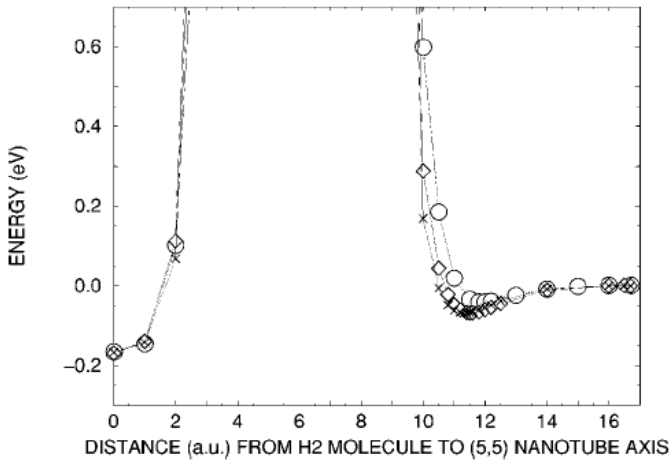

Figure 7.1 Interaction energy of the H_2 molecule and a (5,5) SWNT, obtained in static calculations in which the H-H and all the C-C bond lengths are kept frozen, and only the distance D_a between the molecule and the SWNT axis is varied. In the approach of the molecule to the nanotube, the centre of mass of the molecule is upon the midpoint of a C-C bond with the molecular axis parallel to that bond (circles) or upon the center of a hexagon with the molecular axis parallel (crosses) or perpendicular (diamonds) to the hexagon surface[230].

In this chapter, we propose that physisorption and chemisorption be considered simultaneously when analyzing the phenomenon of H_2 adsorption on and in the CNT. While our calculations suggest that weak interactions between H_2 and CNTs do exist, the H_2 adsorption energy consists predominantly of the weak van der Waals forces. With decreasing distance between the H_2 and the CNT, the structure of the small diameter CNT becomes distorted and subsequently form C-H bonds.

7.2 Computational Methodology

It is very important to develop a systematic way of studying the characteristics of local chemical reactivity which is generally applicable for nanotube based structural designs and applications. In this simulation, the relatively narrow (5,5) carbon nanotubes are approximately 22.6Å long, with the dangling bonds at the ends being tied off with hydrogen atoms. Since the problem is on hydrogen molecules interacting with the tube wall, the effects caused by the caps must be removed, as they have a stronger interaction with hydrogen atoms than the tube wall[137]. In the calculations, the frequency is used to ensure the optimized geometry for the transition and stable intermediate states.

The deficiencies of computational models proposed by most researchers include fixing the CNT while changing the distance between H_2 and CNT and/or using too small a cluster of carbon atoms to model the reaction process, which has been discussed in chapter 6. Here we apply the ONIOM2 method introduced in chapter 4 for the investigation of the chemical reaction process. In this work, we also employ the natural population analysis (NPA)[165] to partition the molecular wavefunctions into natural bond orbitals (NBO)[166] (described earlier in chapter 3), which is well suited for characterizing the bonding and antibonding patterns in chemical terms. These detailed characterizations are important for the study of the interactions between CNTs and hydrogen molecules. All calculations were preformed with the Gaussian 03 suite of programs. Geometry optimizations and all calcu-

lations relevant to the NBO analysis of stereoelectronic interactions for the model system were performed at the B3LYP/6-31G+(d,p) level of theory.

7.3 Results and Discussions

The interaction of atomic and molecular hydrogen with carbon nanotubes and other graphite materials have been studied and discussed by many groups, where the possibilities of hydrogen being physisorbed outside the tube, and also the possible of dissociation of the hydrogen molecule with both resulting atoms being chemisorbed on the tube wall, have been studied separately. However, the entire process from physisorption to chemisorption subsequently the flip-in mechanism into the tube has not been studied. In this work, we carry out such a study, where the starting geometry includes a H_2 molecule outside the SWNT with mutual attraction by weak van der Waal forces. The interaction between the H_2 molecule with a (5,5) armchair carbon nanotube is investigated using the ONIOM2 scheme introduced in chapter 4, where B3LYP is applied for the high-level description, and the Universal Force Field (UFF)[138] for the low-level treatment. For the polarization effect, the 6-31G+(d,p) basis set is used in conjunction with the B3LYP. These ONIOM calculations are performed using Gaussian 03.

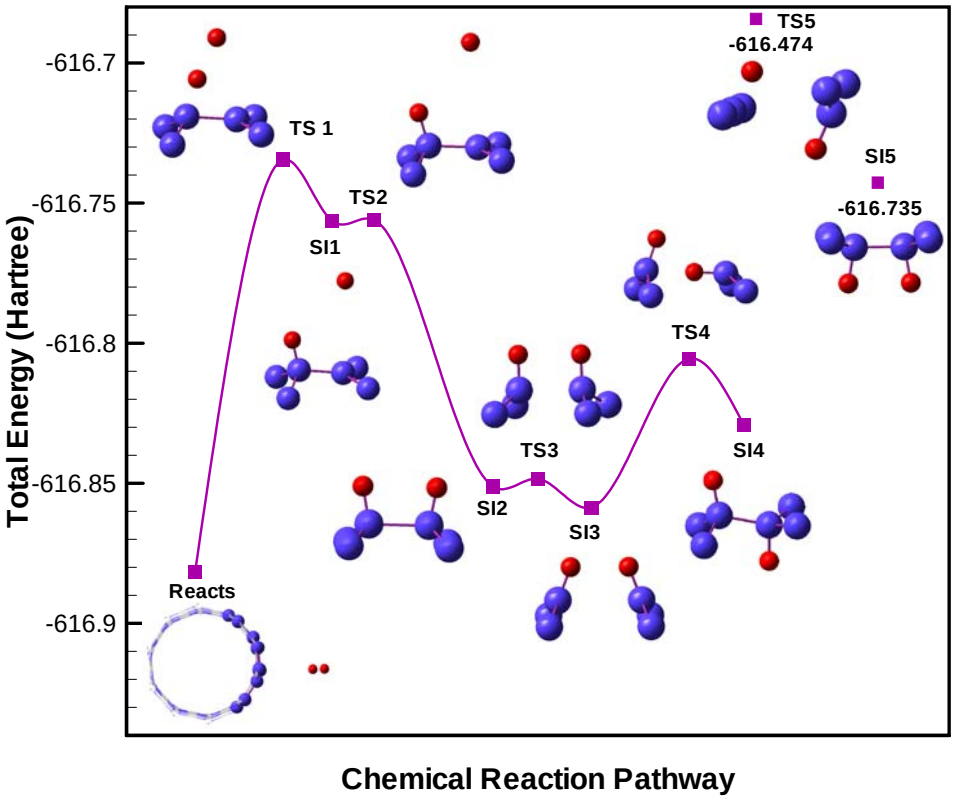

(a)

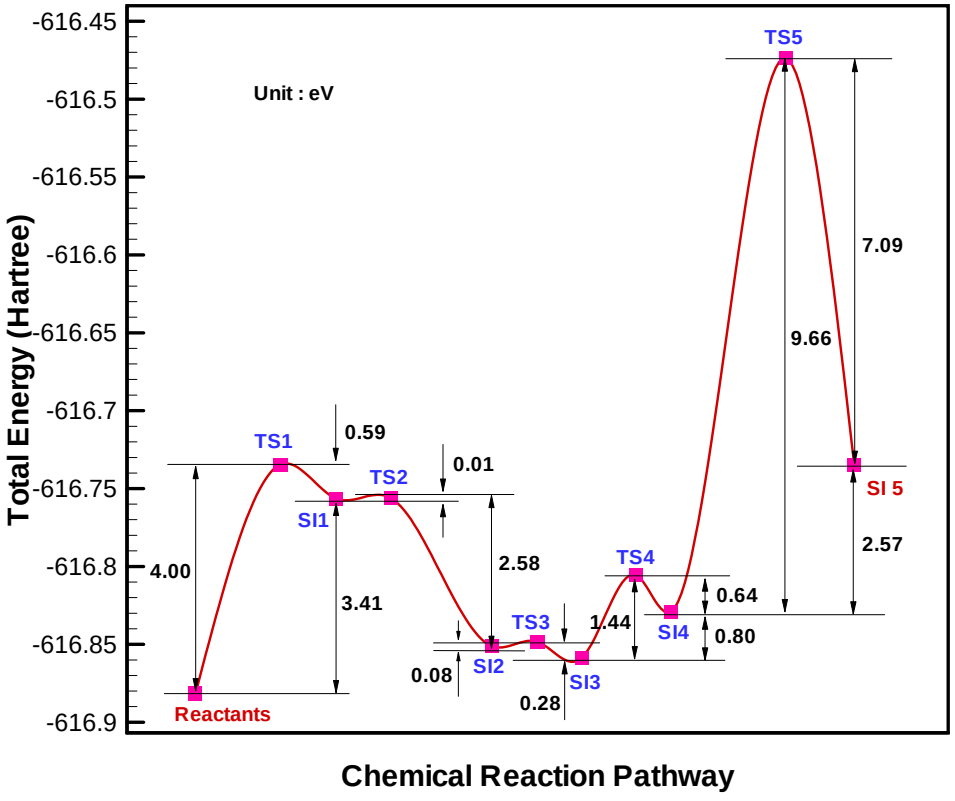

(b)

Figure 7.2 Overview of the chemisorption pathway of hydrogen molecules chemisorbed from the exterior of the tube to the inner side.

Figure 7.2 provides an overview of the energy relation, which begins with the stable physisorption state to the various chemisorption stable intermediate states and finally adsorption into the CNT at absolute temperature. The reaction energy barriers, equivalent to the activation energies are labeled in the diagram. In the following discussion, we will examine these states and their properties in detail.

7.3.1 H_2 Interaction with CNT Exterior

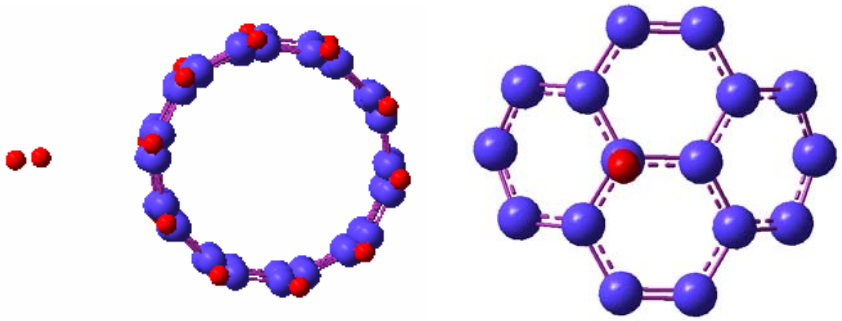

Figure 7.3 One hydrogen molecule is physisorbed outside the nanotube

The parameters of the initial locations of the H_2 molecule outside the (5,5) nanotube is above the center of six-membered ring of the tube, above the middle of the C-C bond and above the top of a carbon atom, where the orientations of the hydrogen molecule are parallel/perpendicular/tilted with respect to the C-C bond and the hexagon surface. The geometry optimization is followed by frequency analysis to ensure that the stable structures have no negative or imaginary frequencies for the relaxed structures. Our simulations show that the equilibrium position for the hydrogen molecule physisorbed at the exterior of the tube is at the top of the carbon atom, see Figure 7.3. For other configurations, we find negative or imaginary frequencies. More than one imaginary frequency is obtained when the H_2 molecule is positioned above the center of a carbon hexagon regardless of whether the molecular axis is parallel or normal to the hexagon. In addition, one imaginary frequency is obtained when H_2 above the middle of the C-C bonds but the axis of the H-H

bond is perpendicular to that of the C-C bond. The same results are obtained even when applying a larger model system for the high-level calculations.

- **Transition State 1 (TS1)**

The transition state is a maximum turning point on the reaction pathway. To verify the geometry obtained, we employ the primary method of computing its vibrational frequencies, which should have only one negative frequency. The vibrational motion with the negative frequency represents the pathway towards the reactants in one direction and the products in the other direction.

Our results indicate that the configuration of the transition state (TS1) linking the physisorption and chemisorption processes involve the H_2 molecule dissociating into two independent hydrogen atoms (radical state), where the distance between these two hydrogen atoms is 1.46Å (see Figure 7.4). It also indicates that the interaction with the carbon nanotube influences this hydrogen dissociation and places one hydrogen atom in contact with the SWNT. The underlying intermolecular interaction induces localized geometry distortion in the SWNT, where adjacent C-C bond is weakened, and the bond length extends from 1.42Å to 1.59Å. The hydrogen atoms have not formed bonds with any carbon atoms yet, and the distance between the H atoms with their adjacent carbon atoms are 1.23Å and 2.69Å respectively.

We now proceed to carry out a population analysis to describe whether the states are localized or more quantitatively to determine the charge density of each atom. In chapter 3, we have already shown that the Mulliken population analysis (MPA)[160] is a scheme for assigning charges by dividing the orbital overlap evenly between the atoms involved. However, this method is somewhat arbitrary, and usually leads to results with incorrect physical interpretations. This is especially so if diffuse basis functions are used. For example, the Mulliken population analysis often generates charges of more than 2e (it should be

between 0 to 2e) due to the basis orbitals centered at one atom erroneously describing the electron density close to another nucleus. Due to this disadvantage, we will employ a population analysis based on natural atomic orbitals[165,166], an approach which is physically more relevant as it fits charges at the atomic position based on the molecular electrostatic potential measured at designated grid points. This approach has been used to obtain detailed descriptions of the electronic structure of many related compounds, and is packaged in the Gaussian software.

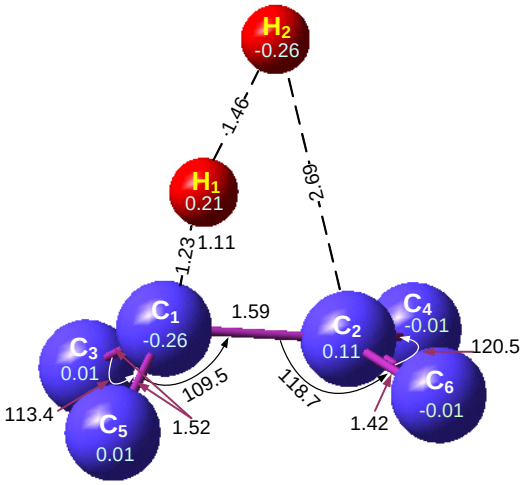

Figure 7.4 The geometry parameters and NBO charges for the Transition State 1 (TS1)

In chapter 3, we have already introduced the natural bond orbital Analysis, see Eqs. (3.47) and (3.48). The NBO summary of the C_1-C_2 bond has the following formations for bonding and antibonding.

$$\sigma_{C_1-C_2} = 0.720\left(sp^{2.51}\right)C_1 + 0.694\left(sp^{2.53}\right)C_2 \tag{7.1}$$

$$\sigma^*_{C_1-C_2} = 0.694\left(sp^{2.51}\right)C_1 - 0.720\left(sp^{2.53}\right)C_2 \tag{7.2}$$

For the C_1-C_2 bond, 1.900 electrons are bonding, while 0.041e are antibonding, and no π bonding exists. Eq. (7.1) summarizes the natural atomic hybrids and atom labels of which the NBO is composed, where the $sp^{2.51}$ (28.52% *s*-character, and 71.43% *p*-

character) hybrid on C_1 interacts with an $sp^{2.53}$ (28.29% for *s*-character, and 71.66% *p*-character) hybrid on C_2. The polarization coefficients c_A and c_B are 0.720 and 0.694 for the $\sigma_{C_1-C_2}$ bond, and these give a measure of the relative importance of the two hybrids in the bond formation.

For the H_1-H_2 bond, it displays very strong antibonding of 0.324 electrons, and 1.708 electrons for bonding. The NBO summary is

$$\sigma_{H_1-H_2} = 0.571(s)H_1 + 0.821(s)H_2 \tag{7.3}$$

$$\sigma^*_{H_1-H_2} = 0.821(s)H_1 - 0.571(s)H_2 \tag{7.4}$$

The above results indicate that the dissociation of the H_2 molecule is the result of the interaction between the hydrogen molecules and the CNT. When the H_2 approaches the CNT, the electrons forming the σ-bond between H-H begin to interact with the CNT. The C-C π bond is weakened, while the σ^* antibonding between the H-H is enhanced. Meanwhile, the energy of the occupied antibonding state increases very rapidly, resulting in the loss of the C-C π bond and the H-H σ bond.

In Figure 7.2, the transition barrier for the H_2 to be chemisorbed from the physisorption state are evaluated, and we find that high forward reaction barriers associated with dissociating the H-H bond of hydrogen molecule and distorting the configuration of the carbon nanotube, at about 4.005*eV* (92.293*kcal/mol*). The reaction barrier is lower than the H-H dissociation energy reported by Lide[245] (4.52*eV*) and Yildirim *et al.*[239] (6.65*eV*). The lower energy obtained in this study suggests that the CNT plays a major role in reducing the activation energy of breaking the H-H bond. The reverse energy barrier is much lower at 0.594*eV* (13.698*kcal/mol*).

- **Stable Intermediate State 1 (SI1)**

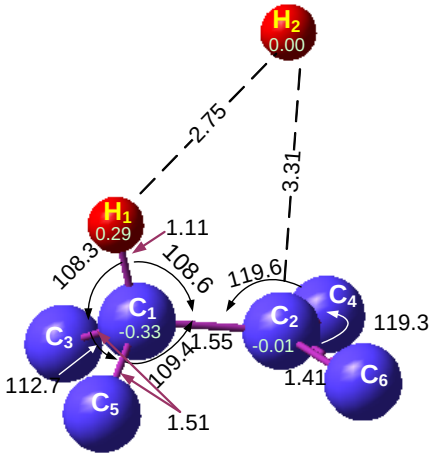

Figure 7.5 Stable intermediate state I, where one of the hydrogen molecule is dissociated, and one H atom is chemisorbed onto a carbon atom, while the other hydrogen atom positions itself above another carbon atom.

From the present simulation, it is observed that as the hydrogen molecule is chemisorbed on the nanotube, the carbon atom directly involved in the bonding induces some appreciable distortion in the neighboring carbon atoms around the adsorption site, and a clear deviation from a uniform circular tube is observed. These sizable extended nonuniform radial deformations significantly alter the structure near the reaction sites, and the optimized geometry parameters are presented in Figure 7.5, which is the first stable intermediate (SI1) state. It shows that one of the hydrogen atoms is chemically bonded with a carbon atom while the other hydrogen atom is yet to be attached to the exterior wall at this stage, which also has been observed in reported works[132,240,246,248,249]. The chemisorbed hydrogen atom induces a local distortion of the surrounding carbon atoms, creating an intermediate sp^2/sp^3 bonding character on neighboring atoms, where the newly formed C-H bond length is 1.11Å, and the immediate neighboring C_1-C_2 bond length now extends to 1.56Å, which is longer than the undeformed C-C bond length of 1.42Å. This distortion induces the degradation of the π bond in the pair of C_1-C_2 atoms and also results in a slight dangling-bond characteristic in its immediate neighborhood. This will inevitably affect the

energetic and kinetics of adsorption of additional hydrogen. The distance between the two H atoms is now elongated to 2.78Å.

To check the bond strength between the pertinent bond lengths, and the changes in geometry distortion at the chemical reaction sites, we need to consider the electronic structure of the carbon atoms C_1 and C_2, and the two adjacent hydrogen atoms H_1 and H_2. According to the NBO analysis, the bonding framework of the carbon tetrahedron is formed for C_1, which forms bonds with its neighbor atoms C_3, C_5 and H_1. The carbon atom C_1 has shaped into sp^3 hybrid orbitals, and thus occupies four σ-orbitals. Charges delocalized from H_1 to C_1 results in the weakness of the π bond between C_1-C_2, with some electron transfer occurring from C_2 to C_1, and we can see that C_2 possesses slightly negative charges of $-0.01e$, see Figure 7.5. Such delocalization processes increase the electronic charge density between the two carbon atoms and elongate their bond length. The overall response of the electronic structure to these interactions is an increase in negative charges of the C_1 atom. According to the natural orbital analysis, the carbon atom of C_1 has negative charges of -0.33e, and the hydrogen atom H_1 which contributes parts of its electrons to C_1, shows positive charges of 0.29e, with the other hydrogen atom still keeping neutral. The dissociated H atom has one unpaired electron in its *s* orbital, thus the formation of the σ bond is preferred. On the other hand, the electron distribution induces localized geometry distortion, with C_1 changing from sp^2 to sp^3 orbitals, and forming σ bonds with the adjacent carbon atoms. The occupancy factor of σ bonding orbitals for C_1-C_2 is 1.960 electrons, where 50.86% comes from the sp^3 hybrid orbital in C_1, and 49.14% from the sp^2 hybrid orbital in C_2. The NBO summary for bonding and antibonding between C_1 and C_2 is shown below

$$\sigma_{C_1C_2} = 0.704\left(sp^{3.04}\right)C_1 + 0.710\left(sp^{2.27}\right)C_2 \tag{7.5}$$

$$\sigma^*_{C_1C_2} = 0.710\left(sp^{3.04}\right)C_1 - 0.704\left(sp^{2.27}\right)C_2 \tag{7.6}$$

No π bond is found between C_1-C_2 indicating the formation of the C-H bond is at the cost of losing the π bond between C_1-C_2. The hybrid orbitals of C_1 are composed of 24.72% *s*-character, and 75.23% *p*-character, which corresponds closely to the qualitative concept of interacting sp^3 hybrids (75% *p*-character). Those of C_2 are composed of 30.55% *s*-character and 69.47% *p*-character, which corresponds closely to the interacting sp^2 hybrids of 66.67% *p*-character. Almost equal electronegativity (same polarization coefficients) for the C_1-C_2 σ bond is observed. A simple diagram of the sp^2-sp^3 orbital forming the σ bond is shown in Figure 7.6.

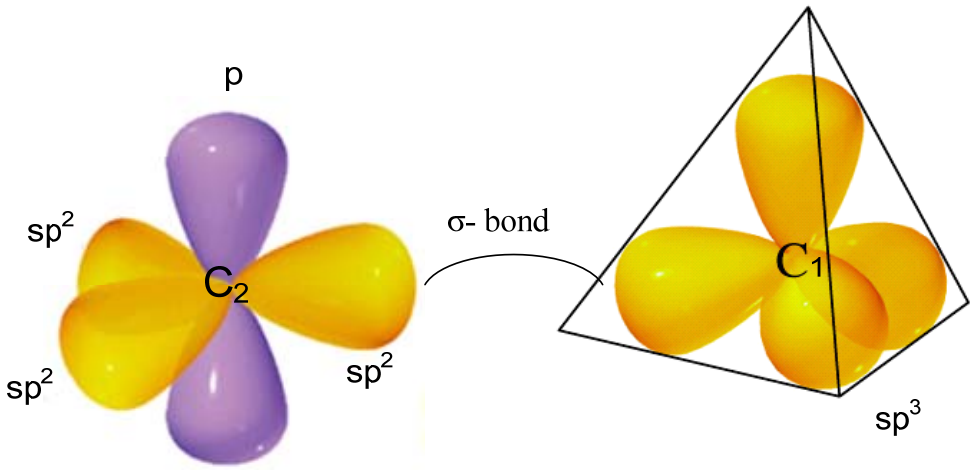

Figure 7.6 σ bond between C_1 and C_2

However, for C_2 which is not directly involved in the chemical reaction at this stage, it still undergoes sp^2 hybridization, and it forms a σ covalent bond with C_1, while the 2*p* orbitals overlap at their boundaries, forming additional nonlocalized π bonds with other carbon atoms. The bond length between C_2-C_4, and C_2-C_6 is about 1.41Å and the angle of $\angle C_5C_2C_7$ is around 120°, which is the typical geometry parameter for the pure undeformed CNT. The NBO analysis further reveals that 1.970 electrons in the σ orbital are bonding while 0.0266 are antibonding. For the π orbital, 0.394 electrons exhibit antibonding, and this strong value indicates the weakening of the π bond between C_2-C_4 and between C_2-C_6.The NBO summaries are

$$\sigma_{C_2C_4} = 0.708\left(sp^{1.88}\right)C_2 + 0.707\left(sp^{1.95}\right)C_4 \tag{7.7}$$

$$\sigma^*_{C_2C_4} = 0.707\left(sp^{1.88}\right)C_2 - 0.708\left(sp^{1.95}\right)C_4 \tag{7.8}$$

$$\pi_{C_2C_4} = 0.756\left(2p\right)C_2 + 0.654\left(2p\right)C_4 \tag{7.9}$$

$$\pi^*_{C_2C_4} = 0.654\left(2p\right)C_2 - 0.756\left(2p\right)C_4 \tag{7.10}$$

For the bond between C_1-C_3, no π bond exists, revealing that it is severed due to the formation of the C_1-H_1 bond.

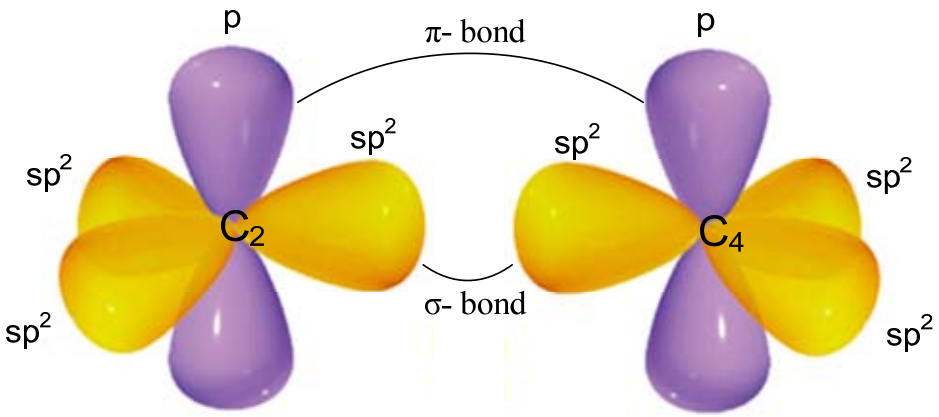

Figure 7.7 σ and π bonds between C_2-C_4 and C_2-C_6.

The C_1-H_1 NBO summary is

$$\sigma_{C_1H_1} = 0.792\left(sp^{3.65}\right)C_1 + 0.610\left(s\right)H_1 \tag{7.11}$$

$$\sigma^*_{C_1H_1} = 0.610\left(sp^{3.65}\right)C_1 - 0.792\left(s\right)H_1 \tag{7.12}$$

The bond framework of C_1 forms the σ-bond type with the H_1 atom, where the occupancy factor for bonding is 1.935 electrons, with 0.0356 electrons being antibonding.

It is therefore has been clearly shown that when hydrogen molecules approach the exterior surface of the carbon nanotube, the hydrogen molecules will first be dissociated into two separate hydrogen atoms. One of them is then chemisorbed onto the adjacent carbon atom, with some electrons (about 0.291e using NBO analysis) being transferred from

the H atom to the carbon atom by the overlap between the C and H atoms. The formation of the C-H bond causes the loss of the π bond between the two carbon atoms, forming a relatively stronger antibonding state.

However, this SI1 state will become a more stable state with the other hydrogen atom H_2 also bonded to the nanotube wall. Our simulation results show that carbon atom C_2, which is at the same layer with C_1 is the most favorable site for the next hydrogen addition to the SWNT, forming another C-H bond, as shown in Figure 7.12. This preference is not surprising, as we learn from overlap population contour in Figure 7.8(b) that the bond between C_1 and C_2 forms stronger antibonding at the HOMO level, with the C_2-C_6, C_2-C_4 forming relatively weaker antibonding. This means that the electron density between C_1 and C_2 is significantly reduced by the adsorbed H atom. The density of state (DOS) curve in Figure 7.8(a) , which is analyzed with Gausssum 0.9[250], works as a complement to the overlap population plot, and indicates the energy levels.

The intrinsic chemical reactivity or inertness, and the inherent thermodynamic stability of molecules, are not straightforward and evident in terms of electronic structures drawn in terms of the above mentioned theories of bonding. The relative thermodynamic stabilities and chemical response of different molecules are hardly intelligible in terms of such electronic structures. However, the HOMO-LUMO energy separation can serve as a simple measure of kinetic stability, where the HOMO and LUMO are the frontier orbitals. It has been established that the gap in energy between the HOMO and LUMO is an important stability index, where a large gap implies high stability, and a molecule with a small or no HOMO-LUMO gap is chemically reactive[251-260]. This is because the smaller gap is energetically favorable to add electrons to a high-lying LUMO, and/or to extract electrons from a low-lying HOMO, so as to form the activated complex of any potential reaction[260]. A high gap in turn indicates low chemical reactivity and high stability. The energy and symmetry types of such frontier orbitals are also found to be the principal factor for deter-

mining the occurrence or non-occurrence of chemical reactions and stereo-selective path in intra- and inter-molecular processes. The energy, symmetry type and charge distribution in HOMO, as well as the energy and symmetry type of LUMO, are known to determine the structures of molecules[253]. Pearson[253,255-257] showed that the HOMO-LUMO gap represents the chemical hardness of the molecule. For the stable intermediate state 1 (SI1), we obtained $E_{\mathrm{LUMO}} = -1.59eV$ and $E_{\mathrm{HOMO}} = -4.75eV$, and therefore $E_{\mathrm{gap}} = 3.16eV$.

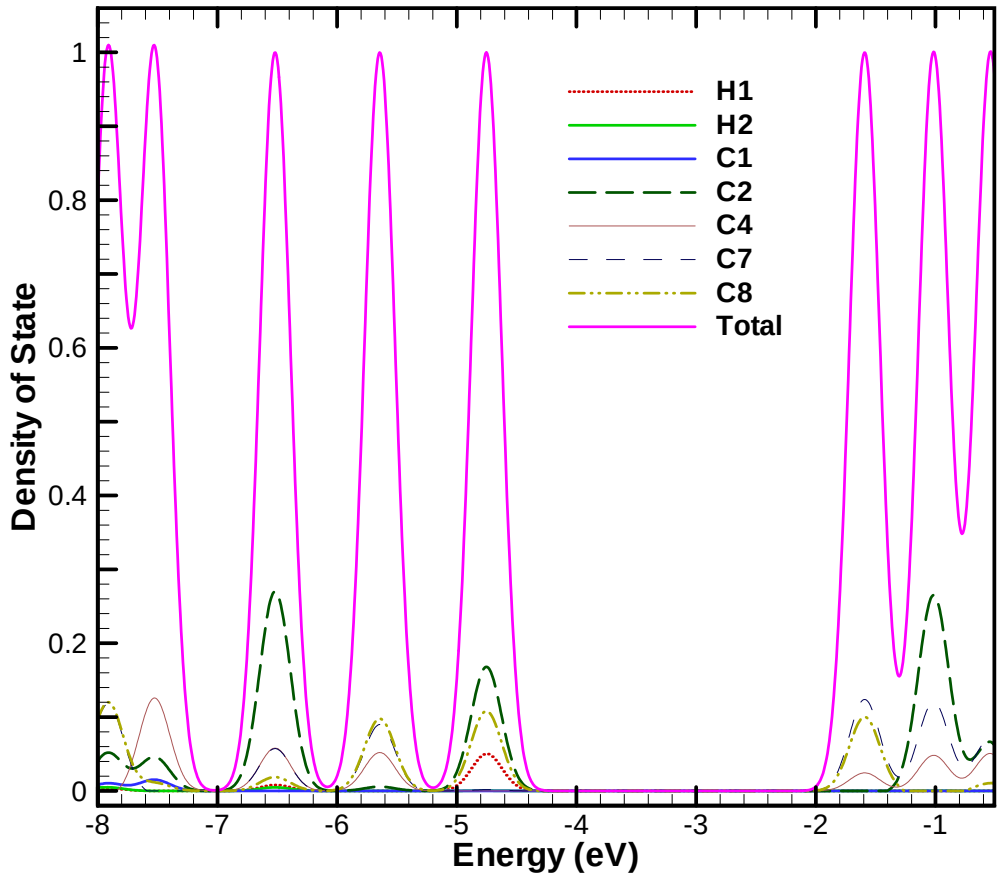

(a)

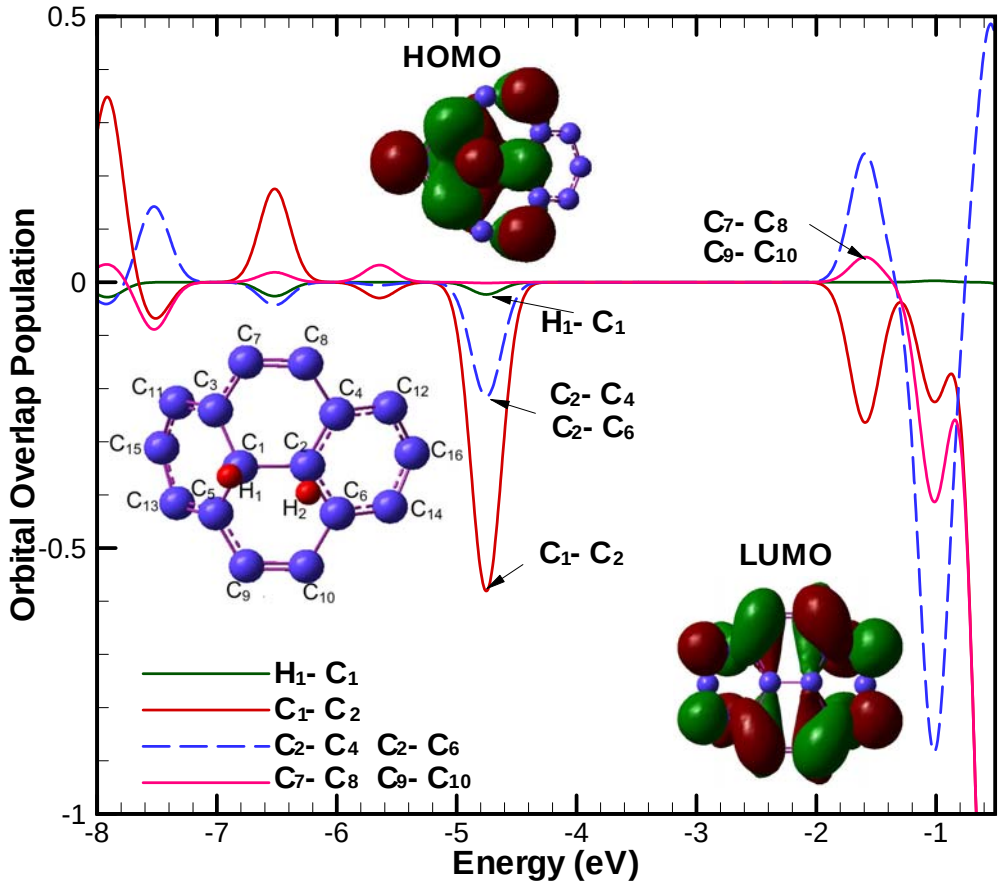

(b)

Figure 7.8 Density of State and the orbital overlap population for the stable intermediate state 1 (SI1).

Our simulation results also show that the first hydrogen attachment is more costly from an energy point of view compared with the second one, since there is the need to in the first to breaks the *p* ring conjugation. The subsequent hydrogen is much easier to attach. During the reaction of H_1 with C_1, the localized structure converts from sp^2 to sp^3, making further chemisorption energetically favorable. Nevertheless, due to the constraints imposed by the SWNT, it is not so easy to create sp^3-like buckling around the chemisorbed hydrogen compared with smaller molecules. For instance, the bond angles in benzene can adjust relatively freely to accommodate nearby sp^2 and sp^3 atom.

- **Transition State 2 (TS2)**

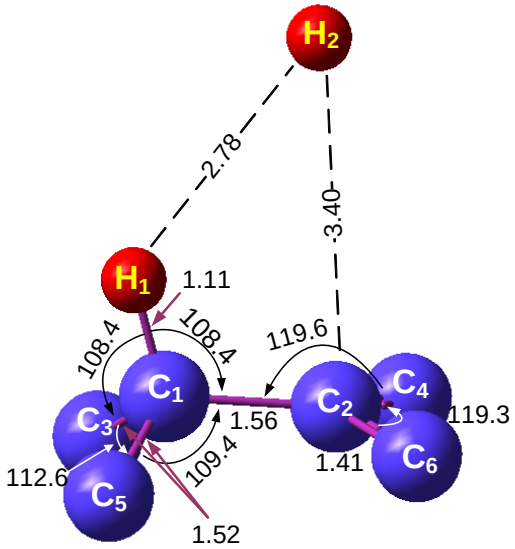

Figure 7.9 Transition state 2 (TS2)

The reaction in which the radical hydrogen atom H_2 reacts with the SWNT and forms the second C-H bond requires a lower energy transition state on the reaction path that has to be traversed before the stable intermediate of SI3 forms. In order to reach this transition state, the reactants must adsorb energy and orient themselves in a suitable configuration. Our calculation shows that the transition state 2 (TS2) between stable intermediate 1 (SI1) and stable intermediate 2 (SI2), needs to overcome $0.013eV$ activation energy, which is much lower than the $4eV$ required for the H_1 atom to be chemisorbed onto the SWNT. The distance between the two hydrogen atoms is 2.78Å, 1.11Å for the H_1-C_1 bond length, 3.40Å for the distance between C_2 and H_2, and 1.56Å for the C_1-C_2 bond which is composed of the sp^2 and sp^3 hybrid orbitals. We note that all these bond lengths and relative atomic distances are correspondingly longer than that in SI1 (see Figure 7.9). The TS2 state is validated by the vibrational frequency calculation, which yields an exclusive imaginary frequency.

- **Stable Intermediate State 2 (SI2)**

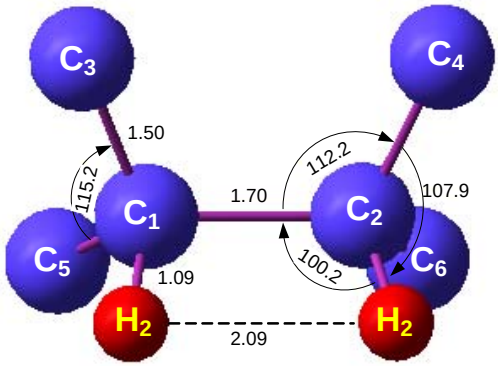

Figure 7.10 Top view of H atoms chemisorbed on adjacent carbon atoms, which is at the same layer for the armchair SWNT.

For the stable intermediate state 2 (SI2), both the hydrogen atoms are chemically bonded to the CNT as shown in Figure 7.10. The NBO result indicates negative charges of -0.29eV distributed in C_1 and C_2, and positive charges of 0.30eV distributed in both the H_1 and H_2 atoms. This implies that during the chemisorptions process, the hydrogen atoms transfer about 0.3eV electrons charge to their adjacent carbon atoms. The charge transfer leads to the geometry distortion. Both of the carbon atoms have valence configuration of $2s2p^{3.94}$, in this hybrid orbital, with 20.25% occupying the *s*-orbital and 79.72% the *p*-orbital. The NBO summary of the C_1-C_2 bond is shown in Eqs. (7.13) and (7.14). The occupancy factor for bonding has decreased to 1.893e (should be between 0 and 2 electrons for each bond) and that for antibonding has risen up to 0.0882e, suggesting that the C_1-C_2 bond is not stable, and having the inclination to break and subsequently achieve a new stable intermediate configuration. These numerical data are consistent with the actual optimized geometry parameters for SI2, where the bond length of C_1-C_2 has elongated to 1.70Å.

$$\sigma_{C_1C_2} = 0.707\left(sp^{3.94}\right)C_1 + 0.707\left(sp^{3.94}\right)C_2 \tag{7.13}$$

$$\sigma^*_{C_1C_2} = 0.707\left(sp^{3.94}\right)C_1 - 0.707\left(sp^{3.94}\right)C_2 \tag{7.14}$$

The bonding occupancy factor for both C_2-C_4 and C_2-C_6 is 1.972e, which is much stronger than that of C_1-C_2, while the antibonding factor of 0.0282e for both C_2-C_4 and C_2-C_6 is much lower than that of C_1-C_2.

The C_1-C_3 NBO summary is

$$\sigma_{C_1C_3} = 0.712\left(sp^{2.47}\right)C_1 + 0.702\left(sp^{2.21}\right)C_3 \tag{7.15}$$

$$\sigma^*_{C_1C_3} = 0.702\left(sp^{2.47}\right)C_1 - 0.712\left(sp^{2.21}\right)C_3 \tag{7.16}$$

Compared with the C-H bond in the SI1 state, the bonding factor is stronger, increasing from 1.935e (SI1) to 1.944e, while the antibonding is correspondingly decreased from 0.0356e (SI1) to 0.0165e, suggesting that the C-H bond is strengthened.

$$\sigma_{C_1H_1} = 0.803\left(sp^{3.51}\right)C_1 + 0.596\left(s\right)H_1 \tag{7.17}$$

$$\sigma^*_{C_1H_1} = 0.596\left(sp^{3.51}\right)C_1 - 0.803\left(s\right)H_1 \tag{7.18}$$

From the above discussion, we can conclude that the current hydrogenated configuration is not stable, and the breaking of the C_1-C_2 bond eminent, upon which a new geometry is formed whereby the system reorganizes into a more stable configuration.

To validate the present results, we compare the activation energy with that reported by Han *et al.*[249], who obtained a reaction energy barrier of 78.827*kcal/mol* using the density functional theory for a (10,0) SWNT. We also calculated the energy difference between the physical adsorption state and TS2 which is consistent with the only TS configuration Han *et al.*[249] reported. The result we obtained is 78.864*kcal/mol*, which is about 0.027*kcal/mol* higher. This result also indicates that the reaction from the physisorption state to chemisorbed state SI2 is endothermic and not spontaneous, which is in agreement with Chan *et el.*[125], Bauschlicher[131] and Han *et al.*[249]. Our calculations also reveal that the

chemical reaction energy between the physisorbed state and the chemisorbed state SI2 is 19.279*kcal/mol* for a hydrogen molecule being chemisorbed and forming two C-H bonds at SI2 state. Han *et al.*'s[249] results showed 18.352*kcal/mol* for the case of a (10,0) CNT, and Chan *et al.*[125] reported 10.377kal/mol for a (6,6) CNT.

- **Transition State 3 (TS3)**

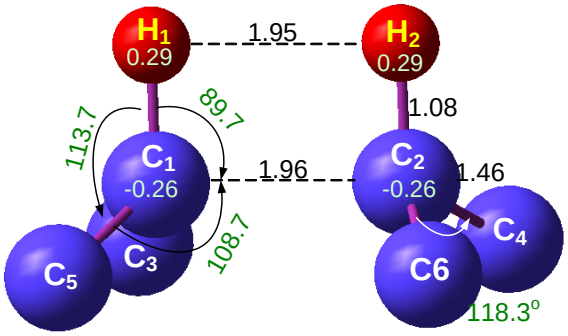

Figure 7.11 Side view of the transition state 3 (TS3)

In the reaction pathway, the transition state 3 links the SI2, and the next stable state, where the C_1-C_2 finally broken. The optimized structure shows that the C_1-C_2 bond has extended to 1.96Å, and the two H_1 and H_2 atoms are almost vertically above the C_1 and C_2 atoms respectively. The angle $\angle C_3C_1C_5$ has increased to 118.3° implying that in the next stable state, the bond angle may likely be restored to the typical 120° in an unde-formed SWNT. The TS geometry (see Figure 7.11) is similar to that obtained in chapter 6, with the slight difference due to the diffusion and polarization function introduced in the 6-31G+(d,p) basis set.

- **Stable Intermediate State 3 (SI3)**

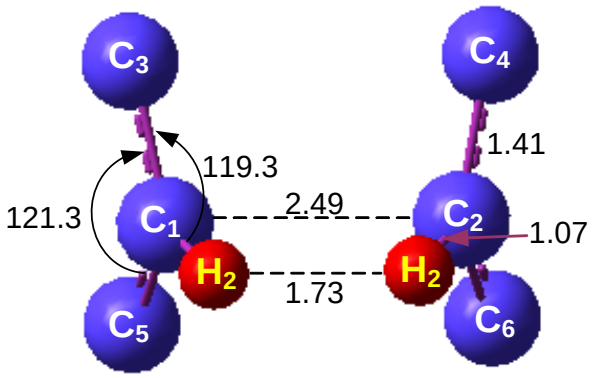

Figure 7.12 Top view of the stable state where the uncoupled hydrogen atoms are chemisorbed onto the exterior of SWNT, which in turn assist in breaking the bond between the two carbon atoms they bonded with.

The most significant feature of the stable intermediate state 3 (SI3) is the breaking of the C_1-C_2 bond, where the distance between these two atoms increases from 1.70Å (in SI2) to 2.49Å (in SI3). This separation is significantly larger than the bond length 1.42Å in pure carbon nanotubes. The optimized bond length of C-H is 1.07Å, and the distance between the two hydrogen atoms reduces from 2.09Å (SI2) to 1.73Å (SI3), see Figure 7.12.

The severing of the C-C bond leads us to carry out our additional investigation with regard to the energy and conformation of the molecule, and the NBO analysis is also performed to examine the effect of the bond polarity and atomic charge on the conformational preferences of the stable intermediate state 3 (SI3). The atomic charges calculated at the B3LYP/6-31G+(d,p) level show that a large negative charge develops on the carbon atom (-0.20e), and considerable positive charge develops on the adjacent hydrogen atom (0.26e). This is because carbon is more electronegative than the hydrogen, and the adjacent H_1 and H_2 atoms will thus lose some charges by overlapping with the C_1 and C_2 carbon atoms. The electro-negativity difference also affects the bond polarization for the C-H bond. The polarization for the SI2 state, see Eqs. (7.17) and (7.18), indicates it is initially polar-

ized toward the carbon atoms. According to present calculations, the natural population analysis showed that the detached C-C is caused by electron delocalization, which is strongly affected by electron population changes due to the interaction between specific orbitals around the carbon atoms. The population of the antibonding $\sigma^*_{C_1C_2}$ orbital strongly prevents atomic charge redistribution in the SI2 state, and the polarization for the interaction of $\sigma_{C_1H_1}$ is thus intensified. The sp^3 orbitals of the C_1 are then expected to overlap more effectively with the sp^2 orbitals of its neighboring atoms, thus forming π bonds with C_3 and C_5. It is the same for C_4 and C_6 around the C_2 atom. Consequently, the conformational stabilization for the sp^3 orbital (in SI2) is replaced by the sp^2 orbital (in SI3), and the C_1-C_2 bond is broken as the new stabilized structure forms (see Figure 7.12). Energy is released in this reaction.

The corresponding bonding and antibonding parameters for the new structures are

$$\sigma_{C_1C_3} = 0.702\left(sp^{1.88}\right)C_1 + 0.712\left(sp^{1.90}\right)C_3 \tag{7.19}$$

$$\sigma^*_{C_1C_3} = 0.712\left(sp^{1.88}\right)C_1 - 0.702\left(sp^{1.90}\right)C_3 \tag{7.20}$$

$$\pi_{C_1C_3} = 0.700\left(2p\right)C_1 + 0.715\left(2p\right)C_3 \tag{7.21}$$

$$\pi^*_{C_1C_3} = 0.715\left(2p\right)C_1 - 0.700\left(2p\right)C_3 \tag{7.22}$$

The above discussion is validated by results obtained Eqs. (7.19) to (7.22), where no C_1-C_2 bond exists, but the sp^2 hybrid orbital is formed for the C_1-C_3 bond and one more π bond exist between them to enhance the orbital overlap.

The bonding and antibonding between C_1-H_1 consists of the sp^2 orbital of C_1 with the electron in the s orbital of H_1

$$\sigma_{C_1H_1} = 0.793\left(sp^{2.27}\right)C_1 + 0.712\left(s\right)H_1 \tag{7.23}$$

$$\sigma^{*}_{C_1H_1} = 0.712\left(sp^{2.27}\right)C_1 - 0.793\left(s\right)H_1 \tag{7.24}$$

In the process, around $0.077eV$ ($1.776kcal/mol$) activation energy is required to overcome the energy barrier for the SI2 state transformation to a more stable state of SI3, which is much lower than that from physisorption state to the SI1 state. The reverse energy barrier is about $0.278eV$ ($6.412kcal/mol$), thus the reaction process gives a net negative energy value of -$0.805eV$ (-$4.636kcal/mol$). This indicates that the energy used in bond breaking is lower than the energy released, and this negative value also implies that this reaction is energetically favorable.

7.3.2 H_2 Interaction with CNT - Flip-In Process

In the first part of this chapter, we have studied the physical and chemical mechanisms for the chemisorption of a hydrogen molecule onto the exterior wall of the CNT. With regard to how hydrogen atoms are inserted into the nanotubes, researchers have suggested the capillarity effect through the open ends of the CNT[10,41,182]. However, due to the high aspect ratio of CNTs (usually up to 10^4~10^6), it is very unlikely that the capillarity effect through the open ends of the nanotube is the exclusive mechanism through which hydrogen is inserted into the CNT. Thus, we need to investigate if it is possible that for hydrogen atoms to enter the CNT through its sidewall. This intriguing possibility triggered us to examine the H-insertion mechanism though the tube wall, and to assess if it may be one of the possible solutions. We searched for a reaction pathway, and the transition is confirmed by Gaussview, to ensure it connects the two adjacent stable intermediate states.

The cleavage of the C_1-C_2 also provides a possibility that more hydrogen molecules could possibly enter the tube though the C-C bond scission sites. However, this raises another question as to whether the C-C will recover after the insertion of the hydrogen molecules, ensuring the molecules remain inside. In this study, the flip-in mechanism is

suggested and explored.

The starting configuration is the stable structure of SI3 shown in Figure 7.12, where the C_1-C_2 bond has been broken. All calculations here are carried out via the Gaussian 03 suite of programs, using the hybrid B3LYP functional[151,155] with 6-31G+(d,p) basis set for the small model system, and the Universal Force Field (UFF) for the real part, within the ONIOM scheme framework. The nature of the stationary points was assessed by frequency analysis.

- **Transition State for Flip-In Geometry (TS4)**

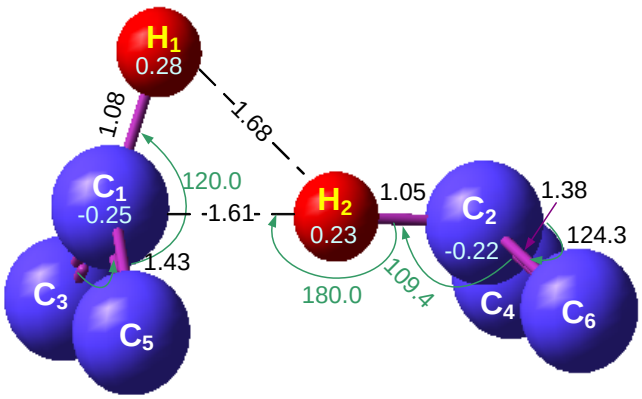

Figure 7.13 Transition state 4 (TS4)

The TS4 was relaxed in the direction of the reaction coordinate to verify that it connects the stable intermediate states SI3 and SI4. The stable complexes related to this reaction pathway is shown in Figure 7.13. The calculated activation barrier from the stable intermediate SI3 is 1.444*eV*. The calculated chemical reaction energy is 0.805*eV*, indicating that the process is an endothermic one. The distance between C_1 and C_2, and the internal angles of the small model system for this transition state complex undergo significant modifications. The distance between C_1 and C_2 increases further to 2.658Å. The $\angle C_1C_2H_2$ angle is changed from 69.16° to 180°, indicating that these three atoms are aligned in TS4.

The C_2-C_4, and C_2-C_6 bonds shorten to 1.38Å. The H-C bonds also shorten in the flip-in process when compared with a typical H-C bond of 1.09Å. The bond length of C_1-H_1 is now 1.08Å, while the C_2-H_2 bond is stronger with bond length of 1.05Å. In addition, the bond lengths for C_1-C_3 and C_1-C_5 have both elongated to 1.426Å.

The electron occupancy in the σ-bond of C_1-C_3 is about 1.976e, and around 1.600 electrons form the π-bond. Very similar results are obtained for the C_2-C_4 bond. The detailed NBO summaries are

$$\sigma_{C_1C_3} = 0.706\left(sp^{1.87}\right)C_1 + 0.708\left(sp^{1.89}\right)C_3 \tag{7.25}$$

$$\sigma^*_{C_1C_3} = 0.708\left(sp^{1.87}\right)C_1 - 0.706\left(sp^{1.89}\right)C_3 \tag{7.26}$$

$$\pi_{C_1C_3} = 0.703\left(p\right)C_1 + 0.711\left(p\right)C_3 \tag{7.27}$$

$$\pi^*_{C_1C_3} = 0.711\left(p\right)C_1 - 0.703\left(p\right)C_3 \tag{7.28}$$

Approximately 1.971 electrons occupy the σ-type orbitals between C_2-C_4, and the NBO summary is

$$\sigma_{C_2C_4} = 0.701\left(sp^{1.88}\right)C_2 + 0.714\left(sp^{1.92}\right)C_4 \tag{7.29}$$

$$\pi_{C_2C_4} = 0.723\left(p\right)C_2 + 0.691\left(p\right)C_4 \tag{7.30}$$

For the σ bond between C_1 and H_1, 1.961 electrons in the σ bond between C_1 and H_1 are bonding, while 0.0299 electrons are antibonding, and the NBO summary is

$$\sigma_{C_1H_1} = 0.801\left(sp^{2.26}\right)C_1 + 0.599\left(s\right)H_1 \tag{7.31}$$

$$\sigma^*_{C_1H_1} = 0.599\left(sp^{2.26}\right)C_1 - 0.801\left(s\right)H_1 \tag{7.32}$$

For the σ bond between C_2 and H_2, 1.924 electrons are bonding, while 0.0516 electrons are antibonding, and the NBO summary is

$$\sigma_{C_2H_2} = 0.787\left(sp^{2.5}\right)C_2 + 0.617\left(s\right)H_2 \tag{7.33}$$

$$\sigma^*_{C_2H_2} = 0.617\left(sp^{2.5}\right)C_2 - 0.787\left(s\right)H_2 \tag{7.34}$$

In the TS4 structure, there is it is a critical point at which the hydrogen atom of H_2 can be flipped inside, and that is when the energy is sufficient for $\angle C_1C_2H_2$ to become negative. When this condition is met, the H_2 atom will flip into the CNT and the trans group is thus formed. From a topological point of view, the transition state 4 (TS4) resembles the SI3 structure, which is in line with a low exothermicity process (isomerization energy = 0.805*eV* (18.558*kcal/mol*)) with a reverse energy barrier height of 0.639*eV* (14.7188*kcal/mol*), representing almost half the forward reaction barrier of 1.444*eV* (33.276*kcal/mol*).

- **Stable Intermediate State 4 (SI4) -Endoexdohydrogenation**

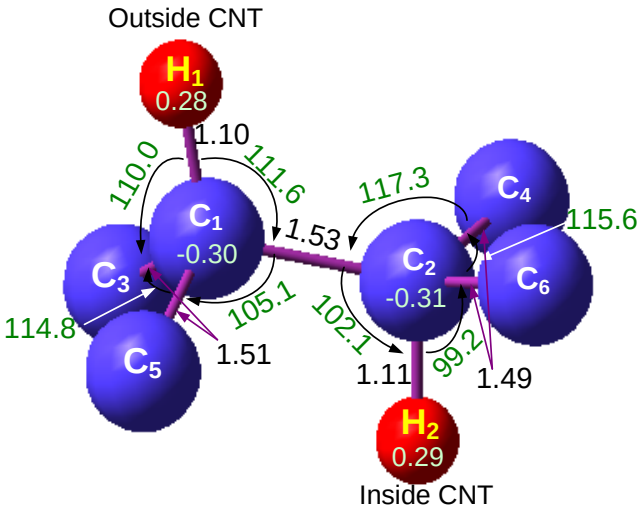

Figure 7.14 Zigzag-type hydrogen formation on the nanotube (SI4).

Figure 7.14 represents the next stable geometry, where the C_1 and C_2 show a change to sp^3-like hybridization and reform the σ bond, while the H atoms are stored in a zigzag-type arrangement. This is termed endoexdohydrogenation where a hydrogenated

CNT has alternating inside/outside bound hydrogen atoms. Lee *et al.*[238] reported that this kind of structure is more stable, by 0.55*eV*, compared to the hydrogenated CNT with all its hydrogen atoms bound outside, when taking the (5,5) CNT as an example. The difference in surface curvature of the interior and the exterior of the nanotube may lead to different configurations. Some internal angles and bond lengths of the molecules involved in the flip-in process undergo significant changes. The bond length of the recovered C_1-C_2 bond is about 1.531Å, and the bond length of C_2-H_2 is 1.11Å, a little longer than the corresponding external C_1-H_1 of 1.10Å.

The conformational change from the SI3 to the SI4 requires the reorientation as shown in Figure 7.14, which is dependent on the coupling of the carbon atoms C_1 and C_2. To better understand this structure and predict its stability, we carry out the orbital overlap population analysis to investigate the bonding and antibonding for those critical atoms involved in the reaction, and the results are shown in Figure 7.15. For the SI4, we obtain E_{HOMO}=-5.09*eV*, E_{LUMO} = -2.22*eV*, and thus E_{gap} =2.87*eV*. The magnitude depends on the coupling overlap and the size of the polarity coefficients in the molecular orbital under consideration. According to the results in Figure 7.15, the inside of the nanotube exhibits stronger bonding between C-H than that which is outside, where C_2-H_2 shows bonding at both HOMO and LUMO levels, but C_1-H_1 displays weak antibonding at the HOMO level, and nonbonding at the LUMO level. The very strong antibonding at the HOMO level for the neighboring C_1 and C_2 atoms suggests that the atomic orbital between them are combined out of phase thus forming very strong antibonding interactions, and the NBO summary is provided in Eq. (7.35).

The E_{chemical} value is found to be positive according to the definition given in Eq. (7.43), indicating an endothermic reaction, which further indicates that the "exterior" (SI3) and "interior" (SI4) states are separated by a high-energy barrier. This energy barrier is calculated to be 0.805*eV* (18.558*kcal/mol*). Thus, hydrogen penetration of the sidewall of the

nanotube is not a spontaneous process. The associated natural orbital analysis is carried out, where and it shows about 1.957 electrons in the σ orbital exhibiting bonding while 0.028 electrons are antibonding.

$$\sigma_{C_1C_2} = 0.704\left(sp^{3.11}\right)C_1 + 0.710\left(sp^{2.64}\right)C_2 \tag{7.35}$$

For the C_1-C_3 bond, 1.967 electrons are bonding while 0.029 electrons are anti-bonding, and the NBO summary is

$$\sigma_{C_1C_3} = 0.713\left(sp^{2.79}\right)C_1 + 0.701\left(sp^{2.24}\right)C_3 \tag{7.36}$$

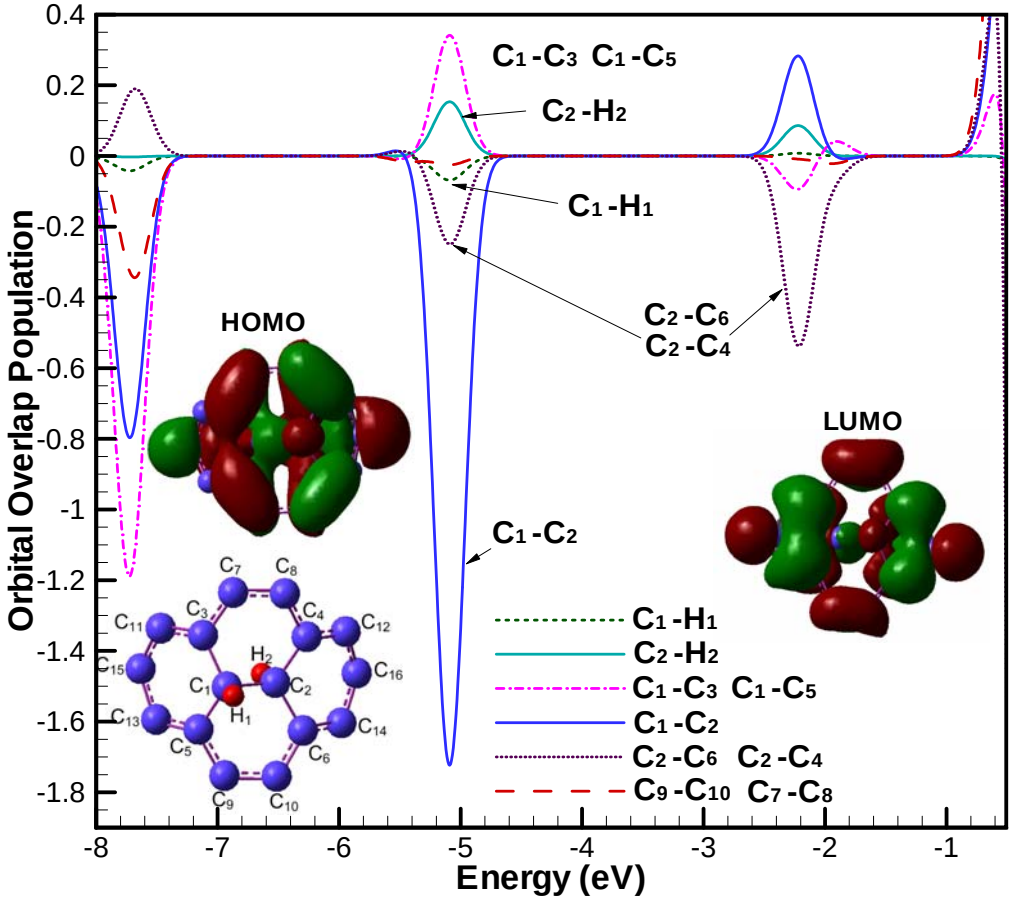

Figure 7.15 Overlap population analysis for the stable intermediate state 4 (SI4).

Apparently present simulation results are not consistent with those reported by Lee *et al.*[129,238], who suggested that the zigzag-type configuration for hydrogen being chemi-sorbed on the wall is much more stable than that which are exclusively on the exterior wall.

Our simulation indicates a stronger antibonding for the C_1-C_2 bond, and an energy level of about $0.805eV$ higher than the case where the hydrogen are bound exclusively outside the CNT.

- **Transition State 5 (TS5) and Stable Intermediate State 5 (SI5) - Endohydrogenation**

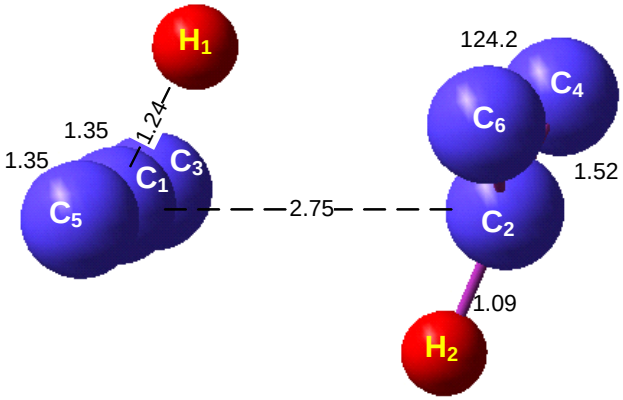

(a)

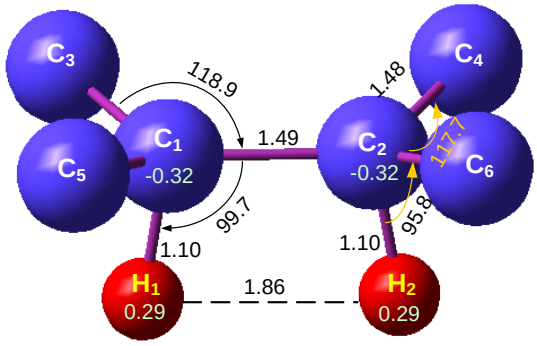

(b)

Figure 7.16 Transition state 5 (TS5) and stable intermediate state 5 (SI5)

Finally, we consider the state where both of the hydrogen atoms are chemisorbed inside the tube as shows in Figure 7.16, having a final cis-like structure. It is important to note at the onset of this discussion that the SI5 state is not energetically favorable due to the extremely high energy barrier from SI4 to SI5. It is observed from the optimized ge-

ometry that the C_1-C_2 bond recovers when the two hydrogen atoms are chemisorbed inside the nanotube. Nevertheless the structure is quite severely deformed near the adsorbed sites. The C_1-C_2 bond length is now 1.49Å, longer than the 1.42Å found in the pure CNTs. Most of the electrons tend to distribute onto the carbon atoms C_1 and C_2, which show slightly stronger negative charges of -0.32eV, while the hydrogen atoms have positive charges of 0.29eV. The cis-like configuration is a minimum on the potential energy surface. However, the theoretical computations reveal that the energy of this cis-form SI5 state is at a much higher energy level compared with trans-like structure of SI4 state by 2.572eV (59.266$kcal/mol$).

The NBO analysis is then carried out, where it is found that for the C_1-C_2 bond, 1.974 electrons exhibit bonding while 0.032 electrons are antibonding. The summary is obtained as

$$\sigma_{C_1-C_2} = 0.707\left(sp^{2.47}\right)C_1 + 0.707\left(sp^{2.47}\right)C_2 \tag{7.37}$$

$$\sigma^*_{C_1-C_2} = 0.696\left(sp^{2.67}\right)C_1 - 0.719\left(sp^{2.53}\right)C_2 \tag{7.38}$$

An interesting aspect of the bond between the carbon and hydrogen atoms is that multiple bonding exists between them, as shown in Eqs. (7.39) and (7.40). For the C_1-H_1 bond, 1.923 electrons are bonding while 0.0279 electrons populate the antibonding orbital. The summary is obtained as

$$\sigma_{C_1H_1} = 0.801\left(sp^{4.96}\right)C_1 + 0.599\left(s\right)H_1 \tag{7.39}$$

$$\sigma^*_{C_1H_1} = 0.599\left(sp^{4.96}\right)C_1 - 0.801\left(s\right)H_1 \tag{7.40}$$

We now examine the possibility of the interaction between the H_1 atom and three other neighboring carbon atoms. Due to the pyramidalization, three other carbon atoms will be close to the H_1 atom, where the C_1-C_2, C_1-C_3 and C_1-C_5 bond length are formed to

be 1.49Å, 1.48Å and 1.48Å respectively, which is smaller than the typical bond length of 1.541 in diamond, thus leading to multiple electrons bonding to the H_1 atom[261].

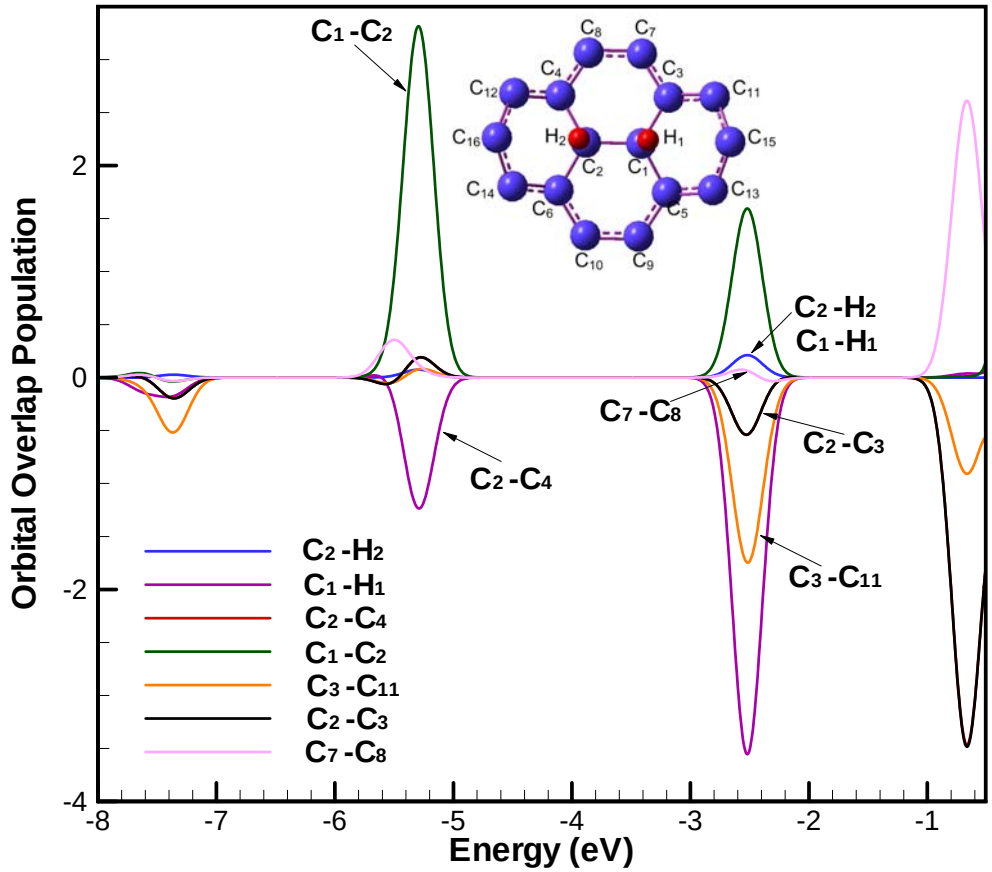

Figure 7.17 Overlap population analysis for the stable intermediate state 5 (SI5).

The overlap population analysis in Figure 7.17 further indicates that the bonds of C_2-C_4, C_2-C_6, C_1-C_3 and C_1-C_5 shows antibonding at the HOMO energy level, while the bond of C_1-C_2 shows strong bonding. This is corroborated by the NBO analysis, where results show that the bonding between C_1-C_3 has weaker bonding than that between C_1-C_2, with stronger antibonding of 0.0322 electrons, and only about 1.9642 electrons in the bonding orbital.

$$\sigma_{C_1C_3} = 0.719\left(sp^{2.67}\right)C_1 + 0.696\left(sp^{2.35}\right)C_3 \tag{7.41}$$

$$\sigma_{C_1C_3} = 0.696\left(sp^{2.67}\right)C_1 - 0.719\left(sp^{2.35}\right)C_3 \tag{7.42}$$

Our results reveal that for the flip-in mechanism of the H atoms, which is initially chemisorbed outside the tube in SI4, the activation energy barrier is extremely high, where the C_1-C_2 bond will break again by adsorbing of $9.664eV$ ($222.711kcal/mol$) from the environment. Overall, the internal part of the CNT is less reactive than the external surface, and this is consistent with the conclusions reported by Haddon *et al.*[262] and Seongjun *et al.*[261]. The latter used H and P atoms to probe the chemical reactivity at the exterior and interior surfaces of C_{36} and C_{60}.

The chemisorption energy and the physisorption energy calculated in this chapter is of a relative form

$$E_{\text{chemical}} = E_{\text{CNT-H}} - E_{\text{CNT}} - E_{\text{H}} \tag{7.43}$$

where $E_{\text{CNT-H}}$, E_{CNT}, and E_{H} are the total energy of the fully optimized CNT-H system, pure carbon nanotube energy and the atomic hydrogen energy, respectively. According to this definition, a stable system is expected to have a negative energy. Similarly, the physisorption energy is calculated according to

$$E_{\text{physical}} = E_{\text{CNT-H}_2} - E_{\text{CNT}} - E_{\text{H}_2} \tag{7.44}$$

where a negative E_{physical} corresponds to energetically favorable adsorption. The definitions of $E_{\text{CNT-H}_2}$ and E_{CNT}, E_{H_2} are similar to those described above for the chemical adsorption energies.

Larger tube diameter such as those of (10,10) and (11,11) CNTs have also been studied in our simulation so as to have a more complete picture of the problem, and we did not find the chemical reactivity in these cases. This may due to the different curvature of these tubes, where larger curvatures significantly enhance the chemisorption reaction barrier. The smaller radii nanotubes are under greater strain, especially those C-C bonds which are perpendicular to the tube axis[242,243], and these are more susceptible to detach-

ment under high hydrogen density circumstances.

7.3.3 Conclusion

In this chapter, we carried out a systematic study, based on the multiscale ONIOM2 scheme, to analyze the flip-in mechanism of hydrogen atoms through (5,5) carbon nanotube surfaces. Several key stable intermediate states of the hydrogen adsorption process are identified. We find that near the surface, the H_2 molecule is adsorbed through weak van der Waal's interactions through a small polarization of its electronic charge. For the hydrogen to be chemically bonded onto the nanotube, it has to overcome the forward activation barrier of $4.00eV$ during the process. The surface structure of the (5,5) armchair nanotube is able to dissociate the hydrogen molecule and allow the hydrogen atoms to be chemisorbed onto the nanotube, concurrently weakening the C-C bonds in the vicinity of the reaction. From the physisorption to the first stable intermediate when one hydrogen atom is chemisorbed, the reaction is not energetically favorable, requiring the adsorption of $3.41eV$. The second hydrogen atom is much more easily chemisorbed, and will release $2.57eV$. The resulting state of the sp^3 bonds leads to very strong antibonding and breaks the C-C bond and thus unzipping the tube. We also conclude that hydrogen atoms can be flipped inside the tube forming a zig-zag type configurations, and this flip-in process requires the absorption $0.80eV$ for the reaction to take place. The stable state at which both hydrogen atoms are flipped inside is extremely unfavorable, requiring the high adsorption of $9.664eV$ ($222.711kcal/mol$) from environment to break the C-C bond a second time.

CHAPTER 8

THERMODYNAMIC PROPERTIES OF THE REACTIONS

The ONIOM scheme described in chapter 4 has been used in chapters 6 and 7 to simultaneously investigate the physisorption and chemisorption characteristics of hydrogen on and into (5,5) single wall carbon nanotube (SWNT) walls. In the process of our investigations, exdohydrogenated, exdoendohydrogenated and endohydorgenated CNT structures have been encountered. Investigations into the transition states and the reaction pathways for the entire chemisorption process have also been carried out. In this chapter, through determining the changes of Gibbs free energy with temperature, the thermodynamic properties of the reaction process is studied.

8.1 Introduction

In chapters 5 6 and 7, we have discussed the physisorption within the carbon nanotube, as well as the full chemical reaction of initially exterior hydrogen molecules being chemisorbed into the nanotube at absolute temperature. The analyses were based on first principle electronic structure calculations, which provide an accurate description of the interaction of hydrogen with carbon nanotubes involving bond formation and bond breaking. In this chapter, we extend the investigation further by studying the chemical reaction as a function of temperature. The interaction of atomic hydrogen atoms with single-wall carbon

nanotubes (SWNTs) is studied using the ONIOM scheme introduced in chapter 4, where we will explore the effects of temperature on the bond formation. The ONIOM scheme is used to obtain the frequencies while molecular thermodynamics theory[263], utilizing the Boltzmann factor and partition function, is employed to establish the temperature dependence of the Gibbs free energy of the reaction.

8.2 Model and Methodology

The carbon nanotube chosen for this study is again the narrow (5,5) carbon nanotube, with tube length of 22.6Å, and consisting of 180 carbon atoms. In order to study the chemical properties of the side wall during the reaction process, the caps are removed since the caps have a higher binding energy than the side wall. The presence of the cap can also indirectly affect the hydrogen atoms at the side wall near the cap-tube interface[137].

8.2.1 Boltzmann Factor and the Partition Function

In chapter 3, we have shown that the energy states of atoms and molecules can be solved according to the Schrödinger equation. A practical question that arises now is how the molecular vibrations vary over these energy states at a given temperature. According to the Molecular Thermodynamics theory, Wilson *et al.*[263], the central themes to solve this problem are the Boltzmann factor and the partition function.

Consider a system which can be described by specifying the number of particles, N, the volume V, and the forces between the particles; we can consider its Hamiltonian operator and its associated wavefunctions using the information in chapter 3. The Schrödinger equation for this N-body system satisfies Eq. (3.6), and can be written as

$$\hat{H}_N \psi_j = E_j \psi_j \tag{8.1}$$

where the energy at state j, E_j, depends upon both N and V, which is emphasized by writing $E_j(N,V)$.

Now by introducing the Boltzmann factor P_j, which expresses the "probability" of a state of energy E_j relative to the probability of a state of zero energy, the temperature T is brought into the quantum level formulation. For a system with energy states E_1, E_2, E_n, the probability of P_j that the system will be in the state E_j depends exponentially on the energy of that state

$$P_j = \frac{\exp(-\beta E_j)}{\sum_i \exp(-\beta E_i)} \tag{8.2}$$

where P_j is the probability that the randomly chosen system will be in state j with energy E_j. Also, β is a function of temperature T

$$\beta = (k_B T)^{-1} \tag{8.3}$$

with k_B being the Boltzmann constant and T the temperature in Kelvin.

Eq. (8.2) is a well known expression central to physical chemistry. Letting the denominator of the P_j expression be denoted by Q, and if we specifically include the dependence of E_j on N and V, then we have the partition function of this system

$$\begin{aligned} Q(N,V,\beta) &= \sum_{j=0}^{\infty} \exp\left[-\beta E_j(N,V)\right] \\ &= \frac{1}{1-\exp\left[-\beta E_j(N,V)\right]} \end{aligned} \tag{8.4}$$

Using Eq. (8.4), we can calculate the average energy of a system in an ensemble of systems by

$$\langle E \rangle = \sum_j P_j E_j(N,V) = \sum_j \frac{E_j(N,V)\exp\left[-\beta E_j(N,V)\right]}{Q(N,V,\beta)} \tag{8.5}$$

Note that $\langle E \rangle$ is a function of N, V and β.

The partial differential of $\ln Q(N,V,\beta)$ with respect to β is

$$\begin{aligned}
\left.\frac{\partial \ln Q(N,V,\beta)}{\partial \beta}\right|_{N,V=\text{constant}} &= \frac{1}{Q(N,V,\beta)} \cdot \left.\frac{\partial}{\partial \beta}\exp\left[-\beta E_j(N,V)\right]\right|_{N,V=\text{constant}} \\
&= \frac{1}{Q(N,V,\beta)} \cdot \left.\sum_j \left[-\beta E_j(N,V)\right] \cdot \exp\left[-\beta E_j(N,V)\right]\right|_{N,V=\text{constant}} \\
&= -\left.\sum_j \frac{E_j(N,V)\exp\left[-\beta E_j(N,V)\right]}{Q(N,V,\beta)}\right|_{N,V=\text{constant}}
\end{aligned} \tag{8.6}$$

Comparing Eq. (8.5) with Eq. (8.6), the average energy $\langle E \rangle$ is

$$\langle E \rangle = \left.\frac{\partial \ln Q}{\partial \beta}\right|_{N,V=\text{constant}} \tag{8.7}$$

and since $\beta = (k_B T)^{-1}$, then

$$\langle E \rangle = k_B T^2 \left.\frac{\partial \ln Q}{\partial T}\right|_{N,V=\text{constant}} \tag{8.8}$$

This is the general result that is valid for arbitrary systems. To apply it, we need to have the set of eigenvalues $\{E_j(N,V)\}$ for the N-body Schrödinger equation. From chapter 3, we have noted that the total energy of the system can be treated as a sum of individual energies as shown in Eq. (3.20). This procedure leads to a significant simplification of the partition function by considering that the system consists of independent, distinguishable particles. We shall denote the individual particle energy by $\{\varepsilon_i^a\}$, where the super-

script denotes the particle and the subscript denotes the i^{th} energy state of the particle. Thus the total energy of the system $E_j(N,V)$ can be written as the sum of the N individual particle energies

$$E_j(N,V) = \sum_a^N \varepsilon_i^a \tag{8.9}$$

and the partition function of Eq. (8.4) becomes

$$\begin{aligned} Q(N,V,T) &= \sum_{j=0}^{\infty} \exp\left[-\beta \sum_a^N \varepsilon_i^a\right] \\ &= q_a(V,T)\, q_b(V,T)\, q_c(V,T)\ldots \end{aligned} \tag{8.10}$$

$q(V,T)$ is the molecular partition function, and as an example $q_a(V,T)$ is given by

$$q_a(V,T) = \sum_i \exp\left(-\beta \varepsilon_i^a\right) = \sum_i \exp\left(-\varepsilon_i^a / k_B T\right) \tag{8.11}$$

where $\{\varepsilon_i\}$ is a set of molecular energies.

Using Eq. (8.11) the average energy in Eq. (8.8) is converted into

$$\begin{aligned} \langle E \rangle &= k_B T^2 \left.\frac{\partial \ln Q}{\partial T}\right|_{N,V=\text{constant}} \\ &= N k_B T^2 \left.\frac{\partial \ln q}{\partial T}\right|_{N,V=\text{constant}} \\ &= N \sum_j \varepsilon_j \frac{\exp\left(-\varepsilon_j / k_B T\right)}{q(V,T)} = N \langle \varepsilon \rangle \end{aligned} \tag{8.12}$$

The energy of a molecule can be written as the sum of

$$\varepsilon = \varepsilon_{\text{trans}} + \varepsilon_{\text{rot}} + \varepsilon_{\text{vib}} + \varepsilon_{\text{elec}} \tag{8.13}$$

indicating that the molecular energy is a result of translational, rotational, vibrational, and electronic motion respectively. Correspondingly, from Eq. (8.11) the molecular partition

energy can be written as

$$q(V,T) = q_{\text{trans}} q_{\text{rot}} q_{\text{vib}} q_{\text{elec}} \tag{8.14}$$

It can now be seen that all important macroscopic quantities associated with a system can be expressed in terms of its partition function $q(V,T)$. Therefore we are able to investigate certain thermodynamic parameters through the partition function.

In the following section, we will provide the equations used to calculate the contributions to entropy *H*, and energy *E*, resulting from translational, electronic, rotational and vibrational motions. The starting point in each case is the partition $q(V,T)$ for the corresponding component of the total partition function.

8.2.2 Thermodynamic Quantities

The partition function from any component can be used to determine the entropy contribution *S* from that component, using the relation:

$$S = R + R\ln\left[q(V,T)\right] + RT \cdot \left.\frac{\partial \ln q}{\partial T}\right|_{N,V=\text{constant}} \tag{8.15}$$

where *R* denotes the molar gas constant (8.314510 $J \cdot K^{-1} \cdot mol^{-1}$). When the first term is moved into the logarithm (as e), we obtain

$$\begin{aligned} S &= R\ln\left[q(V,T)e\right] + RT \cdot \left.\frac{\partial \ln q}{\partial T}\right|_{N,V=\text{constant}} \\ &= R\ln\left(q_{\text{trans}} q_{\text{rot}} q_{\text{vib}} q_{\text{elec}} e\right) + T \cdot \left.\frac{\partial \ln q}{\partial T}\right|_{N,V=\text{constant}} \end{aligned} \tag{8.16}$$

The internal thermal energy *E* can also be obtained from the partition function:

$$E = Nk_B T^2 \cdot \left.\frac{\partial \ln q}{\partial T}\right|_{N,V=\text{constant}} \tag{8.17}$$

These two equations will be used to derive the final expressions used by Gaussian to calculate the different components of the thermodynamic quantities.

8.2.3 Contributions from Vibrational Motion

The vibrational contribution to the internal energy arises from population of the vibrational energy levels. The vibrational partition coefficient, q_{vib}, is given by

$$q_{\text{vib}} = \prod_i \frac{1}{1-\exp(-h\nu_i/k_B T)} \tag{8.18}$$

where h is Planck's constant, and ν_i the i^{th} normal vibration frequency. For a molecule at temperature T, E_{vib} can be calculated according to

$$E_{\text{vib}} = N_a \sum_i \left\{ \frac{h\nu_i}{2} + \frac{h\nu_i \exp(-h\nu_i/k_B T)}{1-\exp(-h\nu_i/k_B T)} \right\} \tag{8.19}$$

Note that the first term in the above equation is the zero-point vibration energy (zpe), E_{zpe}. Hence, the second term is the additional vibrational contribution due to the temperature increase from 0 to T. Thus

$$\begin{aligned} E_{\text{vib}} &= E_{zpe} + E_{vib}(T) \\ E_{\text{zpe}} &= N_a \sum_i \frac{h\nu_i}{2} \\ E_{\text{vib}}(T) &= N_a \sum_i \frac{h\nu_i \exp(-h\nu_i/k_B T)}{1-\exp(-h\nu_i/k_B T)} \end{aligned} \tag{8.20}$$

where N_a is the Avogadro's number, calculated from $N_a = R/k_B$. The vibrational contribution to the entropy S from the component satisfies

$$S_{\text{vib}} = R\sum_i \left\{ \frac{(h\nu_i/k_BT)\exp(-h\nu_i/k_BT)}{1-\exp(-h\nu_i/k_BT)} - \ln\left[1-\exp(-h\nu_i/k_BT)\right] \right\} \tag{8.21}$$

8.2.4 Contributions from Rotational Motion

- **Non-linear molecule**

The rotational partition coefficient q_{rot} is given by:

$$\begin{aligned} q_{\text{rot}} &= \left(\frac{\sqrt{\pi}}{\sigma}\right)\left(\frac{8\pi^2 k_B T}{h^2}\right)^{3/2}\sqrt{I_A I_B I_C} \\ &= \left(\frac{\sqrt{\pi}}{\sigma}\right)\left[\left(\frac{8\pi^2 cI_A}{h^2}\right)\left(\frac{8\pi^2 cI_B}{h^2}\right)\left(\frac{8\pi^2 cI_C}{h^2}\right)\right]^{1/2}\left(\frac{k_BT}{hc}\right)^{3/2} \end{aligned} \tag{8.22}$$

where I_A, I_B and I_C are the moment of inertia of the three principals obtained from $\sum_{j=1}^{n} m_j d_j^2$, where d_j is the distance of the j^{th} nucleus from the center of mass of the molecule.

σ is the Stefan-Boltzmann constant, which can be calculated according to $\sigma = \dfrac{2\pi^5 k_B^4}{15h^3c^2}$, where c is the speed of light, k_B the Boltzmann's constant, and h the Planck's constant.

Expressions for E_{rot} and S_{rot} for a non-linear molecule are defined as

$$E_{\text{rot}} = (3/2)RT \tag{8.23}$$

$$\begin{aligned} S_{\text{rot}} &= \frac{R}{2}\ln\left[\left(\frac{\sqrt{\pi}}{\sigma}\right)\left(\frac{8\pi^2 cI_A}{h^2}\right)\left(\frac{8\pi^2 cI_B}{h^2}\right)\left(\frac{8\pi^2 cI_C}{h^2}\right)\left(\frac{k_BT}{hc}\right)^3\right] + (3/2)R \\ &= \frac{R}{2}\ln\left(I_A I_B I_C\right) + \frac{2}{3}R\ln T - R\ln\sigma - 5.3863921 \end{aligned} \tag{8.24}$$

- **Linear molecule**

Expressions for q_{rot}, E_{rot} and S_{rot} for a linear molecule are defined as

$$q_{\text{rot}} = \frac{8\pi^2 I k_B T}{\sigma h^2} \tag{8.25}$$

where I is the moment of inertia.

$$E_{\text{rot}} = RT \tag{8.26}$$

$$S_{\text{rot}} = R\ln\left[\frac{8\pi^2 I k_B T}{\sigma h^2}\right] + R = R\ln I + R\ln T - R\ln\sigma - 4.349203 \tag{8.27}$$

8.2.5 Contributions from Translation

Expressions for q_{trans}, E_{trans}, S_{trans} and C_{trans} are defined as

$$q_{\text{trans}} = \left(\frac{\sqrt{2\pi m k_B T/N_a}}{h}\right)^3 \tag{8.28}$$

where m is the molecular weight.

$$E_{\text{trans}} = \frac{3}{2}RT \tag{8.29}$$

$$\begin{aligned} S_{\text{trans}} &= R\left[\frac{5}{2} + \frac{3}{2}\ln\left(\frac{2\pi k_B}{h^2}\right) + \ln k_B + \frac{3}{2}\ln\left(\frac{M}{N_a}\right) + \frac{5}{2}\ln T - \ln p\right] \\ &= \frac{5}{2}R\ln T + \frac{3}{2}\ln M - R\ln p - 2.31482 \end{aligned} \tag{8.30}$$

where p is the pressure and M the magnetic moment.

8.2.6 Contributions from Electronic Motion

The contribution from the electronic motion is somewhat special due to the assumption in molecular thermodynamics that the electronic excited state energies are much greater than

$k_B T$, and it is thus assumed to be inaccessible at any temperature, which means that they do not contribute to the thermodynamic properties. This assumption simplifies the electronic partition function to be the spin multiplicity of the molecule of ω_0

$$q_{\text{elec}} = \omega_0 \tag{8.31}$$

Therefore, the entropy due to electronic motion is

$$\begin{aligned} S_{\text{elec}} &= R\left(\ln q_e + T \left.\frac{\partial \ln q_e}{\partial T}\right|_V \right) \\ &= R\left(\ln q_e + 0\right) \end{aligned} \tag{8.32}$$

Since there are no temperature dependent terms in the partition function, the internal energy due to electronic motion are both zero.

8.2.7 Enthalpy and Gibbs Free Energy

The total internal energy U at temperature T is

$$U = E_{el} + \left(E_{\text{vib}} + E_{\text{rot}} + E_{\text{trans}}\right) \tag{8.33}$$

or

$$U = E_{el} + \left[\left(E_{\text{zpe}} + E_{\text{vib}}\left(T\right)\right) + E_{\text{rot}} + E_{\text{trans}}\right] \tag{8.34}$$

where E_{el} the energy calculated from Eq. (3.6).

Enthalpy H for one mole of gas is defined as

$$H = U + pV \tag{8.35}$$

Assumption of an ideal gas (i.e., $pV = RT$) leads to

$$H = U + pV = U + RT \tag{8.36}$$

Thus, the Gibbs free energy G can be obtained through

$$G = H - TS \tag{8.37}$$

8.3 Results and Discussions

In the preceding sub-sections, we derive the enthalpies and free energies of molecular systems. To enhance our understanding of the feasibility and rates of the chemisorption process, we need to consider two thermodynamic properties of the reaction. These are the free-energy difference (ΔG) between the products (the final state) and reactants (the initial state), and the energy required to initiate the conversion of reactants to the transition states ($\Delta G^{\ddagger}$). The former determines whether the reaction will be spontaneous, whereas the latter determines the rate of the reaction. The latter is commonly known as the Gibbs free energy of activation.

Based on the earlier results obtained in the present work, we noted that it is easier for the hydrogen atom to react with the tube than the H_2 molecules. The adsorption of the former one is energetically favorable, suggesting that the chemisorption process is spontaneous, but the latter is an endothermic reaction due to the required energy for breaking of the H-H bond. Thus, in this section, we will use this atomic adsorption as an example to study the thermodynamic properties of the chemisorption process. According to the above definition for entropy, enthalpy and Gibbs free energy described earlier in section 8.2, we calculated them from 20K to 1000K for the reaction, from the reactants to the final products. It can be seen that as the temperature is increased, both the enthalpy and entropy decrease, while the free energy change increases. The maximum value of the free energy is still negative, about -33*kcal/mol* at 1000K. This affirms that hydrogen being chemisorbed on the side wall of the nanotube is a spontaneous process from 20K to 1000K. The negative

Gibbs free energy also indicates that the system releases energy to its surroundings as the chemisorption process occurs, which is an exergonic process. During the chemical process, the reactants change into the products, release the stored energy and gradually the system reaches a stable condition of equilibrium. The magnitude of the free energy change is a measure of the "driving force" behind the reaction. The larger this magnitude is, which in this case occurs at lower temperatures, indicates that the reaction process is more likely to take place. The reaction with ΔG = -95*kcal/mol* at 20*K* has a better chance of happening than that of ΔG = -33*kcal/mol* at 1000*K*, see Figure 8.1.

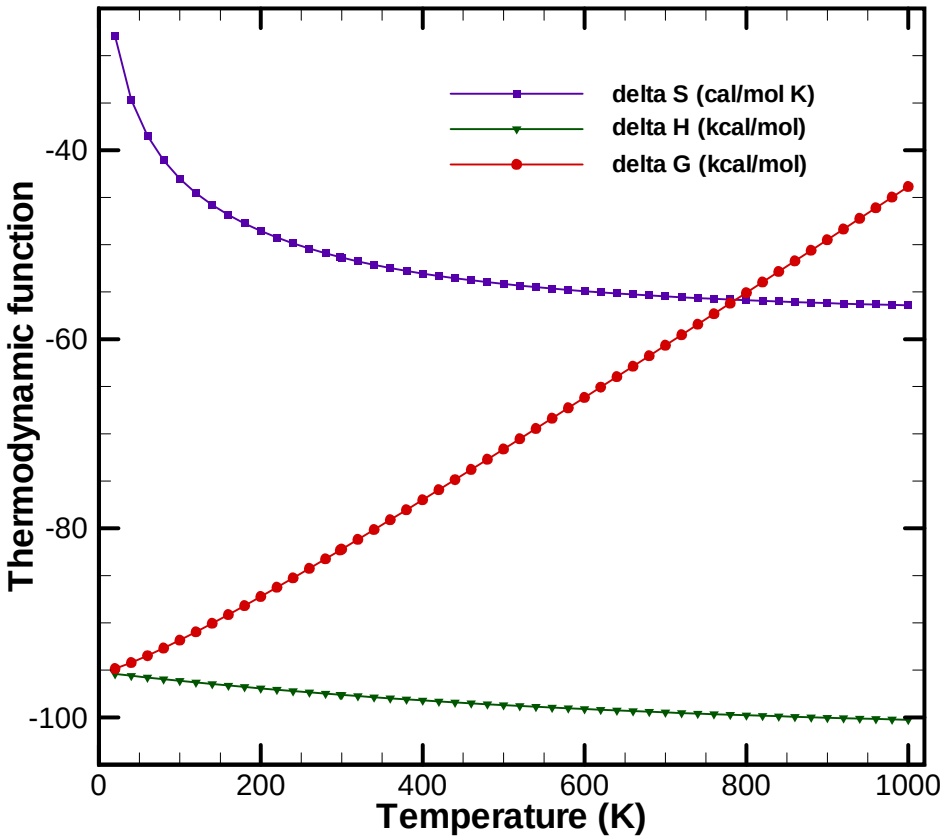

Figure 8.1 Variation of thermodynamic properties with temperatures for the reaction of two hydrogen atoms chemisorbs on the side wall of (5,5) SWNT, from reactants to products.

The next question that arises is, whether we can explain the reaction rate in terms

of thermodynamic properties? The free-energy difference between reactants and products accounts for the equilibrium of the reaction, and a negative ΔG only provides information that a reaction can occur spontaneously, but it does not reveal whether it will proceed at a perceptible rate. In another words, the reaction speed is largely unrelated to the ΔG of the reaction. To determine how quickly the equilibrium is attained, the Gibbs free energy of activation ($\Delta G^{\ddagger}$) which determines the rate of the reaction has to be considered here. The free energy of activation $\Delta G^{\ddagger}$ is sometimes simply called the activation energy, and is the difference in free energy between the transition-state intermediate (TS) and the reactant (R). As $\Delta G^{\ddagger}$ generally has a very large positive value, only a small fraction of the reactant molecules will at any one time acquired this free energy, and the overall rate of the reaction will be limited by the rate of formation of the TS. Thus, we have to consider not the end points of the reaction but the chemical pathway between the end points.

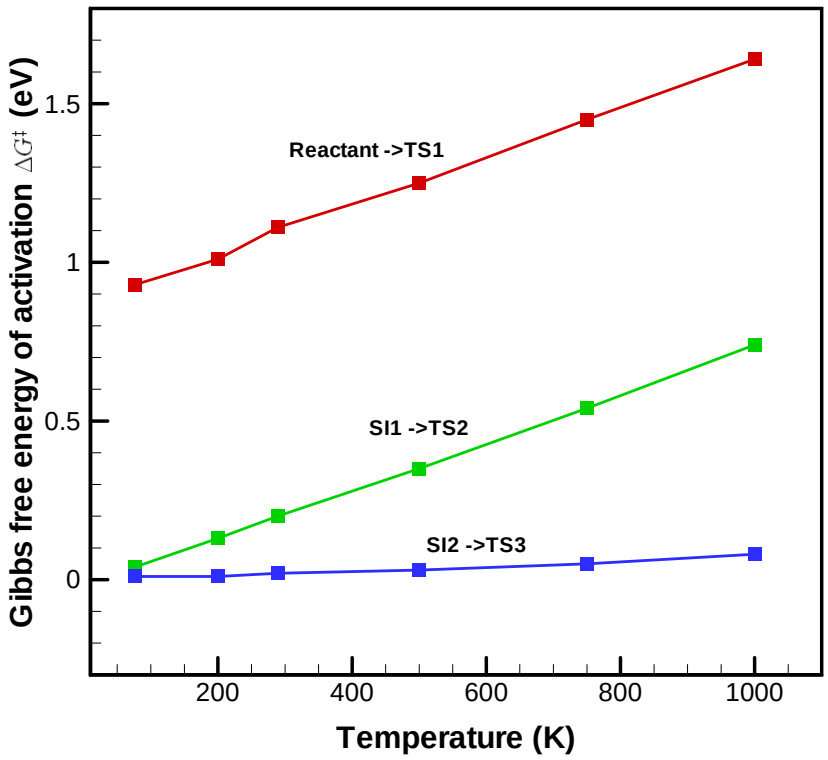

Figure 8.2 Gibbs free energies of activation, calculated for the reactants, products, the stable intermediates and the transition states.

We plotted Figure 8.2 and Figure 8.3 to better understand the variation of $\Delta G^{\ddagger}$ at different typical temperatures. It is revealed that the reaction is more accelerated at lower temperatures due to the resulting lower activation energy between the reactants and its transition state intermediate. Thus, even though a pristine CNT can interact with hydrogen atoms at ambient temperatures, since the reaction for the chemisorption occurs spontaneously, if want to improve the reaction rate, the activation energy should be small. This can be clearly seen in Figure 8.3. At 77*K*, the activation energies from the reactants and SI states to the respective subsequent TS states are lower than at other higher temperatures.

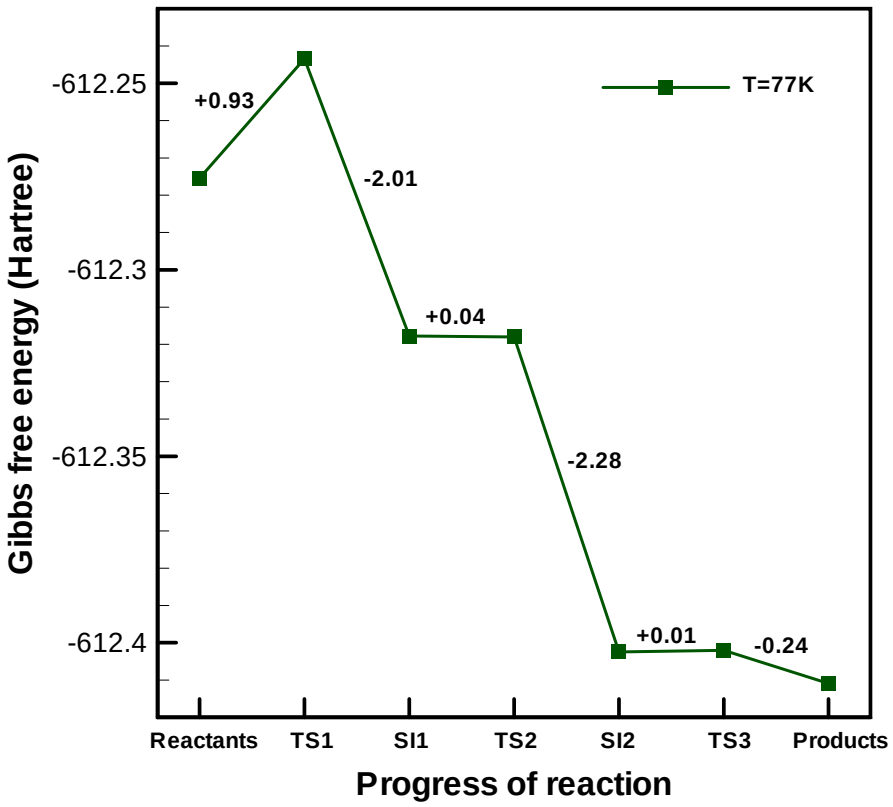

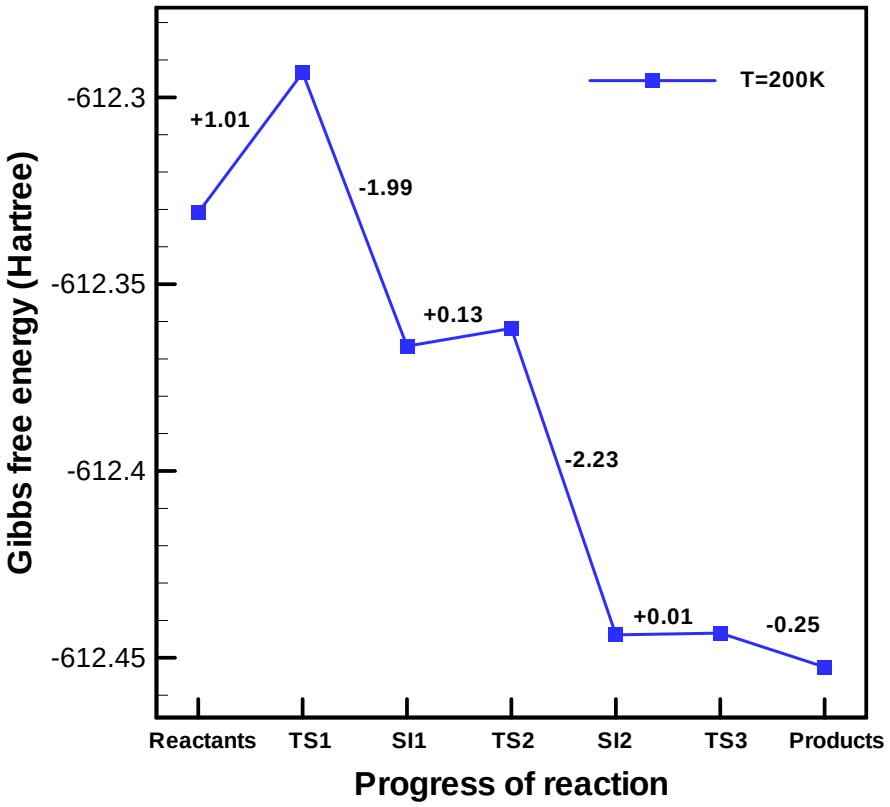

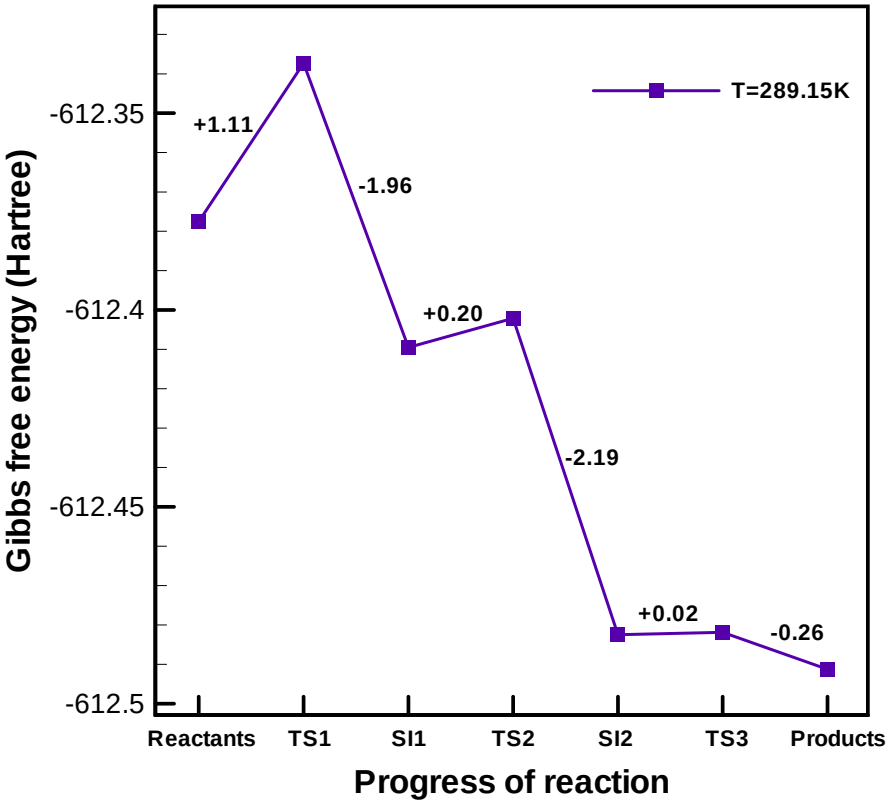

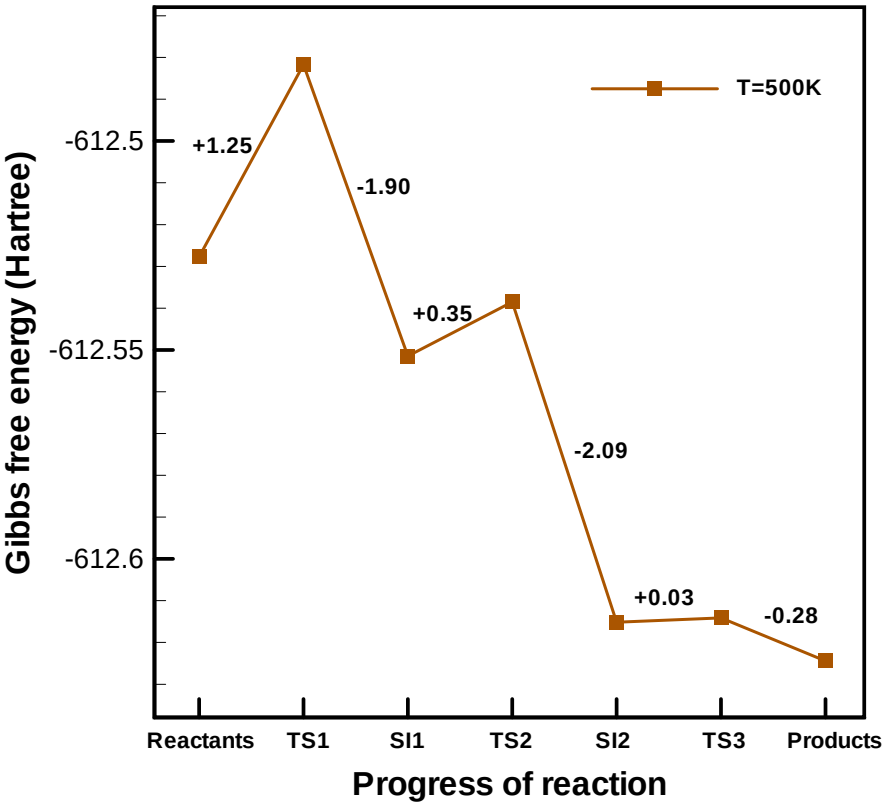

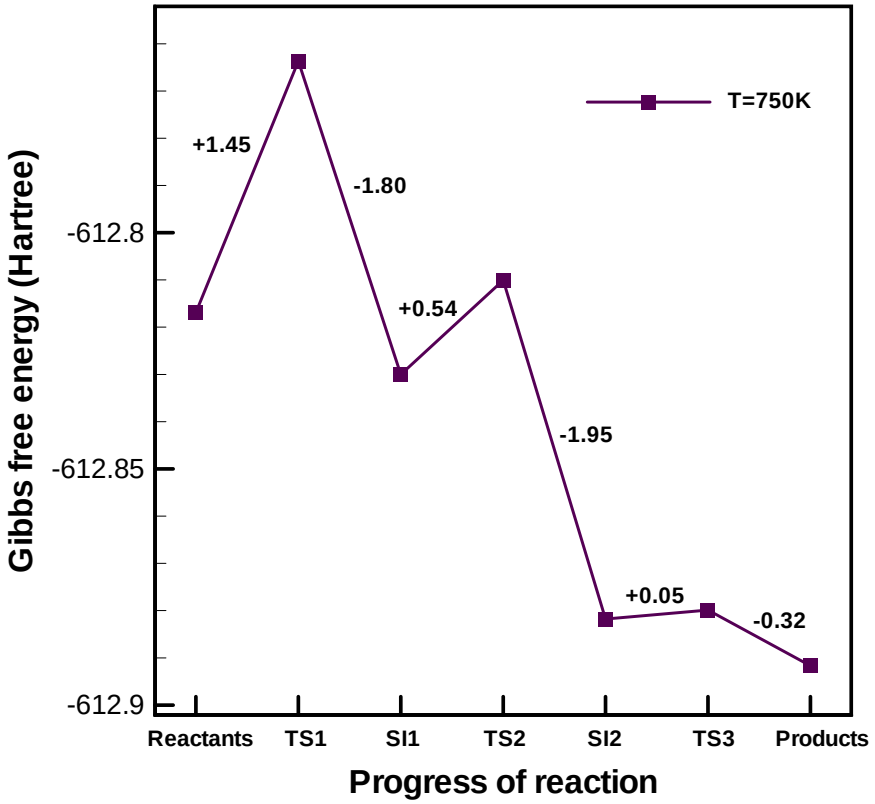

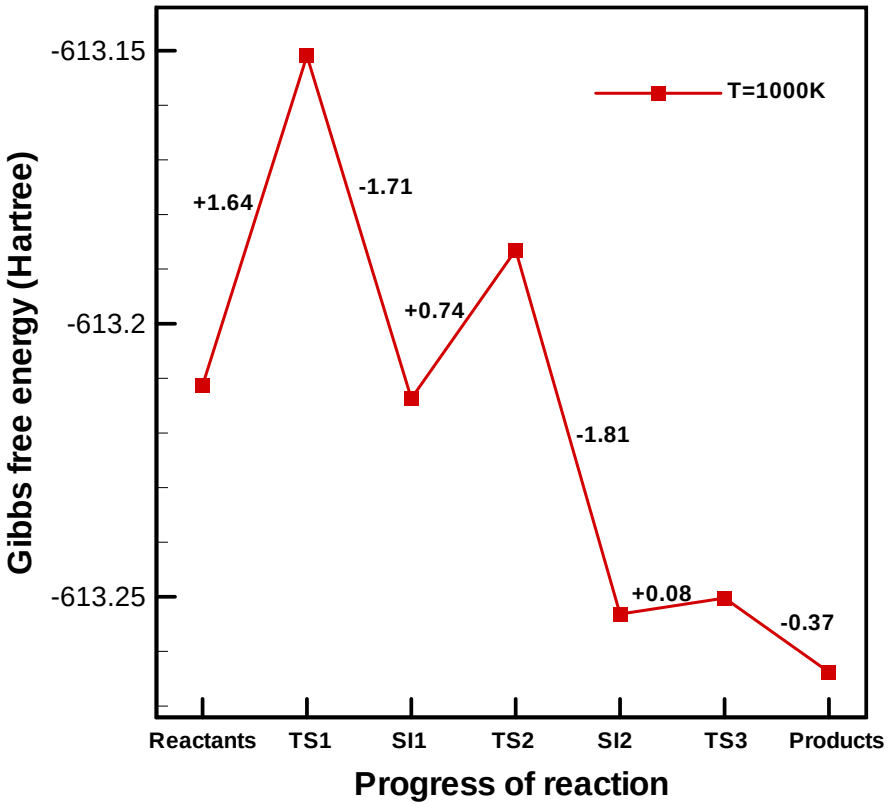

Figure 8.3 Reaction process at difference temperature and Gibbs free energy changes are labeled.

To provide an illustration of the physical time-scales involved, we will consider the rates of reaction. The key equation for calculation reaction rates is[263]

$$k(T) = \frac{k_B T}{hc^o} e^{-\Delta G^{\ddagger}/RT} \tag{8.38}$$

where c^o is a concentration constant, and h is the Planck's constant.

Comparing the reaction rates at $77K$ and $1000K$ for overcoming the energy of activation from the reactants to the first stable intermediate state, we have k(77K): k(1000K) = 1:133. It show that an increase of $0.71eV$ in $\Delta G^{\ddagger}$ leads to a 133-fold decrease in the reaction rate. Thus relatively small changes in $\Delta G^{\ddagger}$ can lead to large changes in the overall rate of the reaction. Therefore, we can see that the reaction at high temperature is indeed slower, as we would expect.

8.3.1 Conclusion

In this chapter, we have examined the thermodynamic properties of the atomic adsorption of hydrogen on the sidewall of (5,5) carbon nanotubes. We take the atomic adsorption of hydrogen onto the exterior wall as an example. The results suggest that the reaction is possible at ambient temperature, but it is more favorable than at lower temperatures. For example, at ambient temperature, the reaction has to overcome an activation energy of 25.240*kcal/mol*, which is higher than that of 21.394*kcal/mol* at a lower temperature of 77*K*. We thus conclude that reaction rates are higher at lower temperature.

CHAPTER 9

CONCLUSIONS AND FUTURE WORK

This chapter summarizes the major achievements and contributions of the present research project, and outlines the possible future directions for these areas of research as well.

9.1 Conclusions of Results

In chapter 5 of this thesis, we studied the relationship between the configurations of H_2 molecules in C_{60} fullerene and (5,5) nanocapsule, with the H_2-H_2 and H_2-wall repulsive energies. This was carried out using PM3 semi-empirical method for geometry optimization, and *ab initio* DFT for energy calculation. Also, polarization functions were included in the analysis to allow for non-uniform displacement of charges away from atomic nuclei. It was found that the storage capacity and the configuration of the enclosed H_2 molecules have close relation with the two kinds of repulsive energies. Due to the coupled effects of these two repulsive energies, the H_2 molecules transition from 1D to 2D, and then to different 3D phases. Seven different phases are observed, namely the axis phase (1D), zigzag phase (2D), disordered phase (3D), shell phase (3D), shell-axis coexist phase (3D), shell-zigzag coexist phase (3D), and shell-disordered coexist phase (3D). Present results suggest that high-capacity hydrogen storage (>6.5*wt.%*) cannot be simply explained through physisorption, and appropriate and viable chemisorption processes need to be put

forth and elucidated. The present physisorption results show maximum 6.05*wt.%* uptake for the H_2-C_{60} system and maximum 6.02*wt.%* uptake for the H_2-nanocapsule system.

Chapter 6 of this thesis provided insight into the atomic adsorption process of hydrogen onto carbon nanotubes. Present results suggest that the lowest energy states of the system are achieved for hydrogen atoms chemisorbed on the wall of the nanotube. Three transition states and two stable intermediate products are observed in the chemisorption process. These results point to the possibility of hydrogen storage provided the hydrogen atoms can approach sufficiently near to the surface of the tube wall, and this can be achieved via high pressure or injection of hydrogen atoms with high kinetic energies into the reaction cell. The first hydrogen atom weakens the π bond of the C-C bond and forms a H-C covalent bond. Following this, the next approaching hydrogen atom will react with the neighboring carbon of the same layer perpendicular to the nanotube axis and form another H-C covalent bond. The original C-C bond is then further weakened and finally breaks when the two H atoms are adsorbed, and this is also a consequence of the mutual attraction of the two hydrogen atoms. Our simulation results show that the adsorption of H atoms on the outside of the tube is exothermic and stable, and is hence entirely feasible.

In chapter 7 of this thesis, we presented a systematic study, based on the multiscale ONIOM2 scheme, to analyze the physisorption and chemisorption characteristics of hydrogen atoms on the exterior and interior of (5,5) carbon nanotubes. As a result of this study, significant new insight is obtained about the flip-in mechanism of hydrogen atoms through nanotube surfaces. Several key stable intermediate states of the hydrogen adsorption process are identified. We find that near the surface, the H_2 molecule is adsorbed through weak van der Waal's interactions through a small polarization of its electronic charge. For the hydrogen to be chemically bonded onto the nanotube, it has to overcome the forward activation barrier of 4.00*eV* during the process. The surface structure of the (5,5) armchair nanotube is able to dissociate the hydrogen molecule and allow the hydro-

gen atoms to be chemisorbed onto the nanotube, concurrently weakening the C-C bonds in the vicinity of the reaction. From the physisorption to the first stable intermediate when one hydrogen atom is chemisorbed, the reaction is not energetically favorable, requiring the adsorption of 3.41eV. The second hydrogen atom is much more easily chemisorbed, and will release 2.57eV. However, the resulting state of the sp^3 bonds leads to very strong antibonding and breaks the C-C bond, suggesting that the hydrogen atmosphere can act as catalyst for unzipping the tube. We also conclude that hydrogen atoms can be flipped inside the tube forming a zig-zag type configurations, and this flip-in process requires the absorption 0.80eV for the reaction to take place. The stable state at which both hydrogen atoms are flipped inside is extremely unfavorable, requiring the high adsorption of 9.664eV (222.711$kcal/mol$) from environment to break the C-C bond again. Based on the orbital overlap theory, and the natural bond orbital analysis, the adsorption behavior related to the bond breaking and formation is examined and explained in detail.

Chapter 8 of this thesis provided an insight into the thermodynamic properties of the atomic adsorption of hydrogen on the sidewall of (5,5) carbon nanotubes. We take the atomic adsorption of hydrogen onto the exterior wall as an example. The results suggest that the reaction is possible at ambient temperature, but it is more favorable than at lower temperatures. For example, at ambient temperature, the reaction has to overcome an activation energy of 25.240$kcal/mol$, which is higher than that of 21.394$kcal/mol$ at a lower temperature of 77K.

Once again, it should be stressed that we have presented results performed on a relatively small diameter nanotube, and that the unzipping phenomenon is not observed for larger diameter nanotubes.

9.2 Future Work

The results presented in this thesis indicate that the future for *ab initio* computa-

tional simulation in the nano discipline is extremely promising. Without a doubt, the next ten to twenty years will see dramatic advances in the field of nanodevices, nanostructure synthesis including protein structures prediction, and nanomaterial simulation is a powerful tool to investigate nanoscale phenomena which are difficult to observe experimentally. From there, we will need to determine the structures of these molecules, the means in which they form, and from there how they interact and regulate different processes. Better algorithms and computers will allow us to analyze new nanostructures and nanodevices with improved accuracy in the next decades.

9.2.1 Future Direction of This Work

The results presented in this thesis demonstrates the effective and accurate prediction of the hydrogen interaction with the pure carbon nanotubes. Extending the current research to more complicated carbon nanotube based nanodevices, is in itself, a significant task. The large surface area and its empty cavity make SWNTs, in principle, relatively easily attached or filled by a wide range of different molecules, such as H_2O, bioactive molecules, quantum dots (such as CdSe, having unique optical and electronic properties based on its size and structure), and even the large protein molecules, which raises the possibility of for an SWNT drug carrier. Additionally, our results have demonstrated that nanotubes can open and close in response to chemical stimuli, and it is thus possible to use nanotubes for drug delivery and controlling drug encapsulation and release.

The current work could also be extended to the time-dependent situations, so as to obtain accurate and reliable predictions for the excited state properties for the related stable intermediates and the transition states. The stationary DFT is confined to groundstate properties and the response of this groundstate to static external perturbations such as electric fields. In future work, we will investigate in detail to the time dependent density functional

theory that can be applied to the dynamic linear and no-linear response properties. This will enable us to calculate excitation energies and oscillator strengths in a consistent way, thus freeing DFT from its groundstate limitations.

9.2.2 Future Directions in the Field of Molecular Simulation

First principle *ab initio* methods have been known for several decades and have been used successfully in atomistic simulation models of interacting particles to describe the molecular systems and chemical processes. However, the extensive computational requirement inherent in even the most efficient *ab initio* methods preclude their application to simulations of large systems in the near future. It will be important to continue to develop more efficient methods which account for electronic structure for chemical reaction and physical characterization studies.

While it is possible to perform very reliable *ab initio* calculations on small molecular systems, and molecular dynamics for hundreds and thousands of atoms/molecules, however, many important processes, particular those in engineering materials, involve events on different length and time scales that require different levels of accuracy in their treatment, concurrent multiscale modeling is required for this purpose. Thus, the seamless integration or compiling of existing techniques from quantum mechanics through to continuum numerical techniques is required to treat such problems. By applying this scheme, the electronic details such as bond breaking or bond formation at critical regions, as well as the continuum elastic response in the long range can be simultaneously studied.

BIBLIOGRAPHY

1. Gregg, S. J.; Sing, K. S. W., *Adsorption, Surface Area and Porosity*. Academic Press: London, New York, 1967.

2. Veziroglu, T. N., Hydrogen energy system as a permanent solution to global energy environmental problems. *Chem Ind* **1999,** 53, 383-393.

3. Veziroglu, T. N.; Barbir, F., Hydrogen: The wonder fuel. *Int J Hydrogen Energy* **1992,** 17, 391-401.

4. Schur, D. V.; Tarasov, B. P.; Yu. Zaginaichenko, S.; Pishuk, V. K.; Veziroglu, T. N.; Shul'ga, Y. M.; Dubovoi, A. G.; Anikina, N. S.; Pomytkin, A. P.; Zolotarenko, A. D., The prospects for using of carbon nanomaterials as hydrogen storage systems. *Int J Hydrogen Energy* **2002,** 27, (10), 1063-1069.

5. Agarwal, R. K.; Noh, J. S.; Schwarz, J. A.; Davini, P., Effect of surface acidity of activated carbon on hydrogen storage. *Carbon* **1987,** 25, (2), 219-226.

6. Amankwah, K. A. G.; Noh, J. S.; Schwarz, J. A., Hydrogen storage on superactivated carbon at refrigeration temperatures. *International Journal of Hydrogen Energy* **1989,** 14, (7), 437.

7. Chambers, A.; Park, C.; Baker, R. T. K.; Rodriguez, N. M., Hydrogen storage in graphite nanofibers. *J Phys Chem B* **1998,** 102, 4253-4256.

8. Park, C.; Anderson, P. E.; Chambers, A.; Tan, C. D.; Hidalgo, R.; Rodriguez, N. M., Further studies of the interaction of hydrogen with graphite nanofibers. *Journal of Physical Chemistry B.* **1999,** 103(48), 10572-10581.

9. Ahn, C. C.; Ye, Y.; Ratnakumar, B. V.; C. Whitlam; Bowman, R. C.; Fultz, B., Hydrogen desorption and adsorption measurements on graphite nanofibers. *Appl Phys Lett* **1998,** 73, (23), 3378-3380.

10. Dillon, A. C.; Jones, K. M.; Bekkedahl, T. A.; Kiang, C. H.; Bethune, D. S.; Heben, M. J., Storage of hydrogen in single-walled carbon nanotubes. *Nature* **1997,** 386, 377-379.

11. Chen, P.; Wu, X.; Lin, J.; Tan, K. L., High H2 uptake by alkali-doped carbon nanotubes under ambient pressure and moderate temperatures. *Science* **1999,** 285, (5424), 91.

12. Chahine, R.; Bose, T. K., Low-pressure adsorption storage of hydrogen. *Int J Hydrogen Energy* **1994,** 19, (2), 161.

13. Bentley, J.; Fuller, W.; Hynek, S., Hydrogen Storage by Carbon Sorption. *Int J Hydrogen Energy* **1997,** 22, (6), 601-610.

14. Ströbel, R.; Jörissen, L.; Schliermann, T.; Trapp, V.; Schutz, W.; Bohmhammel, K.; Wolf, G.; Garche, J., Hydrogen adsorption on carbon materials. *J Power Sources* **1999,** 84, (2), 221-224.

15. Benard, P.; Chahine, R., Modeling of adsorption storage of hydrogen on activated carbons. *Int J Hydrogen Energy* **2001,** 26, (8), 849-855.

16. Güther, V.; Otto, A., Recent developments in hydrogen storage applications based on metal hydrides. *Journal of Alloys and Compounds* **1999,** 293-295, 889.

17. Nakatsuka, K.; Yoshino, M.; Yukawa, H.; Morinaga, M., Roles of the hydride forming and non-forming elements in hydrogen storage alloys. *Journal of Alloys and Compounds* **1999,** 293-295, 222.

18. Ye, Y.; Ahn, C. C.; Witham, C.; Fultz, B.; Liu, J.; Rinzler, A. G.; Colbert, D.; Smith, K. A.; Smalley., R. E., Hydrogen adsorption and cohesive energy of single-walled carbon nanotubes. *Appl Phys Lett* **1999,** 74, 2307 - 709.

19. Fan, Y. Y.; Liao, B.; Liu, M.; Wei, Y. L.; Lu, M. Q.; Cheng, H. M., Hydrogen uptake in vapor-grown carbon nanofibers. *Carbon* **1999,** 37, 1649-1652.

20. Dewar, J., *Collected Papers of Sir James Dewar*. Lady Dewar ed.; Cambridge: University Press: 1927; p 678-691.

21. Zaluska, A.; Zaluski, L.; Ström-Olsen, J. O., Hydrogen storage in carbon nanos-

tructures - still a long road from science to commerce? *Appl Phys A: Mater Sci Process* **2001,** 72, (2), 147 - 151.

22. Orimo, S.; Fujii, H., Materials science of Mg-Ni-based new hydrides. *Appl Phys A: Mater Sci Process* **2001,** 72, (2), 167 - 186.

23. Huot, J.; Liang, G.; Schulz, R., Mechanically alloyed metal hydride systems. *Appl Phys A: Mater Sci Process* **2001,** 72, (2), 187 - 195.

24. Reule, H.; Hirscher, M.; Weihardt, A.; Kronmuller, H., Hydrogen desorption properties of mechanically alloyed MgH2 composite materials. *J Alloys Compd* **2000,** 305, (1-2), 246-252.

25. Bogdanovic, B.; Brand, R. A.; Marjanovic, A.; Schwickardi, M.; Tolle, J., Metal-doped sodium aluminium hydrides as potential new hydrogen storage materials. *J Alloys Compd* **2000,** 302, (1-2), 36-58.

26. Dillon, A. C.; Heben, M. J., Hydrogen storage using carbon adsorbents: past, present and future. *Appl Phys A: Mater Sci Process* **2001,** 72, (2), 133 - 142.

27. Bose, T.; Chanine, R., Low-pressure Adsorption Storage of Hydrogen. *Int J Hydrogen Energy* **1994,** 19, 161-164.

28. Ernst, S.; Fritz, M.; Weitkamp, J., Zeolites as Media for Hydrogen Storage. *Int J Hydrogen Energy* **1995,** 20, (12), 967-970.

29. Catlow, C., Zeolites: Structure, Synthesis and Properties ?An Introduction. In: Modeling of Structure and Reactivity in Zeolites,. *Ed. Catlow, Academic Press,UK* **1992**.

30. Kishi, T.; Matsumoto, A.; Mizushima, A.; Nishimiya, N.; Tsutsumi, K., Hyperstoichiometric Hydrogen Occlusion by Palladium Nanoparticles Included in NaY Zeolite. *J. Alloys and Compounds* **2001,** 319, 312-321.

31. Darkrim, F.; Levesque, D., High Adsorptive Property of Opened Carbon Nanotubes at 77 K. *J Phys Chem B* **2000,** 104, (29), 6773-6776.

32. Darkrim, F. L.; Malbrunot, P.; Tartaglia, G. P., Review of hydrogen storage by adsorption in carbon nanotubes. *Int J Hydrogen Energy* **2002,** 27, (2), 193-202.

33. Cheng, H.; Pez, G. P.; Cooper, A. C., Mechanism of Hydrogen Sorption in Single-Walled Carbon Nanotubes. *J Am Chem Soc* **2001,** 123, (24), 5845 - 5846.

34. Cheng, H. M.; Yang, Q. H.; Liu, C., Hydrogen storage in carbon nanotubes. *Carbon* **2001,** 39, (10), 1447-1454.

35. Dillon, A. C.; Gennett, T.; Alleman, J. L.; Jones, K. M.; Parilla, P. A.; Heben, M. J., Carbon nanotube materials for hydrogen storage. *Proceedings of the 1999 US DOE Hydrogen Program Review, Vol. II* **1999**.

36. Dillon, A. C.; Gennett, T.; Alleman, J. L.; K.M. Jones; Parilla, P. A.; Heben, M. J., Carbon nanotube materials for hydrogen storage. *Proceedings of the 2000 US DOE Hydrogen Program Review, Vol. II* **2000**.

37. Liu, C.; Fan, Y. Y.; Liu, M.; Cong, H. T.; Cheng, H. M.; Dresselhaus, M. S., Hydrogen Storage in Single-Walled Carbon Nanotubes at Room Temperature. *Science* **1999,** 286, (5442), 1127-1129.

38. Dresselhaus, M. S.; Williams, K. A.; Eklund, P. C., Hydrogen adsorption in carbon materials. *MRS Bulletin* **1999,** 24, (11), 45-50.

39. Brown, S. D. M.; Dresselhaus, G.; Dresselhaus, M. S., Reversible hydrogen uptake in carbon-based materials. *Recent Advances in Catalytic Materials; Materials Research Society Symposium - Proceedings* **1998,** 497, 157-163.

40. Brown, C. M.; Yildirim, T.; Neumann, D. A.; Heben, M. J.; Gennett, T.; Dillon, A. C.; Alleman, J. L.; Fischer, J. E., Quantum rotation of hydrogen in single-wall carbon nanotubes. *Chem Phys Lett* **2000,** 329, (3-4), 311-316.

41. Pederson, M. R.; Broughton, J. Q., Nanocapillarity in fullerene tubules. *Phys Rev Lett* **1992,** 69, (18), 2689-2692.

42. Krishnan, A.; Dujardin, E.; Treacy, M. M. J.; Hugdahl, J.; Lynum, S.; Ebbesen, T. W., Graphitic cones and the nucleation of curved carbon surfaces. *Nature* **1997,** 388, (6641), 451-454.

43. Atkinson, K.; Roth, S.; Hirscher, M.; Grunwald, W., Carbon nanostructures: An efficient hydrogen storage medium for fuel cells. *Fuel Cells Bulletin* **2001,** 4, (38),

9-12.

44. Duret, B.; Saudin, A., Microspheres for on-board hydrogen storage. *Int J Hydrogen Energy* **1994,** 19, (9), 757-764.

45. Eklund, G.; Von Krusenstierna, O., Storage and transportation of merchant hydrogen. *Int J Hydrogen Energy* **1983,** 8, (6), 463-470.

46. Iijima, S., Helical microtubules of graphitic carbon. *Nature* **1991,** 354, (6348), 56-58.

47. Dresselhouse, M. S.; Dresselhouse, G.; Eklund, P. C., Science of Fullerenes and Carbon Nanotubes. *Academic Press, New York* **1996**.

48. Avouris, P.; Hertel, T.; Martel, R.; Schmidt, T.; Shea, H. R.; Walkup, R. E., Carbon nanotubes: nanomechanics, manipulation, and electronic devices. *Appl Surf Sci* **1999,** 141, (3-4), 201-209.

49. Dresselhaus, M. S.; Dresselhaus, G.; Saito, R., Carbon fibers based on C_{60} and their symmetry. *Physical Review B: Condensed Matter* . **1992,** 45, 6234–6242.

50. Srivastava, D.; Menon, M.; Cho, K., Computational Nanotechnology with Carbon Nanotubes and Fullerenes. *Computing in Science and Engineering, Invited Article for a thematic issue on Nanotechnology* **2001,** July/Aug issue, 42-55.

51. Liu, J.; Rinzler, A. G.; Dai, H.; Hafner, J. H.; Bradley, R. K.; Boul, P. J.; Lu, A.; Iverson, T.; Shelimov, K.; Huffman, C. B.; Rodriguez-Macias, F.; Shon, Y.-S.; Lee, T. R.; Colbert, D. T.; Smalley, R. E., Fullerene Pipes. *Science* **1998,** 280, (5367), 1253-1256.

52. Komatsu, K.; Murata, M.; Murata, Y., Encapsulation of Molecular Hydrogen in Fullerene C_{60} by Organic Synthesis. *Science* **2005,** 307, (5707), 238-240.

53. Han, J., Energetics and structures of fullerene crop circles. *Chem Phys Lett* **1998,** 282, (2), 187-191.

54. Dunlap, B. I., Connecting carbon tubules. *Phys Rev B: Condens Matter* **1992,** 46, (3), 1933-1936.

55. Chernozatonskii, L. A., Carbon nanotube elbow connections and tori. *Phys Lett A* **1992,** 170, (1), 37-40.

56. Haddon, R. C., Electronic properties of carbon toroids. *Nature* **1997,** 388, (6637), 31-32.

57. Ihara, S.; Itoh, S.; Kitakami, J., Toroidal forms of graphitic carbon. *Phys Rev B: Condens Matter* **1993,** 47, (19), 12908-12911.

58. Martel, R.; Shea, H. R.; Avouris, P., Ring formation in single-wall carbon nanotubes. *J Phys Chem B* **1999,** 103, (36), 7551-7556.

59. Ponomarenko, O.; Radny, M. W.; Smith, P. V., Structure and energetics of hydrogenated and dehydrogenated carbon tori. *Carbon* **2005,** 43, (6), 1165-1173.

60. Mommer, N.; Hirscher, M.; Cuevas, F.; Kronmuller, H., Influence of the microstructure on the desorption kinetics of single- and multiphase LaNiFe alloys. *J Alloys Compd* **1998,** 266, (1-2), 255-259.

61. Lee, S. M.; Park, K. S.; Choi, Y. C.; Park, Y. S.; Bok, J. M.; Bae, D. J.; Nahm, K. S.; Choi, Y. G.; Yu, S. C.; Kim, N.-G.; Frauenheim, T.; Lee, Y. H., Hydrogen adsorption and storage in carbon nanotubes. *Synth. Met.* **2000,** 113, (3), 209-216.

62. Nützenadel, C.; Züttel, A.; Chartouni, D.; Schlapbach, L.; Electrochem, Electrochemical Storage of Hydrogen in Nanotube Materials. *Solid State Lett.* **1999,** 2, 30-32.

63. Züttel, A.; Nützenadel, C.; Sudan, P.; Mauron, P.; Emmenegger, C.; Rentsch, S.; Schlapbach, L.; Weidenkaff, A.; Kiyobayashi, T., Hydrogen sorption by carbon nanotubes and other carbon nanostructures. *J Alloys Compd* **2002,** 330-332, 676-682.

64. Thess, A.; Lee, R.; Nikolaev, P.; Dai, H.; Petit, P.; Robert, J.; Xu, C.; Lee, Y. H.; Kim, S. G.; Rinzler, A. G.; Colbert, D. T.; Scuseria, G. E.; Tomanek, D.; Fischer, J. E.; Smalley, R. E., Crystalline Ropes of Metallic Carbon Nanotubes. *Science* **1996,** 273, (5274), 483-487.

65. Jourent, C.; Maser, W. K.; Bernier, P.; Loiseau, A.; Chapelle, M. L. D. L.; Lefrant,

S.; Deniard, P.; Lee, R.; Fischer, J. E., Large-scale production of single-walled carbon nanotubes by the electric-arc technique. *Nature (London)* **1997,** 38, 756-758.

66. Govindaraj, A.; Rao, C. N. R., Organometallic precursor route to carbon nanotubes. *Pure Appl Chem* **2002,** 74, (9), 1571-1580.

67. Haddon, R. C., Carbon Nanotubes. *Accounts of Chemical Research (Editorial)* **2002,** 35, (12), 997-997.

68. Tohji, K.; Goto, T.; Takahashi, H.; Shinoda, Y.; Shimizu, N.; Jeyadevan, B.; Matsuoka, I.; Saito, Y.; Kasuya, A.; Tetsu Ohsuna; Hiraga, K.; Nishina, Y., Purifying single-walled nanotubes. *Nature (London)* **1996,** 383, 679-679.

69. Tohji, K.; Takahashi, H.; Shinoda, Y.; Shimizu, N.; Jeyadevan, B.; Matsuoka, I.; Saito, Y.; Kasuya, A.; Ito, S.; Nishina, Y., Purification Procedure for Single-Walled Nanotubes. *J Phys Chem B* **1997,** 101, (11), 1974 -1978.

70. Bandow, S.; Rao, A. M.; Williams, K. A.; Thess, A.; Smalley, R. E.; Eklund, P. C., Purification of Single-Wall Carbon Nanotubes by Microfiltration. *J Phys Chem B* **1997,** 101, (44), 8839 -8842.

71. Shelimov, K. B.; Esenaliev, R. O.; Rinzler, A. G.; Huffman, C. B.; Smalley, R. E., Purification of single-wall carbon nanotubes by ultrasonically assisted filtration. *Chem Phys Lett* **1998,** 282, (5-6), 429-434.

72. Rinzler, A. G.; Liu, J.; Dai, H.; Nikolaev, P.; Huffman, C. B.; Rodriguez-Macias, F. J.; Boul, P. J.; Lu, A. H.; Heymann, D.; Colbert et, a., Large-scale purification of single-wall carbon nanotubes: Process, product, and characterization. *Appl Phys A: Mater Sci Process* **1998,** 67, (1), p 29-37.

73. Dujardin, E.; Ebbesen, T. W.; Krishnan, A.; Treacy, M. M. J., Purification of Single-Shell Nanotubes. *Adv Mater (Weinheim, Ger)* **1998,** 10, (8), 611 - 613.

74. Dillon, A. C.; Gennett, T.; Jones, K. M.; Alleman, J. L.; Parilla, P. A.; Heben, M. J., A Simple and Complete Purification of Single-Walled Carbon Nanotube Materials. *Adv Mater (Weinheim, Ger)* **1999,** 11, (16), 1354-1358.

75. Zimmerman, J. L.; Bradley, R. K.; Huffman, C. B.; Hauge, R. H.; Margrave, J. L.,

Gas-Phase Purification of Single-Wall Carbon Nanotubes. *Chem Mater* **2000.,** 12 (5), 1361 -1366.

76. Chiang, I. W.; Brinson, B. E.; Smalley, R. E.; Margrave, J. L.; Hauge, R. H., Purification and Characterization of Single-Wall Carbon Nanotubes. *J Phys Chem B* **2001,** 105 (6), 1157 -1161.

77. Martínez, M. T.; Callejas, M. A.; Benito, A. M.; Maser, W. K.; Cochet, M.; Andrés, J. M.; Schreiber, J.; Chauvet, O.; Fierro, J. L. G.; , C. C., , (), , Microwave single walled carbon nanotubes purification. *Chem Commun (Cambridge, U K)* **2002,** 9, 1000 - 1001.

78. Duesberg, G. S.; Blau, W.; Byrne, H. J.; Muster, J.; Burghard, M.; Roth, S., Chromatography of carbon nanotubes. *Synth Met* **1999,** 103, (1-3), 2484-2485.

79. Holzinge, M.; Hirsch, A.; Bernier, P.; Duesberg, G. S.; Burghard, M., A new purification method for single wall carbon nanotubes (SWNTs). *Appl Phys A: Mater Sci Process* **2000,** 70, 599-602.

80. Dalton, A. B.; Stephan, C.; Coleman, J. N.; McCarthy, B.; Ajayan, P. M.; Lefrant, S.; Bernier, P.; Blau, W. J.; Byrne, H. J., Selective interaction of a semiconjugated organic polymer with single-wall nanotubes. *J Phys Chem B* **2000,** 104, (43), 10012-10016.

81. Panhuis, M. I. H.; Munn, R. W.; Blau, W. J., Optical polymer characteristics for nanotube solubility. *Synth Met* **2001,** 121, 1187-1188.

82. Hirscher, M.; Becher, M.; Haluska, M.; Dettlaff-Weglikowska, U.; Quintel, A.; Duesberg, G. S.; Choi, Y.-M.; Downes, P.; Hulman, M.; Roth et, a., Hydrogen storage in sonicated carbon materials. *Appl Phys B: Lasers Opt* **2001,** 72, (2), 129-132.

83. Dillon, A. C.; Gennett, T.; Alleman, J. L.; Jones, K. M.; Gilbert, K. E. H.; Parilla, P. A.; Heben, M. J. *in Proceedings of the 2000 U.S. DOE Hydrogen Program Review, National Renew-able Energy Laboratory, Golden, Colorado, NREL/CP-507-28 890. (see www.eere.energy.gov/hydrogenandfuelcells/hydrogen/annual_review2001.html);* 2000.

84. Dillon, A. C.; Gilbert, K. E. H.; Alleman, J. L.; T. Gennett, K. M. J.; Parilla, P. A.;

Heben, M. J. *in Proceedings of the 2001 U.S. DOE Hydrogen Program Review, National Renew-able Energy Laboratory, Golden, Colorado, NREL/CP-570-30535. (see www.eere.energy.gov/hydrogenandfuelcells/hydrogen/annual_review2001.html)*; 2001.

85. Stepanek, I.; Maurin, G.; Bernier, P.; Gavillet, J.; Loiseau, A.; Edwards, R.; Jaschinski, O., Nano-mechanical cutting and opening of single wall carbon nanotubes. *Chem Phys Lett* **2000,** 331, (2-4), 125-131.

86. Orimo, S.; Majer, G.; Fukunaga, T.; Züttel, A.; Schlapbach, L.; Fujii, H., Hydrogen in the mechanically prepared nanostructured graphite. *Appl Phys Lett* **1999,** 75, (20), 3093-3095.

87. Hirscher, M.; Becher, M.; Haluska, M.; Quintel, A.; Skakalova, V.; Choi, Y.-M.; Dettlaff-Weglikowska, U.; Roth, S.; Stepanek, I.; Bernier, P., Hydrogen storage in carbon nanostructures. *J. Alloys and Compounds* **2002,** 330-332, 654-658.

88. Parilla, P. A.; Dillon, A. C.; Gennett, T.; Alleman, J. L.; Jones, K. M.; Heben, M. J., *Mater Res Soc Symp Proc* **2001,** 633, A14.36.1.

89. Dillon, A. C.; Gilbert, K. E. H.; Parilla, P. A.; Alleman, J. L.; Hornyak, G. L.; Jones, K. M.; Heben, M. J. In *in Proceedings of the 2002 U.S. DOE Hydrogen Program Review, National Renew-able Energy Laboratory, Golden, Colorado, NREL/CP-610-32405.(see www.eere.energy.gov/hydrogenandfuelcells/hydrogen/annual_review2002.html)*, 2002; 2002.

90. Smith, M. R.; Bittner, E.; Bockrath, B., in Proceedings of the 25th International Conference on Carbon, CARBON ’01, American Carbon Society, Lexington, Ky, Paper no. 36.5 In 2000.

91. Adu, C. K. W.; Sumanasekera, G. U.; Pradhan, B. K.; Romero, H. E.; Eklund, P. C., Carbon nanotubes: A thermoelectric nano-nose. *Chem Phys Lett* **2001,** 337, (1-3), 31-35.

92. Pradhan, B. K.; Sumanasekera, G. U.; Adu, K. W.; Romero, H. E.; Williams, K. A.; Eklund, P. C., Experimental probes of the molecular hydrogen-carbon nanotube in-

teraction. *J Phys: Condens Matter* **2002,** 323, (1-4), 115-121.

93. Zandonella, C., Is it all just a pipe dream? *Nature (London)* **2001** 410, 734-735.

94. Hirscher, M.; Becher, M., Hydrogen storage in carbon nanotubes. *J Nanosci Nanotechnol* **2003,** 3, (1-2), 3-17.

95. Chen, P.; Wu, X.; Lin, J.; Tan, K. L., High H_2 uptake by alkali-doped carbon nanotubes under ambient pressure and moderate temperatures. *Science* **1999,** 285, 91-93.

96. Yang, R. T., Hydrogen storage by alkalidoped carbon nanotubes - revisited. *Carbon* **2000,** 38(4), 623-626.

97. Kelly, K. F.; Chiang, I. W.; Mickelson, E. T.; Hauge, R. H.; Margrave, J. L.; Wang, X.; Scuseria, G. E.; Radloff, C.; Halas, N. J., Insight into the mechanism of sidewall functionalization of single-walled nanotubes: an STM study. *Chem Phys Lett* **1999,** 313, (3-4), 445-450.

98. Zhu, H. W.; Chen, A.; Mao, Z. Q.; Lu, C. L.; Xiao, X.; Wei, B. Q.; Liang, J.; Wu, D. H., The effect of surface treatments on hydrogen storage of carbon nanotubes. *J Mater Sci Lett* **2000,** 19, 1237-1239.

99. Pinkerton, F. E.; Wicke, B. G.; Olk, C. H.; Tibbetts, G. G.; Meisner, G. P.; Meyer, M. S.; Herbst, J. F., Thermogravimetric measurement of hydrogen absorption in alkali-modified carbon materials. *Journal of Physical Chemistry B.* **2000,** 104(40), 9460-9467.

100. Nützenadel, C.; Züttel, A.; Schlapbach, L., Electrochemical storage of hydrogen in carbon single wall nanotubes. **1999**, (486), 462.

101. Dresselhause, M. S.; Dresselhaus, G.; Eklund, P. C., *Science of fullerenes and carbon nanotubes*. Academic Press: New York, 1996.

102. Bessel, C. A.; Laubernds, K.; Rodriguez, N. M.; R.T.K.Baker, Graphite nanofibers as an electrode for fuel cell applications. *Journal of Physical Chemistry B.* **2001,** 105(6), 1115-1118.

103. Orimo, S.; Zuttel, A.; Schlapbach, L.; Majer, G.; Fukunaga, T.; Fujii, H., Hydrogen interaction with carbon nanostructures: current situation and future prospects. *J Al-*

loys Compd **2003,** 356-357, 716-719.

104. Cheng, H. M.; Liu, C.; Fan, Y. Y.; Li, F.; Su, G.; Cong, H. T.; He, L. L.; Liu, M., Synthesis and hydrogen storage of carbon nanofibers and single-walled carbon nanotubes. *Z. Metallkd* **2000,** 91, 306-311.

105. Wu, X. B.; Chen, P.; Lin, J.; Tan, K. L., Hydrogen uptake by carbon nanotubes. *Int J Hydrogen Energy* **2000,** 25(3), 261-265.

106. Tibbetts, G. G.; Meisner, G. P.; Olk, C. H., Hydrogen storage capacity of carbon nanotubes, filaments, and vapor-grown fibers. *Carbon* **2001,** 39, (15), 2291-2301.

107. Ritschel, M.; Uhlemann, M.; Gutfleisch, O.; Leonhardt, A.; Graff, A.; Taschner, C.; Fink, J., Hydrogen storage in different carbon nanostructures. *Appl Phys Lett* **2002,** 80, (16), 2985-2987.

108. Froudakis, G. E., Hydrogen interaction with carbon nanotubes: a review of ab initio studies. *J Phys: Condens Matter* **2002,** 14, R453-R465.

109. Peterson, B. K.; Gubbins, K. E., Phase transitions in a cylindrical pore. Grand canonical Monte Carlo, mean field theory and the Kelvin equation. *Mol Phys* **1987,** 62, (1), 215-226.

110. Frenkel, D.; Smit, B., Understanding molecular simulation : from algorithms to applications. *San Diego, Calif. : Academic Press* **c2002**.

111. Leach, A. R., *Molecular Modelling: Principles and Applications*. Prentice Hall, 2001; p 97.

112. Haile, J. M., *Molecular Dynamics Simulation : Elementary Methods*. c1992.

113. Darkrim, F.; Levesque, D., Monte Carlo simulations of hydrogen adsorption in single-walled carbon nanotubes. *J Chem Phys* **1998,** 109, (12), 4981-4984.

114. Rzepka, M.; Lamp, P.; Casa-Lillo, M. A. d. l., Physisorption of Hydrogen on Microporous Carbon and Carbon Nanotubes. *J Phys Chem B* **1998,** 102, (52), 10894-10898.

115. Wang, Q.; Johnson, J. K., Molecular simulation of hydrogen adsorption in single-

walled carbon nanotubes and idealized carbon slit pores. *J Chem Phys* **1999,** 110, (1), 577-586.

116. Simonyan, V. V.; Johnson, J. K., Hydrogen storage in carbon nanotubes and graphitic nanofibers. *J Alloys Compd* **2002,** 330-332, 659-665.

117. Williams, K. A.; Eklund, P. C., Monte Carlo simulations of H2 physisorption in finite-diameter carbon nanotube ropes. *Chem Phys Lett* **2000,** 320, (3-4), 352-358.

118. Wang, Q.; Johnson, J. K., Hydrogen adsorption on graphite and in carbon slit pores from path integral simulations. *Mol Phys* **1998,** 95, 299 - 309.

119. Wang, Q.; Johnson, J. K., Computer Simulation of Hydrogen Adsorption on Graphite Nanofibres. *J Phys Chem B* **1999,** 103, (2), 277-281.

120. Wang, Q.; Johnson, J. K., Optimization of carbon nanotube arrays for hydrogen adsorption. *J Phys Chem B* **1999,** 103, (23), 4809-4813.

121. Simonyan, V. V.; Phong, D.; Johnson, J. K., Molecular simulation of hydrogen adsorption in charged single-walled carbon nanotubes. *J Chem Phys* **1999,** 111, (21), 9778-9783.

122. Yin, Y. F.; Mays, T.; McEnaney, B., Molecular simulations of hydrogen storage in carbon nanotube arrays. *Langmuir* **2000,** 16, (26), 10521-10527.

123. Claye, A.; Fischer, J. E., Short-range order in disordered carbons: where does the Li go? *Electrochim Acta* **1999,** 45, (1-2), 107-120.

124. Ma, Y.; Xia, Y.; Zhao, M.; Wang, R.; Mei, L., Effective hydrogen storage in single-wall carbon nanotubes. *Phys Rev B: Condens Matter* **2001,** 63, 115422.

125. Chan, S. P.; Gang, C.; Gong, X. G.; Liu, Z. F., Chemisorption of Hydrogen Molecules on Carbon Nanotubes under High Pressure. *Phys Rev Lett* **2001,** 87, (20), 205502.

126. Pierre, D.; Pierre, C., Modeling of molecular hydrogen and lithium adsorption on single-wall carbon nanotubes. *Phys Rev B: Condens Matter* **2001,** 63, (24), 241402.

127. Barajas-Barraza, R. E.; Guirado-López, R. A., Clustering of H_2 molecules encapsu-

lated in fullerene structures. *Phys Rev B: Condens Matter* **2002,** 66, 155426.

128. Jeloaica, L.; Sidis, V., DFT investigation of the adsorption of atomic hydrogen on a cluster-model graphite surface. *Chem Phys Lett* **1999,** 300, (1-2), 157-162.

129. Lee, S.; Lee, Y., Hydrogen storage in single-walled carbon nanotubes. *Appl Phys Lett* **2000,** 76, (20), 2877-2879.

130. Seifert, G.; Kohler, T.; Frauenheim, T., Molecular wires, solenoids, and capacitors by sidewall functionalization of carbon nanotubes. *Appl Phys Lett* **2000,** 77, (9), 1313-1315.

131. Bauschlicher, J.; Charles, W., Hydrogen and fluorine binding to the sidewalls of a (10,0) carbon nanotube. *Chem Phys Lett* **2000,** 322, (3-4), 237.

132. Froudakis, G. E., Hydrogen Interaction with Single-Walled Carbon Nanotubes: A Combined Quantum-Mechanics/Molecular-Mechanics Study. *Nano Lett* **2001,** 1, (4), 179 - 182.

133. Bauschlicher, C. W., Jr., High Coverages of Hydrogen on a (10,0) Carbon Nanotube. *Nano Lett* **2001,** 1, (5), 223-226.

134. Dapprich, S.; Komaromi, I.; Byun, K. S.; Morokuma, K.; Frisch, M. J., A new ONIOM implementation in Gaussian98. Part I. The calculation of energies, gradients, vibrational frequencies and electric field derivatives. *J Mol Struc-Theochem* **1999,** 461-462, 1-21.

135. Lee, S. M.; An, K. H.; Lee, Y. H.; Seifert, G.; Frauenheim, T., A hydrogen storage mechanism in single-walled carbon nanotubes. *J Am Chem Soc* **2001,** 123, (21), 5059.

136. Lee, S. M.; An, K. H.; Kim, W. S.; Lee, Y. H.; Park, Y. S.; Seifert, G.; Frauenheim, T., Hydrogen storage in carbon nanotubes. *Synth. Metals* **2001,** 121, (1-3), 1189-1190.

137. Bauschlicher, C. W., Jr.; So, C. R., High Coverages of Hydrogen on (10,0), (9,0) and (5,5) Carbon Nanotubes. *Nano Lett* **2002,** 2, 337.

138. Rappe, A. K.; Casewit, C. J.; Colwell, K. S.; Goddard, W. A.; Skiff, I. W. M., UFF,

a full periodic table force field for molecular mechanics and molecular dynamics simulations. *J Am Chem Soc* **1992,** 114, (25), 10024-10035.

139. Szabo, A.; Ostlund, N. S., *Modern quantum chemistry : introduction to advanced electronic structure theory*. c1989.

140. Foresman, J. B.; Head-Gordon, M.; Pople, J. A.; Frisch, M. J., Toward a Systematic Molecular Orbital Theory for Excited States. *J Phys Chem* **1992,** 96, 135-149.

141. Adams, W. H., Intermolecular perturbation theory: Renormalized interaction energies. *Int. J. Quantum Chem* **1996,** 60, 1279-1289.

142. Leininger, M. L.; Allen, W. D.; III, H. F. S.; Sherrill, C. D., Is Møller–Plesset perturbation theory a convergent ab initio method? . *J Chem Phys* **2000,** 112, (21), 9213-9222.

143. Koch, W.; Holthausen., M. C., *A chemist's guide to density functional theory*. c2001.

144. Hohenberg, P.; Kohn, W., Inhomogeneous Electron Gas. *Physical Review* **1964,** 136, B864-B871.

145. Thomas, L. H., The calculation of Atomic Fields. *Proc. Camb. Phil. Soc.* **1927,** 23, 542.

146. Kohn, W.; Sham, L. J., Self-Consistent Equations Including Exchange and Correlation Effects. *Physical Review* **1965,** 140, A1133-1138.

147. Perdew, J. P.; Burke, K.; Ernzerhof, M., Generalized Gradient Approximation Made Simple. *Phys Rev Lett* **1996,** 77, 3865-3868.

148. Perdew, J. P.; Wang, Y., Accurate and simple analytic representation of the electron-gas correlation energy. *Phys Rev B: Condens Matter* **1992,** 45, 13244-3249.

149. Langreth, D. C.; Mehl, M. J., Beyond the local-density approximation in calculations of ground-state electronic properties. *Phys Rev B: Condens Matter* **1983,** 28, 1809.

150. Becke, A. D., Density-functional exchange-energy approximation with correct as-

ymptotic behavior. *Phys Lett A* **1988**, (38), 3098-3100.

151. Lee, C.; Yang, W.; Parr, R. G., Development of the Colle-Salvetti correlation-energy formula into a functional of the electron density. *Phys Rev B: Condens Matter* **1988,** 37, 785-789.

152. Becke, A. D., Density functional calculations of molecular bond energies. *J Chem Phys* **1986,** 84, (8), 4524-4529.

153. Becke, A. D., Density-functional thermochemistry I. The effect of the exchange-only gradient correction. *J Chem Phys* **1992,** 96, (3), 2155-2160.

154. Becke, A. D., Density-functional thermochemistry II. The effect of the Perdew-Wang generalized-gradient correlation correction. *J Chem Phys* **1992,** 97, (12), 9173-9177.

155. Becke, A. D., Density-functional thermochemistry III. The role of exact exchange. *J Chem Phys* **1993,** 98, (7), 5648-5652.

156. Becke, A. D., A new mixing of Hartree-Fock and local density-functional theories. *J Chem Phys* **1993,** 98, (2), 1372-1377.

157. Becke, A. D., Density-functional thermochemistry IV. A new dynamical correlation functional and implications for exact-exchange mixing. *J Chem Phys* **1996,** 104, (3), 1040-1046.

158. Becke, A. D., Density-functional thermochemistry V. Systematic optimization of exchange-correlation functionals. *Journal of Chemical Physics* **1997,** 107, (20), 8554-8560.

159. Filatov, M.; Thiel, W., A new gradient-corrected exchange-correlation density functional. *Mol Phys* **1997,** 91, 847-859.

160. Mulliken, R. S., Electronic populations analysis on LCAO-MO molecular wave functions. *J. Chem. Phys* **1955,** 23, 1833, 1841, 2338, 2343.

161. Stout, E. W.; Politzer, P., *Theor Chim Acta* **1968,** 12, 379.

162. Ros, P.; Schuit, G. C. A., *Theor Chim Acta* **1966,** 4, 1.

163. Cusachs, L. C.; Politzer, P., On the problem of defining the charge on an atom in a molecule. *Chem Phys Lett* **1968,** 1, 529.

164. Löwdin, P. Q., On the orthogonality problem. *Advances in Quantum Mechanics* **1970,** 5, 185.

165. Reed, A. E.; Weinstock, R. B.; Weinhold, F., Natural population analysis. *J Chem Phys* **1985,** 83, (2), 735.

166. Reed, A. E.; Curtiss, L. A.; Weinhold, F., Intermolecular interactions from a natural bond orbital, donor-acceptor viewpoint. *Chem Rev* **1988,** 88, 899-926.

167. Kerdcharoen, T.; Morokuma, K., ONIOM-XS: an extension of the ONIOM method for molecular simulation in condensed phase. *Chem Phys Lett* **2002,** 355, (3-4), 257-262.

168. Svensson, M.; Humbel, S.; Froese, R.; Matsubara, T.; Sieber, S.; Morokuma, K., ONIOM : A multilayered integrated MO+MM method for geometry optimizations and single piont energy predictions. A test for Diels-Alder reactions and Pt(P(t-Bu)$_3$)$_2$+H$_2$ oxidative addition. *J Phys Chem* **1996,** 100, (50), 19357-19363.

169. Vreven, T.; Morokuma, K., The ONIOM (our own N-layered integrated molecular orbital + molecular mechanics) method for the first singlet excited (S$_1$) state photoisomerization path of a retinal protonated Schiff base. *J Chem Phys* **2000,** 113, (8), 2969-2975

170. Vreven, T.; Morokuma, K.; Farkas, Ö.; Schlegel, H. B.; Frisch, M. J., Geometry optimization with QM/MM, ONIOM, and other combined methods. I. Microiterations and constraints. *J Comput Chem* **2003,** 24, (6), 760-769.

171. Maseras, F.; Morokuma, K., IMOMM: a new integrated ab initio+molecular mechanics geometry optimization scheme of equilibrium structures and transition states. *J Comput Chem* **1995,** 16, (9), 1170-1179.

172. Charles W. Bauschlicher, Jr.; Harry, P., A modification of the Gaussian-2 approach using density functional theory. *J Chem Phys* **1995,** 103, (5), 1788-1791.

173. Karadakov, P. B.; Morokuma, K., ONIOM as an efficient tool for calculating NMR

chemical shielding constants in large molecules. *Chem Phys Lett* **2000,** 317, (6), 589-596.

174. Davies, D. W., *The theory of the electric and magnetic proeprties of molecules*. Wiley: New York, 1967.

175. Kroto, H. W.; Heath, J. R.; O'Brien, S. C.; Curl, R. F.; Smalley, R. E., C_{60}: buckminsterfullerene. *Nature* **1985,** 318, (6042), 162-163.

176. Piskoti, C.; Yarger, J.; Zettl, A., C_{36}, a new carbon solid. *Nature* **1998,** 393, 771-774.

177. Smalley, R. E., Self-assembly of the fullerenes. *Acc Chem Res* **1992,** 25, 98-105.

178. Hunter, J.; Fye, J.; Jarrold, M. F., Carbon rings. *J Phys Chem* **1993,** 97, (14), 3460-3462.

179. Rohlfing, C.; Kaldor, J., Production and characterization of supersonic carbon cluster beams. *Chem Phys Lett* **1984,** 81, 3322-3330.

180. Krätschmer, W.; Lamb, L. D.; Fostiropoulos, K.; Huffman, D. R., Solid C_{60}: a new form of carbon. *Nature* **1990**, (347), 354-358.

181. Diederich, F.; Whetten, R. L., Beyond C_{60}: the higher fullerenes. *Acc Chem Res* **1992,** 25, (3), 119-26.

182. Iijima, S.; Ichihashi, T., Single-shell carbon nanotubes of 1-nm diameter. *Nature* **1993,** 363, 603-605.

183. Bethune, D. S.; Kiang, C. H.; de Vries, M. S.; Gorman, G.; Savoy, R.; Vazquez, J.; Beyers, R., Cobalt-catalyzed growth of carbon nanotubes with single-atomic-layer walls. *Nature* **1993,** 363, (6430), 605-607.

184. Ruoff, R. S.; Lorents, D. C.; Chan, B.; Malhotra, R.; Subramoney, S., Single crystal metals encapsulated in carbon nanoparticles. *Science* **1993,** 259, (5093), 346-348

185. Saito, Y.; Yoshikawa, T.; Inagaki, M.; Tomita, M.; Hayashi, T., Growth and structure of graphitic tubules and polyhedral particles in arc-discharge. *Chem Phys Lett* **1993,** 204, (3-4), 277-282.

186. Oku, T.; Hirano, T.; Kuno, M.; Kusunose, T.; Niihara, K.; Suganuma, K., Synthesis, atomic structures and properties of carbon and boron nitride fullerene materials. *Mat Sci Eng B-SOLID* **2000,** 74, (1-3), 206-217.

187. Sattler, K., Scanning tunneling microscopy of carbon nanotubes and nanocones. *Carbon* **1995,** 33, (7), 915-20.

188. Saito, Y.; Matsumoto, T., Carbon nano-cages created as cubes. *Nature* **1998,** 392, 237.

189. Saito, Y.; Yoshikawa, T.; Okuda, M.; Fujimoto, N.; Sumiyama, K.; Suzuki, K.; Kasuya, A.; Nishina, Y., Carbon nanocapsules encaging metals and carbides. *J Phys Chem Solids* **1993,** 54, (12), 1849-1860.

190. Ugarte, D., Curling and closure of graphitic networks under electron-beam irradiation *Nature* **1992,** 359, 707-709.

191. Takenobu, T.; Shiraishi, M.; Yamada, A.; Ata, M.; Kataura, H.; Iwasa, Y., Hydrogen storage in C_{70} encapsulated single-walled carbon nanotube. *Synth Met* **2003,** 135-136, 787-788.

192. Haufler, R. E.; Conceicao, J.; Chibante, L. P. F.; Chai, Y.; Byrne, N. E.; Flanagan, S.; Haley, M. M.; O'Brien, S. C.; Pan, C.; Xiao et, a., Efficient production of C_{60} (Buckminsterfullerene), $C_{60}H_{36}$, and the solvated Buckide ion. *J Chem Phys* **1990,** 94, (24), 8634-8636.

193. Seifert, G., Hydrogen on and in carbon nanostructures. *Solid State Ionics* **2004,** 168, (3-4), 265-269.

194. Türker, L.; Erkoç, S., AM1 treatment of endohedrally hydrogen doped fullerene, $nH_2@C_{60}$. *J Mol Struct :THEOCHEM* **2003,** 638, (1-3), 37-40.

195. Dunlap, B. I.; Brenner, D. W.; Mintmire, J. W.; Mowrey, R. C.; White, C. T., Geometric and electronic structures of $C_{60}H_{60}$, $C_{60}F_{60}$ and $C_{60}H_{36}$. *J Phys Chem* **1991,** 95, (15), 5763-5768.

196. Scuseria, G. E., Ab initio theoretical predictions of the equilibrium geometries of C_{60}, $C_{60}H_{60}$ and $C_{60}F_{60}$. *Chem Phys Lett* **1991,** 176, (5), 423-427.

197. Türker, L., Hydrogen storage behavior of C_{116} system-AM1 treatment. *Int J Hydrogen Energy* **2003,** 28, (10), 1115-1119.

198. Oku, T.; Kuno, M.; Narita, I., Hydrogen storage in boron nitride nanomaterials studied by TG/DTA and cluster calculation. *J Phys Chem Solids* **2004,** 65, (2-3), 549-552.

199. Oku, T.; Narita, I., Calculation of H_2 gas storage for boron nitride and carbon nanotubes studied from the cluster calculation. *Physica B: Condensed Matter* **2002,** 323, (1-4), 216-218.

200. Oku, T.; Kuno, M., Synthesis, argon/hydrogen storage and magnetic properties of boron nitride nanotubes and nanocapsules. *Diamond Relat Mater* **2003,** 12, (3-7), 840-845.

201. Stewart, J. J. P., Optimization of parameters for semiempirical methods I. Method. *J Comput Chem* **1989,** 10, (2), 209-220.

202. Stewart, J. J. P., Optimization of parameters for semiempirical methods II. Applications. *J Comput Chem* **1989,** 10, (2), 221-264.

203. Saunders, M.; Cross, R. J.; Jiménez-Vázquez, H. A.; Shimshi, R.; Khong, A., Noble Gas Atoms Inside Fullerenes. *Science* **1996,** 271, 1693-1697.

204. Weiske, T.; Hrusak, J.; Böhme, D. K.; Schwarz, H., Formation of endohedral carbon-cluster noble-gas compounds with high-energy bimolecular reactions: $C_{60}He^{n+}$ (n=1,2). *Chem Phys Lett* **1991,** 186, (4-5), 459-462

205. Niedermayer, C.; Reid, I. D.; Roduner, E.; Anssaldo, E. J.; Bernhard, C.; Binninger, U.; Glückler, H.; E. Recknagel; Budnick, J. I.; Weidinger, A., Simultaneous observation of muonium and multiple free radicals in muon-implanted C_{70}. *Phys Rev B: Condens Matter* **1993,** 47, 10923-10926.

206. Chen, J.; Kuriyama, N.; Yuan, H.; Takeshita, H. T.; Sakai, T., Electrochemical Hydrogen Storage in MoS2 Nanotubes. *J Am Chem Soc* **2001,** 123, (47), 11813 - 11814.

207. Jurewicz, K.; Frackowiak, E.; Beguin, F., Electrochemical storage of hydrogen in

activated carbons. *Fuel Process Technol* **2002,** 77-78, 415-421.

208. Dewar, M. J. S.; Thiel, W., Ground states of molecules. 38. The MNDO method. Approximations and parameters. *J Am Chem Soc* **1977,** 99, (15), 4899-4907.

209. Davis, L. P.; Guidry, R. M.; Williams, J. R.; Dewar, M. J. S.; Rzepa, H. S., MNDO calculations for compounds containing aluminum and boron. *J Comput Chem* **1981,** 2, (4), 433-445.

210. Frisch, M. J.; Head-Gordon, M.; Pople, J. A., A direct MP2 gradient method. *Chem Phys Lett* **1990,** 166, (3), 275-280.

211. Frisch, M. J.; Head-Gordon, M.; Pople, J. A., Semi-direct algorithms for the MP2 energy and gradient. *Chem Phys Lett* **1990,** 166, (3), 281-289.

212. Head-Gordon, M.; Head-Gordon, T., Analytic MP2 frequencies without fifth-order storage. Theory and application to bifurcated hydrogen bonds in the water hexamer. *Chem Phys Lett* **1994,** 220, (1-2), 122-128.

213. Saebo, S.; Almlof, J., Avoiding the integral storage bottleneck in LCAO calculations of electron correlation. *Chem Phys Lett* **1989,** 154, (1), 83-89.

214. Anders, E.; Koch, R.; Freunscht, P., Optimization and application of lithium parameters for PM3. *J Comput Chem* **1993,** 14, (11), 1301-1312.

215. Dewar, M. J. S.; Jie, C.; Zoebisch, E. G., AM1 calculations for compounds containing boron. *Organometallics* **1988,** 7, (2), 513-521.

216. Dewar, M. J. S.; Holder, A. J., AM1 parameters for aluminum. *Organometallics* **1990,** 9, (2), 508-511.

217. Haser, M.; Almlof, J.; Scuseria, G. E., The equilibrium geometry of C_{60} as predicted by second-order (MP2) perturbation theory. *Chem Phys Lett* **1991,** 181, (6), 497-500.

218. Hawkins, J. M.; Meyer, A.; Lewis, T. A.; Loren, S.; Hollander, F. J., Crystal structure of osmylated C_{60}: confirmation of the soccer ball framework. *Science* **1991,** 252, (5003), 312-313.

219. Yannoni, C. S.; Bernier, P. P.; Bethune, D. S.; Meijer, G.; Salem, J. R., NMR determination of the bond lengths in C_{60}. *J Am Chem Soc* **1991,** 113, (8), 3190-3192.

220. Disch, R. L.; Schulman, J. M., On symmetrical clusters of carbon atoms: C_{60}. *Chem Phys Lett* **1986,** 125, (5-6), 465-466.

221. Murphy, T. A.; Pawlik, T.; Weidinger, A.; Höhne, M.; Alcala, R.; Spaeth, J.-M., Observation of Atomlike Nitrogen in Nitrogen-Implanted Solid C_{60}. *Phys Rev Lett* **1996,** 77, 1075-1078.

222. Xia, Y.; Zhao, M.; Ma, Y.; Liu, X.; Ying, M.; Mei, L., Condensation and phase transition of hydrogen molecules confined in single-walled carbon nanotubes. *Phys Rev B: Condens Matter* **2003,** 67, (11), 115117.

223. Gordillo, M. C.; Boronat, J.; Casulleras, J., Zero-Temperature Equation of State of Quasi-One-Dimensional H_2. *Phys Rev Lett* **2000,** 85, 2348–2351.

224. Diep, P.; Johnson, J. K., An accurate H_2-H_2 interaction potential from first principles. *J Chem Phys* **2000,** 112, (10), 4465-4473.

225. Diep, P.; Johnson, J. K., Erratum: "An accurate H_2-H_2 interaction potential from first principles" [Journal of Chemical Physics 112, 4465 (2000)]. *J Chem Phys* **2000,** 113, (8), 3480-3481.

226. Roy, G. G.; Yung Sik, K., Theory for the Forces between Closed-Shell Atoms and Molecules. *J Chem Phys* **1972,** 56, (6), 3122-3133.

227. Alonso, J.; Arellano, J.; Molina, L.; Rubio, A.; Lopez, M., Interaction of molecular and atomic hydrogen with single-wall carbon nanotubes. *IEEE TRANS NANOTECHNOL* **2004,** 3, (2), 304-310.

228. Nikolaev, P.; Thess, A.; Rinzler, A. G.; Colbert, D. T.; Smalley, R. E., Diameter doubling of single-wall nanotubes. *Chem Phys Lett* **1997,** 266, (5-6), 422.

229. Terrones, M.; Terrones, H.; Banhart, F.; Charlier, J. C.; Ajayan, P. M., Coalescence of Single-Walled Carbon Nanotubes. *Science* **2000,** 288, (5469), 1226-1229.

230. Arellano, J. S.; Molina, L. M.; Rubio, A.; Lopez, M. J.; Alonso, J. A., Interaction of molecular and atomic hydrogen with (5,5) and (6,6) single-wall carbon nanotubes.

J Chem Phys **2002,** 117, (5), 2281-2288.

231. Verónica, B.; Jochen, H.; Gustavo, E. S., Interaction of atomic hydrogen with single-walled carbon nanotubes: A density functional theory study. *J Chem Phys* **2004,** 120, (15), 7169- 7173.

232. Yang, F. H.; Yang, R. T., Ab initio molecular orbital study of adsorption of atomic hydrogen on graphite:: Insight into hydrogen storage in carbon nanotubes. *Carbon* **2002,** 40, (3), 437-444.

233. Froese, R. D. J.; Morokuma, K., Accurate calculations of bond-breaking energies in C_{60} using the three-layered ONIOM method. *Chem Phys Lett* **1999,** 305, (5-6), 419-424.

234. Tschumper, G. S.; Morokuma, K., Gauging the applicability of ONIOM (MO/MO) methods to weak chemical interactions in large systems: hydrogen bonding in alcohol dimers. *J. of Mol. Structure.: THEOCHEM* **2002,** 592, (1-3), 137-147.

235. Bauschlicher, C. W., Jr., High Coverages of Hydrogen on a (10,0) Carbon Nanotube. *Nano Lett* **2001,** 1, (5), 223-226.

236. Basiuk, V. A., ONIOM Studies of Chemical Reactions on Carbon Nanotube Tips: Effects of the Lower Theoretical Level and Mutual Orientation of the Reactants. *J Phys Chem B* **2003,** 107, (34), 8890 -8897.

237. Han, S.; Lee, H., Adsorption properties of hydrogen on (10,0) single-walled carbon nanotube through density functional theory. *CARBON* **2004,** 42, (11), 2169-2177.

238. Lee, E. C.; Kim, Y. S.; Jin, Y. G.; Chang, K. J., First-principles study of hydrogen adsorption on carbon nanotube surfaces. *Phys Rev B: Condens Matter* **2002,** 66, 073415(1)-073415(4).

239. Yildirim, T.; Gülseren, O.; Ciraci, S., Exohydrogenated single-wall carbon nanotubes. *Phys Rev B: Condens Matter* **2001,** 64, (7), 075404.

240. Gülseren, O.; Yildirim, T.; Ciraci, S., Tunable Adsorption on Carbon Nanotubes. *Phys Rev Lett* **2001,** 87, (11), 116802.

241. Han, S. S.; Lee, H. M., Adsorption properties of hydrogen on (10,0) single-walled

carbon nanotube through density functional theory. *Carbon* **2004,** 42, (11), 2169-2177.

242. Blase, X.; Benedict, L. X.; Shirley, E. L.; Louie, S. G., Hybridization effects and metallicity in small radius carbon nanotubes. *Phys Rev Lett* **1994**, (72), 1878-1881.

243. Sánchez-Portal, D.; Artacho, E.; Soler, J. M.; Rubio, A.; Ordejón, P., Ab initio structural, elastic, and vibrational properties of carbon nanotubes. *Phys Rev B: Condens Matter* **1999,** 59, 12678-12688.

244. Gang, L.; Henry, S.; Nicholas, K., Hydrogen-induced unzipping of single-walled carbon nanotubes. *Phys Rev B: Condens Matter* **2003,** 68, (20), 205416.

245. Lide, D. R., *CRC Handbook of Chemistry and Physics*. 75th ed ed.; CRC Press, Boca Raton , Florida: 1995; p 1913-1995.

246. Gülseren, O.; Yildirim, T.; Ciraci, S., Effects of hydrogen adsorption on single-wall carbon nanotubes: Metallic hydrogen decoration. *Phys Rev B: Condens Matter* **2002,** 66, (12), 121401.

247. Li, J.; Furuta, T.; Goto, H.; Ohashi, T.; Fujiwara, Y.; Yip, S., Theoretical evaluation of hydrogen storage capacity in pure carbon nanostructures. *J Chem Phys* **2003,** 119, (4), 2376-2385.

248. Meregalli, V.; Parrinello, M., Review of theoretical calculations of hydrogen storage in carbon-based materials. *Appl Phys A: Mater Sci Process* **2001,** 72, (2), 143 - 146.

249. Han, S. S.; Lee, H. M., Adsorption propeties of hydrogen on (10,0) single-walled carbon nanotube through density functional theory. *Carbon* **2004,** 42, 2169-2177.

250. O'Boyle, N. M.; Vos, J. G. GaussSum 0.9, Dublin City University, . Available at http://gausssum.sourceforge.net.

251. Hess, B. A., Jr.; Schaad, L. J., Hueckel molecular orbital pi resonance energies. Benzenoid hydrocarbons. *J Am Chem Soc* **1971,** 93, 2413.

252. Haddon, R. C.; Fukunaga, T., Unified theory of the thermodynamic and kinetic criteria of aromatic character in the [4n+2]annulenes. *Tetrahedron Lett* **1980,** 21, (13),

1191-1192.

253. Pearson, R. G. In *Absolute electronegativity and hardness correlated with molecular orbital theory*, Proc Natl Acad Sci U S A, 1986; 1986; p 22.

254. Pearson, R. G., Electronic spectra and chemical reactivity. *J Am Chem Soc* **1988,** 110, (7), 2092-2097.

255. Pearson, R. G., Absolute electronegativity and hardness: applications to organic chemistry. *J Org Chem* **1989,** 54, (6), 1423-1430.

256. Zhou, Z.; Parr, R. G.; F. Garst, J., Absolute hardness as a measure of aromaticity. *Tetrahedron Lett* **1988,** 29, (38), 4843-4846.

257. Zhou, Z.; Parr, R. G., New measures of aromaticity: absolute hardness and relative hardness. *J Am Chem Soc* **1989,** 111, (19), 7371-7379.

258. Diener, M. D.; Alford, J. M., Isolation and properties of small-bandgap fullerenes. *Nature* **1998,** 393, (6686), 668-671.

259. Liu, X.; Westre, S. G.; Getty, J. D.; Kelly, P. B., Examination of the ketene 1B1 state photodissociation dynamics by far-ultraviolet resonance Raman spectroscopy. *Chem Phys Lett* **1992,** 188, (1-2), 42-48.

260. Manolopoulos, D. E.; May, J. C.; Down, S. E., Theoretical studies of the fullerenes: C_{34} to C_{70}. *Chem Phys Lett* **1991,** 181, (2-3), 105-111.

261. Seongjun, P.; Deepak, S.; Kyeongjae, C., Local reactivity of fullerenes and nanodevice applications. *Nanotechnology* **2001,** 12, (3), 245.

262. Haddon, R. C.; Hebard, A. F.; Rosseinsky, M. J.; Murphy, D. W.; Duclos, S. J.; Lyons, K. B.; Miller, B.; Rosamilia, J. M.; Fleming, R. M.; Kortan, A. R.; Glarum, S. H.; Makhija, A. V.; Muller, A. J.; Eick, R. H.; Zahurak, S. M.; Tycko, R.; Dabbagh, G.; Thiel, F. A., Conducting films of C_{60} and C_{70} by alkali-metal doping. *Nature (London)* **1991,** 350, 320 - 322.

263. McQuarrie, D. A.; Simon, J. D., *Physical chemistry : a molecular approach*. University Science Books: c1997.